Modeling the Diffusion of Interstitial Impurities and their Impact on the Ageing of Ferritic Steels

Rafael Herschberg Basualdo

NNT: 2018 SACLS 443

Modeling the Diffusion of Interstitial Impurities and their Impact on the Ageing of Ferritic Steels

Thèse de doctorat de l'Université Paris-Saclay
préparée *à* l'Université Paris-Sud

École doctorale n°564 Physique en Ile-de-France (PIF)
Spécialité de doctorat : Physique

Thèse présentée et soutenue à Gif-sur-Yvette, le 4 décembre 2018, par

Rafael Herschberg Basualdo

Composition du Jury :

Fabienne Berthier Directrice de Recherche, Université Paris-Sud (ICMMO)	Présidente du jury
Cristelle Pareige Maitre de conférences, Université et INSA de Rouen (GPM)	Rapporteur
Michel Perez Professeur, INSA Lyon (MATEIS)	Rapporteur
Alain Portavoce Chargé de Recherche, Université d'Aix-Marseille et de Toulon (IM2NP)	Examinateur
Maylise Nastar Directrice de Recherche, CEA Saclay (SRMP)	Directice de thèse
Frédéric Soisson Ingénieur de Recherche, CEA Saclay (SRMP)	Encadrant

Thèse de doctorat

Table of contents

Acknowledgments

Acknowledgments

It is amazing how time flies when doing a PhD. It is even more surprising the amount of people you get to meet during this period and who gives you a helping hand in times of need. This is the moment to properly thank them.

I want to thank my director, Dr. Maylise Nastar, and my encadrant, Dr. Frédéric Soisson, for guiding me through out these years. Because of your teachings and your wisdom, I have learnt everything I know about multiscale modelling, Monte Carlo simulations and how to perform good quality scientific research. I also want to thank Dr. Chu-Chun Fu for her DFT database and for insightful discussions about my pair interaction models.

I am thankful with the members of my jury for taking the time to analyze in-depth my manuscript and for their fruitful discussions during my presentation: Dr. Michel Perez, Dr. Cristelle Pareige, Dr. Fabienne Berthier and Dr. Alain Portavoce.

I am indebted with Dr. Jean-Luc Bechade for giving me the opportunity to do research at SRMP and for his constant support during these three years. I also want to thank the other PhD students who welcomed me in SRMP: Anton, Elric, Camille and Lisa.

CEA Saclay is a multicultural environment where I was able to meet and befriend with several PhD students, some postdocs and a few permanents. I am deeply thankful to Aninda, Ashish, Malik, Lomello, Sandra and so many others who helped me during this period.

I want to thank the members of my family who gave me their support and their blessing in order to do my PhD in France: my mother Virginia, my brother Miguel. I also fondly remember those who are not here with us but they still have a huge influence in my life: my father Miguel and my grandmother Esperanza.

I am fondly grateful with Chanel Valera for her constant love and support, and for staying by my side through thick and thin.

I am as well grateful with Mme. Fu, one of my very first teachers who passed me her passion for mathematics and physics.

Moreover, there is a big probability that I have forgotten to mention a lot of people who also deserve recognition. If that is the case, I am sorry and I will personally thank them for their help during these years.

Introduction

Ferritic steels, based on the binary body centered cubic (bcc) Fe-Cr system, have a very large range of applications because of their corrosion resistance and mechanical properties. In the nuclear industry they are considered as structural materials of future fusion and fission reactors (e.g. for fuel cladding and structures in high flux zones), because of a good resistance to some irradiation effects, especially to void swelling. But these alloys are subject to other irradiation effects, such as an acceleration of the precipitation of a Cr-rich (α') phase, which may damage the mechanical properties. Previous experimental and theoretical studies have shown that such non-equilibrium processes are highly dependent on the properties of point defects: vacancies and self-interstitials.

It is also common to find interstitial impurities in ferritic alloys, such as carbon, oxygen and nitrogen, which have a smaller size than substitutional solutes. Because of this difference in size, they are located in octahedral sites of the bcc lattice and diffuse by the direct interstitial mechanism. It has been shown that interstitial impurities have a strong interaction with vacancies and self-interstitials, which might affect the diffusion of these point defects. If the interstitials are able to slow down the diffusion of vacancies and self-interstitials, it would produce a retardation of the accelerated precipitation under irradiation. The present study focuses on these issues. The first step is to understand the diffusion of interstitial atoms, at various length scales, in both dilute and concentrated alloys.

As often in solid state diffusion, a central question is to establish the link between the atomic mechanisms of diffusion (i.e. the jump frequencies of individual point defects and atoms) and the experimental transport coefficients. Most of the experimental studies in the literature focus on the tracer diffusion (TD) and inter-diffusion coefficients. These experiments are performed at high temperature and provide a characterization of the long-range diffusion (a few microns). To study the interstitial diffusion one additional technique is available: internal friction (IF), which yields information on the short-range diffusion and which may be performed at lower temperatures. In Fe-Cr-C alloys, there are TD and IF experimental data in both dilute and concentrated alloys, but they present puzzling contradictions. Theoretical models that analyze the direct interstitial diffusion are much less developed than those devoted to substitutional diffusion which occurs by the vacancy-exchange mechanism. The relationship between the elementary jumps of interstitials and the IF peak [1,2] as well as the transport coefficient [3] has been extensively studied in dilute alloys, but it is still not well-known for concentrated alloys.

This thesis is divided in four chapters. In chapter 1 we explain our multiscale approach, developed to model interstitial diffusion – and more particularly internal friction – in concentrated alloys and we examine the previous models found in the literature. Our modelling approach consists in three distinctive steps. First, we obtain precise information

about the interactions between interstitial atoms and substitutional solutes (binding energies and migration barriers) using Density Functional Theory (DFT) calculations. Second, we develop pair interaction models fitted on these data in order to compute the migration barriers for any local chemical environment. Third, we use these models in our Atomistic Kinetic Monte Carlo (AKMC) codes in order to model TD and IF experiments.

In chapter 2 we model the carbon diffusion in random Fe-Cr solid solutions. The AKMC helps us to understand the different experimental observations, which disagree on the effect of the Cr concentration on C diffusion. In Fe-rich alloys, we find that repulsive C-Cr interactions play a key role in understanding this disagreement. In Cr-rich alloys, an original behavior is predicted: the average migration enthalpies measured by TD and IF experiments are different due to an attractive C-Fe interaction, resulting in strong trapping and correlation effects. Unfortunately, there are no experimental results of the carbon diffusion in Cr-rich alloys, where the C-Fe interactions are attractive, in order to compare with our predictions.

In chapter 3 we test the same method on a quite different case: dilute Nb-V-O alloys. Unlike Cr-rich alloys, this is a well-known system from an experimental point of view, where the strong oxygen-vanadium attraction plays a key role. This interaction is responsible of the formation of distinct IF peaks which provide a direct insight on the stability of O-V clusters. We perform a systematic study and compare our results with those found in the experimental literature. We also apply the Koiwa model [1,2] in order to better understand the effects of the cluster distribution and the jump frequencies on the IF response.

In chapter 4 we present a preliminary study on the effect of carbon on the kinetics of the α' precipitation under irradiation. It is known that carbon atoms have an attractive interaction with vacancies, which slows down the diffusion of the latter. During thermal ageing, this does not result in a retardation of the diffusion of substitutional solute atoms (Fe and Cr) and therefore of the precipitation kinetics, because new vacancies are created in order to sustain the vacancy concentration at thermal equilibrium. Under irradiation, high point defect concentrations are sustained and the effect of the retardation of the vacancy diffusion on the α' precipitation is still not well understood. We show that our simulations suggest that it strongly depends on the dominant mechanism for the elimination of excess point defects.

References

[1] M. Koiwa, Theory of the Snoek Effect in Ternary B.C.C alloys, Philos. Mag. 24 (1971) 81–106. doi:http://dx.doi.org/10.1080/14786437108216426.

[2] M. Koiwa, Theory of the Snoek Effect in Ternary B.C.C. Alloys : II. Simplified Treatment, Philos. Mag. 24 (1971) 107–122.

[3] T. Schuler, M. Nastar, Transport properties of dilute α-Fe(X) solid solutions (X = C, N, O), Phys. Rev. B. 93 (2016) 224101. doi:10.1103/PhysRevB.93.224101.

Chapter 1: Models for interstitial diffusion in metals and alloys

The aim of this first chapter is to provide the theoretical framework from which this work was made. First, we will give a broad overview on point defects, their diffusion mechanisms and some key elements on transition state theory. Second, we will introduce the concepts of tracer diffusion coefficient and internal friction (in the particular case of the Snoek relaxation), how they are measured experimentally and what theoretical models have been proposed in the literature. Third, we will present the methodology used in this thesis to simulate tracer diffusion and internal friction in alloys. The problem in which we are interested is in how the atomistic phenomena (i. e. the jump frequency) is connected with the macroscopic variables. In the case of tracer diffusion experiments, this relationship is via the tracer diffusion coefficient, while for internal friction experiments is via the temperature of the Snoek peak. The question we want to answer is: do these macroscopic variables reflect the same average jump frequency in pure metals and in alloys?

1. Introduction

1.1. General remarks

The first equations describing the transport of matter were stated by Fick in 1855 [1]. His approach was purely phenomenological and empirical, without any derivation from first principles or considering the atomic mechanisms of diffusion. His first law describes a linear relationship between the flux of diffusing particles $\vec{J}$ and the gradient of its concentration $C(r,t)$ via the diffusion coefficient D:

$$\vec{J} = -D\vec{\nabla}C(r,t) \tag{1.1}$$

The negative sign indicates opposite directions between $\vec{J}$ and $\vec{\nabla}C(r,t)$. In this analysis, we assume that the concentration is conserved, from which we can formulate the continuity equation:

$$\vec{\nabla}\cdot\vec{J} + \frac{\partial C(r,t)}{\partial t} = 0\,. \tag{1.2}$$

Combining Eqs. (1.1) and (1.2), we obtain the second law of Fick:

$$\frac{\partial C(r,t)}{\partial t} = \vec{\nabla}\bullet\left(D\vec{\nabla}C(r,t)\right) \tag{1.3}$$

In the special case where the diffusion coefficient is independent of the concentration, Eq. (1.3) can be rewritten as:

$$\frac{\partial C(r,t)}{\partial t} = D\nabla^2 C(r,t) \tag{1.4}$$

where ∇^2 is the Laplacian operator.

As we will see in the following pages, one can relate D to the random walk performed by

atoms and to their diffusion mechanisms. This can be done by theoretical modelling or using numerical methods (such as Monte Carlo simulations). Experimentally, there are numerous methods for studying diffusion in solids. They can be grouped roughly into two major categories: direct and indirect methods [1]. The first group consists in experiments based on the phenomenological Fick laws (in other words, based on the measurement of concentration profiles $C(r,t)$), and they represent a measurement of the long-range diffusion. Examples are the measurement of the tracer concentration profiles (e. g. by radiotracer activity measurements, Rutherford backscattering or nuclear reaction analysis). Indirect methods consist in the measurement of jump frequencies by means of short-range diffusion. Examples of these methods are mechanical spectroscopy, magnetic relaxation and quasi-elastic neutron scattering.

Since direct and indirect methods correspond to different ways of exploring the energetic landscape of the jumping interstitial atoms, they may yield different values of average migration enthalpies. In the particular case where the interstitial atoms are diffusing in pure metals, direct and indirect methods yield the same migration enthalpy, as shown in [2] for the diffusion of C in α-Fe. In this thesis, we will compare tracer diffusion (TD) and internal friction (IF) experiments in two different systems: the Fe-Cr-C and dilute Nb-V-O alloys, where the diffusion of the interstitial atoms is affected by substitutional solutes. A multiscale modelling is developed in order to simulate TD and IF, and will be compared to available experimental studies and simple analytical models.

1.2. Point defects: diffusion mechanisms and jump frequencies

In a perfect crystal at 0 K, atoms are arranged in a periodic array. At elevated temperatures, there are defects which are disturbances of the lattice. We can define two distinct categories of defects: extended defects and point defects. The first group corresponds to disturbances extending over many lattice sites. These defects which are not in thermodynamic equilibrium are: dislocations, grain boundaries, twinning and stacking faults [3].

Point defects correspond to imperfections in solids which are localized over a few atomic sites [4] and are present in a solid at thermal equilibrium with its vapor. Examples of such defects are vacancies (missing atoms in a lattice position) and interstitials (atoms in non-lattice positions). A schematic image of point defects can be seen in Figure 1. Point defects can also be classified as intrinsic defects (vacancies and self-interstitials) and extrinsic defects – the addition of atoms of a different species than the metal, such as substitutional impurities and interstitials. We must make an important distinction between two different types of interstitial atoms. First, direct interstitials (or interstitial impurities) are foreign atoms (C, O) that are added to the metallic system and are of a smaller size than the substitutional solute atoms (Fe, Cr, Nb, V). Second, self-interstitials correspond to a configuration where two substitutional solute atoms share a bcc site. These self-interstitials may be produced, for example, by irradiation and usually have a “dumbbell” configuration (in the <110> direction

in Fe-Cr alloys). In order to avoid confusion, we will refer to direct interstitials as 'interstitials' and to self-interstitials as 'dumbbells'. This distinction will become very important in chapter 4.

Point defects usually control the diffusion in solids, and therefore the kinetics of segregation and precipitation. Diffusion phenomena determine important properties of metals and alloys. We will focus our analysis on the diffusion of interstitial atoms and how their diffusion properties are affected by substitutional impurities. This is particularly important in stainless steels, where the interstitial atoms (such as C, N and O) are known to be essential contributors to their mechanical properties and their corrosion resistance.

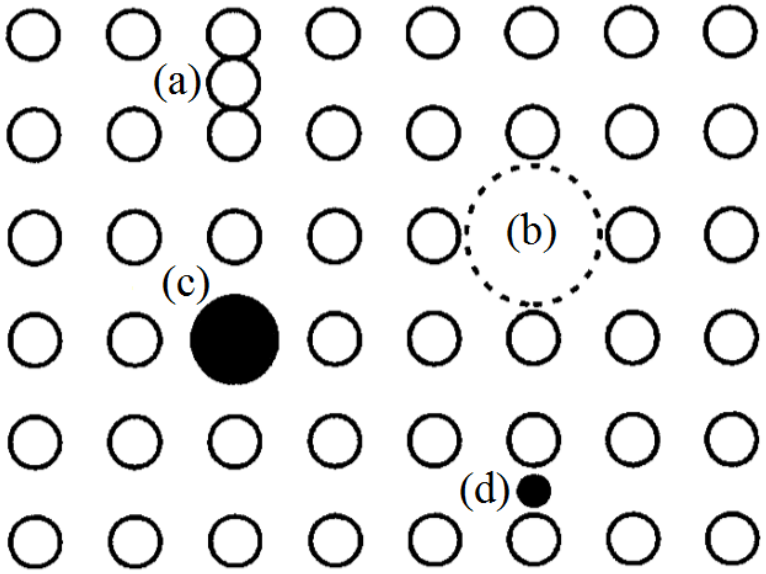

Figure 1: Examples of point defects in a crystal showing a self-interstitial (a), a vacancy (b), a substitutional impurity (c) and an interstitial impurity (d). Image adapted from [4].

It is well known that atoms in a crystal oscillate around their equilibrium positions [1]. Occasionally these oscillations become large enough to allow an atom to change sites and produce the diffusion of atomic species in the metal. In body center cubic (bcc) metals (like Fe, Cr, Nb, V), interstitial atoms (such as C, N and O) have octahedral sites as their equilibrium positions. They diffuse by thermally activated jumps between first nearest neighbors (nn) octahedral sites, through a saddle point located on a tetrahedral site [1], as shown in Figure 2.

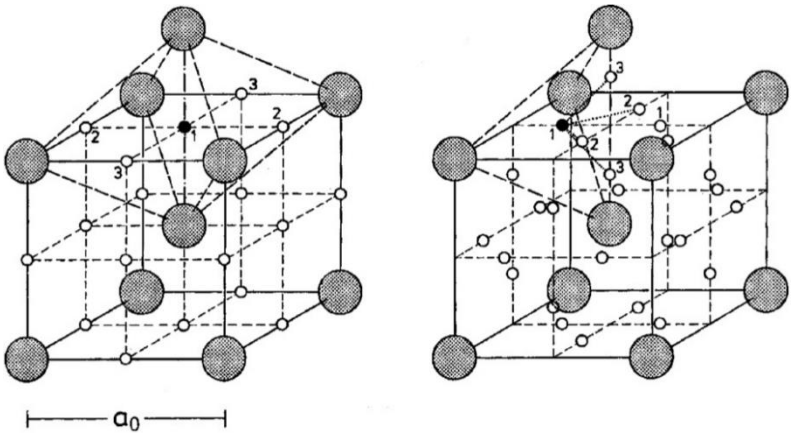

Figure 2: Interstitial atom (black dot) at the octahedral position (left) and at the saddle point (right) in a bcc lattice. Figure is extracted from [5].

1.3. Transition state theory

For the sake of simplicity, let us consider the case of a C atom in pure bcc iron. Transition state theory (TST), developed by Wert [6] and Vineyard [7], studies the rate at which atoms move from one site *i* to a neighboring site j. We start by defining τ as the mean time that a carbon (or a given interstitial atom) stays at *i*:

$$\frac{1}{\tau} = n'\upsilon \exp\left(\frac{-\Delta G_C^m(ij)}{k_B T}\right), \tag{1.5}$$

where n' is the number of equivalent paths of diffusion, υ is a constant, k_B is the Boltzmann constant, T is the temperature and $\Delta G_C^m(ij)$ is:

$$\Delta G_C^m(ij) = G_C^m(SP) - G_C^m(i) \tag{1.6}$$

where $G_C^m(SP)$ is the Gibbs free energy of the system when the C atom is at the saddle point between sites j and i, and $G_C^m(i)$ is the Gibbs free energy of the system when the C atom is at its initial interstitial position. $\Delta G_C^m(ij)$ corresponds to the work done when a single interstitial moves isothermally at a constant pressure between sites i and j [6]. We can also write $\Delta G_C^m(ij)$ in terms of the migration enthalpy $\Delta H_C^m(ij)$ and the migration entropy $\Delta S_C^m(ij)$ via:

$$\Delta G_C^m(ij) = \Delta H_C^m(ij) - T\Delta S_C^m(ij). \tag{1.7}$$

Eq. (1.5) can be written in terms of Eq. (1.7):

$$\frac{1}{\tau} = n'\upsilon \exp\left(\frac{\Delta S_C^m(ij)}{k_B} - \frac{\Delta H_C^m(ij)}{k_B T}\right). \tag{1.8}$$

By defining the jump frequency as $\Gamma_C(ij) = 1/n'\tau$ (the number of jumps per unit time to a particular neighboring site j) [1], Eq. (1.8) can be rewritten as:

$$\Gamma_C(ij) = \upsilon_0 \exp\left[\frac{-\Delta H_C^m(ij)}{k_B T}\right], \tag{1.9}$$

where υ_0 is the attempt jump frequency (an effective frequency associated with the vibration of the interstitial in the direction of the saddle point). In an alloy, the migration enthalpy will depend on the local chemical environment around the interstitial atom.

2. Tracer diffusion

2.1. Random walk theory

In this section we will summarize the random walk theory applied to the calculation of interstitial diffusion in pure metals and in alloys. In the dilute limit, this is equivalent to the calculation of the tracer diffusion coefficient. Our analysis is twofold. First, we study the relationship between the tracer diffusion coefficient and the long-range random walk performed by any tracer atom whatever their diffusion mechanism. Second, we apply this formulation to the interstitial diffusion.

As we have seen in the introduction, Fick's laws are continuum equations, dealing with a concentration field of tracer atoms, without considering the particular motion of the particles in the solid. First, we will assume that the system behaves as a cloud of diffusing particles, who travel a long-range distance R_C during a time t [8,9]. Second, we will assume that the amount of interstitial atoms is small, so that the diffusion coefficient is independent of the interstitial concentration. Third, we will assume that each jump is independent of the previous jumps.

We start our analysis with the Einstein-Smoluchowski relation, which links the mean square displacement $\langle R^2 \rangle$ performed by diffusing particles during a period of time t with the diffusion coefficient D (Eq. (1.1)) [1], regardless of their diffusion mechanism:

$$D = \frac{\langle R^2 \rangle}{6t}. \tag{1.10}$$

As we have seen in section 1.3, interstitial atoms diffuse by thermally activated jumps between first nearest neighbors (nn) octahedral sites. The displacement of a carbon atom after *n* jumps is:

$$R_C = \sum_{i=1}^{n} r_i, \tag{1.11}$$

where r_i is each elemental distance performed by the atoms. The squared magnitude of the displacement is

$$(R_C)^2 = \sum_{i=1}^{n} r_i^2 + 2\sum_{i=1}^{n-1}\sum_{j=i+1}^{n} r_i r_j, \tag{1.12}$$

and if we perform an average over a large number of similar sequences of *n* jumps, we obtain the mean square displacement $\langle R_C{}^2 \rangle$:

$$\left\langle R_C^{\,2}\right\rangle = \sum_{i=1}^{n}\left\langle r_i^{\,2}\right\rangle + 2\sum_{i=1}^{n-1}\sum_{j=i+1}^{n}\left\langle r_i r_j\right\rangle, \tag{1.13}$$

For a C atom in pure iron, all the interstitial sites are equivalent and the jump frequencies are all the same. The C atom performs a true random walk, where every jump is independent from each other, without any memory of the previous jumps. It means that for every jump with displacement r_i we can find another jump r_j which is in the opposite direction. In other words, the second term of Eq. (1.13) cancels out over a large amount of atomic jumps and the expression is reduced to:

$$\left\langle R_C^{\,2}\right\rangle_0 = \sum_{i=1}^{n}\left\langle r_i^{\,2}\right\rangle = n\left(\frac{a_0}{2}\right)^2 \tag{1.14}$$

where a_0 corresponds to the bcc lattice parameter.

The jump frequency Γ_C is the number of jumps given during a time t:

$$\Gamma_C = \frac{n}{Zt}, \tag{1.15}$$

where Z is the number of possible jumps (in this particular case, $Z = 4$ because out of 6 nearest neighbors, 2 are always blocked by Fe atoms on substitutional sites). By combining Eqs. (1.9), (1.10), (1.14) and (1.15), we obtain:

$$D_C = \frac{2}{3}\left(\frac{a_0}{2}\right)^2 \Gamma_C = \frac{2}{3}\left(\frac{a_0}{2}\right)^2 \upsilon_0 \exp\left(-\frac{\Delta H_C^m}{k_B T}\right). \tag{1.16}$$

which relates the diffusion coefficient D_C with the jump frequency Γ_C. Eq. (1.16) is only valid if the atom can only diffuse in the metal with a single migration barrier ΔH_C^m and a single jump frequency Γ_C.

For a C atom diffusing in an alloy, the jump frequencies depend on the local environment, which induces some correlations between successive jumps. An extreme case will be a C atom jumping back and forth between two sites separated by a very low migration barrier, slowing down its long-range diffusion. The correlation factor f_C is defined as [1]:

$$f_C = \lim_{n\to\inf}\frac{\left\langle R_C^{\,2}\right\rangle}{\left\langle R_C^{\,2}\right\rangle_0} = 1 + 2\lim_{n\to\inf}\frac{\sum_{i=1}^{n-1}\sum_{j=i+1}^{n} r_i r_j}{\sum_{i=1}^{n} r_i^{\,2}}, \tag{1.17}$$

f_C characterizes the deviation from a random walk. It depends on the concentration of the alloy as well as on temperature. In a pure metal, $\left\langle R_C^{\,2}\right\rangle = \left\langle R_C^{\,2}\right\rangle_0$ and $f_C = 1$.

In alloys, the jumps are not equally probable due to a spectrum of migration barriers ΔH_C^m. We can still define an average jump frequency $\bar{\Gamma}_C$ (with an associated average migration enthalpy $\Delta \bar{H}_C^m$) by Eq. (1.15) , which gives:

$$D_C = \frac{2}{3}\left(\frac{a_0}{2}\right)^2 f_C \upsilon_0 \exp\left(-\frac{\Delta \bar{H}_C^m}{k_B T}\right) \tag{1.18}$$

2.2. Experimental determination of the tracer diffusion coefficient

The simplest interdiffusion experiment consists in coupling two blocks of different chemical composition and perform an annealing in order to allow a diffusion of atoms of different species. Then, the concentration gradient is measured by chemical analysis or by measuring the specific activity of radiotracers. Thus, we obtain an interdiffusion coefficient. In the following section we will only consider interdiffusion coefficient in dilute alloys, which is also called the tracer diffusion coefficient.

A thin layer of tracer is deposited on the surface of the sample. After an annealing at a temperature T during a time t, the tracer concentration inside the sample is measured. If the thickness of the initial deposited tracer is comparable to the mean diffusion length, the tracer concentration is described by the thin-film solution of Fick's second law (Eq. (1.3)) [10].

Even though there are no restrictions on the composition of the tracer elements, small amounts (in the range of ppm) are used so that the overall alloy composition is almost unchanged. This experimental condition should guarantee that the interactions between tracer atoms and the other atoms of the same species in the metal do not change during the experiment. So, the resulting diffusion coefficient is only dependent on the overall concentration of the alloy. This technique has been considered the most accurate method in order to obtain good-quality diffusion measurements, with a reproducibility of a few percent [11] due to the high sensitivity of nuclear counting facilities. Nevertheless, it is important to highlight that the measured diffusion coefficient depends on the chemistry and the structure of the sample (i. e. the sample must be completely homogeneous). Defects such as impurities, grain boundaries and dislocations can interact with the tracer atoms and mostly produce a decrease of D_C. This technique consists in four different steps: deposition of the tracer, annealing of the sample, sectioning and profile analysis (Figure 3).

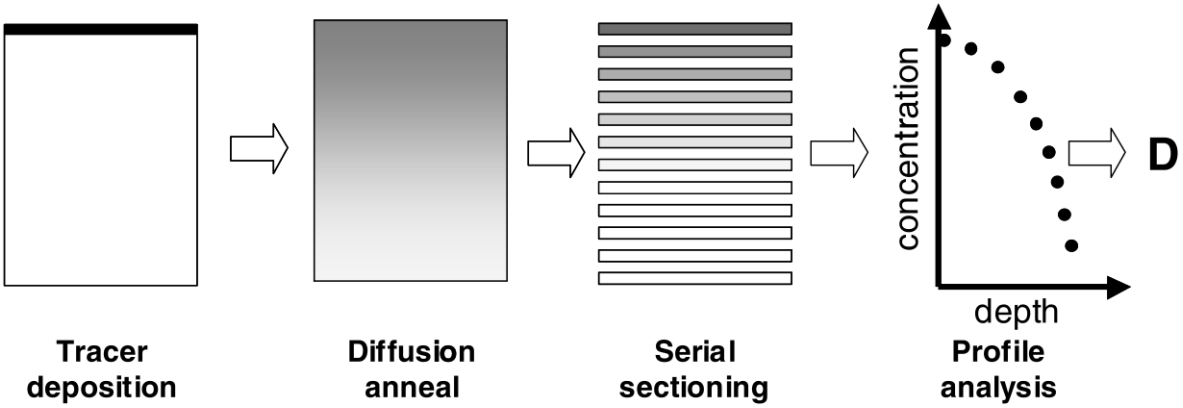

Figure 3: Major steps for the determination of the tracer diffusion coefficient. Image extracted from [1].

The first step consists in the preparation of a diffusion sample which has a flat, strain-free surface. Polishing of metals and oxides is usually done by standard metallographic techniques, followed by etching or electro-polishing to remove cold worked material. Then, the tracer is deposited onto the surface of the diffusion sample. Evaporation, dripping of a liquid solution, and electrodeposition of the radiotracer onto the surface are the major deposition techniques. In this step, the objective is to deposit the tracer so that it can be later dissolved in the base metal at a time much larger than the annealing time. Also, it is important to obtain a good yield of the tracer on the sample with minimum contamination of the equipment.

Following the tracer deposition, an isothermal anneal is performed at a temperature T for a given time t in an atmosphere that where the chemical composition of the sample remains unchanged. The most important factor in this step is the accuracy on the measurement of the temperature. Indeed, most of the dispersion of a diffusion coefficient is given by the uncertainty of T [11]. The measurement of the temperature is done with a sensor attached to the sample. The exact type of heating apparatus depends on the desired temperature range. For temperatures between 500 K and 2000 K, an electric resistance furnace is used. For higher temperatures, more sophisticated annealing techniques (e.g., electron-beam heating) are necessary.

Once the thermal treatment is performed onto the sample, the concentration profile is determined with serial-sectioning techniques. These consist in dividing the diffusion zone into sections and determining both the coordinates of the section and its concentration in the base metal, or the specific activity of the diffusing tracer. Most sectioning is done mechanically, while the exact technique depends on the studied material and the desired thickness of each section. Lathe sectioning is the standard method for ductile metals (such as pure Na, Al, Cu, Ag, Au and polymers) and alloys with $D > 10^{-16}$ m^2/s^{-1}. Grinding sectioning is the standard procedure of sectioning brittle materials (intermetallics, semiconductors, ionic crystals, ceramics and inorganic glasses), and for metals if the thickness of each metallic section has to be between 3 μm and 100 μm.

The final step is to study the concentration-depth profile and to deduce the diffusion coefficient by comparison with the corresponding solution of Fick's second law (Eq. (1.4)). By assuming that a thin layer of tracer atoms was placed on the surface of a semi-infinite sample (the base metal), the tracer concentration $C(x,t)$ after the annealing is described as [1]:

$$C(x,t) = \frac{M}{\sqrt{\pi D t}} \exp\left(-\frac{x^2}{4Dt}\right) \tag{1.19}$$

where M is the number of atoms per unit area, and $\sqrt{Dt}$ is called the diffusion length. A diagram of the logarithm of the tracer concentration $C(x,t)$ versus the penetration distance squared x^2 at a given time t yields a linear relationship as shown in Figure 4 and from its slope the tracer diffusivity is obtained. Note that there are sources that might affect the

measurement of the concentration profile (and consequently the tracer diffusivity) such as the presence of grain boundaries, loss of tracer atoms and evaporation of the base metal.

These techniques have been used for the diffusion of C in pure Fe and O in pure Nb. The details of the experimental results for the tracer diffusion measurements will be discussed in depth in chapters 2 and 3 for the Fe-Cr-C and Nb-V-O alloys, respectively. We must mention that radiotracers such as C^{14} and O^{18} are used in the experimental measurements of the tracer diffusion coefficient in pure metals [12–14], as shown in Figure 4 and 5.

As we observe from the experimental data provided by Landolt and Bornstein [15], we can see that substitutional solutes diffuse at a slower rate than direct interstitials because they need a vacancy. For example at 1000K, the value of self-diffusion coefficient of Fe is 10^{-17} m^2/s while the diffusion coefficient of C in pure Fe is 10^{-11} m^2/s. Moreover at 1250K, the value of self-diffusion coefficient of Nb is 10^{-21} m^2/s while the diffusion coefficient of O in pure Nb is 10^{-11} m^2/s.

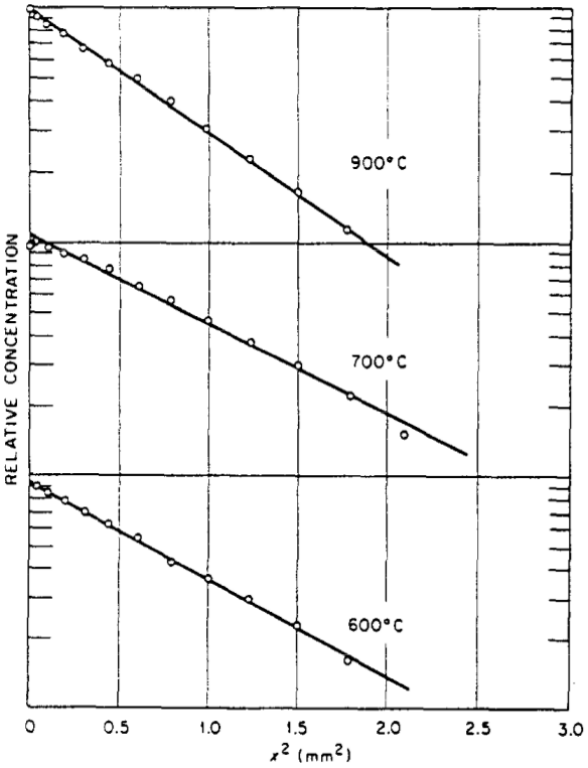

Figure 4: Penetration plots for oxygen diffusion in niobium. Image extracted from [14].

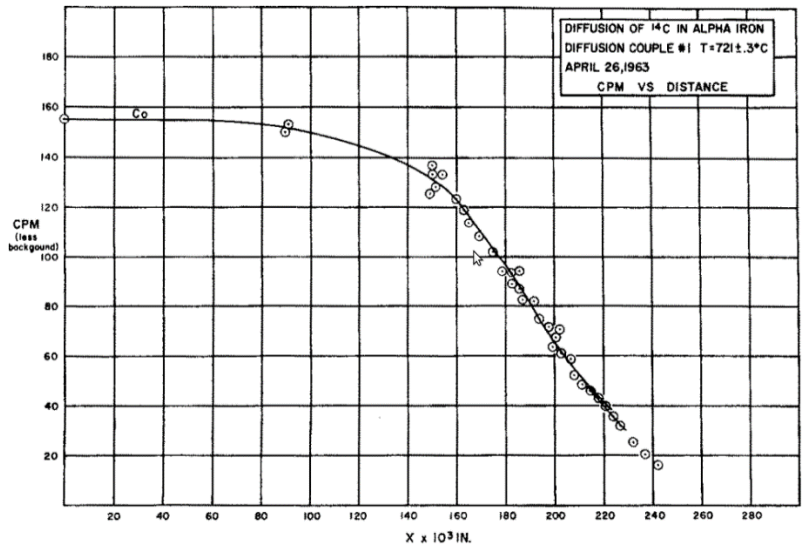

Figure 5: Penetration plot for carbon diffusion in iron. Image extracted from [12].

2.3. Previous modelling of the tracer diffusion coefficient in dilute alloys

In this study we are concerned in the modelling of the diffusion of interstitial atoms in metals and alloys, such as C in Fe-Cr alloys. We study the effect of substitutional solutes on the local migration barriers. The main challenge is to find a relationship between the tracer diffusion coefficient D_C and the average migration enthalpy $\Delta\bar{H}_C^m$. In pure Fe, where a single $\Delta H_C^m\left(Fe\right)$ is found, the relationship is straight forward (Eq. (1.16)). But in the case in alloys it is more difficult to define because of the correlation effects and due to a spectrum of possible ΔH_C^m . There are a few theoretical models that describe the diffusion coefficient of an interstitial in an alloy, compared to those found for the vacancy diffusion such as [16–18].

Several models attempt to relate the diffusivity of interstitials with the binding energy between the substitutional impurities with the interstitial atoms [14,19–23]. They have in common that they involve very dilute substitutional concentrations which are frozen in the lattice and a small concentration of interstitials (or no interstitial-interstitial interactions). The vast majority of the models in the literature assume an attractive binding energy up to 1 nn. Some of these models, such as the ones developed by Koiwa [20] or by Hennessey and Morral [23], are not able to predict the tracer diffusion coefficient where there is a substitutional solute-interstitial repulsion. In the particular case of [23], they argue that if the binding energy would be attractive, the random walk could not be achieved since there would be a high probability for an interstitial to form a pair with the substitutional, but in the case of a repulsive binding energy, the random walk would be affected by regions occupied by substitutional solute atoms, but the interstitials could still perform long-range diffusion far away from these regions (in dilute systems). As we will see, the effective tracer diffusion coefficient is a simple function that depends on D_C in the pure metal and in the binding

energy between interstitials and substitutional solutes.

Perkins and Padgett [14] analyzed the oxygen tracer diffusion in dilute Nb-Zr alloys. They assumed that the binding energy between Zr-O was only up to 1 nn and that the presence of a substitutional solute did not affect the saddle point energy of the migration barrier of oxygen. They computed the average times when the interstitial was trapped and when it was mobile as a combination of elementary jump frequencies. In other words, they assumed that the mean square displacements were equal when the O atom jumped in pure Nb and in dilute Nb-Zr alloys:

$$\left\langle R^2 \right\rangle = 6D_C t_C = 6D_{eff}\left(t_C - t_{eff}\right), \tag{1.20}$$

where D_C and D_{eff} are the tracer diffusion coefficients in pure metal and in the alloy respectively. The terms t_C and t_{eff} are the times spent by an oxygen atom in the pure metal and in close proximity to a trapping atom respectively. They also show that:

$$\frac{D_C}{D_{eff}} - 1 = \frac{\upsilon_T}{\upsilon_E}, \tag{1.21}$$

where υ_T and υ_E correspond to the jump frequencies of a trapped atom and of an oxygen that escapes a Zr atom. Using this model, they found that the binding energy between Zr-O pair was negligible for concentrations of Zr less than 1%.

Blazek [19] developed a very simple model where the substitutional solute atoms acted as traps for the interstitials. He considered a constant attractive binding energy between a single substitutional and a single interstitial and neglected interstitial-interstitial interactions. He then used a statistical thermodynamic distribution in order to find the diffusion coefficient and the correlation factor. His model predicted that the diffusivity in dilute alloys decreased initially with the substitutional concentration but then reached a minimum which was dependent on the "sphere of influence" of the substitutional solute atom around the interstitial. He related the effective diffusion coefficient D_{eff} as:

$$D_{eff} = D_C\left(1 - C_T\right) + D_{TL}C_T f\left(1 - A_T\right) + D_T C_T\left(1 - f\left(1 - A_T\right)\right), \tag{1.22}$$

where C_T is the concentration of trapped interstitials, D_C is the diffusion coefficient in the pure metal, D_T is the diffusion coefficient inside the traps, D_{TL} is the diffusivity of the interstitials that escape the trapping sites, A_T is the fraction of interstitial sites that are in trapping configurations and f is the amount of jumps that an interstitial needs in order to escape an isolated trap. Eq. (1.22) consists of three distinctive contributions. The first term corresponds to the joint contributions of the interstitials jumps in the pure metal and from the pure metal to a trap. The second term corresponds to interstitials that escape a trap. The last term corresponds to the jump from a trapping site to another one.

McLellan [21] also assumed that only 1 nn pairs were formed and that there was an equilibrium between the free and trapped interstitials. He used first-neighbor first-order statistics in order to calculate the temperature and the concentration dependence of the distribution of interstitial atoms between normal sites and trapping sites with a constant

saddle point energy. The form of the distribution function was a modified Fermi-Dirac function in order to avoid the trapping of all the interstitials by substitutional solutes at low temperatures. A calculation of the effect of traps on the diffusivity of interstitial atoms was then carried out based upon absolute rate reaction theory.

Oriani [22] assumed a local equilibrium between mobile and trapped interstitials in dilute alloys. One of the limitations of this model was that the diffusion of interstitials in the pure metal had to be long enough in order to maintain the equilibrium between trapped and non-trapped atoms. Another limitation was that it only works in dilute alloys due to the fact that the diffusion coefficient is also dependent of the total concentration of interstitials. He found a relationship between the effective diffusion coefficient D_{eff}, the diffusion coefficient in the pure metal D_C and the concentration of substitutional solutes X_S as:

$$D_{eff} = \frac{D_C}{\left(1 + 2X_S \exp\left(\frac{-E_b}{k_B T}\right)\right)} \tag{1.23}$$

Schuler and Nastar [24] modeled simultaneously the diffusion of a single vacancy with a single interstitial (C, N and O atoms) in pure Fe using a self-consistent mean field model. They were able to take into account the effect of the substitutional solutes on the thermodynamic properties of the interstitial atoms - based from previous DFT calculations - and study the flux couplings of this system. In spite the fact that each interstitial has a strong attractive binding energy with the vacancy, each interstitial presented a qualitatively different flux-coupling behavior: in the case of Va-O, there was always a positive coupling; whereas for Va-C, it was negative for any given temperature. They also provided an exact expression for the exact computation of the transport coefficients.

Hennessey and Morral [23] developed two different models, making a distinction if the binding energy between the substitutional and the interstitial was attractive or repulsive. In the case where there was an attraction between atomic species, the interstitial tended to form i-s pairs. If the interaction was repulsive, the interstitial would avoid the proximities of the substitutional solute atom but it could still jump close to it. They defined an average jump frequency of the interstitials in the alloy as a function of the jump frequencies when the atom was trapped and when it was diffusing in the pure metal. They found two different expressions for the correlation factor f_C, depending if the interstitial-substitutional interaction was attractive or repulsive. For the first case they found:

$$f_C = 1 - \frac{zX_S\left(1 - P_T\right)}{P_T + zX_S\left(1 - P_T\right)}, \tag{1.24}$$

where X_S is the concentration of substitutional solute atoms, z is the ratio of trap sites to normal sites and P_T is the probability of an interstitial to escape a trap. For the case where there was a repulsion between an interstitial and a substitutional solute atom, the correlation factor f_C was expressed as:

$$f_C = 1 - \frac{zX_S\left(1-P_R\right)\left(2+P_R\right)}{\left(1+P_R\right)}, \tag{1.25}$$

where P_R is the probability of entering a repulsive site.

Koiwa [20] considered a single substitutional interacting with a single interstitial in a bcc alloy. He considered two different processes: trapping of the interstitial by the substitutional and its escape. By assuming that the attractive binding energy only affected the interstitial at 1 nn, he proceeded to write the jump frequencies of interstitials. In order to find the time spent by the interstitial travelling in the alloy, he used the concept of mean first passage time. He found that the change in the saddle point energy by the substitutional solute had a significant effect on the calculated diffusion coefficient at low temperatures. For the special case where there was no change in the saddle point energy, he found a relationship between the effective diffusion coefficient D_{eff} with respect to the diffusion coefficient of the interstitial in the pure metal D_C as:

$$D_{eff} = \frac{D_C}{1-2X_S\left(1-\frac{\upsilon_0}{\upsilon_1}\exp\left(\frac{E_b}{k_BT}\right)\right)}, \tag{1.26}$$

where E_b is the interstitial-substitutional solute binding energy, T is the temperature, X_S is the concentration of substitutional solutes. υ_0 and υ_1 correspond to the attempt jump frequencies (Eq. (1.9)) in the pure metal and when the interstitial escapes a trap.

3. Internal Friction

3.1. Introduction

When a material is under the influence of an applied stress, the induced strain can be divided into two components. The first part corresponds to an instantaneous response, where Hooke's law is observed. The second component corresponds to a time-dependent strain: 'anelasticity' or 'anelastic relaxation'. This component of the strain is reversible: once the applied stress is removed, the sample will recover its initial shape after a certain period of time. Since there is no permanent strain after the application of the stress, anelasticity is not the same as plastic strain. The Internal Friction is defined as the dissipation of mechanical energy caused by anelastic processes occurring in a strained solid [1]. The inverse quality factor Q^{-1} is the ratio between the anelastic strain ε^O and the elastic strain ε^I [25]:

$$Q^{-1} = \frac{\varepsilon^O}{\varepsilon^I}. \tag{1.27}$$

This effect is very useful because it is a very sensitive method and it is possible to study diffusion phenomena at very low temperatures, for which direct methods are more difficult to perform due to the small free mean path of the interstitial. Nevertheless, due to its sensitivity, it is possible to find various sources that cause Internal Friction: point-defect reorientations (Snoek and Zener relaxations), long-range diffusion (Gorsky relaxation),

interactions between interstitials and dislocations [26]. We will focus on the modelling of the Snoek relaxation and we will compare our approach to others, such as those proposed by [25,27–29]. The following section is divided in three parts. First, we will briefly summarize the principles of the Snoek effect. Second, we will analyze how the external stress affects the jump frequency of the interstitial atoms. Last, we will analyze Q^{-1} in terms of the interstitial concentration in different sublattices at different temperatures.

3.2. The Snoek effect

The Snoek effect corresponds to the anelastic relaxation of a material submitted to a time oscillating external stress that can be caused by the stress-induced migration of interstitial atoms (C, N, O) in bcc metals, such as those of groups VB (V, Nb, Ta), VIB (Cr, Mo, W), and for the case of α-Fe [30]. Snoek explained this phenomenon in 1941 for the specific case of C in α-Fe [31]. The advantage of this technique is that it can study the kinetics of interstitials and also it can show evidence of substitutional-interstitials impurities [32,33]. Our interest is to study the evolution of the C and O diffusion properties with respect to Cr and dilute V concentrations respectively.

Interstitial atoms sit on octahedral interstitial sites (the centers of the cube edges or at the centers of the cube faces of the bcc lattice), which are all crystallographically equivalent to one another in a stress-free state. We can identify three different sublattices, depending on the direction of the nn bcc sites: [001], [010] and [100], which are named as 1, 2 and 3 respectively, as shown in Figure 6. In other words, there is a statistically equal number of interstitials in each sublattice.

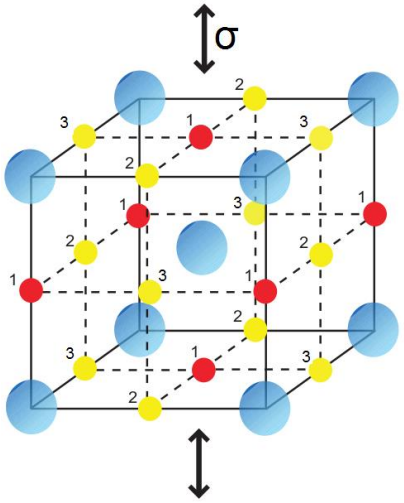

Figure 6: Bcc lattice including octahedral sublattices 1, 2 and 3. Red dots correspond to favored sites under tension, yellow dots correspond to favored sites under compression. The figure is adapted from [25].

The application of a stress σ (so that the elastic strain is in the order of 10^{-5} or smaller) in one particular direction (for example, parallel to sublattice 1, as shown in Figure 6) will produce a strain so that sites 1 will have their openings enlarged, while the other two remaining sites will have their openings reduced. Consequently, the interstitials will tend to occupy preferentially the sites 1 and to induce an extra strain on the alloy. If the diffusion of the interstitial atoms is not rapid enough, this extra strain does not disappear instantaneously once the applied stress is removed. This is the origin of the anelastic relaxation.

IF experiments consist in measuring the strain of the sample when applying an oscillating external stress, $\sigma = \sigma_0 \sin(2\pi ft)$, with a frequency f, at different temperatures. At a given temperature T and under the influence of an applied stress σ, an instantaneous elastic effect is observed followed by a reversible anelastic strain. The total strain ε^T produced by the applied stress is decomposed into two contributions:

$$\varepsilon^T = \varepsilon^E + \varepsilon^C = \varepsilon_0^E \sin(2\pi ft) + \alpha C_1(t), \tag{1.28}$$

where $\varepsilon^E = \sigma / E$ is the elastic strain given by the Hooke's law, E is the Young's modulus and ε^C is the strain produced by the excess of interstitials in sites 1 ($C_1(t)$ is the concentration of interstitials on sites 1). At first order in σ, the evolution of $C_1(t)$ can be divided into two parts:

$$C_1(t) = C_1^I \sin(2\pi ft) + C_1^O \cos(2\pi ft), \tag{1.29}$$

where C_1^I and C_1^O correspond to the contributions in and out of phase with the applied stress. The total strain ε^T is then expressed as:

$$\varepsilon^T = \varepsilon^I \sin(2\pi ft) + \varepsilon^O \cos(2\pi ft), \tag{1.30}$$

where $\varepsilon^I = \varepsilon_0^E + \alpha C_1^I$ and $\varepsilon^O = \alpha C_1^O$. The inverse quality factor Q^{-1} is defined as

$$Q^{-1} = \frac{\varepsilon^O}{\varepsilon^I}. \tag{1.31}$$

In order to understand the evolution of Q^{-1}, we must analyze the evolution of the anelastic strain at different temperatures. When the temperature is low, the interstitials cannot follow the rapid variation of the applied stress: $C_1(t)$ will be almost constant (Eq. (1.28)) and $Q^{-1} = 0$. At very high temperatures the diffusion is rapid so that C_1 remains at equilibrium in phase with the applied stress: $C_1(t) = C_1^I \sin(2\pi ft)$ and $C_1^O \sim 0$, which also gives $Q^{-1} = 0$. At intermediate temperatures, the interstitials produce an anelastic strain but they do not achieve an equilibrium state: $C_1^O \neq 0$ (Eq. (1.29)) and $Q^{-1} \neq 0$. The evolution of Q^{-1} with temperature displays a "Snoek peak" which be seen in Figure 7, for the particular case of oxygen in pure Nb.

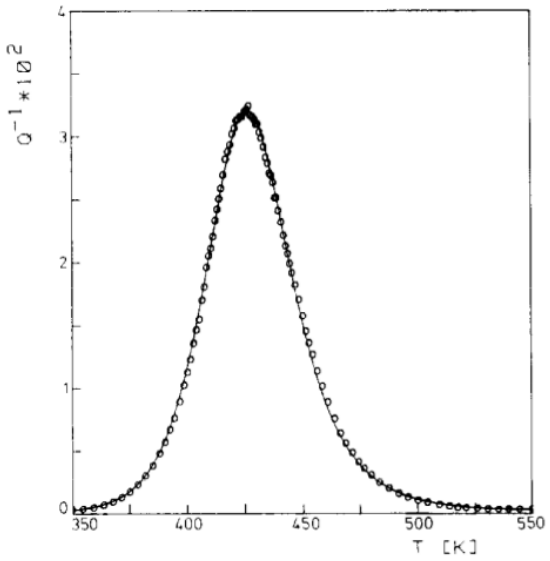

Figure 7: Oxygen Snoek peak in pure Nb. Figure extracted from [34].

It can be shown that Q^{-1} can be described by a Debye equation [31,35]:

$$Q^{-1} = \Delta \frac{\omega\tau}{1+(\omega\tau)^2}, \tag{1.32}$$

where Δ is the relaxation strength, which dictates the amplitude of the Snoek peak. τ is the relaxation time (for a C atom: $\tau = 1/6\Gamma_C$) and $\omega = 2\pi f$. We must notice that Eq. (1.32) is only valid when the jump frequency is determined by a single migration barrier, i.e. in pure metals.

It is worth considering the local distortions produced by the interstitials. The addition of interstitial atoms in the lattice produces local distortions where the symmetry of the lattice is locally reduced. In bcc metals, the interstitials induce permanent elastic dipoles with local tetragonal symmetry [36]. This explains why the Snoek effect cannot be studied in fcc metals, even though interstitial atoms can also be present in octahedral sites in these crystalline structures [1]. In bcc metals, the lattice distortions have tetragonal symmetry, while the distortions in fcc metals have cubic symmetry. In other words, interstitials in fcc metals distort the lattice but do not produce elastic dipoles with a lower symmetry than the lattice. In the Snoek relaxation, the application of an external stress produces an alignment of the elastic dipoles which gives rise to the macroscopic anelastic strain [36].

3.3. Experimental determination of the Snoek peak

We can distinguish two experimental techniques depending on the frequency of the applied stress [37]: resonance methods (which can be low-frequency – 0.01-20 Hz – and medium-frequency – hundred Hz to hundred kHz) and pulse-echo methods (high frequencies, in the order of MHz). We will focus on how to measure the internal friction using low frequency resonance methods: the Kê-type torsion pendulum [38]. One advantage of this technique is

that, since the temperature of the Snoek peak is increased with higher frequencies of the applied stress, the torsion pendulum allows a determination of the jump frequencies at relatively low temperatures, where long-range diffusion is not considered. Nevertheless, one disadvantage is the relatively high strain amplitude at which measurements have to be made. The strain is highly inhomogeneous, being negligible at the axis and maximum at the outer fibers of the sample. Consequently, pendulums have been built allowing measurements to be made at lower strains. This requires in taking precautions to avoid external vibrations as much as possible by resting the pendulum on carefully-designed shock-absorbers.

Figure 8 shows a sketch of the setup usually used in IF experiments. A wire – the sample – has one end rigidly fixed, while the other has attached two iron blocks via an inertia bar and is free to rotate. The wire is given an initial twist and it is fixed at an initial position by the blocks which are in contact with two electromagnets. Once the current is broken in the magnet circuit, the wire is free to oscillate. The amplitude of oscillation can be measured by observing a light beam, reflected by a mirror fixed at the end of the wire. The beam is projected onto a galvanometer scale, where an observer counts the number of cycles it takes for the pendulum to decrease the amplitude of consecutive oscillations.

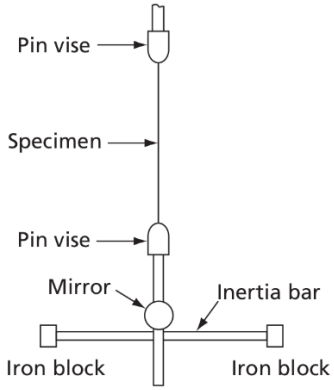

Figure 8: Experimental setup used in IF experiments. Image subtracted from [39].

The typical evolution of the amplitude is shown in Figure 9. The decrease of the amplitude is due to the energy losses inside the wire, due to the internal friction in the metal.

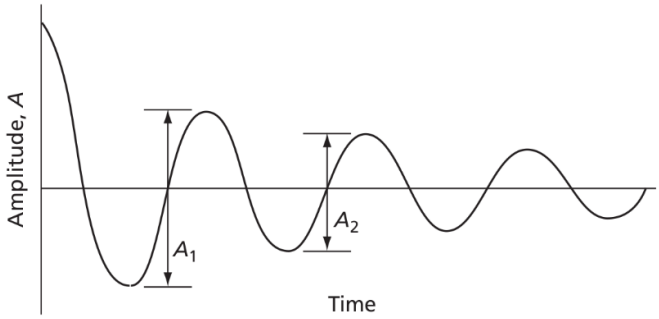

Figure 9: Time-evolution of the amplitude of oscillations in a typical IF experiment. Image extracted from [39].

The energy loss per cycle can be determined directly from Figure 9, where A_1 and A_2 are two adjacent amplitudes and it is assumed that their difference in magnitude is negligible. In an oscillating system, the energy is proportional to the square of the amplitude, so the fractional loss of energy per cycle is:

$$\frac{\Delta E}{E} = \frac{\left(A_2\right)^2 - \left(A_1\right)^2}{\left(A_1\right)^2}, \tag{1.33}$$

where E is the energy of the pendulum and ΔE is the loss of energy during a cycle. A different parameter we can consider is the phase angle δ, which measures the lag between the applied stress and the strain of the metal. If the damping is small, it can be shown that:

$$\tan\delta = \frac{1}{\pi}\ln\frac{A_1}{A_2} = \frac{\delta}{\pi} \equiv Q^{-1} \tag{1.34}$$

Since it is harder to vary the frequency of the external stress than the temperature of the sample, Internal Friction experiments are performed at a constant frequency.

3.4. Previous modelling of the Snoek peak

We found different approaches in the modelling of the IF in metals and alloys [25,27–29,35,40–42]. We can distinguish the approaches in three categories: those who do an atomistic modelling of the Snoek peak [25], those who developed analytic models of Q^{-1} with respect to the jump frequencies and Q^{-1} [27,28,35,42] and those who estimated a set of jump frequencies and used as inputs for each component of the Debye peaks (Eq. (1.32)) [29,40,41,43]. The question to answer is how accurate is the description of the IF in an alloy if we assume that it can be described as a sum of n Debye peaks, each one having an independent relaxation time τ_n and relaxation strength Δ_n:

$$Q^{-1} = \sum_n \Delta_n \frac{\omega\tau_n}{1+\left(\omega\tau_n\right)^2} \tag{1.35}$$

The atomistic approach has been used by Garruchet and Perez [25], who modelled the Snoek peak of C in pure Fe. They first determined $\Delta H_C^m\left(Fe\right)$ with an empirical potential [44] and used molecular statics to simulate the effect of applied stress on the saddle point energy. They later used a kinetic Monte Carlo method to study the distribution of C atoms under different applied stresses and molecular dynamics to calculate the anelastic strain. The main advantage of this method is that they can simulate the Snoek peak by precisely calculating the anelastic strain due to the migration of carbon atoms under stress. This method is limited to interstitials in pure metals, but it could be extended to alloys by assuming additional approximations: this is the approach proposed in the present study.

Sandberg et al. [29] modelled the carbon Snoek peak in concentrated Fe-Cr alloys. Their approach was purely based on DFT calculations, where they calculated the migration barriers ΔH_C^m of a single C atom in several random solid solutions at different Cr concentrations.

They then obtained an average relaxation time $\bar{\tau}$ using the computed ΔH_C^m at each configuration. They then modeled the response of the system as a sum of independent Debye peaks weighted by their probability of occurrence and each one related to a specific $\bar{\tau}$. An advantage of this method is that it can compute the Snoek peak for concentrated alloys. However, since DFT calculations are very time consuming, it is unclear how many ΔH_C^m were computed by Sandberg et al. [29] for their predicted Snoek peaks. Moreover, a more sophisticated model such as the one of Koiwa [27,28] dedicated to dilute systems demonstrates that in general, Debye peaks are not associated with a single jump. In chapter 2 we will compare the model proposed by Sandberg et al. [29] with our AKMC simulations for the carbon Snoek peak in concentrated Fe-Cr alloys.

Monte Carlo simulations have already been performed by Blanter [43] in the system of Nb-1.5%V-0.145%O and Nb-1.5%V-0.29%O. He calculated the energy of oxygen atoms in their stable and saddle point positions using a discrete crystal lattice model, from which he obtained the local migration energy. He then found the equilibrium distribution of oxygen atoms in Nb-V alloys using Monte Carlo simulations. After finding the short-range order of the oxygen atoms, he calculated the migration barriers at these particular configurations and computed the Snoek peak as a sum of Debye equations.

Cannelli et al. [40] modelled the IF peak in order to be applied to dilute metal-hydrogen systems containing trapping centers. First, they computed the population of clusters of different orders as a function of temperature and interstitial concentration using Fermi-Dirac statistics. They also assumed that there was no interstitial-interstitial interaction, and that the substitutional solutes were not close enough to produce complex clusters. Nevertheless, they allowed the formation of higher order clusters with a single substitutional and several interstitials around. They also assumed that the interstitials belonging to different clusters did not interact with each other. They computed Q^{-1} as a sum of independent Debye peaks, where each term contributed equally to the relaxation strength and each cluster only produced one relaxation time. For simplicity they also assumed that the exponential prefactor and the saddle point energy were independent of the local environment.

Yu et al. [41] modelled the IF peak in order to analyze the Snoek relaxation in concentrated Nb-Ti-O alloys. They first computed the probability of finding an oxygen atom in a close vicinity of particular Nb/Ti clusters in ordered systems and alloys with short-range order. They also used Fermi-Dirac statistics since the effect of interstitial-interstitial interactions upon the energy of an octahedral site could be taken into account by adding a concentration-dependent contribution. Once they obtained the most likely configurations of the different cluster configurations around oxygen atoms and their respective migration barriers, they calculated Q^{-1} as a sum of independent Debye peaks.

Koiwa [27,28] developed a theoretical IF model dedicated to infinitely dilute alloys, where he only considered a system with a single interstitial atom interacting with a single substitutional impurity. He analyzed the interstitial distribution on each sublattice, inside a

'sphere of influence' where the jump frequency of the interstitial atom was affected by the substitutional solute atom. The main advantage of this method is that it provides an exact analytical solution of the Snoek peak, where only a few key parameters are needed, such as binding energies, local migration barriers and frequency of the time-oscillating stress. It also shows clearly how each of these parameters affects the Snoek peak and states that assuming a Snoek peak as a sum of independent Debye peaks is not entirely correct. Nevertheless, the main disadvantage is that it only works for very dilute alloys, and does not consider the influence of impurity clusters upon an interstitial. In section 4.4 of chapter 3 we will explain more in detail the Koiwa model and apply it to the IF of dilute Nb-V-O alloys. Since Koiwa developed several models for studying the effect of substitutional solutes on the interstitial diffusion, we will refer to his model in ref. [20] as 'Koiwa model for tracer diffusion (KMTD)' and this present model [27,28] as 'Koiwa model for internal friction (KMIF)'

In conclusion, we have presented several approaches that attempt to simulate the Snoek peak in pure metals and alloys. We have seen that AKMC simulations can be used to model the IF in pure metals [25] and in dilute alloys [43]. Most of these models assume that the Snoek peak can be computed as a sum of independent Debye peaks, each one associated with an elementary relaxation time [29,40,41]. This assumption is challenged by the KMIF [27,28], where it is observed that each Debye peak cannot be associated with an elementary relaxation time but a complex function of them. Nowick and Berry [35] and Chang [42] also arrive to similar expressions of these complex τ. Unfortunately these studies [27,28,35,42] can only be applied to the IF in infinitely dilute alloys. As we will see in chapter 2, our AKMC simulations are not limited to dilute alloys.

4. A multiscale approach for the modelling of interstitial atoms

In order to model TD and IF experiments for Fe-Cr-C and Nb-V-O, we followed a multiscale approach. First, we computed a set of interstitial-substitutional binding energies and migration barriers in dilute alloys using Density Functional Theory (DFT) calculations. These calculations provide precise and reliable information about the interstitial-substitutional interactions and also aid us to model the diffusion kinetics of point defects. Second, since the DFT calculations are time consuming and it is nearly-impossible to obtain every possible binding energy and migration barrier, we decided to fit these values using two different pair interactions models. This approach enables us to predict the binding energies and migration barriers in concentrated alloys and rapidly calculate them in our simulations. Third, we used these models in our AKMC codes in order to simulate TD and IF experiments. These type of multiscale approaches have been extensively applied for the study of the kinetics of phase separation and precipitation [45–50]. In the remaining of this chapter we will present the models and approximations used at the different scales. For the sake simplicity, the results obtained will be illustrated for C diffusion in pure Fe and pure Cr, and validate by comparison with the experimental data shown by Landolt and Bornstein [15] and by Saitoh et al. [51]. The case of alloys will be discussed in the following chapters.

4.1. DFT calculations

Density Functional Theory (DFT) is a very effective technique for studying molecules, atoms, solids and surfaces by directly solving approximate versions of the Schrodinger equation [52]. By combining DFT with high performance computing facilities it is possible to understand and predict material properties. This theory can predict equilibrium structures, binding energies between atoms in a solid system and band structures of semiconductors, among others. Even though this model does not use any fitting parameters and can precisely determine binding energies and migration barriers for a given configuration, it involves various approximations such as exchange-correlation functional and pseudopotentials. Moreover, this technique is also very time consuming (usually it takes 24 hours over 500 processors for the determination of a single migration barrier).

We have used DFT calculations performed by Chu-Chun Fu in the Service de Recherches de Métallurgie Physique (SRMP, CEA Saclay) in Fe-Cr-C and Nb-V-O alloys. These were performed by employing the VASP (Vienna Ab Initio Simulation Package) code [53,54]. They were spin polarized within the collinear magnetism scheme, and adopted the generalized gradient approximation (GGA) [55] within the PBE (Perdew Burke Ernzerhof) scheme [56]. The interaction between ions and electrons was described by projector augmented wave (PAW) potentials [57]. *3d* and *4s* electrons were considered for iron, and chromium, *2s* and *2p* electrons for carbon, *4p*, *4d* and *5s* for niobium, *3p*, *3d* and *4s* for vanadium and *2s* and *2p* electrons for oxygen, as valence electrons. We have verified that the properties of our interest were sufficiently converged by adopting plane-wave basis sets with an energy cut-off of 400 eV.

4.2. Pair interaction models

Due to the computational cost of DFT methods, they cannot be used to compute the migration barriers $\Delta H_C^m(ij)$ for all the possible local environments and use them as inputs in our AKMC simulations. Consequently, we build two pair interaction models (PIM) where the enthalpy is written as a sum of atomic pair interactions fitted to the DFT results, in order to reproduce them and to predict the migration barriers in concentrated alloys.

An interstitial migration barrier between configurations *i* and *j* is defined as:

$$\Delta H_C^m(ij) = H_{i,j}^{SP} - H_i \,, \tag{1.36}$$

where $H_{i,j}^{SP}$ and H_i are the total enthalpies of system, when the interstitial is respectively at the saddle point (SP) and in the initial position. Several pair interaction models have been proposed for AKMC simulations [45–50,58]. In this study we have developed 2 different models:

- Model 1

We write H_i as:

$$H_i = \sum_{n1} VAC_{n1}^i + \sum_{n1} VBC_{n1}^i + \sum_{n2} VCC_{n2}^i + \sum_{n3} VAB_{n3}^i \,, \tag{1.37}$$

where VAB_{n3}^{i} correspond to pair interactions between substitutional solute atoms, VAC_{n1}^{i} and VBC_{n1}^{i} correspond to pair interactions between interstitials and substitutional solute atoms and VCC_{n2}^{i} corresponds to the interstitial-interstitial pair interactions. Each summation corresponds to n nearest neighbors.

We can also write $H_{i,j}^{SP}$ as:

$$H_{i,j}^{SP} = \sum_{m1} VAC_{m1}^{SP} + \sum_{m1} VBC_{m1}^{SP} + \sum_{n2} VCC_{n2}^{i} + \sum_{n3} VAB_{n3}\,, \tag{1.38}$$

where VAC_{m1}^{SP} and VBC_{m}^{SP} are the interstitial-substitutional pair interactions at the saddle point position. Each summation corresponds to m nearest neighbors at the saddle point.

Eq. (1.36) can be rewritten as:

$$\Delta H_C^m(ij) = \left(\sum_{m1} VAC_{m1}^{SP} + \sum_{m1} VBC_{m1}^{SP}\right) - \left(\sum_{n1} VAC_{n1}^{i} + \sum_{n1} VBC_{n1}^{i}\right). \tag{1.39}$$

This first model is used as a first approach to the modelling of the C diffusion in Fe-Cr alloys, and to model the IF of O in dilute Nb-V alloys. As we will see in chapter 2, this modelling approach can reproduce a wide range of migration barriers, but it makes the AKMC simulations very time consuming.

- Model 2

This other method is derived from a standard approach [58], which is to write $H_{i,j}^{SP}$ as:

$$H_{i,j}^{SP} = \frac{H_i + H_j}{2} + \Delta H_C^0\,, \tag{1.40}$$

where H_j is the total enthalpy of the system after the C jump and ΔH_C^0 is considered to be a constant. Note that it implies, for example, the same C migration barrier in pure Fe and in pure Cr. In order to better reproduce the DFT results, we chose to define ΔH_C^0 as:

$$\Delta H_C^0 = \frac{\Delta H_C^m(\mathrm{Fe})\, n_{Fe} + \Delta H_C^m(\mathrm{Cr})\, n_{Cr}}{n_{Fe} + n_{Cr}}\,, \tag{1.41}$$

where $\Delta H_C^m(\mathrm{Fe})$ and $\Delta H_C^m(\mathrm{Cr})$ are the C migration barriers in pure Fe and Cr, and n_{Fe} and n_{Cr} are the numbers of Fe and Cr atoms at the saddle point.

From Eqs. (1.36)-(1.40), we deduce:

$$\Delta H_C^m(ij) = \frac{H_j - H_i}{2} + \Delta H_C^0\,. \tag{1.42}$$

H_i and H_j are computed using Eq. (1.37). We used this model as well for the modelling of the carbon migration barriers in Fe-Cr alloys. As we will see in chapter 2, this approach can make the AKMC simulations less time consuming but it can only well reproduce a narrow range of migration barriers.

For the sake of simplicity we have considered VAC_{n1}^{i}, VBC_{n1}^{i} up to 3 nn (the (210) direction), and VAC_{m1}^{SP} and VBC_{m1}^{SP} up to 2 nn. The interactions are fitted to the DFT database of binding energies and migration barriers. In chapters 2 and 3 we will give the pair interactions used

for the modelling of the Fe-Cr-C and Nb-V-O systems.

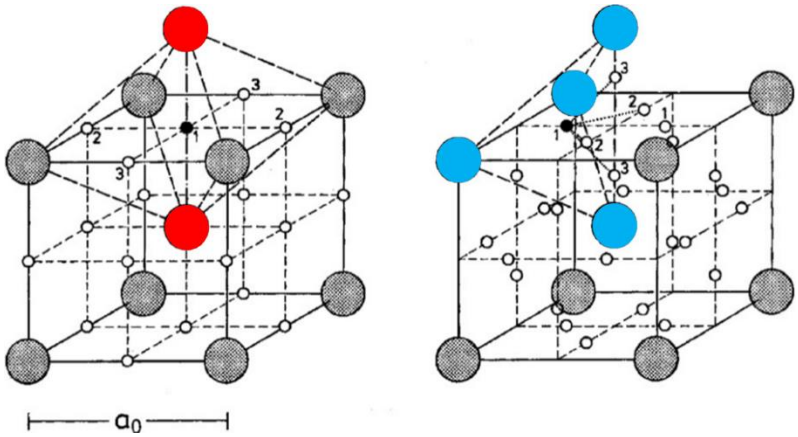

Figure 10: Interstitial atom (black dot) at the octahedral position (left) and at the saddle point (right) in a bcc lattice. Red circles correspond to interstitial-substitutional solute interactions at 1 nn at the initial position. Blue circles correspond to interstitial-substitutional solute interactions at 1 nn at the saddle point. Figure is adapted from [5].

4.3. Atomistic Kinetic Monte Carlo simulations

After fitting our pair interaction model on the DFT values of the migration barriers, we use AKMC simulations in order to model the diffusion of interstitials in alloys. We use a residence time algorithm [59] to select one atomic jump and compute the physical time at each Monte Carlo step. Suppose that at a MC step n, the system is with a given configuration ξ and where we know the total of M configurations Φ from which the system can evolve.

1. For a given ξ, we calculate all the possible local migration barriers for each point defect using a pair interaction model with their associate jump frequency Γ. In the case of interstitial atoms we used Eq. (1.9) and a pair interaction model as described in section 4.2. As we will see in chapter 4, we computed the jump frequencies of vacancies and self-interstitials following the multiscale modeling of Martinez et al. [46] and Senninger et al. [60] respectively.
2. We calculate the residence time $\tau_\Phi = 1 \Big/ \sum_{\Phi=1}^{M} \Gamma_{\xi\to\Phi}$ and the physical time $t_n = t_{n-1} + \tau_\Phi$.
3. We draw a random number $r_n \in [0,1]$.
4. We perform a transition k if:

$$\frac{\sum_{\Phi=1}^{k-1} \Gamma_{\xi\to\Phi}}{\sum_{\Phi=1}^{M} \Gamma_{\xi\to\Phi}} < r_n \leq \frac{\sum_{\Phi=1}^{k} \Gamma_{\xi\to\Phi}}{\sum_{\Phi=1}^{M} \Gamma_{\xi\to\Phi}} . \tag{1.43}$$

5. A point defect performs a jump a we repeat the process from step 1.

The tracer diffusion coefficient of carbon is obtained by measuring the mean square displacement, using a standard technique that we will briefly present first. A new method is proposed for the simulation of IF experiments.

In the following sections we will illustrate this method by modelling TD and IF experiments of C in pure Fe and pure Cr. We will validate our methodological approach by comparing our AKMC results with the available experimental data from [13,15,51,61–64]. In chapters 2 and 3 we will extend this method for the modelling of the interstitial diffusion in alloys by implementing model 1 and model 2 in our AKMC code. In the following sections we will also present analytical models that relate the jump frequency Γ_C with the macroscopic quantities (D_C and Q^{-1}) in pure metals.

4.3.1. Tracer diffusion

Our AKMC simulations measure the mean square displacement $\left\langle R_C^{\,2} \right\rangle$ traveled by the interstitials during a time t. We then obtain D_C by applying the Einstein-Smoluchowski relation [1]:

$$D_C = \frac{\left\langle R_C^{\,2} \right\rangle}{6t}, \tag{1.44}$$

The correlation factor f_C quantifies the deviation from a random path. Using the definition of the correlation factor (Eq. (1.17)):

$$f_C = \frac{\left\langle R_C^{\,2} \right\rangle}{\left\langle R_C^{\,2} \right\rangle_0} \tag{1.45}$$

where $\left\langle R_C^{\,2} \right\rangle_0$ is the non-correlated part of the mean square displacement. By definition, a non-correlated path corresponds to a random walk. According to Eq. (1.14).

$$\left\langle R_C^{\,2} \right\rangle_0 = N_{MCS} \left(\frac{a_0}{2} \right)^2, \tag{1.46}$$

where N_{MCS} is the number of jumps (i.e. with a residence time algorithm, the number of Monte Carlo steps) and $a_0/2$ is the distance between jumps (a_0 is the bcc lattice parameter). Eq. (1.45) is then expressed as:

$$f_C = \frac{\left\langle R_C^{\,2} \right\rangle}{N_{MCS} \left(\frac{a_0}{2} \right)^2} \tag{1.47}$$

As we will see in chapter 2, the carbon migration barriers can be very low due to a strong attraction to substitutional solutes, which prevents their long-range diffusion. In order to overcome this in our AKMC simulations, the carbon atoms must perform a huge number of jumps in order to have a possibility to leave these strong configurations and hence, produce

a long-range diffusion. For the estimation of D_C and f_C in our AKMC simulations, 100 measurements of $< R_C^2 >$ after 10^7 carbon jumps (i. e. a total of 10^9 jumps at each temperature) were performed in a box of 2×15^3 bcc sites, with 7 C atoms.

As we have seen in section 2.1, D_C is related to f_C and $\Delta\bar{H}_C^m$ via:

$$D_C = \frac{2}{3}\left(\frac{a_0}{2}\right)^2 f_C \upsilon_0 \exp\left(-\frac{\Delta\bar{H}_C^m}{k_B T}\right). \quad (1.48)$$

In pure Fe or pure Cr, a carbon atom follows a truly random walk ($f_C = 1$) and $\Delta\bar{H}_C^m = \Delta H_C^m(Fe)$ or $\Delta H_C^m(Cr)$. Figures 11 and 12 compare the results of AKMC simulations performed in pure Fe and Cr, using the carbon migration barriers computed by the DFT calculations: $\Delta H_C^m(Fe) = 0.86$ eV and $\Delta H_C^m(Cr) = 1.21$ eV. They are compared with Eq. (1.48) and with experimental results. The attempt frequency is $\upsilon_0 = 7\times10^{13}$ Hz, fitted on the experiments in pure Fe. This parameter also gives a good agreement in pure C, and in the following will be considered as a constant independent on the alloy composition.

Figure 11 shows that D_C follows an almost perfect Arrhenius behavior over 25 orders of magnitude of D_C and over a large range of temperature (200 K up to 1000K). The small experimental curvature of D_C above 1043 K is due to the transition between ferromagnetic and paramagnetic iron.

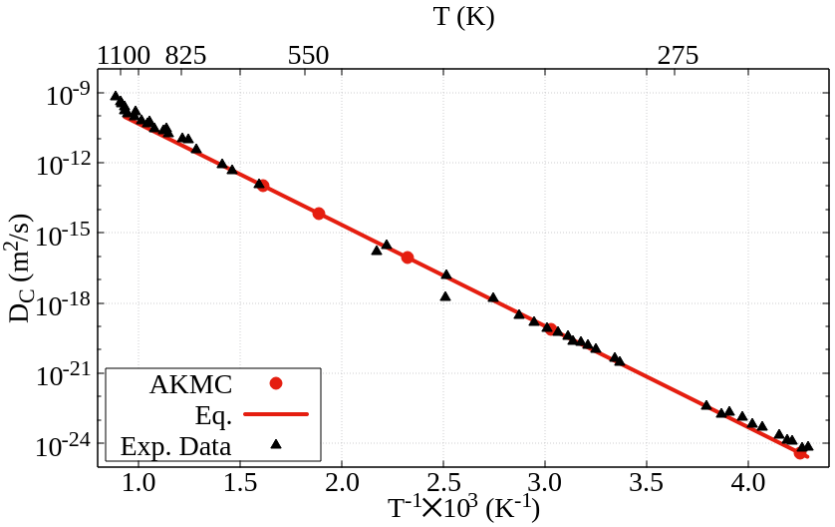

Figure 11: Diffusion coefficients of C in α-Fe, as a function of the temperature. Comparison between AKMC simulations, Eq. (1.48) and experiments [12].

Experimental measurements of D_C in pure Cr [13,61–64] (Figure 12) have been performed at higher temperatures (because of the slower diffusion of C). The results are slightly more scattered than in pure iron, but also show a typical Arrhenius behavior. Keeping the same value of υ_0 as in iron, the results of both AKMC simulations and Eq. (1.16) obtained with $\Delta H_C^m(Cr) = 1.21$ eV are in good agreement with the experiments. Therefore, in the following, υ_0 will be considered as a constant, independent of the local environment.

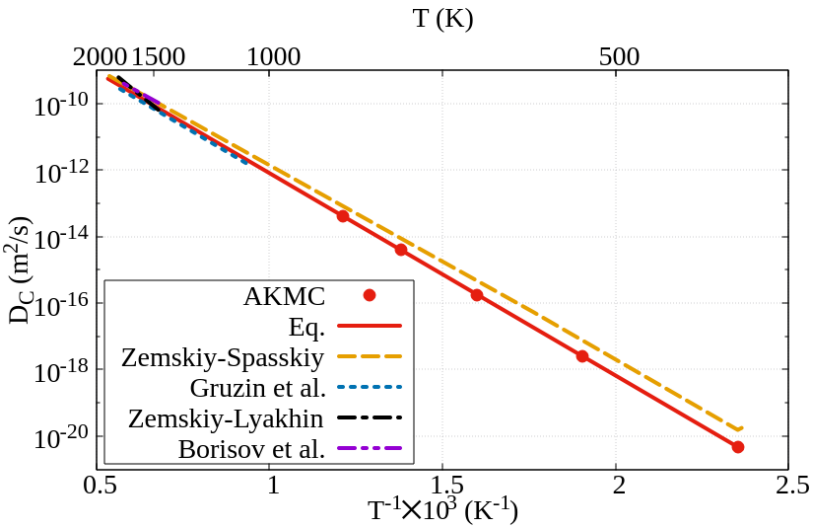

Figure 12: Diffusion coefficients of C in Cr, as a function of the temperature. Comparison between AKMC simulations, Eq. (1.48) and experiments [13,61–64].

Of course, as we can see from Figure 11 and 12, we do not need to use AKMC simulations in order to obtain the tracer diffusion coefficient of an interstitial diffusing in a pure metal since Eq. (1.48) gives the same result. Nevertheless, when an interstitial is in an alloy, where there is a spectrum of possible migration barriers, AKMC simulations are very useful in order to determine the tracer diffusion coefficient, both in dilute [65,66] and in concentrated alloys, as we will see in chapter 2.

4.3.2. Internal friction

In this section we will explain the methodology followed for the modelling of the Snoek peak with our AKMC simulations. First, we will explain how to model the effect of the applied stress on the interstitial concentration in the three different sublattices. Second, we will show an estimation of the most important parameters using DFT calculations and were used as inputs in our AKMC simulations. Third, we will develop analytical models in order to understand the results given by the AKMC. Fourth, we will validate our approach by comparing our modelled carbon Snoek peak in pure Fe with the analytical models, the experimental data by Saitoh et al. [51] and the previous modelling by Garruchet and Perez [25]. For the sake of simplicity, we will explain our modelling approach in terms of the carbon Snoek peak in pure Fe. We will see in chapter 2 how this approach was applied to simulate the carbon Snoek peak in concentrated Fe-Cr alloys.

4.3.2.1. The effect of the external stress on the jump frequency

As we mentioned in section 3.2, the applied stress favors certain types of interstitial sites over others. In order to simulate the effect of an applied stress on the interstitial population, a

segregation enthalpy ΔH_C^{seg} associated with a given sublattice is introduced so that it affects the migration barriers of the jumping atoms:

$$\Delta H_C^{seg} = \frac{\Delta H_0^{seg}}{2}\sin\left(2\pi ft\right), \tag{1.49}$$

where f is the frequency of the applied stress. So, the jump frequencies of interstitials defined by Eq. (1.9), are modified in order to account for the on-site segregation enthalpy:

$$\Gamma_C^{IF}\left(ij\right) = \upsilon_0 \exp\left(-\frac{\Delta H_C^m\left(ij\right) \pm \frac{\Delta H_0^{seg}}{2}\sin\left(2\pi ft\right)}{k_B T}\right), \tag{1.50}$$

where is added to the migration enthalpy ΔH_C^m if an interstitial atom is located on the sublattice parallel to the applied stress ('sublattice 1', Figure 6), and subtracted if elsewhere. Each ΔH_C^m is computed using a pair interaction model (section 4.2) and ΔH_0^{seg} is determined by DFT calculations and assumed constant for the remaining of this thesis.

As illustrated in Figure 13, the resulting migration enthalpy from site *i* to site *j* is different from the reverse jump. For those sites where there is an application of stress, the probability of a C atom jumping from its position is decreased. As a consequence of the segregation enthalpy, there is a greater number of jumps that correspond to going into sites 1 than coming out of them, producing a larger amount of intersitials on sublattice 1 than on the other two sublattices.

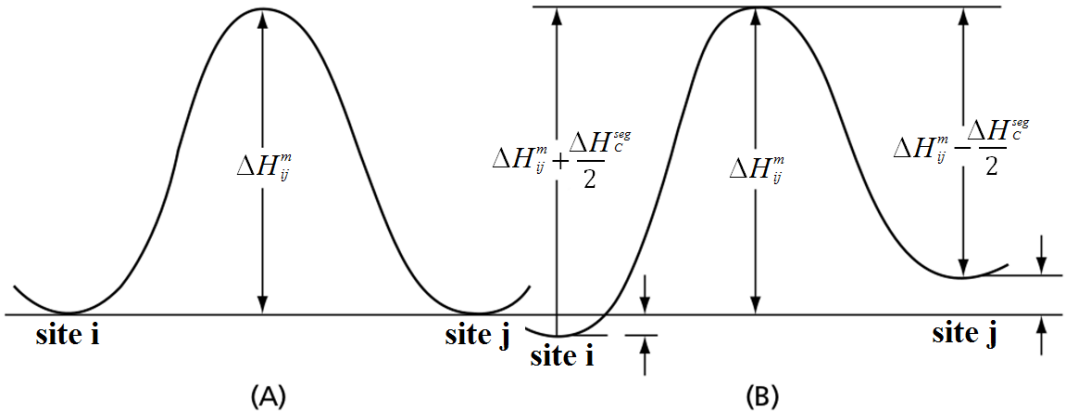

Figure 13: Energetic landscape when there is no applied stress (A) and with the influence of an applied stress (B).

We must notice that what it is important is that the energetic difference between two consecutive sites must be equal to the segregation enthalpy ΔH_C^{seg}. We can also partition the segregation enthalpy in a different way by adding the term ΔH_C^{seg} only on sublattice 1 and $\Delta H_C^{seg} = 0$ eV in the remaining two and we will arrive to the same results.

The jump frequencies defined in Eq. (1.50) are then implemented in the AKMC code in order to measure the instantaneous interstitial concentration at different temperatures. We used the interstitial content on sublattice 1 as inputs for the computation of Q^{-1} by following the definitions of Eqs. (1.28) - (1.31).

AKMC simulations were performed in a box with 2×128^3 bcc sites and at least 3230 C atoms. The frequency $f=1$ Hz was chosen for comparison with the results from [29,67]. Also, in order to compare with the experimental carbon Snoek peak in pure Fe by Saitoh et al. [51], the simulations were performed at 1.5 Hz, with 2×175^3 bcc sites, 12703 C atoms, a segregation enthalpy of $\Delta H_0^{seg}=10^{-3}$ eV ($\varepsilon_0^E=0.01\%$). Moreover, in order to simulate the oxygen Snoek peak in dilute Nb-V alloys and compare our results with those shown in [32,33], simulation boxes of 2×75^3 and 2×50^3 bcc sites and frequencies of 0.25 Hz, 0.35 Hz and 0.56 Hz were chosen.

4.3.2.2. DFT calculations

In this section we will explain briefly how the key parameters of the anelastic strain were calculated using DFT calculations and their orders of magnitude. These have been estimated for the case of carbon in pure Fe.

The segregation enthalpy ΔH_0^{seg} has been estimated in a bcc lattice of 128 Fe atoms, as the energy difference when a C atom is on a site 1, with respect to sites 2 or 3, for a given tensile strain ε_0^E (the dimensions of the computational cell perpendicular to the strain being contracted according to the iron Poisson ratio). When the applied stress is small, it yields a linear relationship between ΔH_0^{seg} and ε_0^E, with $\Delta H_0^{seg}=0.01$ eV for $\varepsilon_0^E=0.1\%$. Moreover, we assumed that the anelastic strain was proportional to the carbon concentration in the sublattice parallel to the applied stress via a constant α - Eq. (1.30). We obtained this value by a DFT calculation, showing that one carbon atom if a box of 128 atom (~1 at.%), was producing a strain of ~0.5%, so that $\alpha\sim0.5$.

4.3.2.3. Analytical models

4.3.2.3.1 Evolution of the interstitial concentration with temperature

In order to understand the evolution of Q^{-1}, we must analyze the evolution of the anelastic strain at different temperatures T. This means that we need to observe the evolution of the interstitial concentration on sublattice 1 and to see if it remains at equilibrium, following the evolution of the applied stress and ΔH_C^{seg} (Eq. (1.28)).

In case there is no segregation enthalpy, the probability of occupation of atoms in each sublattice is equal to one another and at equilibrium we would find the same concentration of atoms in each sublattice i:

$$\frac{C_{TOT}}{3}=C_i^{eq} \qquad (i=1,2,3), \tag{1.51}$$

The applied stress prevents that the probability of occupation being equal on every sublattice.

The equilibrium concentration of interstititals in sublattice 1, $C_1^{eq}(t)$ is:

$$C_1^{eq}(t) = \bar{C} \exp\left(\frac{\Delta H_C^{seg}}{k_B T}\right), \tag{1.52}$$

where $\bar{C}$ is a constant. Since the total concentration of interstitials is conserved, the equilibrium concentration of $C_1(t)$, for a given segregation enthalpy is:

$$C_1^{eq}(t) = C_{TOT} \frac{\exp\left(\frac{\Delta H_C^{seg}}{k_B T}\right)}{2 + \exp\left(\frac{\Delta H_C^{seg}}{k_B T}\right)}. \tag{1.53}$$

Figure 14 shows the comparison between the carbon equilibrium concentration (Eq. (1.53)) and the instantaneous concentration (measured in the AKMC simulations), at three different temperatures for the special case of C in pure Fe. At low T, $C_1(t)$ remains almost constant because the jump frequency of the C atoms is too small ($Q^{-1} = 0$ because $\varepsilon^O = 0$ - Eq. (1.28)). At intermediate temperatures, C atoms diffuse but are not rapid enough to follow the equilibrium distribution on the three sublattices: $C_1(t)$ shows a phase lag with the sinusoidal evolution of the equilibrium concentration $C_1^{eq}(t)$ and a smaller amplitude. At high temperatures, the jump of carbon atoms is very rapid and $C_1(t)$ follows the equilibrium concentration ($Q^{-1} = 0$ because $\varepsilon^O = 0$ - Eq. (1.30)).

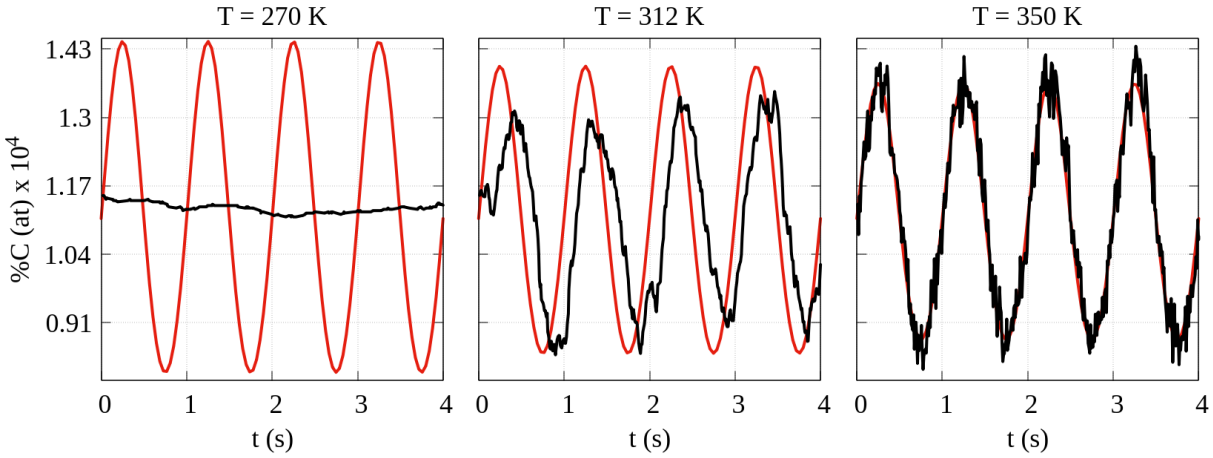

Figure 14: AKMC simulations of the evolution of the carbon concentration on the sublattice 1 in Fe-0.033%C, under a cyclic load of $\sigma_0 = 0.161\,\text{GPa}$ and 1 Hz, at three different temperatures. The concentration $C_1(t)$ (black curve) is compared to the evolution of the equilibrium concentration $C_1^{eq}(t)$ (red curve).

4.3.2.3.2 Analytical model of Q^{-1}

In this section we attempt to establish a link between all the key parameters (ΔH_0^{seg}, ε_0^E, f,

$\Delta\bar{H}_C^m$, C_{TOT}, Γ_C and T) and their contribution to the Snoek peak. The first step is to study the evolution of the interstitial concentration on sublattice 1 C_1 over time. We obtain the following first order differential equation:

$$\frac{dC_1}{dt} = 2C_2\left(1-C_1\right)\Gamma_C^{IF}\left(21\right)+2C_3\left(1-C_1\right)\Gamma_C^{IF}\left(31\right) \\ -2C_1\left(1-C_2\right)\Gamma_C^{IF}\left(12\right)-2C_1\left(1-C_3\right)\Gamma_C^{IF}\left(13\right), \quad (1.54)$$

where $\Gamma_C^{IF}\left(ij\right)$ corresponds to the jump frequency of an interstitial going from a sublattice *i* to the closest sublattice *j* (Eq. (1.50)). C_2 and C_3 are the interstitial concentrations in the other two sublattices. From Eq. (1.54) we identify two different type of contributions to dC_1/dt. The first two terms correspond to the concentration of interstitials that jump from sites 2 and 3 to sites 1. The two last terms correspond to those interstitials that leave sites 1 towards sites 2 and 3.

We start by doing three assumptions. First, the total concentration of interstitials C_{TOT} is conserved. Second, the concentration on each sublattice is small. Third, the segregation enthalpy is very small compared to the local migration enthalpy (for example as we will see in chapter 2, the lowest carbon migration barrier in Cr-rich alloys according to the DFT database is $\Delta H_C^m = 0.2$ eV while the segregation enthalpy is $\Delta H_0^{seg} = 0.01$ eV).

The general solution to this differential equation at a given temperature is:

$$C_1\left(t\right) = \frac{C_{TOT}}{3} + \frac{8C_{TOT}\left(\Gamma_C\right)^2}{\left(\omega^2+\left(6\Gamma_C\right)^2\right)}\frac{\Delta H_0^{seg}}{k_BT}\sin\left(\omega t\right) - \frac{4\omega\Gamma_C C_{TOT}}{3\left(\omega^2+\left(6\Gamma_C\right)^2\right)}\frac{\Delta H_0^{seg}}{k_BT}\cos\left(\omega t\right). \quad (1.55)$$

By direct inspection, we see that the second and third terms correspond to the carbon atoms which are respectively in phase and out of phase with respect to the stress. This expression is also in agreement with Eq. (1.51), for the special case in which there is no applied stress to the system ($\Delta H_0^{seg} = 0$ and $C_1\left(t\right) = C_{TOT}/3$). Combining Eqs. (1.28) and (1.55), the inverse quality factor Q^{-1} is expressed as:

$$Q^{-1} = \left(\frac{4C_{TOT}\alpha\Delta H_0^{seg}}{3\varepsilon_0^E k_BT}\right)\left(\frac{\omega\Gamma_C}{\omega^2+\left(6\Gamma_C\right)^2}\right). \quad (1.56)$$

The first term is usually called 'the relaxation strenght' Δ, which dictates the height of the Snoek peak. The second term shows the dependence of Q^{-1} with the frequency of the applied stress f, the temperature T and ΔH_C^m. We can see that Eq. (1.56) follows a Debye equation, as expected (Eq. (1.32)).

The maximum value of Q^{-1}, Q_{MAX}^{-1}, is given by:

$$\frac{\partial Q^{-1}}{\partial\Gamma_C} = 0 \quad (1.57)$$

which, according to Eq. (1.56), occurs when $2\pi f \approx 6\Gamma_C$. This means that Q_{MAX}^{-1} is achieved when the jump frequency of an interstitial atom is very close to the frequency of the applied

stress. Using the definition of Γ_C given by Eq. (1.9), this condition can be also expressed as:

$$\Delta\bar{H}_C^m = k_B T_{\max} \ln\left(\frac{3\upsilon_0}{\pi f}\right), \tag{1.58}$$

which shows that the temperature position of the Snoek peak, $T_{\max}$, is linearly proportional to $\Delta\bar{H}_C^m$ at a given f in the case of the Snoek peak in a pure metal. In other words, the position of $T_{\max}$ provides the migration barrier that could be found via other experimental techniques, such as tracer diffusion. This linear relationship between $\Delta\bar{H}_C^m$ and $T_{\max}$ has been experimentally observed by Wert and Marx [68]. At $T_{\max} = 312\,\text{K}$ and 440 K, for $f = 1\,\text{Hz}$, it gives $\Delta\bar{H}_C^m = 0.86\,\text{eV}$ and 1.21 eV, the expected carbon migration barriers in pure Fe and in pure Cr respectively.

We must notice that in our derivation of the Debye equation (Eq. (1.56)) we are making two strong assumptions. First we assume that the segregation enthalpy is independent of the local chemical environment (Eq. (1.49)), which is not the case in an alloy. For example, Saitoh et al. [51] show that the amplitude of the carbon Snoek peak in dilute Fe-Cr alloys depends on the concentrations of C and Cr. Since we are mainly interested in the position of the peak, we will keep them constant in this thesis. The second assumption that we make is that the average migration enthalpy can be directly extracted from the Snoek peak using Eq. (1.58), even when in an alloy there are several jump frequencies. In chapter 2 we will see that our assumption is valid as a first approximation because the tracer diffusion simulations show that the relaxation rate obeys an Arrhenius relationship, and because for any given system there is only one carbon Snoek peak. In chapter 3 we will also analyze a system where there are several Snoek peaks (dilute Nb-V-O alloys) [32,33], the position of the peaks may be obtained from a more complex expression of the jump frequencies, such as the KMIF in dilute alloys [27,28] and the model discussed by Nowick and Berry [35].

4.3.2.4. Validation of the AKMC simulations with previous studies

In the previous section we have shown that the average migration entalpy $\Delta\bar{H}_C^m$ only depends on the temperature of the Snoek peak $T_{\max}$ and the frequency of the external stress f. The parameters that define the height of the Snoek peak (ΔH_0^{seg}, α and ε_0^E) have been fitted for the special case of C in pure Fe. In this section we will focus on validate our parameters by comparing the height of the carbon Snoek peak in pure Fe predicted by our AKMC simulations with those found in the literature. We decided to directly compare our results with those provided by Saitoh et al. [51] and by Garruchet and Perez [25].

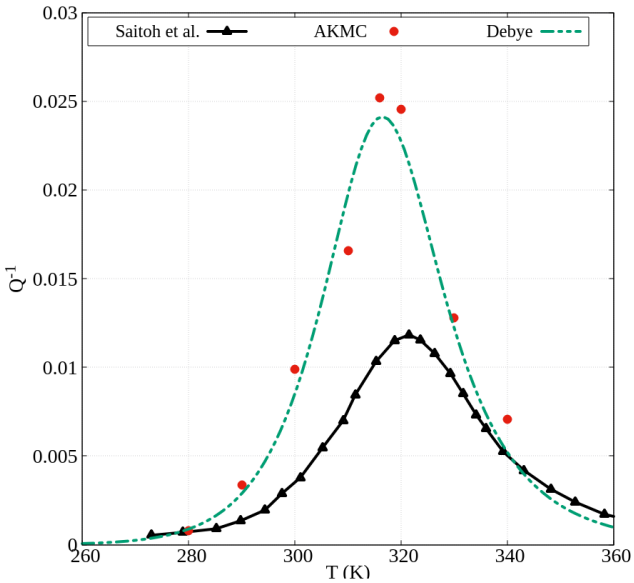

Figure 15: The Snoek peak in Fe-0.12%C, with $f = 1.5$ Hz and $\varepsilon_0 = 10^{-4}$. Comparison between the AKMC simulations, the Debye equation (Eq. (1.56)) and the experimental results from Saitoh et al. [51].

Figure 15 shows a comparison between the Debye equation (Eq. (1.56)), our AKMC simulations and the experimental curve shown by Saitoh et al. [51]. We find a very good agreement between the Debye equation and the AKMC simulations. We see that the AKMC simulations predict the height of the Snoek peak to be in the same order of magnitude but higher by a factor ~ 2 and at a smaller temperature (the experimental $T_{\max} = 321$ K while the AKMC $T_{\max} = 316$ K). This difference in amplitudes seems reasonable due to the fact that experiments are performed in polycrystalline Fe and with a torsion strain, whereas our simulations correspond to monocrystal and tensile strain conditions (Garruchet and Perez [25] estimated that the difference between the two strains resulted in an overestimation of 0.74 of the amplitude of the peak).

Garruchet and Perez [25] also modelled the carbon Snoek peak in pure Fe. Their approach has similarities and differences with our model. Our method is different since it is based on a rigid lattice approximation of diffusion fitted on DFT calculations of binding energies and migration barriers, while they first determined $\Delta \bar{H}_C^m(Fe)$ with an empirical potential [44] and used molecular statics in order to simulate the effect of an applied stress on the saddle point energy. Moreover, we assumed that the anelastic strain was proportional to the carbon concentration in the sublattice parallel to the applied stress, while Garruchet and Perez [25] directly obtained the anelastic strain using molecular dynamics. However, both methods are similar because they use AKMC simulations in order to study the carbon distribution under an applied stress. In spite all of these differences between both approaches, if we use the same carbon concentration, the frequency of the external stress and the ε_0, we obtain a very

good agreement with their results, as shown in Figure 16. In this case, the values of ε_0 and of the carbon concentration are higher than in the experimental literature because they provide a better estimation of the carbon population in the different sublattices.

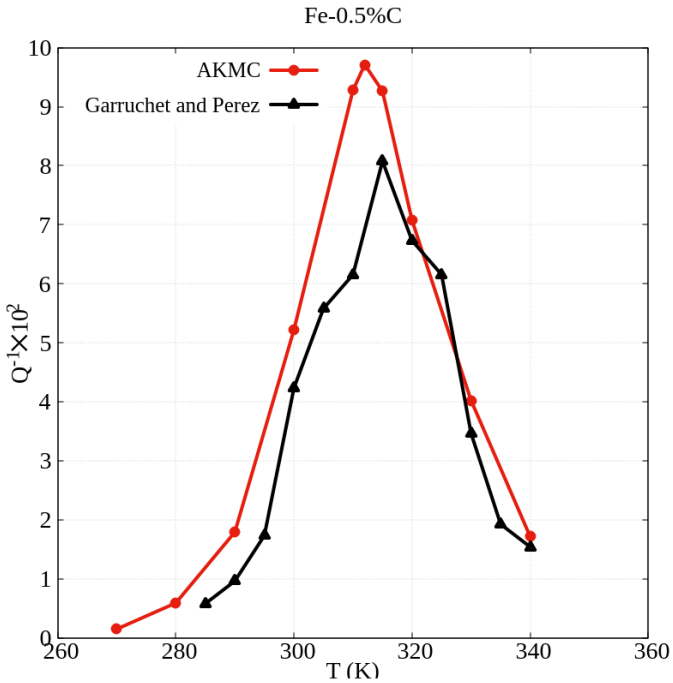

Figure 16: The Snoek peak in Fe-0.5%C, with $f = 1$ Hz and $\varepsilon_0 = 10^{-3}$. Comparison between the AKMC simulations – and the simulations from Garruchet and Perez [25].

As it has been previously shown [25,31,51], the amplitude of the Snoek peak Q_{MAX}^{-1} is proportional to the carbon concentration $\%C$ by a constant K given by:

$$Q_{MAX}^{-1} = K \times (\%C). \tag{1.59}$$

As expected, our AKMC simulations predict a linear relationship between the amplitude of the Snoek peak with the carbon concentration, as shown in Figure 17. Our fit yields a value of $K = 0.201 \pm 0.004\ (\%at)^{-1}$, being in close agreement with the value estimated by Garruchet and Perez [25] of $K = 0.15\ (\%at)^{-1}$ and the value of Saitoh et al. [51] of $K = 0.14\ (\%at)^{-1}$. As already seen in the analysis of Garruchet and Perez [25], our AKMC simulations overestimate the amplitude because we are modelling the carbon Snoek peak in an Fe monocrystal and in tensile strain conditions. Following the reasoning of Garruchet and Perez [25], our K should be corrected to reach the value $K = 0.149 \pm 0.003\ (\%at)^{-1}$.

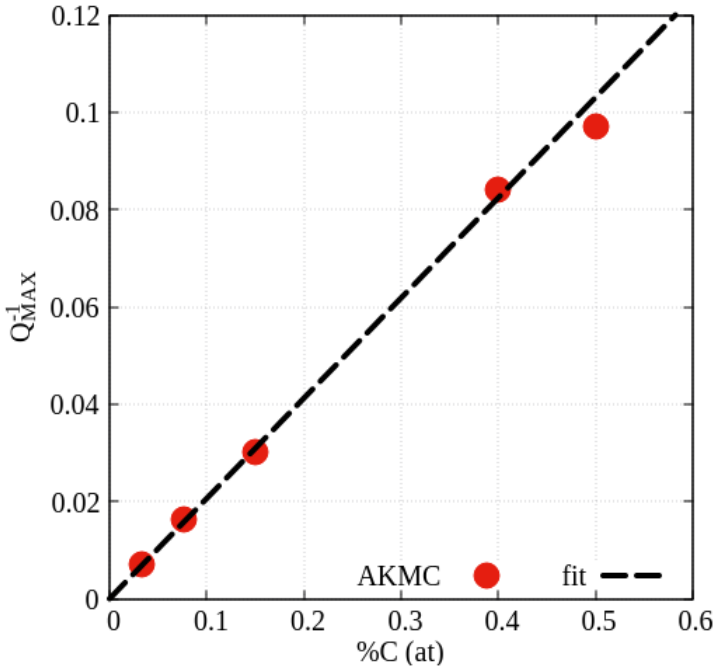

Figure 17: Dependence of the amplitude of the carbon Snoek peak in pure Fe Q^{-1}_{MAX} with the carbon concentration $\%C$.

Since we fitted ΔH_0^{seg}, α and ε_0^E for the case of C in pure Fe and due to the lack of experimental data, we cannot use these parameters in order to analyze the predicted amplitude of the carbon Snoek peak in pure Cr. As a result, we decided to plot the normalized AKMC results and compare it with those given by [63,67]. For an external frequency of 1Hz, the simulations give $T_{\max} = 440$ K ($\Delta H_C^m(Cr) = 1.21$ eV), which is slightly higher than the experimental value of Golovin et al. [67] ($T_{\max} = 433$ K, which corresponded to an experimental $\Delta H_C^m(Cr) = 1.11$ eV) and the one of Zemskiy and Spasskiy [63] ($T_{\max} = 425$ K with an experimental value of $\Delta H_C^m(Cr) = (1.13 \pm 0.03)$ eV).

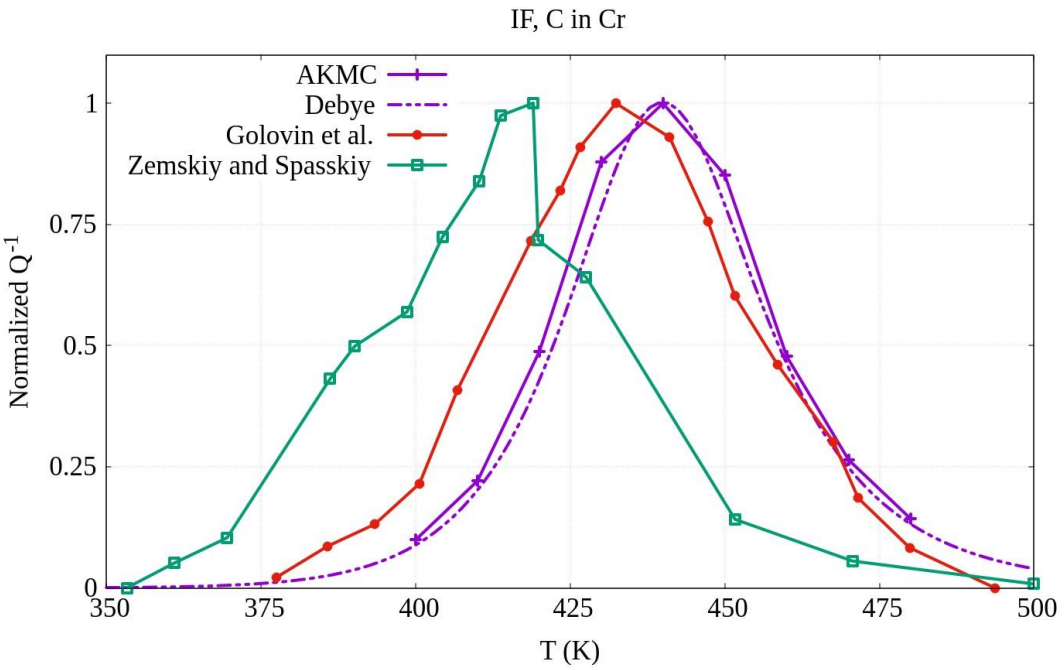

Figure 18: The Snoek peak in Cr-0.033%C, with $f = 1$ Hz and $\sigma_0 = 0.131$ GPa. Comparison between AKMC simulations, the Debye equation and the experimental results from Golovin et al. [67] and Zemskiy and Spasskiy [63].

We have developed a method that can reproduce the carbon Snoek peak in pure Fe accurately, both in its temperature and amplitude. The main advantage of our approach is that it can predict the Snoek peak in both dilute and concentrated alloys. A way to improve our simulated Snoek peaks would be to provide a more realistic model of the segregation enthalpy. Then we would be able to compare our AKMC results with the height of the Snoek peaks given by Saitoh et al. [51].

On the other hand, a segregation enthalpy $\Delta H_0^{seg} = 0.005$ eV (used for the comparison with the results by Saitoh et al. [51]) gives a noisy measurement of the carbon concentration. In order to improve our signal we decided to use a $\Delta H_0^{seg} = 0.01$ eV for the computation of the Snoek peaks in chapters 2 and 3. Since we are mainly interested in analyzing the effect of substitutional solutes on the $\Delta \bar{H}_C^m$ of interstitial atoms, we will keep ΔH_0^{seg}, α and ε_0^E as constants. In the next chapter we will use these methods and apply them for our modelling the carbon Snoek peak in concentrated Fe-Cr alloys.

5. Conclusions

In this chapter we have seen that different macroscopic quantities such as the tracer diffusion coefficient D_C and the temperature of the Snoek peak $T_{\max}$ are directly related to the jump frequencies (associated with a single migration barrier) of interstitials in pure metals. But in an alloy, there is a spectrum of possible migration barriers due to complex interactions

between interstitials and substitutional solute atoms. Consequently, these macroscopic variables actually provide information of an average jump frequency. We are interested to see if D_C and $T_{\max}$ reflect the same evolution on the associated average migration enthalpy.

We have showed that there are very few previous models that attempt to model the effect of substitutional solutes on the interstitial diffusion:

- In the case for the previous modelling of TD experiments, we have seen that most of these studies are constrained for dilute alloys where there is an attractive interaction between interstitials and substitutional solutes. Hennessey and Morral [23] seem to be the only study that attempts to model the TD when there is a repulsion. Moreover, some previous studies [20,22] have shown that if the substitutional solutes do not affect the saddle point energy of the jumping interstitials, the effective diffusion coefficient is related to the diffusion coefficient in the pure metal, the concentration of substitutional solutes and the binding energy between interstitials and substitutional impurities.
- In the case for the previous modelling of IF experiments, we have seen that there are different approaches. We have observed that AKMC simulations can be used to study the interstitial population and later model the Snoek peak [25,43]. We have also shown that other approaches involved computing the Snoek peak as a sum of independent Debye peaks [29,40,41], with each peak having associated an elementary relaxation time. However, this approach has been criticized by Koiwa [27,28] and shows that, in infinitely dilute alloys, each relaxation time is actually a complex function of elementary jump frequencies. We have also presented the model by Sandberg et al. [29] where they predict the carbon Snoek peak in concentrated Fe-Cr alloys using DFT calculations.

In this study, we propose a multiscale modelling approach which involves three defined steps for the simulation of TD and IF experiments in alloys (chapters 2 and 3). First, we will compute a set of interstitial-substitutional solute binding energies and migration barriers in dilute alloys using Density Functional Theory (DFT) calculations. Second, we will fit these values using two different pair interactions models. Third, we will implement these models in our AKMC codes in order to simulate TD and IF experiments. For the simulation of the TD, we will follow a standard approach. For the simulation of IF we present a new method, where we directly measure the interstitial concentration and compute Q^{-1}. Even though we have estimated the values of ΔH_0^{seg}, α and ε_0^E for the particular case of C in pure Fe using DFT calculations, we have showed that these parameters only affect the height of the Snoek peak (Eq. (1.56)) and the $\Delta \bar{H}_C^m$ only depends on the temperature of the Snoeak peak $T_{\max}$ (at a given frequency f, Eq. (1.58)). Since we are only interested in estimating $\Delta \bar{H}_C^m$, we will keep ΔH_0^{seg}, α and ε_0^E as constants for the remaining of this thesis. In the next chapter we will apply our multiscale approach in order to simulate TD and IF experiments of C in concentrated Fe-Cr alloys.

6. References

[1] Helmut Mehrer, Diffusion in Solids. Fundamentals, Methods, Materials, Diffusion-Controlled Processes, Springer, 2007.

[2] J.R.G. da Silvia, R.B. McLellan, Diffusion of carbon and nitrogen in B.C.C. iron, Mater. Sci. Eng. 26 (1976) 83–87. doi:https://doi.org/10.1016/0025-5416(76)90229-9.

[3] A.C. Damask, G.J. Dienes, Point defects in metals, Gordon and Breach, London, 1963.

[4] M. Weller, 2. Point Defect Relaxations, 2001.

[5] M. Weller, The Snoek relaxation in bcc metals—From steel wire to meteorites, Mater. Sci. Eng. A. 442 (2006) 21–30. doi:https://doi.org/10.1016/j.msea.2006.02.232.

[6] C.A. Wert, Diffusion coefficient of C in α-iron., Phys. Rev. B. 79 (1950) 601–605.

[7] G.H. Vineyard, Frequency factors and isotope effects in solid state rate processes, J. Phys. Chem. Solids. 3 (1957) 121–127.

[8] A. Einstein, Über die von der molekularkinetischen Theorie der Wärme geforderte Bewegung von in ruhenden Flüssigkeiten suspendierten Teilchen., Ann. Phys. 322 (1905) 549–560.

[9] M. Von Smoluchowski, Zur kinetischen theorie der brownschen molekularbewegung und der suspensionen, Ann. Phys. 326 (1906) 756–780.

[10] H. Mehrer, Diffusion in intermetallics, Mater. Trans. JIM. 37 (1996) 1259–1280.

[11] G.E. Murch, A.S. Nowick, Diffusion in Crystalline Solids, Academic Press, Inc., United States of America, 1984.

[12] C.G. Homan, Diffusion of carbon in α-Fe, Acta Metall. 12 (1964) 1071–1079.

[13] S.V. Zemskiy, B.P. Lyakhin, Influence of hydrogen on the diffusion of carbon in Chromium, Fiz. Met. Metalloved. 23 (1967) 913–16.

[14] R.A. Perkins, R.A. Padgett Jr., Oxygen diffusion in niobium and Nb-Zr alloys, Acta Metall. 25 (1977) 1221–1230.

[15] H. Landolt, R. Bornstein, Diffusion in solid metals and alloys, Springer, 1990.

[16] S. Choudhury, L. Barnard, J.D. Tucker, T.R. Allen, B.D. Wirth, M. Asta, D. Morgan, Ab-initio based modeling of diffusion in dilute bcc Fe–Ni and Fe–Cr alloys and implications for radiation induced segregation, J. Nucl. Mater. 411 (2011) 1–14.

[17] B.C. Zhou, S.L. Shang, Y. Wang, Z.K. Liu, Diffusion coefficients of alloying elements in dilute Mg alloys: A comprehensive first-principles study, Acta Mater. 103 (2016) 573–586.

[18] R.E. Howard, J.R. Manning, Kinetics of solute-enhanced diffusion in dilute face-centered-cubic alloys, Phys. Rev. 154 (1967) 561–568.

[19] K.E. Blazek, The effect of a substitutional solute element on the diffusivity of an interstitial solute element in a dilute ternary alloy, Trans. Jpn. Inst. Met. 19 (1978) 253–258.

[20] M. Koiwa, Trapping effect in diffusion of interstitial impurity atoms in bcc lattices, Acta Metall. 22 (1974) 1268.

[21] R.B. McLellan, Thermodynamics and diffusion behavior of interstitial solute atoms in non-perfect solvent crystals, Acta Metall. 27 (1979) 1655–1663.

[22] R.A. Oriani, The diffusion and trapping of hydrogen in steels, Acta Metall. 18 (1970) 147–157.

[23] T.P. Hennessey, J.E. Morral, A new model for interstitital diffusion in bcc alloys with traps or repulsive sites, in: High Temp. Corros. Mater. Chem. III, The Electrochemical Society, Inc, Washington DC, 2001: pp. 229–239.

[24] T. Schuler, M. Nastar, Transport properties of dilute α-Fe(X) solid solutions (X = C, N, O), Phys. Rev. B. 93 (2016) 224101. doi:10.1103/PhysRevB.93.224101.

[25] S. Garruchet, M. Perez, Modelling the carbon snoek peak in ferrite: coupling molecular dynamics and kinetic monte-carlo simulations, Comput. Mater. Sci. 43 (2008) 286–292. doi:https://doi.org/10.1016/j.commatsci.2007.11.004.

[26] M. Bouhafs, B. Dubois, Influence of the Carbon Content on the Internal Friction of Iron-17% Chromium Alloys, in: Intern. Frict. Ultrason. Attenuation Solids, Pergamon Press, England, 1979: pp. 343–348. doi:https://doi.org/10.1016/B978-0-08-024771-7.50060-0.

[27] M. Koiwa, Theory of the Snoek Effect in Ternary B.C.C alloys, Philos. Mag. 24 (1971) 81–106. doi:http://dx.doi.org/10.1080/14786437108216426.

[28] M. Koiwa, Theory of the Snoek Effect in Ternary B.C.C. Alloys : II. Simplified Treatment, Philos. Mag. 24 (1971) 107–122.

[29] N. Sandberg, K.O.E. Henriksson, J. Wallenius, Carbon impurity dissolution and migration in bcc Fe-Cr: First-principles calculations, Phys. Rev. B. 78 (2008) 094110. doi:https://doi.org/10.1103/PhysRevB.78.094110.

[30] M.S. Blanter, I.S. Golovin, H. Neuhäuser, H.R. Sinning, Handbook on internal friction in metallic materials., n.d.

[31] J. L. Snoek, Effect of small quantities of carbon and nitrogen on the elastic and plastic properties of iron., Physica. 8 (1941) 711–733. doi:https://doi.org/10.1016/S0031-8914(41)90517-7.

[32] O.. N.. Carlson, H. Indrawirawan, C.V. Owen, O. Buck, Internal Friction Study of Substitutional-Interstitial Interaction in Niobium-Vanadium Alloys, Metall. Trans. A. 18 (1987) 1415–1420. doi:https://doi.org/10.1007/BF02646655.

[33] H. Indrawirawan, O. Buck, O.N. Carlson, Substitutional-interstitial solute interactions in niobium-vanadium-oxygen alloys, Phys. Status Solidi A. 104 (1987) 443–451. doi:10.1002/pssa.2211040133.

[34] G. Haneczok, M. Weller, Analysis of Internal Friction spectra by Snoek-type relaxations, J. Common Met. 159 (1990) 269–276.

[35] A.S. Nowick, B.S. Berry, Anelastic relaxation in crystalline solids, Academic Press, London, 1972.

[36] A.S. Nowick, W.R. Heller, Anelasticity and Stress-induced Ordering of Point Defects in Crystals, Adv. Phys. 12 (1963) 251–298.

[37] R. De Batist, Internal Friction of structural defects in crystalline solids., North-Holland, Amsterdam, 1972.

[38] T.I.S. Kê, Experimental evidence of the viscous behavior of grain boundaries in metals., Phys. Rev. 71 (1947) 533–546.

[39] R. Abbaschian, L. Abbaschian, R.E. Reed-Hill, Physical Metallurgy Principles, Fourth, CENGAGE Learning, United States of America, n.d.

[40] G. Cannelli, R. Cantelli, F. Cordero, Statistical model for the trapping of interstitials by substitutional (interstitial) atoms in solids, Phys. Rev. B. 32 (1985) 3573–3579.

[41] L. Yu, F. Yin, D. Ping, Natural mechanism of the broadened Snoek relaxation profile in ternary body-centered-cubic alloys, Phys. Rev. B. 75 (2007) 174105.

[42] R. Chang, Mechanical relaxation associated with paired point defects in cubic lattices of Oh point group symmetry, J. Phys. Chem. Solids. 25 (1964) 1081–1090.

[43] M.S. Blanter, Influence of Interatomic Interaction on Internal Friction Spectrum in Nb-V-O Alloys (Computer Simulation), Phys. Status Solidi A. 133 (n.d.) 317–323.

[44] C.S. Becquart, J.M. Raulot, G. Bencteux, C. Domain, M. Perez, S. Garruchet, H. Nguyen, Atomistic modeling of an Fe system with a small concentration of C, Comput. Mater. Sci. 40 (2007) 119–129.

[45] O. Senninger, E. Martinez, F. Soisson, M. Nastar, Y. Bréchet, Atomistic simulations of the decomposition kinetics in Fe–Cr alloys: Influence of magnetism, Acta Mater. 73 (2014) 97–106. doi:https://doi.org/10.1016/j.actamat.2014.03.019.

[46] E. Martinez, O. Senninger, C.C. Fu, F. Soisson, Decomposition kinetics of Fe-Cr solid solutions during thermal aging, Phys. Rev. B. 86 (2012) 224109. doi:10.1103/PhysRevB.86.224109.

[47] F. Soisson, C.C. Fu, Cu-precipitation kinetics in α−Fe from atomistic simulations: Vacancy-trapping effects and Cu-cluster mobility, Phys. Rev. B. 76 (2007) 214102.

[48] E. Vincent, C.S. Becquart, C. Pareige, P. Pareige, C. Domain, Precipitation of the FeCu system: A critical review of atomic kinetic Monte Carlo simulations, J. Nucl. Mater. 373 (2008) 387–401.

[49] E. Vincent, C.S. Becquart, C. Domain, Solute interaction with point defects in α Fe during thermal ageing: A combined ab initio and atomic kinetic Monte Carlo approach, J. Nucl. Mater. 351 (2006) 88–99.

[50] S. Schmauder, P. Binkele, Atomistic computer simulation of the formation of Cu-precipitates in steels, Comput. Mater. Sci. 24 (2002) 42–53.

[51] H. Saitoh, N. Yoshinaga, K. Ushioda, Influence of substitutional atoms on the Snoek peak of carbon in b.c.c. iron, Acta Mater. 52 (2004) 1255–1261. doi:10.1016/j.actamat.2003.11.009.

[52] F. Giustino, Materials modelling using density functional theory: properties and predictions, Oxford University Press, 2014.

[53] G. Kresse, J. Furthmüller, Efficient iterative schemes for ab initio total-energy calculations using a plane-wave basis set, Phys. Rev. B. 54 (1996) 11169.

[54] G. Kresse, J. Hafner, Ab initio molecular dynamics for liquid metals, Phys. Rev. B. 47 (1993).
[55] J.P. Perdew, Y. Wang, Accurate and simple analytic representation of the electron-gas correlation energy, Phys. Rev. B. 45 (1992) 13244.
[56] J.P. Perdew, K. Burke, M. Ernzerhof, Generalized gradient approximation made simple., Phys. Rev. Lett. 77 (1996) 3865.
[57] G. Kresse, D. Joubert, From ultrasoft pseudopotentials to the projector augmented-wave method., Phys. Rev. B. 59 (1999) 1758.
[58] C.S. Becquart, F. Soisson, Monte Carlo Simulations of Precipitation Under Irradiation, in: Handb. Mech. Mater., Springer, Singapore, 2018: pp. 1–29.
[59] A.B. Bortz, M.H. Kalos, J.L. Lebowitz, A new algorithm for Monte Carlo simulation of Ising spin systems, J. Comput. Phys. 17 (1975) 10–18.
[60] O. Senninger, F. Soisson, E. Martinez, M. Nastar, C.C. Fu, Y. Bréchet, Modeling radiation induced segregation in iron–chromium alloys, Acta Mater. 103 (2016) 1–11. doi:https://doi.org/10.1016/j.actamat.2015.09.058.
[61] A.D. LeClaire, 8.2 Diffusion tables for C, N, and O in metals, in: Diffus. Solid Met. Alloys, Springer, 1990: pp. 473–485.
[62] P.L. Gruzin, S.V. Zemskiy, I.B. Rodina, Met Met. Pure Met. 4 (1963) 243.
[63] S.V. Zemskiy, M.N. Spasskiy, Carbon diffusion in Chromium, Fiz. Met. Metalloved. 21 (1966) 129–131.
[64] E.V. Borisov, P.L. Gruzin, S.V. Zemskiy, Zzashch Pokrytiya Met. 2 (1968) 104–109.
[65] L. Zhu, H. Wang, Q.M. Hu, G.J. Ackland, R. Yang, Trapping of interstitial defects: filling the gap between the experimental measurements and DFT calculations, J. Phys. Condens. Matter. 25 (2013) 435402.
[66] P. Liu, W. Xing, X. Cheng, D. Li, Y. Li, X.Q. Chen, Effects of dilute substitutional solutes on interstitial carbon in α-Fe: Interactions and associated carbon diffusion from first-principles calculations, Phys. Rev. B. 90 (2014) 024103.
[67] I.S. Golovin, M.S. Blanter, R. Schaller, Snoek Relaxation in Fe-Cr Alloys and Interstitial-Substitutional Interaction, Phys. Status Solidi A. 160 (1997) 49–60. doi:10.1002/1521-396X(199703)160:1<49::AID-PSSA49>3.0.CO;2-P.
[68] C. Wert, J. Marx, A new method for determining the heat of activation for relaxation processes, Acta Metall. 1 (1953) 113–115. doi:https://doi.org/10.1016/0001-6160(53)90047-9.

Chapter 2: Diffusion of C in Fe-Cr alloys

In chapter 1 we have shown the theoretical framework and the multiscale modelling approach used in this thesis. In this chapter we will apply these tools for the simulation of the tracer diffusion and internal friction experiments of C in Fe-Cr alloys. As we have seen in chapter 1, both experiments yield the same carbon migration barrier in pure metals. However, experimental studies have shown contradictory results on how Cr additions affect the migration barrier of carbon atoms in dilute Fe-Cr alloys. We will use our multiscale approach in order to understand this disagreement in the experimental literature and to provide some insight into the carbon diffusion in Cr-rich alloys. This chapter is divided in four parts. First, we will see an overview of the experimental results and previous modelling found in the literature for the tracer diffusion and internal friction experiments of C in Fe-Cr alloys. Second, we will analyze the interactions (i. e. the binding energies) between C and substitutional solute impurities and the kinetics (i. e. the migration barriers of C atoms in particular chemical environments) in dilute alloys using Density Functional Theory (DFT) calculations. Third, we will show two different proposed pair interaction models fitted to the DFT calculations and test their predictions according to their particular advantages and drawbacks. Fourth, we will apply Atomistic Kinetic Monte Carlo simulations in order to simulate the tracer diffusion and internal friction experiments of C in Fe-Cr and we will compare our results with the ones found in the literature. We will show that tracer diffusion and internal friction simulations predict different outcomes and we will provide an analysis of these interesting results.

1. Experimental data and previous modeling

1. 1. Experimental tracer diffusion results and previous modeling

Carbon tracer diffusion experiments in pure metals have been discussed in chapter 1. They show that $\Delta H_C^m(Fe) = 0.86$ eV and $\Delta H_C^m(Cr) = 1.21$ eV, in good agreement with DFT calculations. There are very few experimental data concerning the tracer diffusion of C in dilute Fe-Cr alloys [1–3] (up to 5%Cr), and none for the remaining range of concentrations. As we will see, the conclusions of each study are that the average carbon migration enthalpy in dilute Fe-Cr alloys increases slowly with Cr concentrations (at most 0.1 eV for 3.5%Cr). However, there is a disagreement whether the C-Cr binding energy is attractive or repulsive. The radioisotope C^{14} was used in the experimental literature and the temperatures were in the range of 800 K – 1300 K.

Blazek and Cost [1] performed carbon tracer diffusion experiments in dilute Fe-Cr (up to 3.5% Cr and 0.0005%C - 0.003%C) at four particular temperatures (989 K, 1236K, 1241 K and 1355 K) during 6 hours. They found that an increase of the Cr concentration at a given temperature (Figure 19(a)) barely had an effect on D_C. If we assume that the pre-exponential factor D_C^0 remains independent of the Cr concentration, it means that $\Delta \bar{H}_C^m$ slightly increased

within this range of Cr content (Figure 19(b)). We can see scattered results, where between 0%Cr and 3.5%Cr the increase on $\Delta\bar{H}_C^m$ could be as large as 0.07 eV (1236 K) or as low as 0.007 eV (1355 K). They assumed that the evolution of D_C with Cr concentration could be explained due to an apparent C-Cr attraction. They applied the Koiwa model for tracer diffusion (KMTD) [4] and estimated an attractive binding energy of 0.12 eV.

Matosyan and Golikov [2] performed tracer diffusion experiments in samples of Fe-0.014%C and Fe-1.95%Cr-0.09%C at a temperature of 623 K during 40 hours. They found that D_C decreased with Cr content at a constant temperature (Figure 19). Since the diffusion coefficient decreased by a factor of 4.5, it corresponded to an increase of $\Delta\bar{H}_C^m$ of 0.08 eV if we assume a constant pre-exponential factor D_C^0, a slightly higher increase of $\Delta\bar{H}_C^m$ than Blazek and Cost [1]. Their original objective was to induce a plastic strain on their samples prior to the diffusion annealing in order to create point defects that would affect the diffusion of carbon atoms. They found that the plastic strain decreased D_C, which corresponded to an attractive interaction between carbon atoms and any possible created point defects.

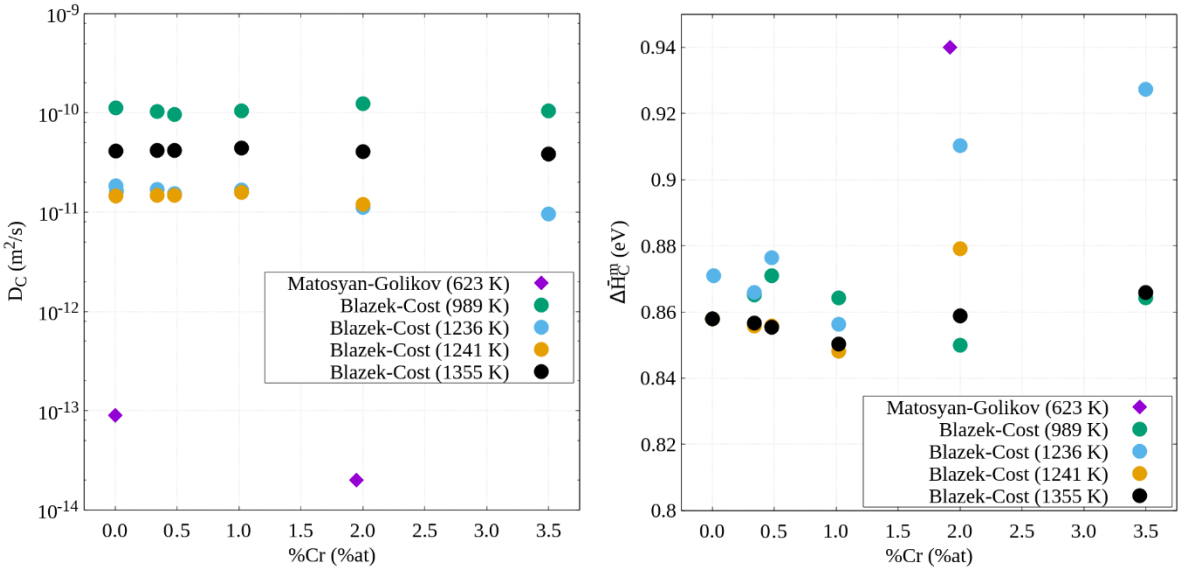

Figure 19: Experimental evolution of (left) D_C and (right) $\Delta\bar{H}_C^m$ in dilute Fe-Cr alloys according to Blazek and Cost [1] and Matosyan and Golikov [2].

Figure 20 shows the compilation of experimental data provided by Landolt and Bornstein [5] for D_C in pure Fe. We can see that Matosyan and Golikov [2] are in agreement with the database but the data points provided by Blazek and Cost [1] present some differences. Blazek and Cost [1] are only in agreement at 989 K, while their measured D_C at higher temperatures are lower, which is inconsistent with the expected Arrhenius behavior. A possible contamination in their diffusion couple or an overestimation in their measurement of the temperature might explain the discrepancy with the experimental data by Landolt and

Bornstein [5].

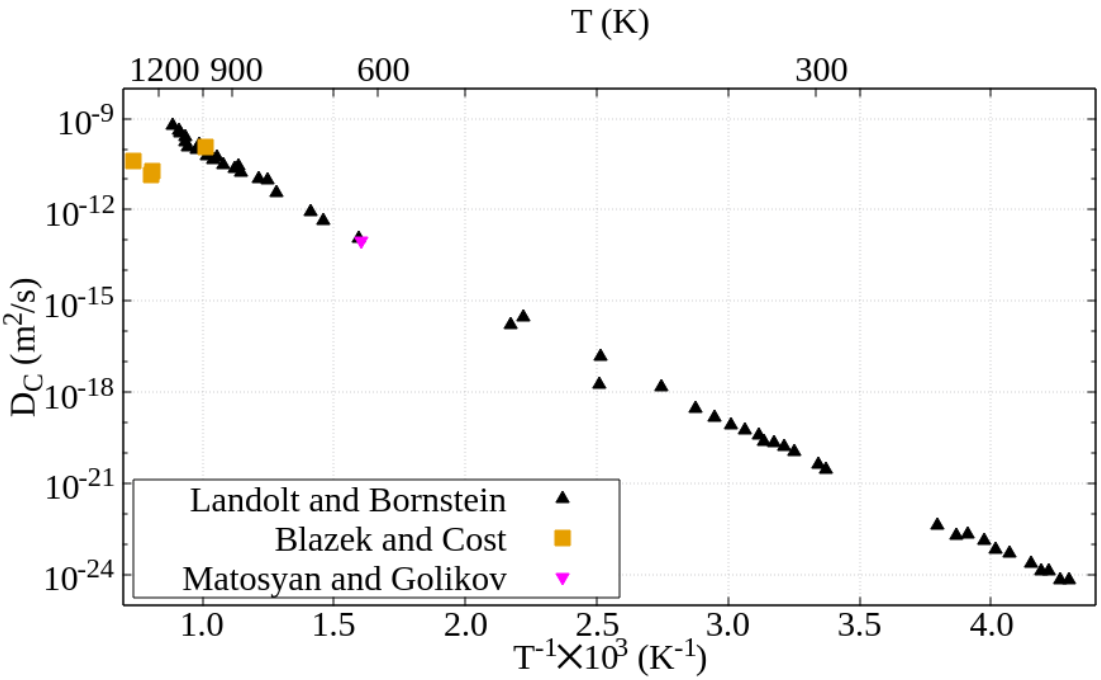

Figure 20: Experimental diffusion coefficient of C in α-Fe, as a function of the temperature. Data extracted from [1,2,5].

An attempt to simulate carbon tracer diffusion experiments via AKMC was performed by Liu et al. [6] in infinitely dilute Fe-Cr alloys, with Cr content up to 1.85%Cr. They considered only the interactions of a single Cr with a single C in Fe. They then computed the corresponding binding energies and migration barriers of carbon in this system. They found that the carbon-chromium binding energies were systematically repulsive and decreased with the distance between Cr and C from -0.31 eV up to -0.07 eV (from 1 nn up to 4 nn). These binding energies are in disagreement with the attraction estimated by Blazek and Cost [1] of +0.12 eV. Their local migration barriers for C in Fe, up to the 4nn of the Cr atom range from 0.77 eV to 0.96 eV, equal or slightly higher than the barrier in pure Fe. Liu et al. [6] then modelled the carbon diffusion and obtained the tracer diffusion coefficient using the Einstein-Smoluchowski relation (Eq. (10) from chapter 1). From these data they obtained the average migration enthalpy of Cr in dilute Fe-Cr alloys and found that it increased 0.1 eV from the value of C in pure Fe (0.83 eV).

1. 2. Experimental internal friction results and previous modeling

IF experiments of carbon in pure metals have been discussed in chapter 1. They show that $\Delta H_C^m(Fe) = 0.86$ eV and $\Delta H_C^m(Cr) = 1.21$ eV, in good agreement with DFT calculations.

There are several experimental data concerning the internal friction of C in dilute Fe-Cr alloys [3,7–10] (up to 5%Cr approximately), only two experimental studies in concentrated alloys [11,12] and none for dilute Cr-Fe alloys. As we will see, most of the experimental studies in dilute Fe-Cr alloys agree that the concentration of Cr has a little effect on the average carbon migration enthalpy $\Delta\bar{H}_C^m$ [3,7–9]. However, in those studies where the effect of Cr in Fe is significant [10–13], it is unclear whether this increase of $\Delta\bar{H}_C^m$ is due to an interaction of C atoms with Cr atoms or with other defects such as vacancies and dislocations. Table 1 shows a summary of the key parameters considered in the experimental literature.

Ref.	%Cr (at)	%C (at)	f (Hz)	ε	$T_{\max}$ (K)
[7]	0 – 1.77	0.012 ± 0.001	1	NA	320
[8]	2.5 – 12	~ 0.1	2	10^{-4}	305
[9]	0 – 1	~ 0.19	1.5	10^{-4}	320
[11]	17	0.044 – 0.18	1	2×10^{-5}	553
[10]	0.87 – 5.82	0.06 – 0.13	1	NA	313
[13]	0.87 – 5.82	0.06 – 0.13	NA	NA	308 ; 473
[12]	<20%Cr	NA	1	NA	$433 < T_{\max} < 530$
[3]	1.22 – 5.29	~ 0.01	NA	NA	~ 313

Table 1: Experimental determination of the temperatures of the IF peak in Fe-Cr-C alloys by [3,7–13].

Numakura [7] performed IF experiments for dilute Fe-Cr alloys (pure Fe, 0.6%Cr, 1.2%Cr and 1.77%Cr). He found all Snoek peaks to be at a temperature of 320 K and a slight decrease of the IF amplitude with increasing Cr content. He concluded that there seemed to be no interaction between Cr and C atoms.

Konstantinovic et al. [8] performed IF experiments in alloys with various Cr concentrations (a fully ferritic Fe-2.5%Cr; and ferritic/martensitic Fe-5%Cr, Fe-9%Cr and Fe-12%Cr). They found a Snoek peak at 305 K for the ferritic Fe-2.5%Cr system, whereas for the other samples they did not find a Snoek peak. They argued that these different results were due to the fact that in the fully ferritic sample, carbon atoms were dissolved in the matrix, whereas for the ferritic/martensitic samples, the carbon atoms were segregated in the grain/lath boundaries associated with carbide precipitation.

Saitoh et al. [9] performed IF experiments in dilute Fe-Cr-C alloys with Cr content between 0%Cr-1%Cr. They found a single IF peak at any Cr content, while its temperature remained unchanged at 320 K. They also found that the addition of substitutional solutes always decreased the amplitude of the Snoek peak. It is well known [14,15] that increasing the

concentration of interstitials also linearly increases the amplitude of the Snoek peak via a constant K. Another interesting result found by Saitoh et al. [9] was that this proportionality constant was also dependent of the Cr concentration: the inverse of K linearly increased with higher Cr content. They also concluded that the decrease of the Snoek peak with Cr additions was due to the strain caused by the difference in atomic size between Cr and Fe atoms.

Bouhafs and Dubois [11] performed IF experiments with Fe-17%Cr alloys. They estimated a dislocation density of 10^{14} m^{-2} (10^{10} cm/cm^3) and they did not find any precipitates in their studied alloys. Their IF experiments showed an asymetric peak at 553 K, a higher temperature that those registered for the carbon Snoek relaxation in pure metals and even in dilute alloys. They assumed a constant pre-exponential factor D_C^0 given by previous studies [2,3] from which they computed an appearent $\Delta \bar{H}_C^m = 1.55$ eV. They did not interpret their results in terms of Snoek peak (i. e. short-range diffusion of C) but rather as a result of a carbon-dislocation attraction of 0.57 eV. They showed that the C concentration only affected the amplitude of the IF peak and not its temperature.

Kristhal and Baranova [10] performed IF experiments in dilute Fe-Cr alloys (0.87%Cr-5.82%Cr). First they performed annealings at 1273 K – 1523 K and quenched their samples in order to obtain the maximum amount of vacancies. They showed a single IF peak at a temperature of 313 K for any given concentration. They found that the thermal treatments decreased the amplitude of the peak due to an excessive formation of vacancies and concluded that the vacancy formation enthalpy increased with higher Cr concentration. On a different study by Kristhal and Baranova [13], they performed IF experiments on Fe-Cr-C alloys with similar Cr content but they annealed their samples at lower temperatures (1073K – 1323K). In this case, they also showed that the increase of the annealing temperature also corresponded to a decrease in the peak maximum. They argued that this decrease corresponded to the decrease of C atoms in the solid solution due to the formation of carbides. For the particular alloy of Fe-0.85%Cr, they found two peaks, the first at 313 K and the second at 443 K. They observe that with Cr additions, this second shifted to higher temperatures. They performed 10% of plastic strain in Fe-0.85%Cr alloys in order to test if this second peak was due to C-Cr interactions or due to interactions with dislocations. They found that after the application of a plastic strain, a peak was found at 553K, whereas the other 2 peaks remained unchanged. They concluded that the 313 K corresponded to the short-range diffusion of C in pure iron and that the 443 K was due to the C-Cr interactions.

Golovin et al. [12] were the only ones who attempted to perform IF experiments in the whole range of Cr concentrations. They found that the Snoek peak of C in pure Fe was at 315 K, and with minor additions of Cr, the temperature of the peak increased very rapidly, reaching a maximum at Fe-38%Cr (550 K) and then decreasing with higher Cr content until reaching the value of C in pure Cr (433 K). Figure 21 shows the evolution of the temperature of the IF peak and the average carbon migration enthalpy at concentrated Fe-Cr alloys. They argued that Cr additions had a more significant impact on the temperature of the peak than the Fe addition in Cr-rich alloys. Another important aspect of their experiments was that, the

addition of Cr only increased the temperature of the peak but did not observe the appearance of extra-peaks as seen in Figure 22. They also observed that the IF peak was always lower than the observed in the pure metals, but they decided not to give details about this evolution since the amplitude of the peak was also dependent on previous thermal treatments and natural ageing. They assumed that the peaks given in their IF experiments are due to Snoek-type relaxations. In order to find the average carbon migration enthalpy they used the linear relationship given by Wert and Marx [16]. We must notice that they included in their analysis the data shown by Krishtal and Baranova [10] for dilute Fe-Cr alloys and interpreted them as averages migration enthalpies for carbon diffusion, disregarding the carbon-vacancy interaction. According to this analysis, there is an increase on $\Delta\bar{H}_C^m$ of 0.5 eV between 0%Cr and 5%Cr. Even if we do not consider the results by Krishtal and Baranova [10], Golovin et al. [12] register a strong increase of $\Delta\bar{H}_C^m$ by 0.6 eV between 0%Cr and 18%Cr.

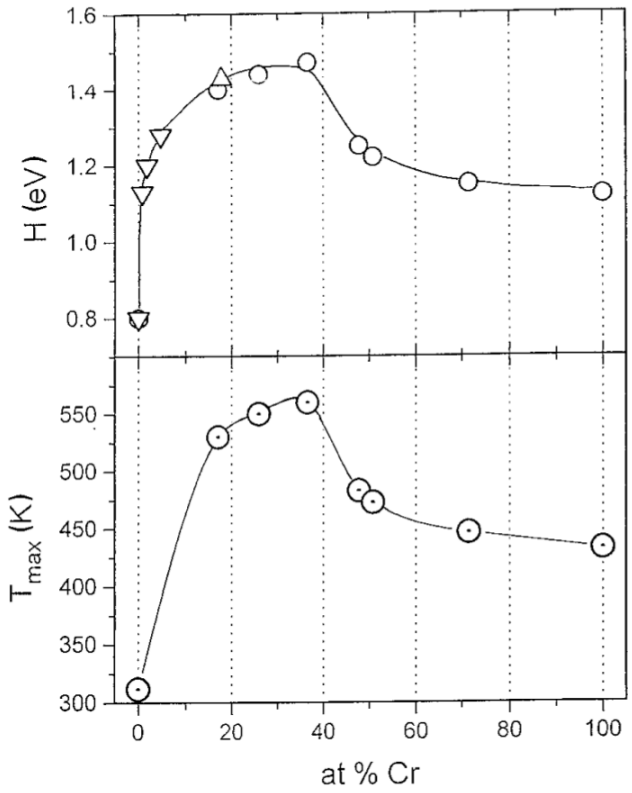

Figure 21: Influence of the average migration enthalpy (top) and of the temperature of the IF peak (bottom) with Cr concentration. Experimental values found by Golovin et al. [12] (circles) and Krishtal and Baranova [10] (inverted triangles).

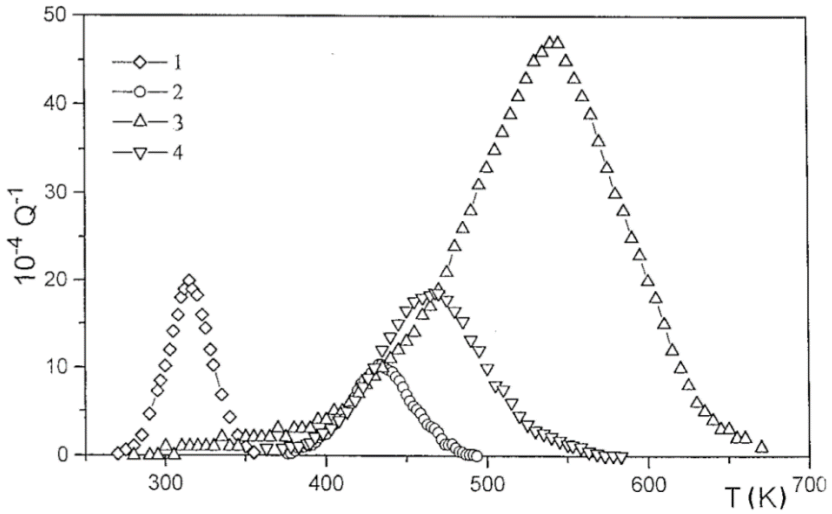

Figure 22: Experimental results shown by Golovin et al. [12], showing the Snoek peaks of Fe-0.033%C (%at) (1), Cr-0.013%C (%at) (2), Fe-17.1%Cr-0.134%C (%at) (3), Fe-71.3%Cr-0.044%C (%at) (4) at $f = 1$ Hz. Figure extracted from [12].

Ward and Leak [3] were the only ones who attempted to perform both internal friction and tracer diffusion experiments of C in dilute Fe-Cr. They first performed internal friction experiments for samples with three different chemical composition (Fe-1.22%Cr, Fe-2.95%Cr and Fe-5.29%Cr) at temperatures between 243 K and 343K. They found that $\Delta\bar{H}_C^m$ decreased slightly with Cr concentration (0.86 ± 0.06 eV for Fe-1.22%Cr, 0.81 ± 0.02 eV for Fe-2.95%Cr and 0.78 ± 0.02 eV for Fe-5.29%Cr). On the other hand, they also performed tracer diffusion experiments for samples with Fe-1.22%Cr and Fe-5.29%Cr alloys at temperatures between 873 K and 1073 K. They found much higher average migration enthalpies at these compositions 1.35 ± 0.07 eV (Fe-1.22%Cr) and 1.5 ± 0.1 eV (Fe-5.29%Cr). For both experiments they found an Arrhenius relationship between D_C and T^{-1}, where at 773 K it changes abruptly as seen in Figure 23. We must also notice that they do not attempt to do both experiments without Cr.

Because of this change in the Arrhenius relationship (Figure 23), they distinguished two different stages. They concluded that the average migration enthalpy found via internal friction experiments corresponded to the short-range diffusion of C atoms. For the $\Delta\bar{H}_C^m$ found by tracer diffusion experiments they proposed two explanations. They first propose that this difference was due to a strong attractive vacancy-carbon binding energy close to 0.7eV. They discarded this possibility because they C-vacancy pair is dissolved at temperatures greater than 523 K and because according to their experiments, the C-vacancy pair diffused faster than its constituents which is unlikely. They later proposed a model where a small concentration of C atoms occupy tetrahedral positions and the atoms instead of jumping from one octahedral site to the next nearest neighbor, they jumped from one tetrahedral site to the next one.

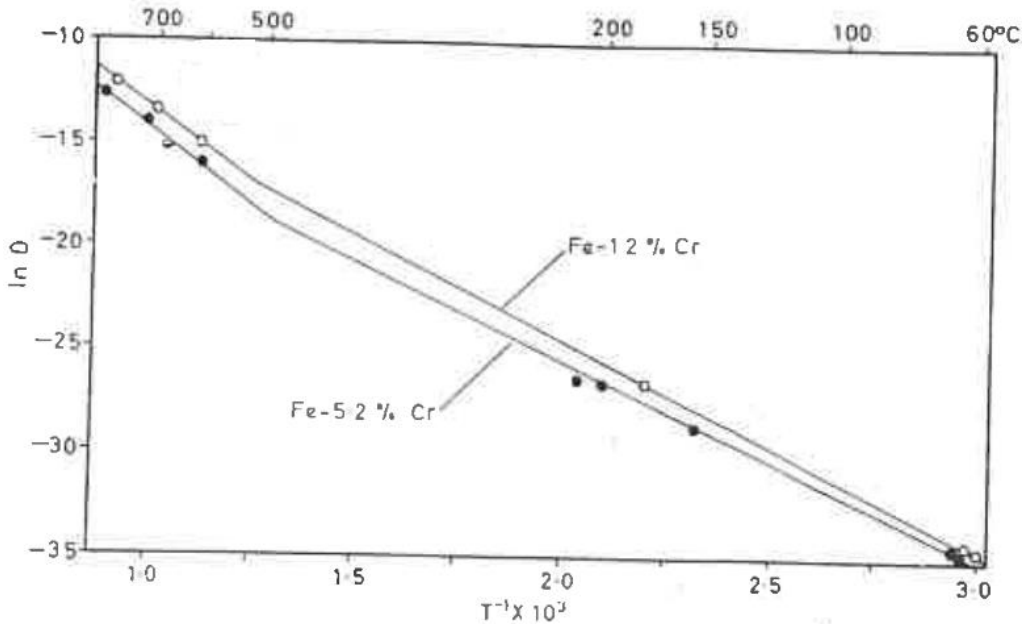

Figure 23: Dependence of the diffusion coefficient with the inverse of the temperature, for dilute Fe-Cr-C, for experimental TD and IF measurements, given by Ward and Leak [3].

Table 1 and Figure 24 show a summary of the main IF results provided by the experimental literature. We can see that usually the temperature of the IF peak $T_{\max}$ is provided and from which $\Delta\bar{H}_C^m$ is extracted. We can observe that most of the experiments were performed at a low frequency (usually 1 Hz). The different studies [3,7–12] agree that the C concentration only affects the amplitude of the IF peak. In other words, at a constant frequency, the main parameter that affects $T_{\max}$ is the interaction between carbon atoms and point defects such as dislocations [11], vacancies [10] and substitutional solute atoms [9]. Most of these experimental studies agree that the addition of Cr concentration mainly affects the height of the IF peak [9] and has no effect on $T_{\max}$ [3,7–9].

The carbon Snoek peak in Fe-Cr alloys has been modelled by Sandberg et al. [17]. Their approach was solely based on DFT calculations, where they calculated the local migration barriers ΔH_C^m of a single C atom in several random solid solutions at different Cr concentrations. At a given Cr content, they used each ΔH_C^m as a basis to compute the Snoek peak as a sum of independent Debye peaks. An advantage of this method is that it can compute the Snoek peak for concentrated alloys quite easily. Although they also found a broadening of the Snoek peak in alloys, they predicted that the addition of substitutional solute atoms produces a second peak, which is in disagreement with the results by Golovin et al. [12] as shown in Figure 25. Nevertheless, the assumption of Sandberg et al. [17] consisting in writing the IF response Q^{-1} as a sum of Debye peaks, each one associated with a specific local configuration of the alloy and an average jump frequency corresponding to the inverse of the residential time of the configuration, has two main drawbacks. First,

AKMC simulations provide a better description because they simulate the diffusion process which controls the IF experiments. Second, according to different theoretical studies [18–21] it is not correct to assume that each Debye peak can be directly associated with an elementary jump frequency.

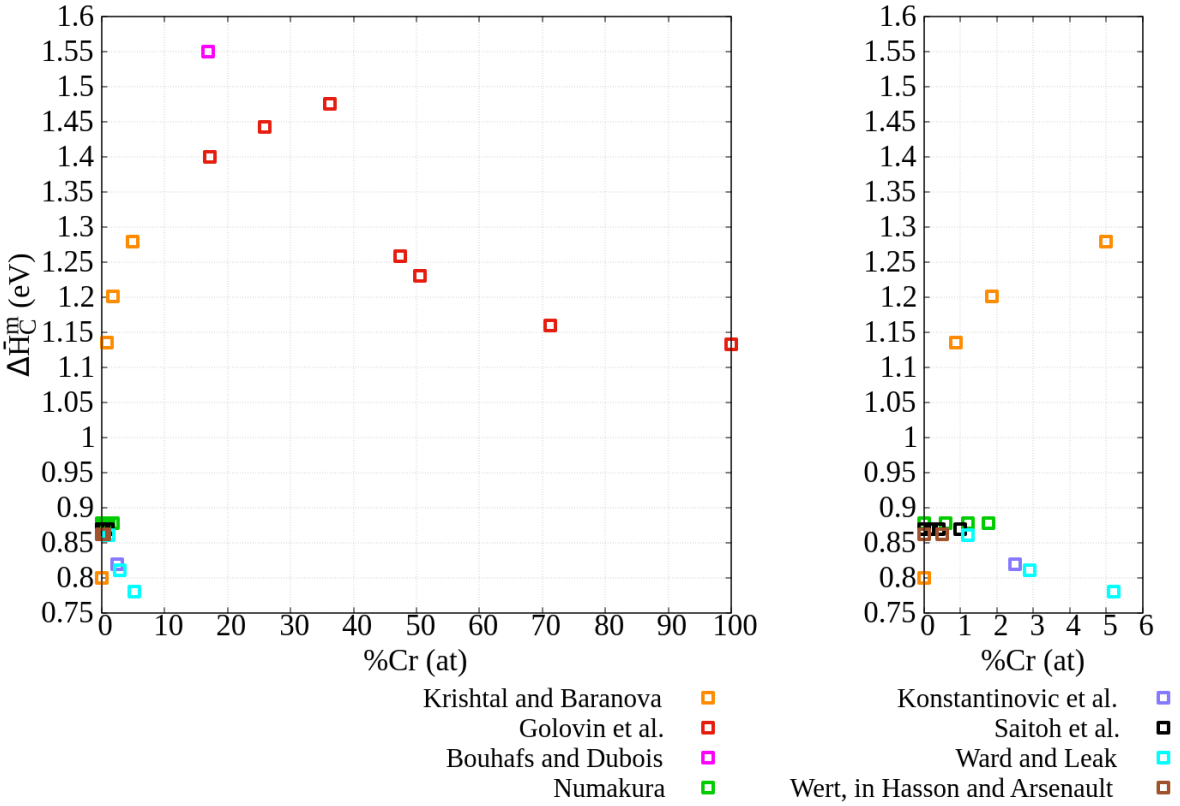

Figure 24: Evolution of $\Delta\bar{H}_C^m$ with Cr content according to the experimental literature [3,7–12,22].

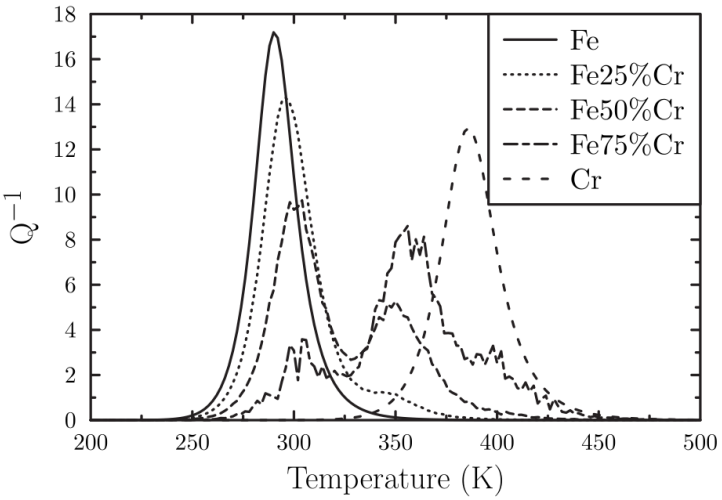

Figure 25: Calculated Snoek peak by Sandberg et al. [17].

In conclusion, Figure 26 shows a summary of the $\Delta\bar{H}_C^m$ extracted by tracer diffusion and internal friction experiments by different authors in the literature. We see that up to Fe-5%Cr, most of the studies of TD and IF agree that the average carbon migration enthalpy should be close to the carbon migration barrier in pure Fe or slightly higher, 0.85 ± 0.10 eV. There are a few experimental studies that do not agree with this general trend. Tracer diffusion measurements performed by Ward and Leak [3] show a high increase but they argue that their value could be related to an attractive binding energy between carbon and vacancies. Bouhafs and Dubois [11] find an average migration enthalpy of 1.55 eV in Fe-17%Cr, but they assume that this high migration enthalpy corresponds to an attractive interaction between carbon atoms and dislocations and not due the short-range of C atoms. Kristhal and Baranova [10] find a single IF peak at an unique temperature of 313K and analyze their IF peaks in terms of the vacancy formation enthalpy in dilute Fe-Cr-C alloys. The study of Golovin et al. [12] is the only one that assumes that this high increase in $\Delta\bar{H}_C^m$ is directly related to a simple Snoek effect and do not discuss the possibility of having interactions between carbon atoms and other defects such as vacancies, dislocations, etc. In this chapter we will compare these experimental results with our multiscale model of TD and IF in Fe-Cr-C alloys, with the objective to explain some of these contradictory data.

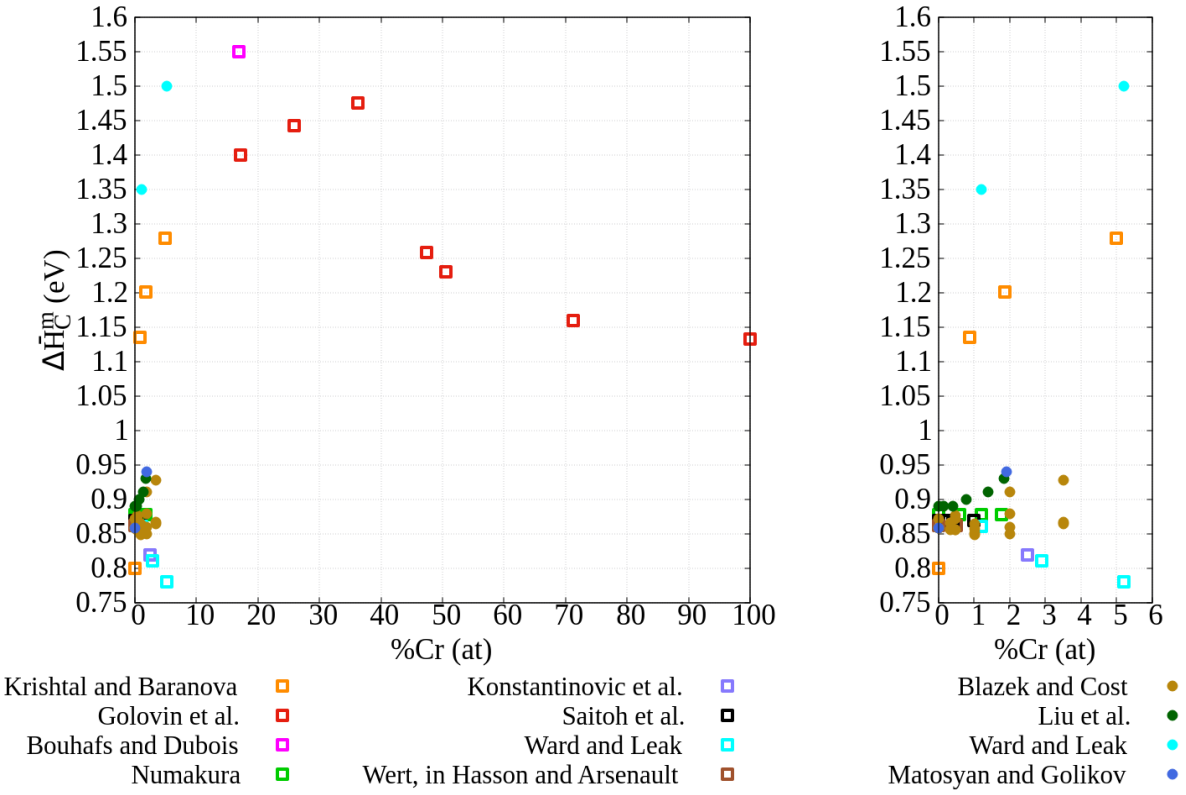

Figure 26: Evolution of the average migration enthalpy with Cr concentration according to experimental IF and TD results. Data values were extracted from [1–3,6–12,22].

2. DFT calculations

2.1. Introduction

We will first use DFT calculations to get reliable information on the interaction between carbon and substitutional solute impurities and their effect on the local migration barrier in dilute alloys. We will try to reveal some general trends found with the DFT calculations. These calculations will be used to parametrize the pair interaction models.

For the determination of the C binding and migration energies in Fe-Cr alloys (in our systems, the difference in energy at constant volume is almost equal to the difference in enthalpy), we used constant-volume calculations using supercells containing 128 bcc lattice sites. We assumed that the calculated equilibrium lattice parameter at 0 K of ferromagnetic (FM) Fe (2.831 Å) and anti-ferromagnetic (AF) Cr (2.853 Å) was constant for Fe-rich and Cr-rich supercells, respectively. All the supercells contained less than 5% of substitutional solutes (Fe or Cr) and one C atom. Three-dimensional periodic boundary conditions were applied. For the Brillouin-zone sampling, the Methfessel-Paxton [23] smearing function of a 0.3 eV width was used. Concerning the k-points, the Monkhorst-Pack scheme [24] was used with a grid of 4×4×4 for the Fe and Cr based 128 sites-supercells considered. A cut-off condition of 10−6 eV for the electronic convergence loops and of 0.02 eV/Å on the residual forces for the structural optimizations were used.

The binding energies and the migration barriers were computed for a total of 50 configurations with the C atom surrounded by a given number of substitutional solute atoms, using the drag method [25]. In all cases the stable positions of the C atoms were found to be on octahedral sites, and their saddle-point on tetrahedral sites.

2.2. Solution energies of C in pure Fe and Cr

We define the solution energy of C in a pure metal as:

$$E_C^S(mM) = E(mM + 1C) - E(mM) - E(1C) \tag{2.1}$$

where $E(mM + 1C)$ is the energy of the pure metal with m substitutional solute atoms (M) and a C atom sitting in an octahedral position in the pure metal, $E(mM)$ is the energy of the pure metal and $E(1C)$ is the energy of a C atom in a reference state (for our calculation we chose to use graphite). Our DFT results yield a solution energy of $E_C^S(Fe) = 0.826$ eV, being in good agreement with previous values found by Souissi et al. [26] ($E_C^S(Fe) = 0.874$ eV), by Jiang and Carter [27] ($E_C^S(Fe) = 0.74$ eV) and by Sandberg et al. [17] ($E_C^S(Fe) = 0.81$ eV). Moreover, we find a solution energy of $E_C^S(Cr) = 1.53$ eV, being slightly lower than the value obtained by Sandberg et al. [17] of $E_C^S(Cr) = 1.96$ eV. We can see that $E_C^S(mM)$ is always positive, which means that the C dissolution to be endothermic, i.e., not energetically favorable to insert one interstitial C in the pure metal (Fe, Cr) matrix. In other words, $E_C^S(mM)$ controls the solubility limit of C in the metal.

In the following, we will consider Fe-Cr alloys with a very low carbon concentration where the precipitation of carbon and carbon-carbon interactions are negligible. We will focus on

substitutional solute-carbon interactions and the relevant quantities are the binding energies and the migration barriers.

2.2. Binding energies between C and substitutional solute atoms in dilute alloys

We define the binding energy as the energetic difference between a C atom when it is in the pure metal (Fe, Cr) and when it is surrounded by a predetermined configuration of substitutional solute atoms:

$$E^b_{C\text{-}nS} = E(mM + 1C) + E((m-n)M + nS) - E((m-n)M + nS + 1C) - E(mM), \quad (2.2)$$

$E\left((m-n)M + nS\right)$ is the energy of the system containing n substitutional solutes (S) with $(m-n)$ substitutional solute atoms (M) in a particular configuration and $E\left((m-n)M + nS + 1C\right)$ is the energy of the C atom close to the particular configuration of substitutional impurities. With this definition, $E^b_{C\text{-}nS}$ is positive when the C-nS interactions are attractive. To describe particular configurations with several substitutional solute impurities, we define $E^b_{C\text{-}nS}(x, y, ...)$ as the binding energy between one C and n atoms S, with x atoms S as 1nn of C, y atoms S as 2nn, etc. This notation can be extended if there are substitutional solute atoms in higher order shells. Moreover, our notation and our pair interaction models will not take into account the particular geometrical configurations of the substitutional solute impurities around the C atom.

For extremely dilute systems, we have determined the relative energy of a C atom at various distances from a single Cr (resp. Fe) atom in a FM-Fe (resp. AF-Cr) lattice, and the corresponding C migration barrier (Figure 27). We note that the Cr-C interaction in Fe is longer range than C-Fe interaction in Cr. The former is significantly repulsive for 1nn, 2nn and 3nn positions ($E^b_{C\text{-}1Cr}(1) = -0.25$ eV, $E^b_{C\text{-}1Cr}(0,1) = -0.24$ eV, $E^b_{C\text{-}1Cr}(0,0,1) = -0.10$ eV) while the latter is highly attractive at only a 1nn distance $E^b_{C\text{-}1Fe}(1) = +0.34$ eV, but negligible beyond. These results are in good agreement with other DFT calculations by Sandberg et al. [17] and Liu et al. [6]. Sandberg et al. [17] found the C-Cr binding energies in Fe-rich alloys equal to -0.28 eV and -0.22 eV at 1nn and 2nn, respectively. Liu et al. [6] found slightly higher values of the C-Cr binding energies in Fe-rich alloys equal to -0.31 eV and -0.26 eV at 1nn and 2nn. Table 2 contains a short summary of the comparison between our calculated binding energies and those found in the literature for Fe-rich alloys. On the other hand, the 1nn C-Fe binding in Cr of Sandberg et al. [17] is 0.28 eV, only slightly smaller than our value. This global trend of a repulsive Cr-C interaction in Fe and an attractive Fe-C interaction in Cr is also consistent with the solution energies, as a result of $E^S_C(Cr)$ being greater than $E^S_C(Fe)$.

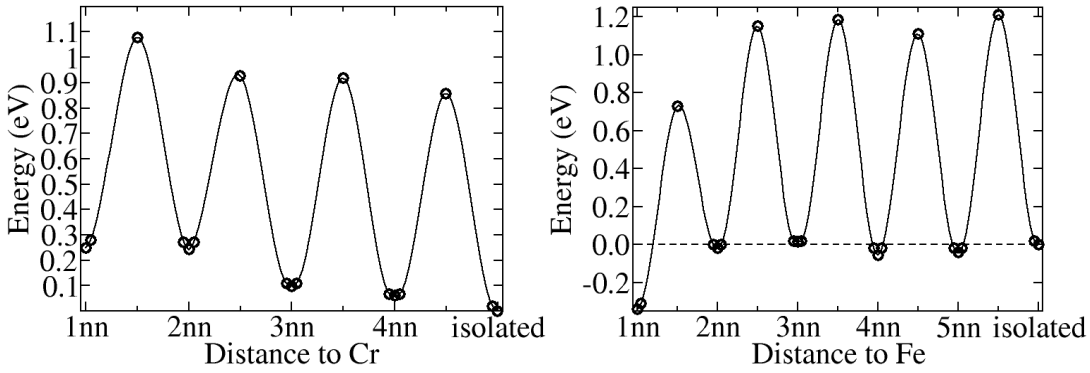

Figure 27: Energetic landscape of a C atom at an ith-nearest neighbor (inn) site from the single Cr atom in a FM-Fe lattice (left), and from the single Fe atom in an AF-Cr lattice (right). The reference state is an isolated C atom, well far from the substitutional solute.

Configurations	This work (eV)	Liu et al. [6] (eV)	Sandberg et al. [17]
$E^b_{C\text{-}1Cr}(1)$	-0.25	-0.31	-0.28
$E^b_{C\text{-}1Cr}(0,1)$	-0.24	-0.26	-0.22
$E^b_{C\text{-}1Cr}(0,0,1)$	-0.10	-0.13	-0.08
$E^b_{C\text{-}1Cr}(0,0,0,1)$	-0.06	-0.07	Not available

Table 2: Comparison between our DFT results and the ones given by ref. [6,17] for Fe-rich alloys.

Figure 28 shows the dependence of the binding energy between a carbon atom and n Cr atoms in Fe ($E^b_{C\text{-}nCr}$) and between a carbon atom and n Fe atoms in Cr ($E^b_{C\text{-}nFe}$). It can be seen that for any local chemical environment of Cr, the C-*n*Cr interaction is always repulsive, having a minimum when there are 3 Cr atoms around a C atom ($E^b_{C\text{-}3Cr}(2,0,0,1) = -0.44$ eV) as shown in Figure 29(a), and then increase with the number of Cr neighbors. On the other hand, the C-*n*Fe interactions in Cr-rich alloys are in general highly attractive. The maximum of attraction is found for $E^b_{C\text{-}4Fe}(2,0,2) = +0.98$ eV as shown in Figure 29 (c). The binding energy decreases with higher numbers of Fe neighbors.

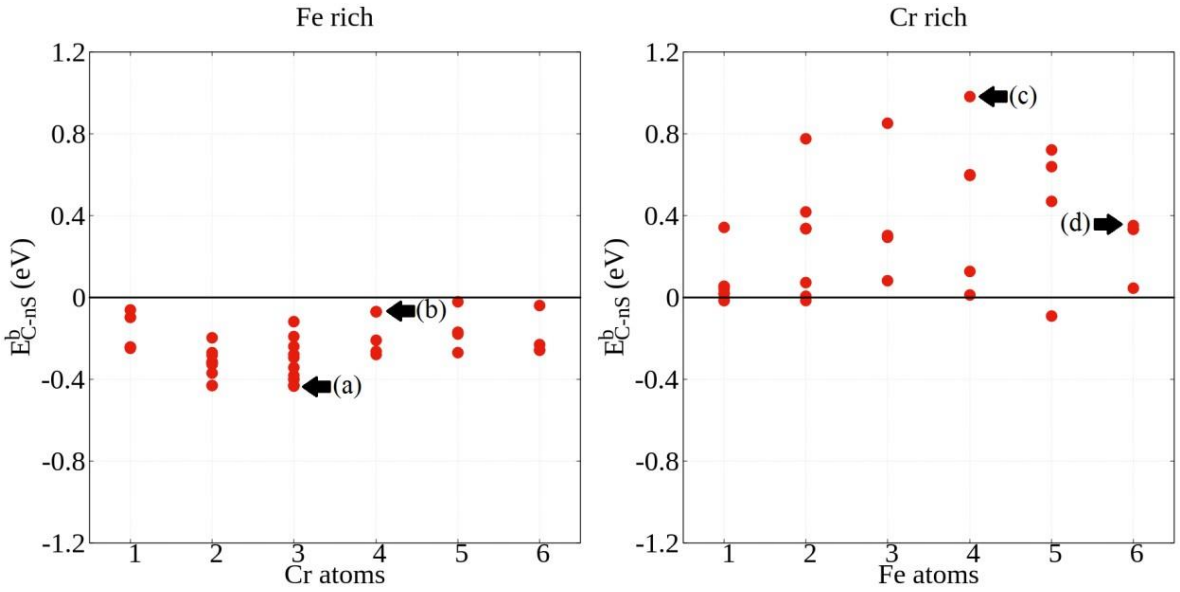

Figure 28: Binding energies as a function of the total number of substitutional solute atoms in the system in Fe-rich alloys (left) and in Cr-rich alloys (right). Labels (a), (b), (c) and (d) correspond to configurations seen in Figure 29.

Magnetic effects contribute to the non-monotonous dependence of the binding energy with the number of neighboring substitutional solutes. For systems very rich in Fe, the formation of Cr clusters is energetically unfavorable due to the emergence of magnetic frustrations [28]. In some cases, the presence of the C atom may partially release the frustration. This is for instance the case shown in Figure 29 (b) presenting one of the less repulsive C-*n*Cr configurations in iron: $E^b_{C\text{-}4Cr}(2,2) = -0.07$ eV, where four Cr atoms form a tetrahedron. Although neighboring Cr atoms tend to be antiferromagnetic to each other, due to the dominance of Fe-Cr interactions, all the Cr atoms have magnetic moments antiparallel to the Fe moments. The magnetic frustration is reflected on the small Cr moments magnitudes without the C atom (0.9 μ_B on each Cr) related to the value of isolated Cr in Fe (1.8 μ_B). The carbon atom screens the Cr-Cr interactions, leading to a decrease of the magnetic frustration and an increase of the local moment on the two Cr atoms 2nn of C from 0.9 μ_B to 1.5 μ_B. On the opposite side, in Cr-rich systems, the magnetic moment of a single Fe atom in AF-Cr is small (0.58 μ_B) due to the emergence of a magnetic frustration [28]. Fe clustering is energetically favorable, and due to the strong ferromagnetic interaction between Fe, local magnetic moment on the Fe atoms is typically around 2.0 μ_B, similar to the value of Fe in bcc FM-Fe (2.2 μ_B). However, the presence of C inside the Fe clusters may screen the Fe-Fe magnetic coupling and significantly decrease the magnetic moment of some of the Fe atoms. For example, in the case shown in Figure 29(d), where the C atom is surrounded by 6 Fe atoms. The resulting local moment of the 1nn Fe atoms is decreased from 2.0 μ_B to 0.1 μ_B. Also, the local moment of the 2nn Fe atoms slightly decreases from 2.0 μ_B to 1.9 μ_B. This may explain a relatively low C-*n*Fe binding energy of 0.35 eV for this configuration,

compared with some other C-*n*Fe configurations containing fewer number of Fe atoms.

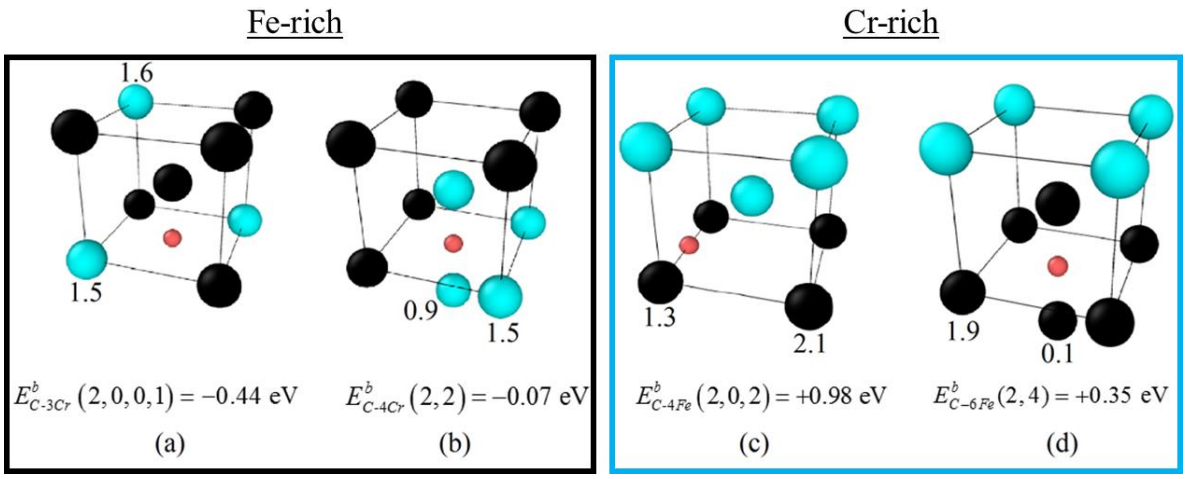

Figure 29: Examples of specific configurations of C atoms (red) in the octahedral position, surrounded by 3 Cr atoms in Fe (a), 4 Cr atoms in Fe (b), 4 Fe atoms in Cr (c), and 6 Fe atoms in Cr (d). Fe atoms are shown in black, Cr atoms in blue and the C atom in red. Local atomic moments (in μ_B) are shown for the substitutional solute atoms. In the Fe-rich cases, Cr moments are always antiparallel to the Fe moments.

2.3. Migration barriers of C in dilute alloys

We find the value of the migration barrier of C in pure Fe, $\Delta H_C^m(\mathrm{Fe})$, equal to 0.86 eV, in excellent agreement with previous experimental results [12,14,29–31] and calculations [17,32]. Concerning pure Cr and Cr-rich systems, the IF experiments of Golovin et al. [12] show Snoek peaks at temperatures above the magnetic transition temperatures (311 K for pure Cr). Therefore, in principle, C migration barriers should be computed considering a paramagnetic (PM) state. At variance with Fe, not only transversal but also longitudinal disorder of local magnetic moments in PM-Cr is important. To our knowledge, the treatment of PM-Cr bulk with defects at a DFT level is still a challenge, and it is beyond the scope of the present study. For simplicity, we consider the AF arrangement between Cr atoms in all the Cr-rich systems. The AF-Cr is the magnetic ground state if the Cr lattice contains a few percent of Fe. The carbon migration barrier found in pure AF-Cr, $\Delta H_C^m(\mathrm{Cr}) = 1.21$ eV, is in good agreement with previous DFT [17] and experimental results [12,33–36]. We also determined the value in another well distinct magnetic state, the NM (nonmagnetic) pure Cr, where a very similar value of 1.18 eV is found. This similarity suggests that C migration barriers may depend only weakly on the Cr magnetic state. A summary of the experimental results from the literature can be found in Figures 11 and 12 of chapter 1.

The local migration barriers for C in Fe, up to the 4nn of the Cr atom ranges from 0.69 eV to 0.86 eV, equal or slightly smaller than the barrier in pure Fe. On the other hand, the C barriers around the Fe atom in Cr, up to the 5nn distance are more scattered, they range from 0.2 eV

to 1.24 eV, as shown in Figure 30. The smallest barrier corresponds to the returning barrier from a 2nn to the lowest-energy nn site of the Fe atom.

The C migration barriers are closely related to the binding energies. In Fe-rich alloys, ΔH_C^m ranges from 0.6 eV to 1.15 eV, with a tendency to increase with higher number of local Cr atoms (Figure 30). Since C-*n*Cr interactions are repulsive, it is not expected to frequently find a C atom surrounded by a high number of Cr atoms in Fe-rich alloys. On the other hand, for Cr-rich alloys, ΔH_C^m presents very scattered values, from around 0.3 eV up to 1.2 eV, reaching a minimum value when there are locally 3 or 4 Fe atoms. The very low barriers occur when C atoms are trapped within a small cluster of Fe atoms. For example, if a C is surrounded by 4 Fe atoms forming a tetrahedron (Figure 29(b)), the saddle-point site is the center of the tetrahedron, while the initial and final octahedral positions are equivalent, that is, with 2 Fe as 1nn and 2 Fe as 2nn ($E_{C-4Fe}^b(2,2) = +0.60$ eV and the $\Delta H_C^m = 0.28$ eV). Due to the great scattering of ΔH_C^m in Cr-rich alloys, it is expected that the addition of Fe in Cr-rich alloys strongly affects the diffusion of C. In particular, highly positive binding energies are expected to produce strong trapping effects and low C migration barriers, and therefore expected to introduce strong correlation effects between successive C jumps.

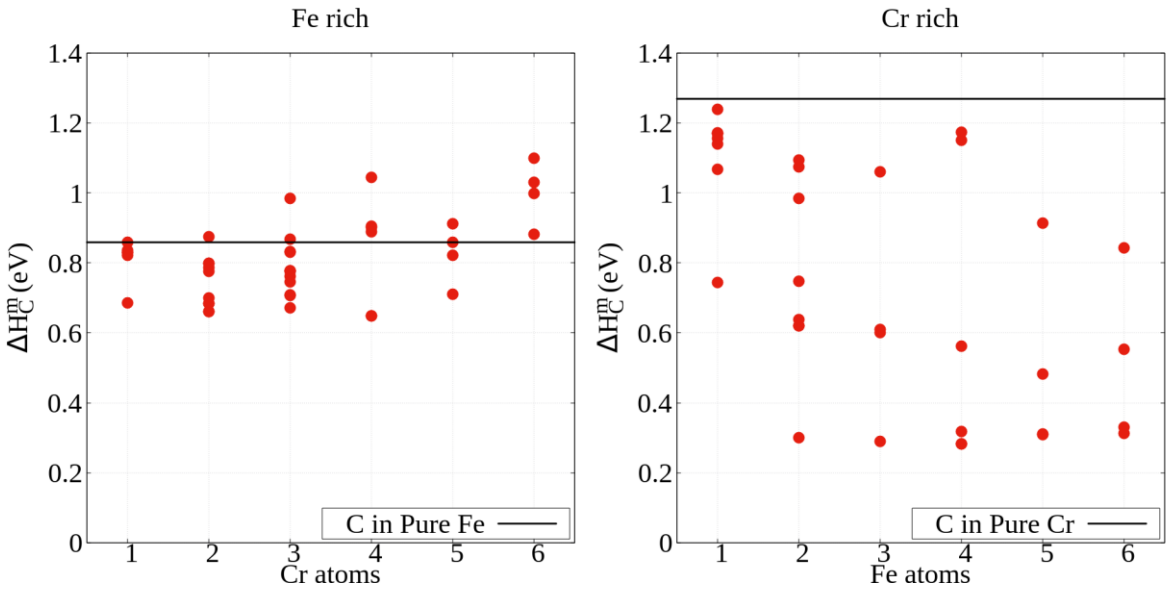

Figure 30: The migration barriers of C as a function of the total number of substitutional solute atoms in the system is in Fe-rich alloys (left) and in Cr-rich alloys (right).

3. Pair interaction models

3.1. Introduction

As we have seen in chapter 1, the objective is to develop a model that is able to reasonably reproduce the DFT results for any given local chemical environment and to predict new

binding energies and migration barriers in concentrated alloys. In this section we will show two different approaches following the same procedure as for the computation of the migration barriers in chapter 1, how well they can reproduce the DFT data, and how they potentially affect the computational time and the final results shown by the AKMC simulations.

The migration barrier of a carbon atom jumping from a site i to a site j is defined as:

$$\Delta H_C^m(ij) = H_{i,j}^{SP} - H_i \tag{2.3}$$

where $H_{i,j}^{SP}$ and H_i are the total enthalpies of system, when the interstitial is respectively at the saddle point (SP) and in the initial position. For our modelling, we considered interactions up to 2 nn at the saddle point and up to 3 nn at the initial octahedral position.

- Model 1:

Due to a low concentration of C atoms, we will consider that C-C interactions are negligible. This approach computes the carbon migration barriers in local chemical environments of substitutional solute atoms as:

$$\Delta H_C^m(ij) = \left(\sum_m VFeC_m^{SP} + \sum_m VCrC_m^{SP}\right) - \left(\sum_n VFeC_n^i + \sum_n VCrC_n^i\right), \tag{2.4}$$

where VSC_m^{SP} correspond to the carbon-substitutional solute S (Fe,Cr) pair interaction formed at the saddle point and VSC_n^i are the pair interactions at the position broken during the jump (fitted to the DFT database of binding energies). Table 3 and Table 4 show the values of the pair interactions at the octahedral position and at the saddle point respectively.

Pair interaction	Value (eV)
$VFeC_1^i$	-1.00
$VCrC_1^i$	-0.81
$VFeC_2^i$	-0.26
$VCrC_2^i$	-0.21
$VFeC_3^i$	-0.50
$VCrC_3^i$	-0.40

Table 3: Fe-C and Cr-C pair interactions at the octahedral position i and as n nearest neighbors.

Pair interaction	Value (eV)
$VFeC_1^{SP}$	0.88
$VCrC_1^{SP}$	1.00
$VFeC_2^{SP}$	-2.43
$VCrC_2^{SP}$	-2.12

Table 4: Fe-C and Cr-C pair interactions at the saddle point SP and as m nearest neighbors used for the computation of migration barriers of model 1.

- Model 2:

We also tried a second type of modelling of the migration barriers of C. This other method is derived from a standard approach [37], which is to write $H_{i,j}^{SP}$ as:

$$H_{i,j}^{SP} = \frac{H_i + H_j}{2} + \Delta H_C^0, \tag{2.5}$$

where H_j is the total enthalpy of the system after the C jump and ΔH_C^0 is considered to be a constant. Note that it implies, for example, the same C migration barrier in pure Fe and in pure Cr. In order to better reproduce the DFT results, we defined ΔH_C^0 as:

$$\Delta H_C^0 = \frac{\Delta H_C^m(\mathrm{Fe}) n_{Fe} + \Delta H_C^m(\mathrm{Cr}) n_{Cr}}{n_{Fe} + n_{Cr}}, \tag{2.6}$$

where $\Delta H_C^m(\mathrm{Fe})$ and $\Delta H_C^m(\mathrm{Cr})$ are the C migration barriers in pure Fe and Cr (0.86 eV and 1.21 eV respectively). n_{Fe} and n_{Cr} are the total amount of Fe and Cr neighbors at the saddle point.

Combining equations (2.3) and (2.5), we deduce:

$$\Delta H_C^m(ij) = \frac{H_j - H_i}{2} + \Delta H_C^0. \tag{2.7}$$

$H_j - H_i$ is computed by counting the number of C-Fe and C-Cr pair interactions broken in the initial configuration *i* and formed in the final configuration *j*, using the parameters given by Table 3.

3.2. Agreement between the DFT and PIM binding energies

In order to analyze how well the pair interaction models can reproduce the DFT data, we introduce the standard error, which is defined as:

$$SE = \frac{1}{N}\sum_{n=1}^{N}\left(X_n^{DFT} - X_n^{PIM}\right)^2, \tag{2.8}$$

where N corresponds to the total number of configurations considered, X_n^{DFT} is a particular value (binding energy, migration barrier) given by the DFT calculations and X_n^{PIM} is the corresponding value predicted by a pair interaction model.

Figure 31 shows a comparison between the DFT and PIM binding energies. In Fe-rich alloys, the PIM reproduces the main DFT trends: the C-*n*Cr interactions are systematically repulsive and the C-*n*Fe interactions are highly attractive. We have a good agreement for the average values even if particular configurations are poorly reproduced (the standard error is 0.068 and 0.046 for the Fe-rich and Cr-rich systems respectively). The PIM sometimes overestimates the repulsion in Fe-rich alloys: contrary to DFT results, it predicts binding energies below -0.4 eV (the lowest is ~ -0.7 eV) when a carbon atom is surrounded by 2 Cr atoms as 1nn and at least 2 Cr as 2 nn. Nevertheless, those local Cr environments with a highly repulsive binding energy will have a negligible effect on the diffusion of C since their probability of occurrence will be very small. Likewise, the PIM values of E^b_{C-nFe} in Cr-rich alloys (almost always attractive) are in good agreement with the DFT calculations, even though there is a significant scattering of the E^b_{C-nFe} values ranging from 0.4 eV to 0.8 eV. Some binding energies are poorly reproduced in that case. For example, the PIM predicts a large attraction of the 5 Fe cluster with $E^b_{C\text{-}5Fe}(1,4) = +0.38$ eV, instead of the moderate repulsion $E^b_{C\text{-}5Fe}(1,4) = -0.092$ eV found by DFT. On the contrary, PIM underestimates a few binding energies in highly attractive configurations: $E^b_{C\text{-}2Fe}(2) = +0.3845$ eV instead of +0.776 eV, $E^b_{C\text{-}3Fe}(2,0,1) = +0.4825$ eV instead of +0.852 eV, $E^b_{C\text{-}5Fe}(2,0,3) = +0.5805$ eV instead of +0.981 eV. In Cr-rich alloys this discrepancy may have a higher impact on the diffusion properties because the positive binding energy indicates that these are stable configurations for C atoms.

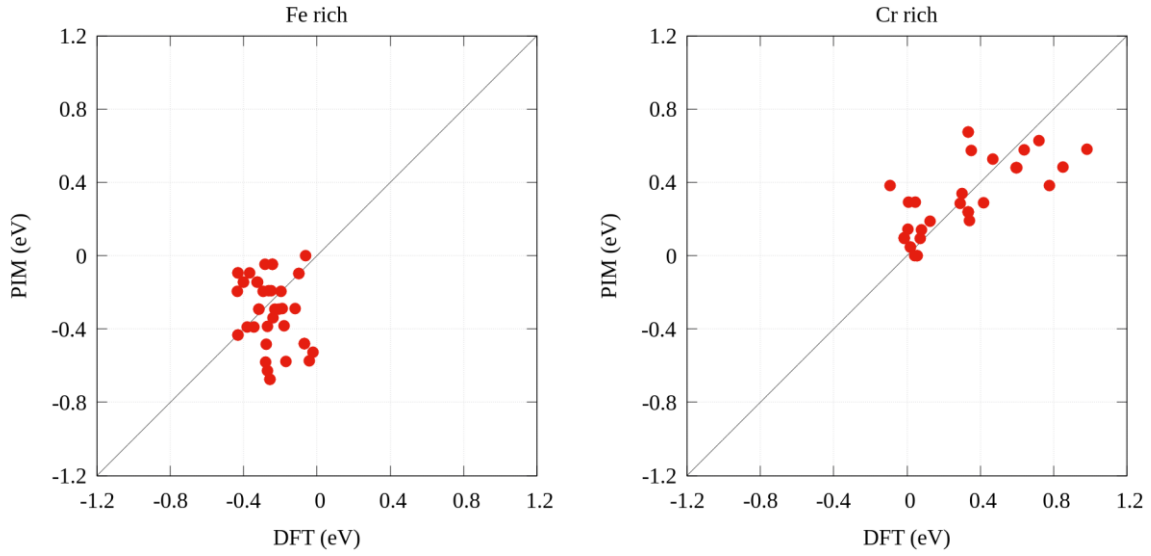

Figure 31: Comparison between the PIM and the DFT values of binding energies between C and Cr atoms in Fe-rich environments (left) and between C and Fe atoms in Cr-rich environments (right).

3.3. Agreement between the DFT and PIM migration barriers

Since the binding energy is related to the probability of finding a particular chemical local environment, it is a qualitative indicator on how likely a C atom might jump with a particular migration barrier. Figure 32 and Figure 33 show the comparison between the migration barriers computed by the DFT and the pair interaction model as a function of the DFT values of the binding energy before the jump (E_i^b), for model 1 and model 2 respectively.

Figure 32 shows how accurate are reproduced the DFT migration barriers by model 1, for Fe-rich and Cr-rich alloys. In pure Fe and Cr, both models precisely reproduce the ΔH_C^m . In Fe-rich configurations, the DFT predicts that the values of ΔH_C^m are within the range 0.6-1.2eV, but our model predicts a wider range of values (between 0.8 and 1.6 eV). Moreover, most of the migration barriers in Fe-rich alloys are overestimated by this first approach. But the main advantage of this model lies in Cr-rich configurations: the model reproduces the large dispersion in the DFT results (0.4 eV up to 1.2 eV). In other words, it can give a more accurate description of the migration barriers in this range of concentration. Nevertheless, it must be noted that the ΔH_C^m are best described within the range of 0.6 eV up to 1 eV, where the binding energy of the system before the jump is between 0 eV and 0.5 eV. In other words, model 1 fails to reproduce some migration barriers with a high binding energy (i. e. with a high probability of occurrence).

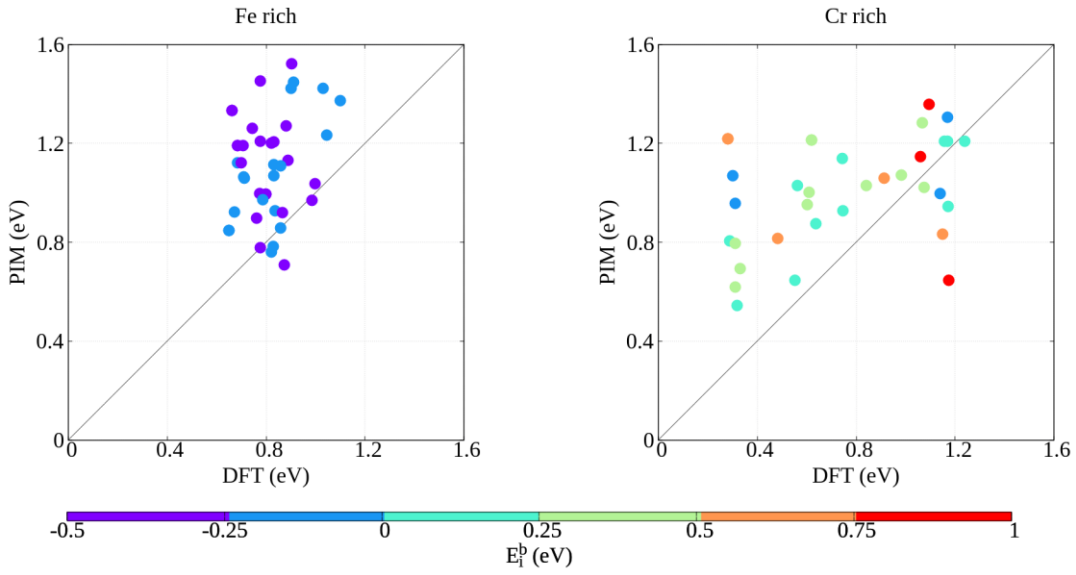

Figure 32: Comparison between model 1 with the DFT values for ΔH_C^m when the C atom is in Fe-rich environments (left) and when it is in Cr-rich environments (right). The color code gives the DFT values of the binding energy before the jump (E_i^b).

Figure 33 shows the comparison between model 2 with the DFT calculations, as function of the binding energy of the C atom before the jump. We can see that this model reproduces

more accurately the migration barriers in Fe-rich alloys (the values are distributed between 0.8 eV and 1.2 eV). In Fe-rich configurations, the DFT predicts that ΔH_C^m increases with a higher number of local Cr atoms and that the values of ΔH_C^m are within the range 0.6 - 1.2eV, which is well reproduced by model 2 (the standard error between the DFT values and the PIM is 0.058). On the other hand, it does not reproduce very well the migration barriers in Cr-rich alloys. This is due to the computation of the ΔH_C^0 factor: since it is an 'average' of the migration barriers in the pure components, it underestimates the dispersion of the migration barriers by overestimating ΔH_C^m and it fails to reproduce migration barriers which are as low as 0.2 eV (as seen in Cr-rich alloys). Nevertheless, this model has also its advantages. First, it slightly reproduces more accurately the migration barriers in Fe-rich alloys, where the migration barriers are close to $\Delta H_C^m(Fe)$ and the dispersion of ΔH_C^m is due to the C-Cr repulsion which is modelled by the pair interaction models. Second, most of the previous experimental work has been done in dilute Fe-Cr-C alloys. Third, even though there is an underestimation of the range of ΔH_C^m in Cr-rich alloys, those configurations with a high initial binding energy (which have a high probability of occurrence) are well reproduced compared to those predicted by model 1. Fourth, as we will see later, this model has its advantage: this overestimation in the ΔH_C^m limits the correlation effects in the AKMC simulations and significantly reduces the computation time. Using model 2, we will also simulate the IF for the whole range of concentrations and compare it with the results shown by Golovin et al. [12].

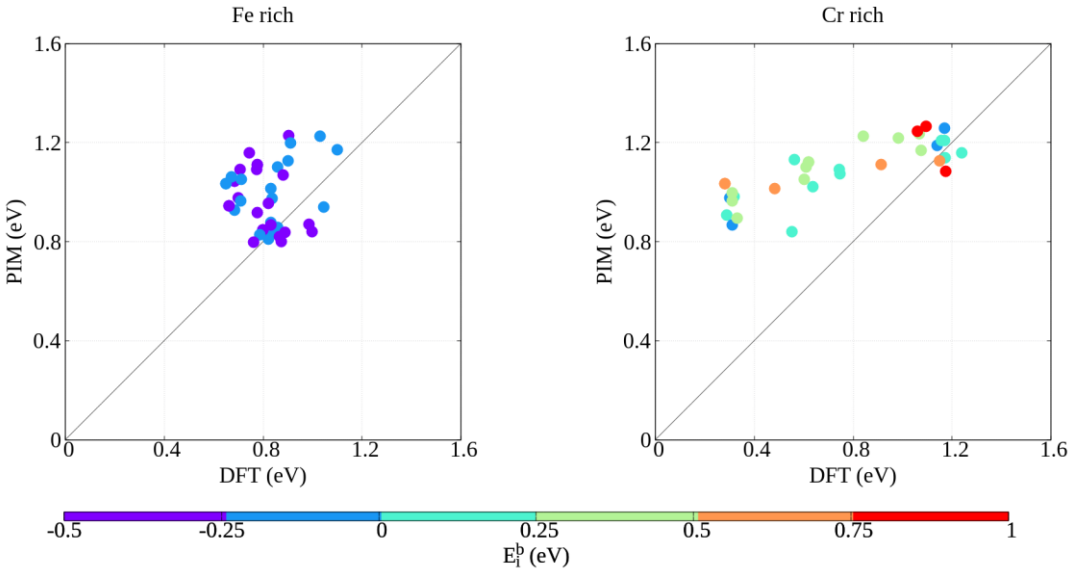

Figure 33: Comparison between model 2 with the DFT values for ΔH_C^m when the C atom is in Fe-rich environments (left) and when it is in Cr-rich environments (right). The color code gives the DFT values of the binding energy before the jump (E_i^b).

In the following pages, we will use both models as inputs for our AKMC simulations in order to model tracer diffusion and internal friction experiments. From these simulations we will extract an average carbon migration enthalpy ($\Delta\bar{H}_C^m$) in Fe-Cr alloys and compare them with the ones shown in the experimental literature. We will also see how the large dispersion of the ΔH_C^m values affect the efficiency of the AKMC simulations. We will conclude this chapter by analyzing the evolution of $\Delta\bar{H}_C^m$ as a function of Cr concentration and to mention similarities and differences in the results using the different models.

4. AKMC simulations of Tracer Diffusion

The carbon tracer diffusion coefficients in solid solutions of different compositions, measured with the method described in chapter 1, are showed in Figure 34, comparing model 1 and model 2. We can explain the following results in terms of 'trapping' and 'correlation'. We refer to trapping effects when the C atoms are pinned down close to particular local configurations of substitutional solute atoms due to a strong attraction. We refer to correlation when the carbon atoms jump back and forth several times within these interstitial sites and do not produce long-range diffusion. We must notice that both approaches differ by the way the saddle point energy is computed. In other words, the trapping effects are the same for both models since they are related to the binding energies. But the correlation effects might be different for model 1 and model 2.

We can see similarities and differences in the tracer diffusion coefficient obtained using model 1 and model 2 (Figure 34). First, in most cases both models yield an Arrhenius relationship. At Cr concentrations up to 20%Cr, we observe in the case of model 2 a stronger decrease of D_C with Cr additions at a given temperature. This might be due to the fact that model 1 predicts lower values of ΔH_C^m which maintain the value of D_C relatively constant. By increasing even more the Cr concentration, model 1 and model 2 predict a decrease of D_C. Moreover, we see that in the case of model 1 D_C does not follow and Arrhenius relationship for Fe-75%Cr and Fe-95%Cr. Since model 1 predicts some extremely low values of ΔH_C^m in Cr-rich alloys, it produces strong correlation effects and D_C lacks sufficient precision. Even though the migration barriers computed by model 2 never are as small as the lowest barriers of model 1 due to the ΔH_C^0 factor, it provides better results for the computation of D_C in the AKMC simulations. Even though each model differently computes the local migration barrier, the C atoms are trapped in Fe-rich configurations.

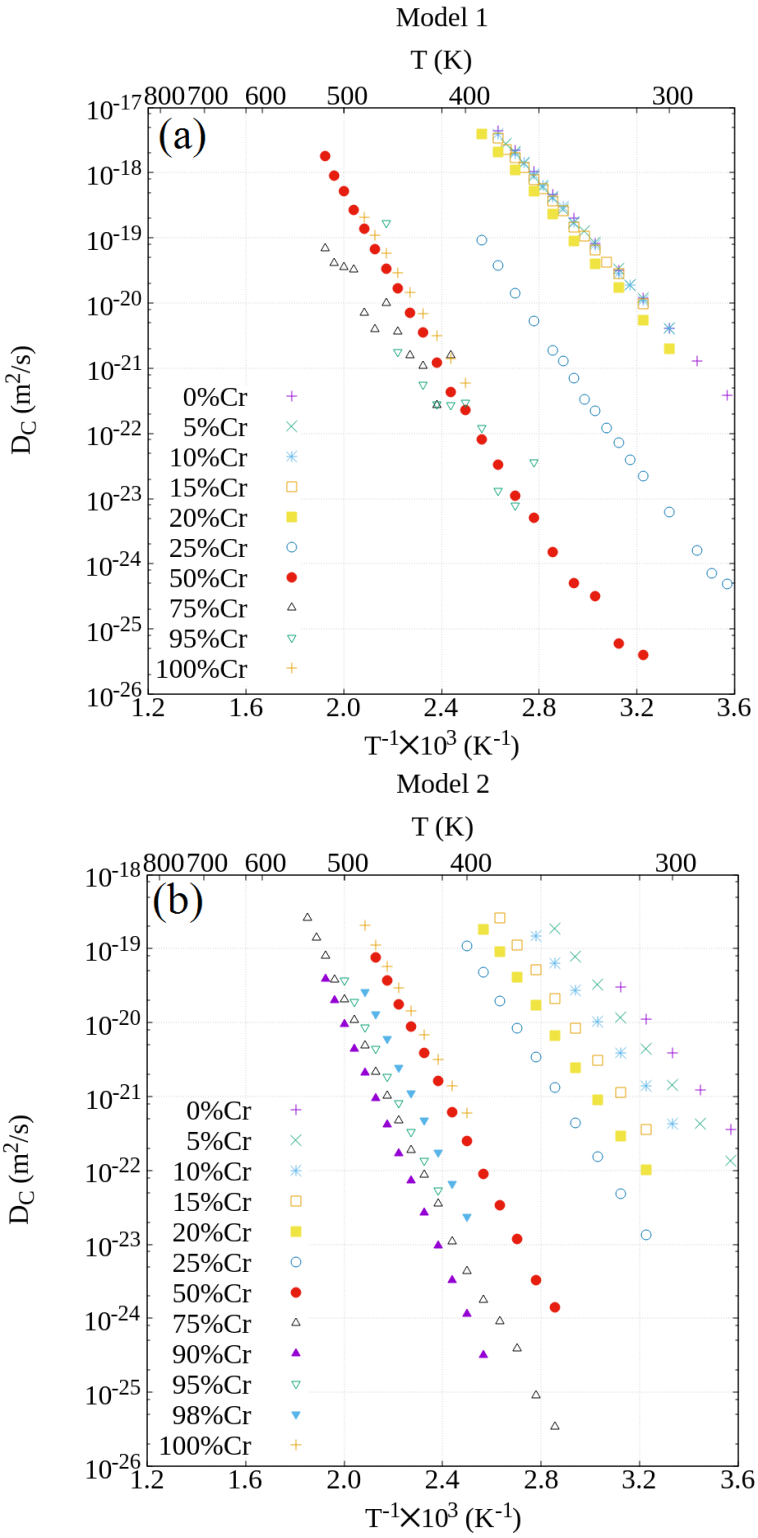

Figure 34: Evolution of the tracer diffusion coefficient of carbon in Fe-Cr solid solutions, as a function of the temperature and the Cr concentration (AKMC simulations).

Figure 35 gives the evolution of the correlation factor f_C as a function of the concentration and the temperature. As expected, in the case of direct interstitial diffusion in pure metals, $f_C = 1$: the diffusion of C atoms follows a perfect random walk. In the case of model 1, f_C continuously decreases and its dependence on temperature becomes important as the concentration of Cr increases in the system. When the alloy has a Cr concentration greater than 20%Cr, the correlation factor decreases abruptly and can reach values as low as 10^{-8} at 75%Cr at 400 K, and the correlation factor seems to vary exponentially with temperature. We see similar effects with the simulations where model 2 was used: as the Cr concentration increases, f_C decreases as well at a faster rate up to 20%Cr. As f_C decreases with Cr composition, it reaches a minimum at 75%Cr (at 400 K $f_C \approx 10^{-5}$). Nevertheless, with higher Cr concentrations, f_C increases until reaching unity at 100%Cr. Even though the decrease of f_C using both models is expected, we must emphasize that they do not decrease at the same rate: for example at 50%Cr and at 400K, the correlation factor using model 1 is $f_C \approx 10^{-8}$ whereas with model 2 is $f_C \approx 10^{-5}$. This very low f_C explains why model 1 is not suitable from a computational point of view: due to very strong correlation effects of C atoms, these jump back and forth several times and do not let the whole system to evolve. As a result, we see that for highly concentrated Fe-Cr alloys, the Arrhenius plot is not completely linear but it presents a huge scattering in the D_C values (Figure 34).

This is due to the trapping effect of C atoms, resulting from the strong Fe-C attractions in Cr which lead to very low carbon migration barriers compared to $\Delta \bar{H}_C^m$. The jumps of C atoms between two trapping configurations are associated with low migration barriers, leading to strongly correlated jump sequences including a large number of forward and backward jumps. In order to produce long-range diffusion, the C atoms have to exit the trapped configurations which are isolated from each other. The lowest exit frequency controls the diffusion coefficient of C. For example, in the case of model 1 in Fe-50%Cr, the average migration enthalpy is 1.2 eV, but some barriers are as low as 0.5 eV (before the jump has 1 Fe in 1nn, 4 Fe in 2nn and 5 Fe in 3nn). In the case for model 2 in Fe-50%Cr, the average migration enthalpy is $\Delta \bar{H}_C^m \simeq 1.3\,\text{eV}$ (Figure 36), but some barriers are as low as 0.6 eV (where before the jump has 4 Fe in the 2nn and 3 Fe in the 3nn) and 0.63 eV (before the jump has 2 Fe in 1nn, 4 Fe in 2nn and 2 Fe in 3nn), as a consequence, f_C can be as low as 10^{-6} between 350 K and 400 K.

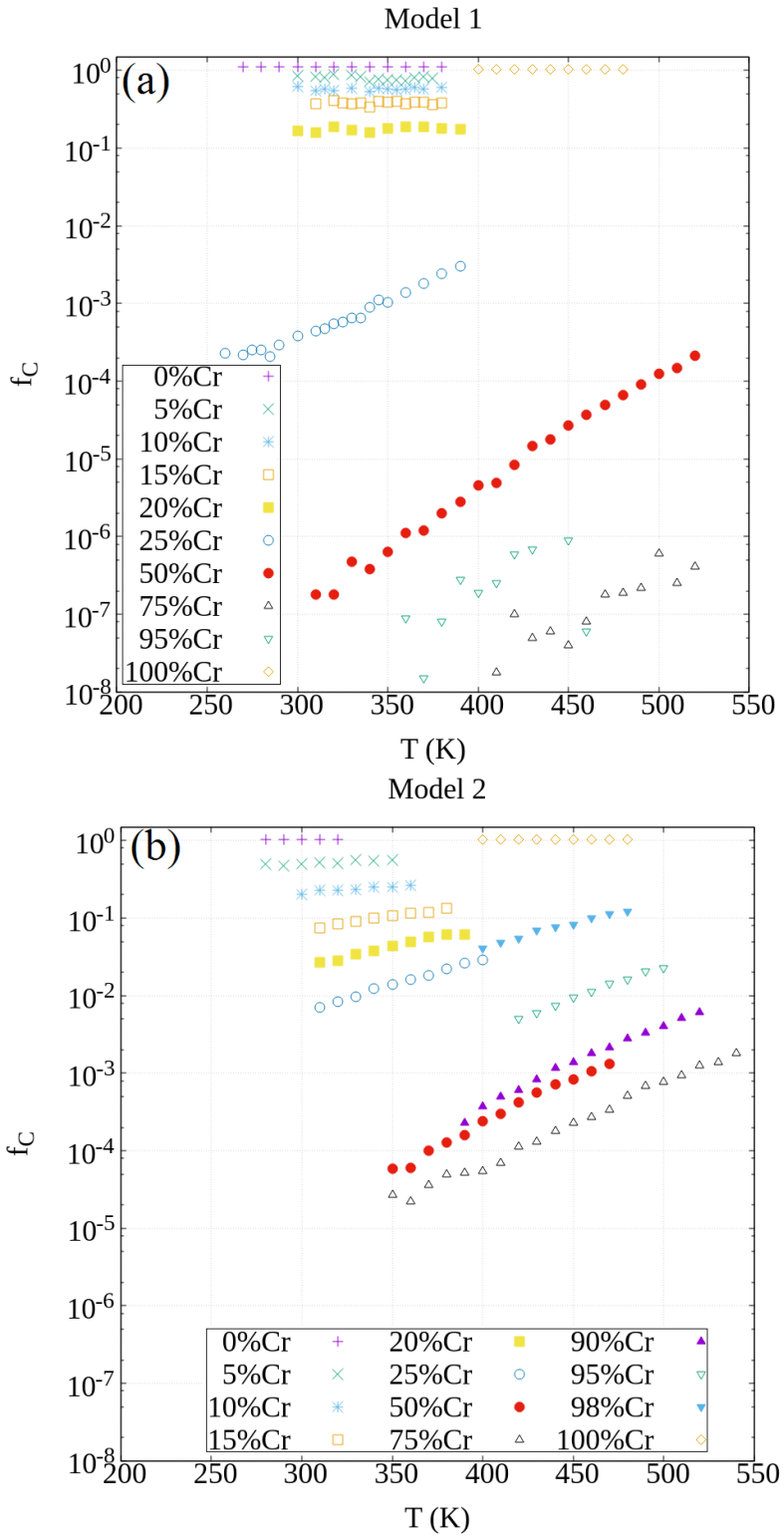

Figure 35: Correlation factor, for the diffusion of C in Fe-Cr solid solutions, as a function of temperature and Cr concentration (AKMC simulations).

The slope of the curves in Figure 34 yields the average migration enthalpies $\Delta\bar{H}_C^m$ which are shown in Figure 36 for model 1 and model 2. In the case for model 1, we observe that $\Delta\bar{H}_C^m$ remains fairly constant up to 20%Cr (close to the value of the carbon migration barrier in pure Fe), but then it rapidly increases up to 1.2 eV at Fe-50%Cr. Unfortunately, due to the trapping effects associated with model 1, it was not possible to obtain an average migration enthalpy for compositions with more than 75%Cr, within reasonable uncertainties. On the contrary, it was possible to obtain $\Delta\bar{H}_C^m$ for any given Fe-Cr concentration when model 2 was used. We see that $\Delta\bar{H}_C^m$ increases with Cr concentration, starting from its value in pure Fe, $\Delta H_C^m(Fe) = 0.86$ eV, and continuously increasing until reaching a maximum at 90%Cr (1.565 eV) and then abruptly decreasing to its value in pure Cr, $\Delta H_C^m(Cr) = 1.21$ eV. For the limited range where the $\Delta\bar{H}_C^m$ was obtained, we can see that both models give very similar results for the range of 25%Cr – 50%Cr. We can see that model 2 produces a more progressive increase of $\Delta\bar{H}_C^m$ between 0%Cr and 10%Cr which comes from the fact that the migration barriers involve the ΔH_C^0 parameter which is an interpolation between $\Delta H_C^m(Fe)$ and $\Delta H_C^m(Cr)$, while model 1 predicts a larger spectrum of ΔH_C^m, which can result in slightly lower values of $\Delta\bar{H}_C^m$.

According to model 2, the substitutional solutes have a stronger effect on the C atoms in Cr-rich alloys than in Fe-rich alloys (Figure 36). The addition of 10%Cr in Fe increases $\Delta\bar{H}_C^m$ by 0.04 eV while an addition of 10%Fe in Cr increases $\Delta\bar{H}_C^m$ by 0.36 eV. This is consistent with the fact that C-Cr interactions are repulsive whereas C-Fe interactions are attractive. In other words, for alloys with low Cr content, the C atoms mostly diffuse in Fe-rich environments and avoid Cr atoms in their vicinity. On the other hand, for Cr-rich alloys, the C atoms are frequently trapped by Fe atoms instead of jumping in Cr-rich environments. This is also reflected in Figure 34: f_C is much greater for Fe-5%Cr than for Fe-95%Cr for both models. Unfortunately, there is no experimental data on the carbon tracer diffusion coefficient in dilute Cr-Fe alloys.

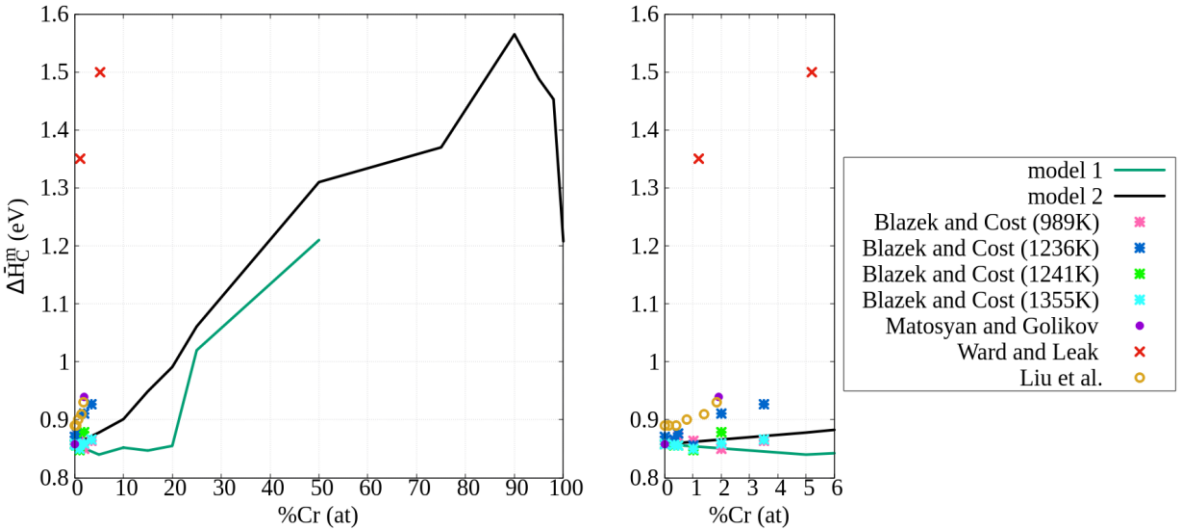

Figure 36 : Evolution of the average carbon migration enthalpy $\Delta\bar{H}_C^m$ given by TD, as a function of Cr concentration (a), evolution of $\Delta\bar{H}_C^m$ in dilute Fe-Cr alloys (b). Comparison with experimental results from [1,2] and AKMC by [6].

These results are in good agreement with the experiments performed in Fe-rich alloys (Figure 36) by Blazek and Cost [1] and by Matosyan and Golikov [2], who found a small increase of $\Delta\bar{H}_C^m$ in Fe-rich alloys up to 3.5%Cr. They are in disagreement with those by Ward and Leak [3], who found high values of $\Delta\bar{H}_C^m$ in dilute Fe-Cr alloys, but they relate the high increase with the attractive binding energy between C atoms and vacancies. Our results are in good agreement with the AKMC simulations by Liu et al. [6], who found a higher increase of $\Delta\bar{H}_C^m$ within this range of Cr concentrations (an addition of 1.85%Cr corresponded to an increase of $\Delta\bar{H}_C^m$ by 0.1 eV). This difference might be caused by an underestimation of the C-Cr binding energies by our pair interaction model.

5. AKMC simulations of Internal Friction

Figure 37 shows the results of AKMC simulations of IF in Fe-Cr solid solutions with various compositions, at a frequency of oscillation of 1 Hz, for model 1 and model 2. The temperature of the Snoek peak is 312 K in pure Fe and 440 K in pure Cr. When they can be compared, both models give overall similar results for the IF spectrum at different Cr concentrations. In the case of model 1, additions of Cr increase the temperature of the peak $T_{\max}$, decreases the amplitude of the Snoek peak and makes the spectrum wider in temperature. Due to very strong correlations, it was impossible to obtain results of the Snoek peak at higher Cr concentrations. On the other hand, we were able to obtain the Snoek peak at any Cr content for model 2. We see the same evolution of the IF profile as seen for model 1. The height of the Snoek peak using model 2 reaches a minimum at 50%Cr, and it starts increasing until the alloy reaches the composition of pure Cr. As well, by increasing the Fe content in Cr-rich

alloys, the Snoek peak decreases in height and it also becomes broader. We also found that for 90%Cr and 95%Cr alloys, the temperature of the peak is greater than the temperature of the carbon Snoek peak in pure Cr. The broadening of the peak is due to the fact that when C atoms diffuse in pure Fe or in pure Cr, a single migration enthalpy determines the jump frequency of the interstitial atoms. But when the C atoms diffuse in the Fe-Cr alloy, they present a spectrum of migration barriers ΔH_C^m. As a first approximation, we could consider that the overall IF response could be analyzed as a sum of Debye peaks, each one having an associated ΔH_C^m. Moreover, every peak is weighted by the configuration probability associated with a specific $T_{\max}$. In agreement with the observations of Golovin et al. [12], only one peak is observed in the whole composition range, rather than several separated ones as can be seen in other alloys [38,39] (Figure 22). Unlike our AKMC simulations, the temperature of the peak $T_{\max}$ shown in [12] was always higher for the carbon Snoek peaks in Fe-Cr alloys than in the pure metals. Golovin et al. [12] also found that the Snoek peak in alloys was broader than a Debye curve and that their amplitude decreased with higher additions of substitutional impurities but they do not systematically analyze this evolution. On the other hand, simulations performed by Sandberg et al. [17] simulated the carbon Snoek peak in concentrated Fe-Cr alloys. They found that the Snoek peak smoothly shifted to higher $T_{\max}$, decreased its amplitude and became broader with Cr additions. But they argue that this evolution of the Snoek was via a double peak mechanism (Figure 25), in disagreement with our AKMC results and the experiments shown by Golovin et al. [12].

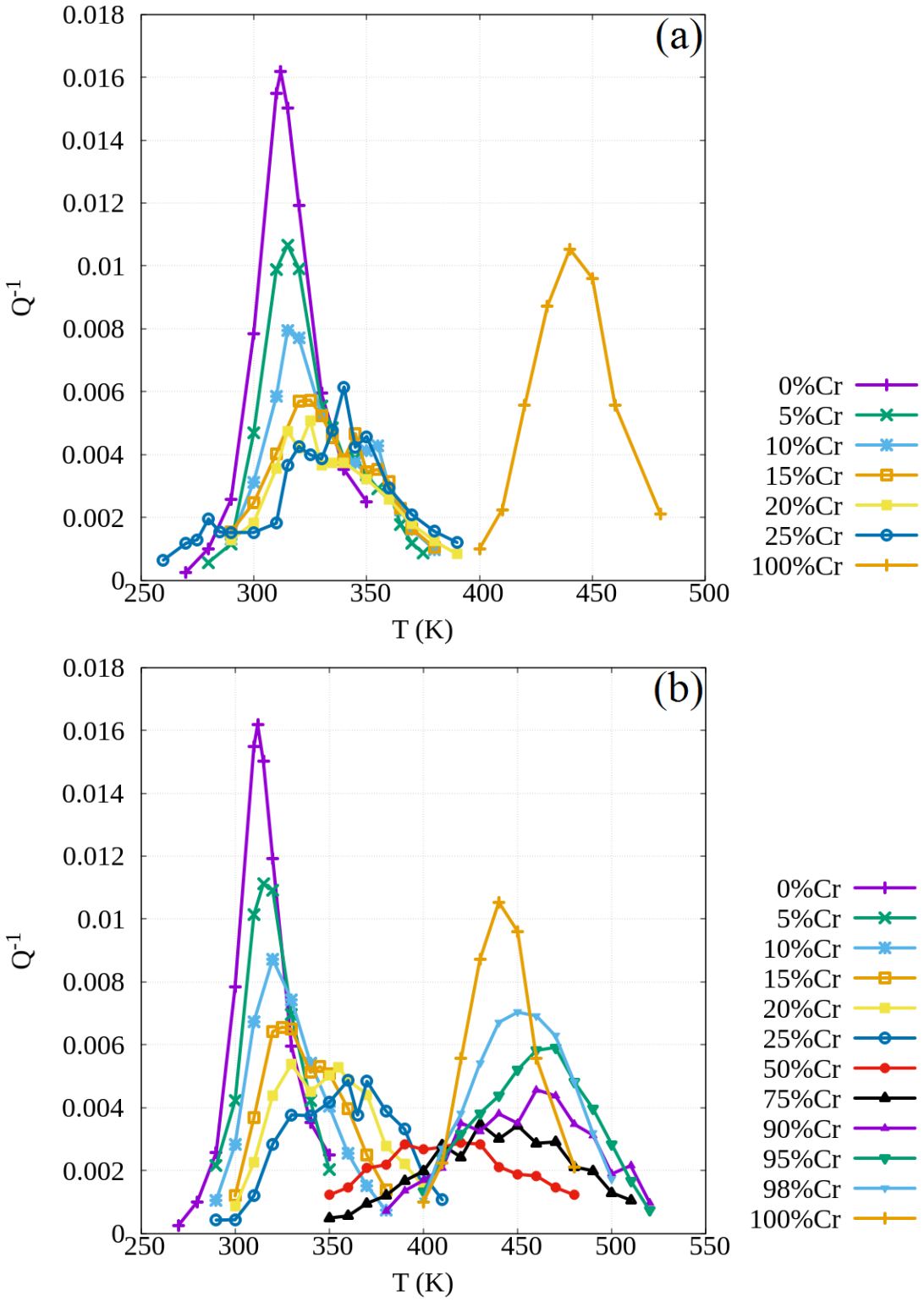

Figure 37: AKMC simulations of internal friction of C in Fe-Cr alloys at various Cr concentrations.

The experimental studies often just report the position of the Snoek peak, T_{max} , because the height of the Snoek peak depends on each experimental setup, such as thermal treatments and the induced strain. We extracted an estimated $\Delta\bar{H}_C^m$ from each study by using our value of υ_0 and the linear relationship between T_{max} and $\Delta\bar{H}_C^m$, as seen in chapter 1. The results are shown in Figure 38. For dilute concentrations (up to 6%Cr), our AKMC simulations show that $\Delta\bar{H}_C^m$ remains almost constant, which is in good agreement with most experimental studies [7,9,22]. The results shown by Ward and Leak [3] and by Konstantinovic et al. [8] show a decrease of $\Delta\bar{H}_C^m$ in this range of Cr concentration, but their values of $\Delta\bar{H}_C^m$ are close to our AKMC results. However, our AKMC simulations are in disagreement with those of Golovin et al. [12], which shows a much more rapid increase: $\Delta\bar{H}_C^m \approx 1.2$ eV for 2%Cr and 1.3 eV for 5%Cr.

For more concentrated alloys, we also show that $\Delta\bar{H}_C^m$ slowly increases from 0.86 eV to 0.9 eV between 0 and 25%Cr for model 1 and model 2. At higher Cr concentrations, the simulations predict a regular increase of $\Delta\bar{H}_C^m$, from 0.90 eV to 1.30 eV between 20%Cr and 95%Cr, then a decrease between 95%Cr and 100%Cr, down to its value in pure Cr, 1.21 eV. The evolution of $\Delta\bar{H}_C^m$ with Cr concentration is also in disagreement with the experiments of Golovin et al. [12] which show first an increase of $\Delta\bar{H}_C^m$, up to a maximum of 1.45 eV at 38%Cr, then a decrease to 1.10 eV in pure Cr. Our results are in partial agreement with Golovin et al. [12] between 50%Cr and 100%Cr, since $\Delta\bar{H}_C^m \approx 1.2 \pm 0.1$ eV .

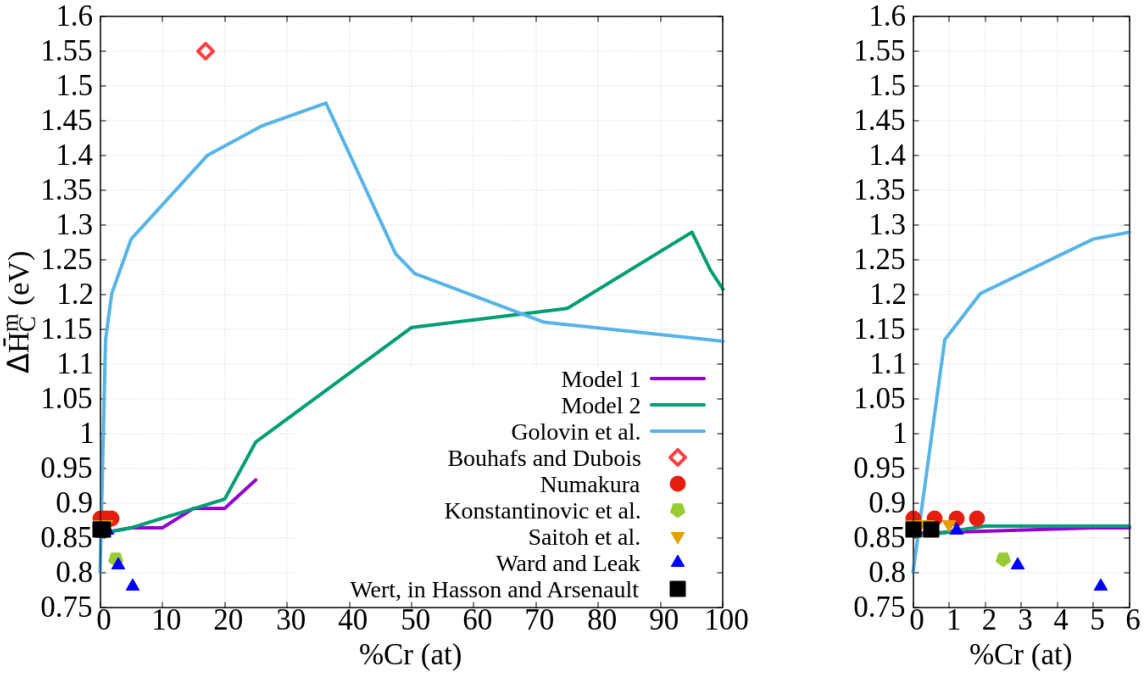

Figure 38: Evolution of the average migration enthalpy $\Delta\bar{H}_C^m$ of C in Fe-Cr solid solutions, as a function of the Cr concentration, obtained with AKMC simulations of IF (a), evolution of $\Delta\bar{H}_C^m$ in dilute Fe-Cr alloys (b). Comparison with IF experiments from [7–9,12,22].

This very high increase at very low Cr content does not seem to be likely due to a carbon Snoek peak. First, because in Fe-rich alloys, Cr-C interactions are repulsive. Second, it seems to disagree with other experimental studies [3,7–9,22]. Due to the high sensitivity of mechanical spectroscopy techniques, the Snoek peaks may be affected by other physical phenomenon. For example, IF experiments performed by Bouhafs and Dubois [11] in a ferritic Fe-17%Cr-C alloy, show an asymmetric peak at 553 K, which corresponds to a high value of $\Delta\bar{H}_C^m$ (1.55 eV), close to the results of Golovin et al. [12]. However, they assumed that the peak was not due to the diffusion of C in the alloy, but due to the binding of C atoms with dislocations. Moreover, experiments performed by Krishtal and Baranova [10] found a single peak at 313 K for alloys with Cr concentrations up to 6%Cr. Nevertheless, they relate the decrease of the amplitude of the Snoek peak due to the different thermal treatments with a vacancy formation enthalpy in dilute Fe-Cr-C. Golovin et al. [12] takes these results and interprets that these values correspond to the $\Delta\bar{H}_C^m$ in Fe-Cr alloys.

Our results are slightly different from the ones of Sandberg et al. [17] (Figure 25). Although they also find a broadening of the Snoek peak in alloys, they predict that the addition of substitutional solute atoms produces a second peak. The assumption of Sandberg et al. [17] consisting in writing the IF response Q^{-1} as a sum of Debye peaks, each one associated with a specific local configuration of the alloy and an average jump frequency corresponding to the inverse of the residential time of the configuration – unlike the AKMC, which exactly computes the residential time in each configuration – is not entirely correct according to the KMIF [18,19], where the Snoek peak can be written as a sum of Debye peaks, although the associated jump frequency is a complex function of the elementary jump frequencies. In chapter 3 we will study the KMIF in more detail and apply it to the oxygen Snoek peak in dilute Nb-V alloys.

6. Comparison of migration enthalpies obtained by TD and IF simulations

As we have seen in chapter 1, in the pure component TD and IF experiments give the same value of the migration enthalpy of an interstitial atom. In this section we will see if this still holds true for an interstitial in an alloy. Since we only obtained the average migration enthalpies in the whole spectrum of concentrations using model 2, we will use it in order to compare the $\Delta\bar{H}_C^m$ found by TD and IF. The results are shown in Figure 39. The values are the same in pure metals, and very similar in Fe-rich alloys, below 10% of Cr. At higher Cr concentrations, the evolutions are qualitatively similar, but more pronounced for TD than for IF, especially in the Cr-rich side. For example, $\Delta\bar{H}_C^m$ associated with TD undergoes a decrease of 0.55 eV between 90% and 100% of Cr while the IF is only 0.10 eV between 95%Cr and 100%Cr. Unfortunately, there are no experimental data of carbon tracer diffusion experiments on alloys with concentrations higher than 25%Cr in order to validate our predicted $\Delta\bar{H}_C^m$.

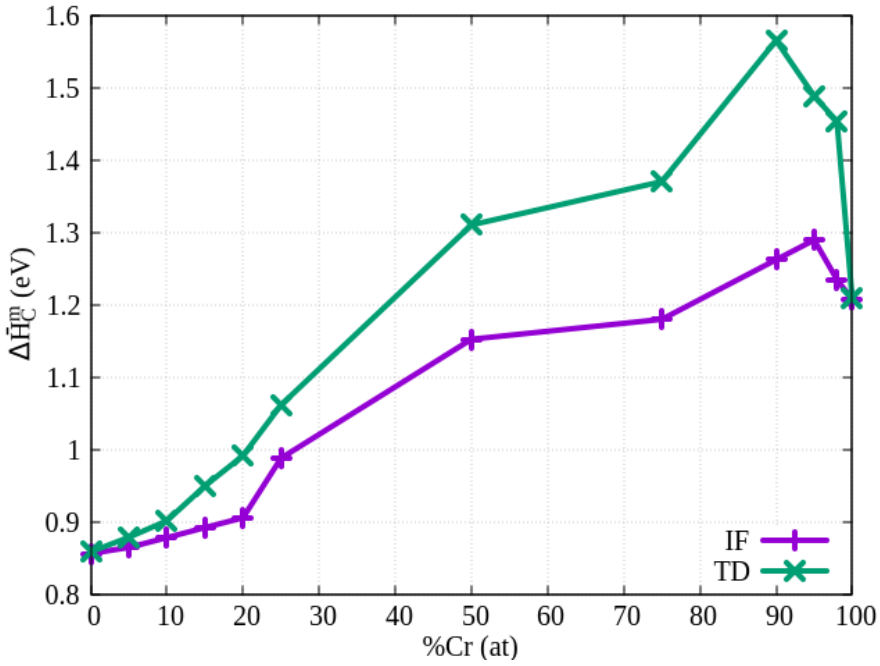

Figure 39: Evolution of $\Delta\bar{H}_C^m$ with the Cr concentration, according to the AKMC simulations (using exclusively model 2) of tracer diffusion and internal friction.

TD and IF experiments reflect different diffusion properties of C, measured during displacements where C atoms explore the energetic landscape of the solid solution, with its local distributions of Fe and Cr atoms, by following different pathways. TD simulations and experiments correspond to a long-range diffusion of carbon atoms. By comparison, IF only requires that C atoms can move from one octahedral sublattices to another, i.e. only short-range diffusion. In section 2, we have seen that C atoms can be trapped in small Fe-rich clusters within a Cr-rich matrix, due to the strong binding energies. This means that the C atoms stay for a long time in these particular sites and do not perform a long-range diffusion, which leads to an increase in $\Delta\bar{H}_C^m$ in TD simulations. Moreover, due to very low migration barriers, the C atoms perform many correlated jumps which leads to an effective $\Delta\bar{H}_C^m$ which is larger than every local ΔH_C^m. For example, at Fe-90%Cr, the average $\Delta\bar{H}_C^m$ measured by TD is 1.57 eV, with a correlation factor $f_C = 1.83\times10^{-3}$. However, the C atoms trapped in these local clusters can still move from one to another interstitial sublattice, and give a significant IF signal.

This effect is illustrated in Figure 40, in the case of a solid solution with 90%Cr. Figure 40(a) shows the probability of the carbon configurations with respect to their corresponding migration barrier and to their respective local environment. Figure 40(b) gives the fraction of carbon jumps that are performed with respect to a corresponding barrier during an IF simulation at 460 K. At this composition, the average $\Delta\bar{H}_C^m$ measured by IF is 1.27 eV. We observe that the majority of C atoms are in local environments associated with migration

barriers within the interval 1.2 - 1.3 eV: the Snoek peak appears when these atoms can jump. However, the largest number of C jumps are those with a barrier close to 1.0 eV, even if it corresponds to less than 2% of the local environments. These atoms are trapped in small Fe-rich regions where they have small migration barriers and perform many jumps from one sublattice to another. But since they represent a negligible fraction of C atoms, they do not significantly affect the evolution of $C_1(t)$. This trapping makes the simulations very time consuming: in order to obtain results for the diffusion of C in pure metal, it takes a few hours, but for the case of concentrated alloys, it can even take several days. In the case of using model 1 for concentrated alloys, it can take several months to obtain results, due to the very low migration barriers and the high correlation effects. In other words, AKMC simulations are very difficult to use when jumps with very different frequencies operate simultaneously, since the only rapid events are performed (using a model that can precisely reproduce the wide distribution of migration barriers in Cr-rich alloys, standard AKMC would be impossible to perform).

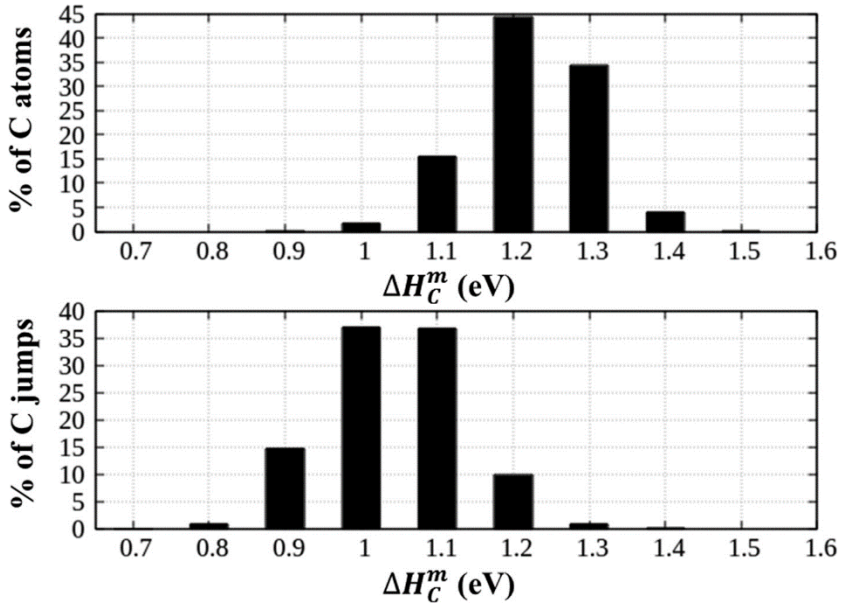

Figure 40: Distribution of C atoms with a migration barrier ΔH_C^m in the solid solution (top) and distribution of C jumps performed with a migration barrier ΔH_C^m (bottom), during the AKMC simulation of IF in Fe-90% Cr at 460 K. Image extracted from [40].

As we have seen in section 3, the pair interaction models do not fully reproduce the DFT results in Cr-rich alloys and they give an approximation of the real energetic landscape. The fact that the obtained $\Delta \bar{H}_C^m$ by the IF simulations is slightly above the value in pure Cr (for example, a maximum of 1.289 eV at Fe-95%Cr instead of 1.208 eV in pure Cr), maybe due to the slight overestimation of some of the most probable migration barriers and a better model could correct this effect. It is difficult to build a model with a precision of less than

0.1 eV for all configurations in the whole composition range. Nevertheless, we think that the difference of behavior between TD and IF is correct: the same local migration barriers yield a higher $\Delta\bar{H}_C^m$ in tracer diffusion than in IF simulations due to an attractive Fe-C binding energy, which lead to the trapping of C atoms.

7. Effect of Cr and C on the amplitude of the Snoek peak in dilute Fe-Cr-C alloys

In this chapter we have mainly focused on the temperature of the Snoek peak because it is directly related to the diffusion properties. As we have seen in chapter 1, we fitted the values of the segregation enthalpy ΔH_C^{seg} and ε_0^E for the particular case of C in pure Fe. We have also shown that the amplitude of the carbon Snoek peak in pure Fe and the interstitial concentration are proportional via a constant K, our results being in agreement with those found experimentally by Saitoh et al. [9] and theoretically by Garruchet and Perez [15]. Saitoh et al. [9] showed as well that for dilute Fe-Cr alloys, the inverse of K increased linearly with Cr additions. We wanted to test if this increase was due to carbon-chromium interactions. Figure 41 shows a comparison between the values from [9] and our AKMC values. We can see that there is a disagreement between both studies. Our results could be improved by computing a chromium-dependent segregation enthalpy.

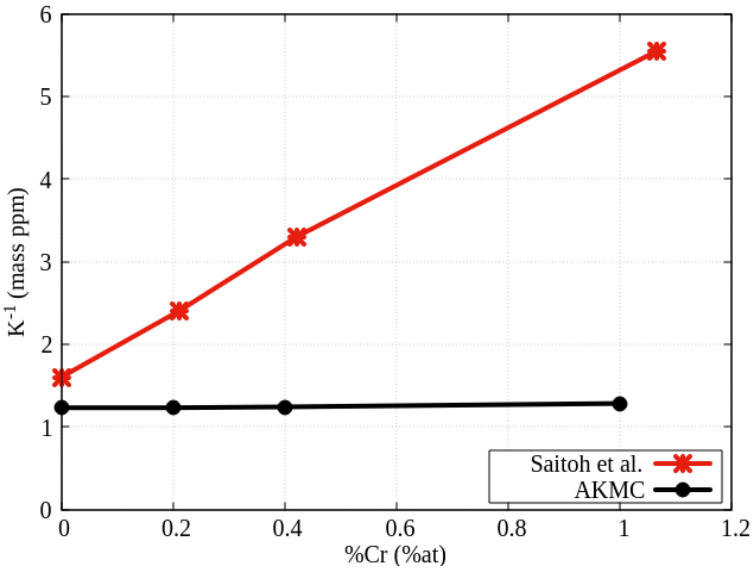

Figure 41: Dependence of the K^{-1} parameter with Cr additions in dilute Fe-Cr alloys. Comparison between values given by AKMC and by Saitoh et al. [9].

8. Conclusions

In this chapter, we propose an atomistic modelling of IF in concentrated alloys, applied to the Fe-Cr-C system. Two different pair interaction models are fitted to a set of DFT calculations in order to compute the migration barriers of C jumps and the diffusion response

to an external stress. Then the models are integrated in the AKMC code to simulate the evolution of the carbon occupation of the three octahedral sublattices, under a cyclic external stress. Simulations provide the evolution of the Snoek peak and an effective enthalpy associated with the position of the peak in Fe-Cr alloys. Tracer diffusion coefficients are also estimated by AKMC simulations, using a standard method by measuring the mean square displacement during a certain period of time.

Model 1 and model 2 reproduce the qualitative trends of the substitutional solute-C binding energies in dilute alloys: the C-*n*Cr interactions are systematically repulsive and the C-*n*Fe interactions are highly attractive. The PIM sometimes overestimates the repulsion in Fe-rich alloys but those particular Cr environments with a highly repulsive binding energy have a negligible effect on the diffusion of C since their probability of occurrence is very small. Likewise, the PIM sometimes underestimates the attractive C-Fe binding energies in Cr-rich alloys. This divergence between the DFT data and the predicted values by the PIM may have a higher impact on the diffusion properties because the positive binding energy indicates that these are stable configurations for C atoms. In spite of these limitations, model 1 and model 2 can reproduce the average trends of the carbon atoms with substitutional impurities: a C-Cr repulsion in Fe-rich alloys and a C-Fe attraction in Cr-rich alloys.

The two different models have advantages and drawbacks. In Fe-rich solid solutions, model 2 better reproduces the calculated DFT migration barriers, whereas model 1 predicts a larger dispersion of ΔH_C^m. On the other hand, in Cr-rich solid solutions model 1 reproduces fairly well the DFT migration barriers, whereas model 2 overestimates most of them and tends to underestimate the variation of ΔH_C^m with the local environments. However, model 2 qualitatively better reproduces the migration barriers with a high probability of occurrence (i.e. high binding energies) than model 1 in Cr-rich alloys. In spite of these differences, models 1 and 2 give very similar results when the comparison is possible. This shows that it is more important to reproduce the general trends of the binding energies and the local migration barriers rather than to exactly reproduce ΔH_C^m. Even though model 1 reproduces slightly better the migration barriers in Cr-rich alloys, it produces stronger correlation effects than model 2, which makes the AKMC simulations very inefficient.

In Fe-rich solid solutions, for very dilute Fe-Cr alloys (less than 6%Cr), we do not find a significant increase of $\Delta \bar{H}_C^m$ with Cr additions. This evolution is consistent with the fact that Cr-C interactions are repulsive, so C atoms will tend to avoid Cr environments. Our AKMC simulations are in agreement with the results shown by [1,2,7–9,22] but not with the IF experimental study of Golovin et al. [12], the only one that covers the full range of compositions and which predicts a stronger slowing down of C diffusion with the Cr concentration. So we conclude that the high increase of $\Delta \bar{H}_C^m$ registered by [12] must be produced by the interaction of carbon with other defects (such as dislocations and vacancies) or due to the formation of martensite or other stable phases in the alloy. Moreover, as it was shown by Saitoh et al. [9], the addition of Cr in dilute Fe-Cr alloy also affects the amplitude of the Snoek peak, which we are unable to reproduce. It would be interesting to improve our

model in order to better describe the evolution of the amplitude of the Snoek peak with Cr additions by modelling the segregation enthalpy as a function of the local chemical environment by computing the elastic dipole of C in various Fe-Cr environments via DFT calculations, such as in [26,41].

In Cr-rich solid solutions, the pair interaction model does not reproduce so well the DFT results. It qualitatively reproduces the strongly attractive Fe-C binding energies in Cr, but with significant differences. Moreover the ΔH_C^0 factor tends to overestimate the C migration barriers with the local Fe environments. In spite of this limitation, AKMC simulation of IF gives a C diffusion enthalpy of 1.2 ± 0.1eV between 50%Cr and 100%Cr, in agreement with the IF experiments of Golovin et al. [12].

Moreover, the simulations predict an interesting effect: the C diffusion properties measured by IF and TD present significant differences in Cr-rich solid solutions. This can be explained by the fact that the trapping of C atoms in small Fe-rich areas has a stronger effect on the long-range than on the short-range diffusion. Even though both models differently reproduce the correlation effects, they are both fitted on the same binding energies which are a result from robust DFT calculations. The IF response is mainly due to the kinetic response of the most probable local configurations of the C atoms. To confirm this prediction, it would be worth improving our diffusion model, in order to better reproduce the DFT results in this range of composition. This could be done, e.g. by introducing multiplets in addition to pair interactions. However, this would lead to a broader range of migration barriers and stronger correlation effects, which could make AKMC simulations inefficient. One may consider two different ways to overcome these limitations: the development of Mean-Field diffusion models for concentrated alloys [42] and the application of parallel modelling techniques, such as [43,44]. Nevertheless, due to the lack of experimental data at concentrated Fe-Cr alloys, we think that a systematic IF and TD experimental study would be interesting – especially in the range of 50%Cr to 100%Cr in order to directly compare with our results.

9. References

[1] K.E. Blazek, J.R. Cost, Carbon Diffusivity in Iron-Chromium Alloys, Trans. Jpn. Inst. Met. 17 (1976) 630–636. doi:http://doi.org/10.2320/matertrans1960.17.630.

[2] M.A. Matosyan, V.M. Golikov, Effect of prior cold plastic deformation on diffusion of Carbon in alloys with iron base, Fiz. Met. Metalloved. 25 (1968) 377–379.

[3] C.R. Ward, G.M. Leak, Mobilita di piccole aggiunte di elementi interstiziali in leghe ferrose, Metall. Ital. 62 (1970) 302–306.

[4] M. Koiwa, Trapping effect in diffusion of interstitial impurity atoms in bcc lattices, Acta Metall. 22 (1974) 1268.

[5] H. Landolt, R. Bornstein, Diffusion in solid metals and alloys, Springer, 1990.

[6] P. Liu, W. Xing, X. Cheng, D. Li, Y. Li, X.Q. Chen, Effects of dilute substitutional solutes on interstitial carbon in α-Fe: Interactions and associated carbon diffusion from first-principles calculations, Phys. Rev. B. 90 (2014) 024103.

[7] H. Numakura, Solute–Solute Interaction in α IRON: The Status QUO, Arch. Metall. Mater. 60 (2015) 2061–2068. doi:https://doi.org/10.1515/amm-2015-0349.

[8] M.J. Konstantinovic, W. Van Renterghem, M. Matijasevic, B. Minov, M. Lambrecht, T. Toyama, M. Chiapetto, L. Malerba, Mechanical and microstructural properties of neutron irradiated Fe–Cr–C alloys, Phys. Status Solidi A. 213 (2016) 2988–2994. doi:10.1002/pssa.201600316.

[9] H. Saitoh, N. Yoshinaga, K. Ushioda, Influence of substitutional atoms on the Snoek peak of carbon in b.c.c. iron, Acta Mater. 52 (2004) 1255–1261. doi:10.1016/j.actamat.2003.11.009.

[10] M.A. Krishtal, V.I. Baranova, Temperature Dependence of the vacancy concentration in iron-chromium and iron-molybdenum, Fiz. Met. Metalloved. 16 (n.d.) 626–628.

[11] M. Bouhafs, B. Dubois, Influence of the Carbon Content on the Internal Friction of Iron-17% Chromium Alloys, in: Intern. Frict. Ultrason. Attenuation Solids, Pergamon Press, England, 1979: pp. 343–348. doi:https://doi.org/10.1016/B978-0-08-024771-7.50060-0.

[12] I.S. Golovin, M.S. Blanter, R. Schaller, Snoek Relaxation in Fe-Cr Alloys and Interstitial-Substitutional Interaction, Phys. Status Solidi A. 160 (1997) 49–60. doi:10.1002/1521-396X(199703)160:1<49::AID-PSSA49>3.0.CO;2-P.

[13] M.A. Krishtal, V.I. Baranova, Damping peaks in alloyed ferrite, Fiz. Met. Metalloved. 18 (1964) 464–467.

[14] J. L. Snoek, Effect of small quantities of carbon and nitrogen on the elastic and plastic properties of iron., Physica. 8 (1941) 711–733. doi:https://doi.org/10.1016/S0031-8914(41)90517-7.

[15] S. Garruchet, M. Perez, Modelling the carbon snoek peak in ferrite: coupling molecular dynamics and kinetic monte-carlo simulations, Comput. Mater. Sci. 43 (2008) 286–292. doi:https://doi.org/10.1016/j.commatsci.2007.11.004.

[16] C. Wert, J. Marx, A new method for determining the heat of activation for relaxation

processes, Acta Metall. 1 (1953) 113–115. doi:https://doi.org/10.1016/0001-6160(53)90047-9.

[17] N. Sandberg, K.O.E. Henriksson, J. Wallenius, Carbon impurity dissolution and migration in bcc Fe-Cr: First-principles calculations, Phys. Rev. B. 78 (2008) 094110. doi:https://doi.org/10.1103/PhysRevB.78.094110.

[18] M. Koiwa, Theory of the Snoek Effect in Ternary B.C.C alloys, Philos. Mag. 24 (1971) 81–106. doi:http://dx.doi.org/10.1080/14786437108216426.

[19] M. Koiwa, Theory of the Snoek Effect in Ternary B.C.C. Alloys : II. Simplified Treatment, Philos. Mag. 24 (1971) 107–122.

[20] R. Chang, Mechanical relaxation associated with paired point defects in cubic lattices of Oh point group symmetry, J. Phys. Chem. Solids. 25 (1964) 1081–1090.

[21] A.S. Nowick, B.S. Berry, Anelastic relaxation in crystalline solids, Academic Press, London, 1972.

[22] D.F. Hasson, R.J. Arsenault, Substitutional-interstitial interactions in bcc alloys, in: Treatise Mater. Sci. Technol. Mater. Sci. Ser., 1972nd ed., n.d.

[23] M.P.A.T. Methfessel, A.T. Paxton, High-precision sampling for Brillouin-zone integration in metals, Phys. Rev. B. 40 (1989) 3616.

[24] H.J. Monkhorst, J.D. Pack, Special points for Brillouin-zone integrations, Phys. Rev. B. 13 (1976) 5188.

[25] H. Jónsson, G. Mills, K.W. Jacobsen, Nudged elastic band method for finding minimum energy paths of transitions., in: Class. Quantum Dyn. Condens. Phase Simul., B. J. Berne, G. Cicotti, D. F. Coker, 1998: pp. 385–404.

[26] M. Souissi, Y. Chen, M.H.F. Sluiter, H. Numakura, Ab initio characterization of B, C, N, and O in bcc iron: Solution and migration energies and elastic strain fields, Comput. Mater. Sci. 124 (2016) 249–258.

[27] D.E. Jiang, E.A. Carter, Carbon dissolution and diffusion in ferrite and austenite from first principles, Phys. Rev. B. 67 (2003) 214103. doi:https://doi.org/10.1103/PhysRevB.67.214103.

[28] C.C. Fu, M.Y. Lavrentiev, R. Soulairol, S.L. Dudarev, D. Nguyen-Manh, Low- and high-temperature magnetism of Cr and Fe nanoclusters in iron-chromium alloys, Phys. Rev. B. 91 (2015) 094430. doi:https://doi.org/10.1103/PhysRevB.91.094430.

[29] C. Wert, C. Zener, Interstitial Atomic Diffusion Coefficients, Phys. Rev. 76 (1949) 1169–1175.

[30] A.E. Lord, D.N. Beshers, The mechanical damping of Iron from Room temperature to 400C at 7 megacycles/sec, Acta Metall. 14 (1966) 1659–1672. doi:https://doi.org/10.1016/0001-6160(66)90018-6.

[31] J.R.G. da Silvia, R.B. McLellan, Diffusion of carbon and nitrogen in B.C.C. iron, Mater. Sci. Eng. 26 (1976) 83–87. doi:https://doi.org/10.1016/0025-5416(76)90229-9.

[32] C.S. Becquart, J.M. Raulot, G. Bencteux, C. Domain, M. Perez, S. Garruchet, H.

Nguyen, Atomistic modeling of an Fe system with a small concentration of C, Comput. Mater. Sci. 40 (2007) 119–129.

[33] S.V. Zemskiy, B.P. Lyakhin, Influence of hydrogen on the diffusion of carbon in Chromium, Fiz. Met. Metalloved. 23 (1967) 913–16.

[34] S.V. Zemskiy, M.N. Spasskiy, Carbon diffusion in Chromium, Fiz. Met. Metalloved. 21 (1966) 129–131.

[35] P.L. Gruzin, S.V. Zemskiy, I.B. Rodina, Met Met. Pure Met. 4 (1963) 243.

[36] E.V. Borisov, P.L. Gruzin, S.V. Zemskiy, Zzashch Pokrytiya Met. 2 (1968) 104–109.

[37] C.S. Becquart, F. Soisson, Monte Carlo Simulations of Precipitation Under Irradiation, in: Handb. Mech. Mater., Springer, Singapore, 2018: pp. 1–29. doi:10.1007/978-981-10-6855-3_24-1.

[38] O.. N.. Carlson, H. Indrawirawan, C.V. Owen, O. Buck, Internal Friction Study of Substitutional-Interstitial Interaction in Niobium-Vanadium Alloys, Metall. Trans. A. 18 (1987) 1415–1420. doi:https://doi.org/10.1007/BF02646655.

[39] H. Indrawirawan, O. Buck, O.N. Carlson, Substitutional-interstitial solute interactions in niobium-vanadium-oxygen alloys, Phys. Status Solidi A. 104 (1987) 443–451. doi:10.1002/pssa.2211040133.

[40] R. Herschberg, C.C. Fu, M. Nastar, F. Soisson, Atomistic modelling of the diffusion of C in Fe-Cr alloys, Acta Mater. 165 (2019) 638–653.

[41] E. Clouet, S. Garruchet, H. Nguyen, M. Perez, C. Becquart, Dislocation interaction with C in α-Fe: A comparison between atomic simulations and elasticity theory, Acta Mater. 56 (2008) 3450–3460.

[42] T. Schuler, M. Nastar, Transport properties of dilute α-Fe(X) solid solutions (X = C, N, O), Phys. Rev. B. 93 (2016) 224101. doi:10.1103/PhysRevB.93.224101.

[43] E. Martinez, P.R. Monasterio, J. Marian, Billion-atom synchronous parallel kinetic Monte Carlo simulations of critical 3D Ising systems, J. Comput. Phys. 230 (2011) 1359–1369.

[44] E. Martinez, J. Marian, M.H. Kalos, J.M. Perlado, Synchronous parallel kinetic Monte Carlo for continuum diffusion-reaction systems, J. Comput. Phys. 227 (2008) 3804–3823.

Chapter 3: Internal Friction of dilute Nb-V-O alloys

In chapter 2 we have studied the carbon Snoek peak in Fe-Cr alloys, where C-Cr interactions are repulsive in Fe-rich alloys and C-Fe interactions are attractive in Cr-rich alloys. Since most of the experimental results only focus in Fe-rich alloys, we focused our analysis in these ranges of concentration. We showed that a repulsive substitutional solute-interstitial interaction has a negligible effect on the temperature of the Snoek peak, it decreases the amplitude of the peak and broadens the IF profile.

Unfortunately, there are no experimental studies of the carbon Snoek peak in dilute Cr-Fe alloys where the substitutional solute-interstitial interaction is attractive (Golovin et al. [1] measured the Snoek peak containing at least 25%Fe). We decided to study a simple system featuring a highly attractive substitutional solute-interstitial interaction, leading to interesting effects on the Snoek peak. Our choice is the dilute Nb-V-O system. It has been shown by [2,3] that the oxygen Snoek peak in the dilute Nb-V system is highly dependent on the relative concentrations of vanadium and oxygen, which modifies the IF spectrum in two distinctive ways. First, small additions of vanadium shift the oxygen Snoek peak in pure Nb to higher temperatures. Second, when the concentrations of oxygen and vanadium are high enough, we observe two Snoek peaks.

The following chapter is divided in four parts. First, we show previous experimental results found in the literature. Second, we present the binding energies and migration barriers calculated by DFT and the diffusion model. Third, we show the results found by our AKMC simulations and compare them with the experimental results found by [2,3]. Fourth, we apply the Koiwa model for internal friction (KMIF) [4,5] and evaluate its validity for these systems and use it for the analysis of the IF response.

1. Previous experiments and modeling

1.1. Introduction

In this section we will give a brief overview of the existing studies on the diffusion of O in pure Nb and in dilute Nb-V systems by tracer diffusion and IF experiments. We will also pay special attention to the effects of the relative concentrations of oxygen and of vanadium on the IF peak. We will also present previous modelling studies.

1.2. Tracer diffusion and diffusion couple experiments

Fedorov et al. [6] used the O^{18} tracer in order to perform tracer diffusion experiments of O in pure Nb. They performed diffusion annealings in the range of 670 K ~ 1070 K, whereas the diffusion times where in the range of 90 hrs (at low T) and 2.5 hrs (at high T). From the

Arrhenius plot of the diffusion coefficient with the inverse temperature, they found a migration barrier of 1.21 ± 0.08 eV.

Tseng et al. [7] studied the effect of V on the diffusivity of O in Nb-V alloys at two particular atomic fractions (Nb-0.5%V and Nb-10%V). They performed diffusion annealings at temperatures between of 1375 K ~ 1725 K, during 110 hrs (at low T) and during 4.5 hrs (at high T). Instead of estimating the oxygen concentration inside the sample using a radiotracer, they performed a diffusion couple experiment. They found an Arrhenius relationship for both the studies alloys, as shown in Figure 42. They found a sharp increase of the average migration enthalpy with V content: 1.82 ± 0.09 eV for Nb-0.5%V and 2.01 ± 0.09 eV for Nb-10%V. From both results, they estimated an oxygen-vanadium binding energy close to 0.6 eV.

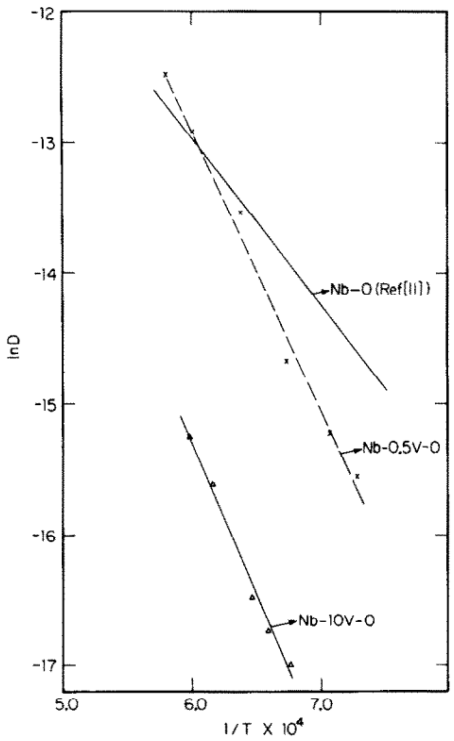

Figure 42: Arrhenius plots for Nb-0.5%V and Nb-10%V alloys. Data extracted from [7].

1.3. Internal Friction experiments

1.3.1. Internal Friction experiments in the Nb-O system

Results in the experimental literature agree on the value of the oxygen migration barrier in pure Nb using Internal Friction methods [8–13] to be close to 1.15 eV. There has been experimental evidence that, at higher oxygen concentrations, the Snoek peaks are broader on the high-temperature side and that are shifted to slightly higher temperatures, as shown in Figure 43.

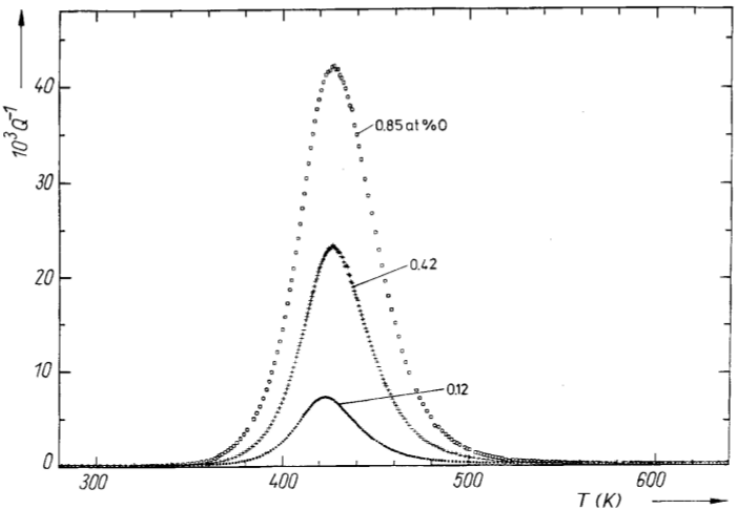

Figure 43: Internal Friction experiments for Nb with 0.12%O, 0.42%O and 0.85%O at a frequency of 1 Hz. Figure extracted from [11].

There have been two different approaches in order to explain this change in the shape of the IF peak:

- Ahmad and Szkopiak [13] performed IF experiments in samples with a composition of Nb-0.3%O-0.085%N at a frequency of 1 Hz. They decomposed the Snoek peak into a sum of Debye peaks. Since the main interstitial component in their samples was oxygen, they assumed that each Debye peak is due to free oxygen or due to clusters of oxygen. They claimed that the highest cluster is composed by 3 O atoms.
- At first, Weller et al. [11] performed IF experiments of oxygen in highly pure Nb, with varying compositions from 0.12%O up to 0.85%O. They found that for very dilute alloys, the Debye equation could describe the Snoek peak, but with increasing O content, the Snoek peak became broader. From frequency shift analysis they found that the oxygen migration barrier in pure Nb was 1.15 eV, and remained constant whatever the O content. They tried to reproduce these experimental results with the clustering model, following a similar approach as Ahmad and Szkopiak [13]. They found that this model was not satisfactory to explain the evolution of the Nb-O peak due to three reasons. First, because the temperature for each elementary peak shifted in temperature with higher oxygen concentrations. Second, the temperature of the main Snoek peak decreased to lower temperatures. Third, at very high oxygen concentrations the model predicted an unexpected peak at very low temperatures. They concluded that this approach was contradictory with the main assumptions of the clustering model and that the evolution of the Snoek peak was due to a continuous spectrum of relaxation times given by long-range oxygen-oxygen strain interactions.
- Haneczok et al. [14] used the data provided by Weller et al. [11] and as a second step they proposed a mean field model using a random cooperative strain interaction

approach in order to justify these effects. Their first assumption was that the oxygen-oxygen interactions were long-range and depended on their relative distance. They defined a temperature T_C. When an external stress was applied and $T > T_C$, the elastic dipoles were oriented at random but at $T < T_C$, one type of dipole was preferred on one type of sublattice. This model was able to reproduce qualitatively the effects of increasing oxygen: a decrease in the amplitude of the Snoek peak, a shift to higher temperatures, a broadening of the peak and an oxygen migration barrier in pure Nb independent of the oxygen concentration in the metal. In order to get quantitative results, they used a nonlinear regression procedure to fit the parameters.

1.3.2. Internal Friction experiments in dilute Nb-V-O alloys

The effect of vanadium on the Snoek peak is much stronger [15,16]. As we have seen, the temperature of the oxygen Snoek peak in pure Nb at a frequency of 1 Hz is close to 420 K [12]. The first main effect of vanadium is to produce a new peak at a temperature close to 500 K and in some cases to switch off the oxygen Snoek peak in pure Nb around 400 K. For example, experiments performed by [2,3,17] in Nb-0.24%V and Nb-0.50%V have shown that the evolution of the IF spectrum was divided in two regimes depending on the relative concentrations of vanadium and oxygen. In the first one they found a Snoek peak at a temperature of 500 K at an external frequency of 0.35 Hz, provided that the concentration of vanadium was greater than the concentration of oxygen. At the second regime, when the concentration of oxygen was greater, they found an extra second peak at a lower temperature (405 K). In order to maintain the notation used in [2,3], we will call the high-temperature and the low-temperature peaks 'P2' and 'P1' respectively, as shown in Figure 44 and Figure 45. We can also see that during the first stage, the amplitude of P2 increases with higher oxygen concentrations. During the second stage, the amplitude of P2 remains constant while the amplitude of P1 increases with higher O content. It is argued that a strong oxygen-vanadium attraction may explain the formation of the P2 peak which would correspond to the diffusion of single oxygen atoms close to single vanadium atoms while P1 would correspond to the oxygen diffusion far from vanadium atoms. At each concentration they performed IF experiments at different frequencies (between 0.25 Hz and 1.5 Hz) and found the temperature of the peaks P1 and P2. For both experiments they found an Arrhenius relationship between f and $1/T_{\max}$. They estimated the average oxygen migration enthapy from the slope and the attempt jump frequency from the y-intercept. They found that the average migration enthalpies of P1 and P2 were equal to 1.12 eV and 1.40 eV respectively. The attempt frequencies for P1 and P2 were estimated to be close to 5×10^{13} Hz and 3×10^{13} Hz respectively.

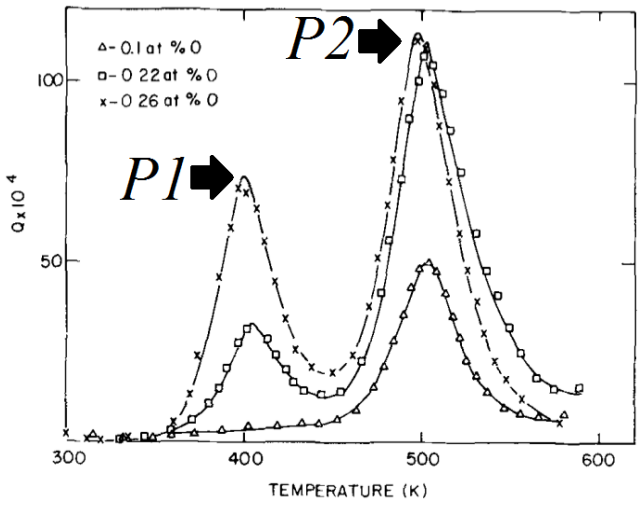

Figure 44: Experimental IF curves for Nb-0.24%V alloys at different oxygen concentrations. Experimental curve extracted from [2].

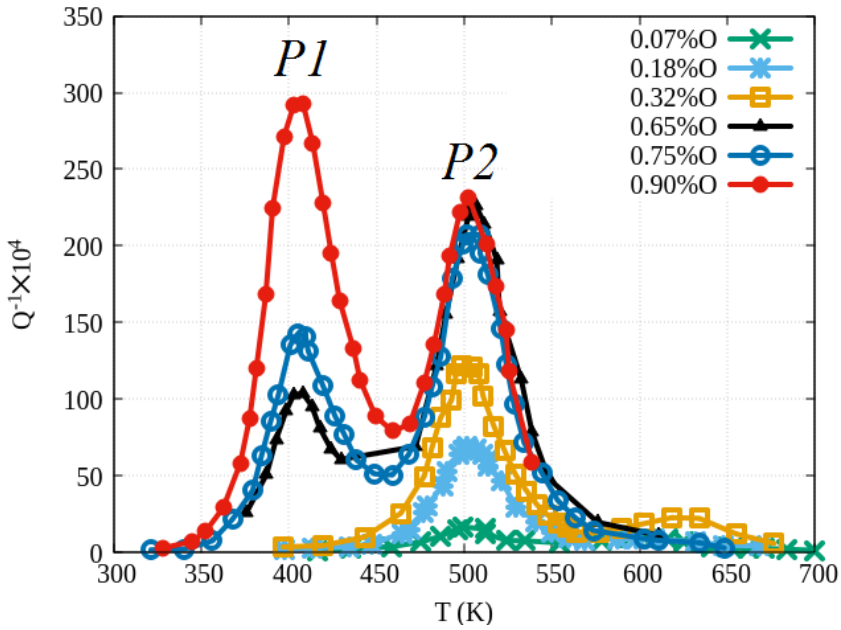

Figure 45: Experimental IF curves for Nb-0.50%V alloys at different oxygen concentrations. Experimental curve extracted from [2].

Indrawirawan et al. [3] have also performed IF experiments in Nb-1.50%V-0.75%O and Nb-2.50%V-0.50%O alloys. They found a main peak at 516 K and experimental evidence of a second one at 630 K at a frequency of 0.56 Hz. These results were also in agreement with those by Szkopiak and Smith [15] who found a single Snoek peak in Nb-1%V-0.258%O (%at) alloys at a temperature of 520 K and at a frequency of 1 Hz. It can be also deduced that

P1 was not present in these experiments because the concentration of oxygen was lower than the vanadium content. But these results seem to be in disagreement with those by Kushnareva and Snejko [17] who performed IF experiments in Nb-1.9%V with different oxygen compositions in the alloy. They found P1 (553 K) and P2 (688 K) when the oxygen concentration was lower than 0.08%O. When the oxygen concentration was higher, they found a third peak at 638 K and argued that it was due to the trapping of an oxygen by two vanadium atoms.

Indrawirawan et al. [3] also performed IF experiments in Nb-5%V with different oxygen compositions and found a qualitatively similar behavior than those reported by Carlson et al. [2]. They found a single peak at a temperature of 635 K with an external frequency of 0.55Hz and 0.21%O. By increasing the oxygen content, they found a second peak at a lower temperature (515 K). They observed as well an increase of both peaks with O content. They identified the low temperature peak as P2 and named the other peak as P3 and argued that it was due to the binding of single oxygen atoms with 2 vanadium atoms. Kushnareva and Snejko [17] also performed IF experiments in Nb-7%V with oxygen concentrations between 0.05%O and 0.50%O observed 4 different Debye peaks and argued it was due to different clusters of oxygen-vanadium atoms (single oxygen atoms, OV, OV_2, OV_3 and OV_4).

Internal Friction experiments in highly concentrated alloys have been performed as well, up to Nb-50%V [17,18]. In these experiments, it was found that the Nb-O Snoek peak shifted to higher temperatures with vanadium content. Moreover, it was found a broadened single peak for all studied alloys and a loss of the Gaussian shape in concentrated alloys (Nb-20%V and Nb-50%V). Kushnareva et al. [18] argued that, for alloys with a concentration higher than 7%V, it was possible to fit the IF peak as a sum of four elementary Debye peaks. By analogy, they argued that each contribution of these Debye peaks corresponded to the binding of an oxygen atom with different clusters of oxygen-vanadium atoms.

Static Monte Carlo simulations have already been performed by Blanter [19] in order to simulate the Snoek relaxation of alloys with compositions Nb-1.5%V-0.145%O and Nb-1.5%V-0.29%O. He calculated the energy of the oxygen atoms in their stable and saddle point positions using a discrete crystal lattice model, from which he obtained the local migration energy. He then proceeded to perform Monte Carlo simulations, where the vanadium atoms were frozen until an equilibrium short- range order was achieved, and then computed Q^{-1} as a sum of independent Debye peaks. He concluded that the addition of vanadium shifted the oxygen Snoek peak in pure Nb at higher temperatures and the resulting IF peaks were due to single vanadium atoms and OV pairs. Even though he showed that the IF can be modelled by Monte Carlo simulations, there are still some issues. First, he did not explain properly the effects of the cluster distribution on the IF peaks and stated that a single type of cluster could even be responsible of multiple new Snoek peaks. Second, he stated that single vanadium atoms could produce extra Snoek peaks, which seems to disagree with the

theory of the Snoek relaxation.

1.4. Diffusion of oxygen in dilute Nb-V-O alloys

Even though we have not found any experimental data on the oxygen tracer diffusion in dilute Nb-V-O alloys, Zhu et al. [20] performed AKMC simulations in order to model the long-range diffusion of oxygen in dilute Nb-V alloys ($\sim 0.02\%$). First, they computed the oxygen migration barrier in pure Nb and when it was closed to a single V atom up to 3 nn using DFT calculations and used these values as inputs. They then used a residence time algorithm [21] in order to select an O jump and to compute the physical time at each Monte Carlo step. The tracer diffusion coefficient was then obtained by measuring the mean square displacement of the O atom and applying the Einstein-Smoluchowski relation. They found that the oxygen tracer diffusion coefficient in dilute Nb-V alloys followed an Arrhenius relationship with the inverse temperature. They then used the Oriani model [22] in order to extract an effective V-O binding energy of 0.63 eV. They concluded that the main contribution of this effective binding energy – and on the oxygen tracer diffusion coefficient – is mainly influenced by the most attractive O-V interaction in its strongest trapping site. Moreover, they found an average migration enthalpy of 1.58 eV, which is higher than the local migration barriers of O close to the V atom. This discrepancy may be explained by the simplifying assumption of the Oriani model that does not consider a change in the oxygen saddle point energy due to V atoms and does not consider kinetic correlations. Nevertheless, they did not discuss the stability of the oxygen-vanadium pairs, the effects of oxygen-oxygen interactions and how these variables influenced the effective diffusivity and average oxygen migration enthalpy in dilute Nb-V alloys.

2. DFT calculations

The sets of binding energies and migration barriers for oxygen in Nb-V alloys were determined using the same approach as for the study of C in Fe-Cr alloys. The main difference is that in this chapter we restricted the exploration of the oxygen configurations to 3 V atoms in the first, second and third shells.

We found the value of the oxygen migration barrier in pure Nb, $\Delta H_O^m\left(Nb\right) = 0.991$ eV, being in agreement with previous DFT calculations made by Zhu et al. [20] (0.92 eV). Internal Friction experiments [8–12], tracer diffusion experiments [6] and diffusion couple technique [7] found a slightly higher value, closer to 1.2 eV. Table 5 shows a comparison between our calculated $\Delta H_O^m\left(Nb\right)$, the available experimental results and the DFT calculations by Zhu et al. [20]. The oxygen migration barrier in pure V was found to be $\Delta H_O^m\left(V\right) = 1.184$ eV, in good agreement with previous DFT [23] and internal friction experiments [12].

Reference	$\Delta H_O^m(Nb)$ (eV)
This study (DFT)	0.991
Fedorov et al. [6]	1.21 ± 0.08
Tseng et al. [7]	1.11
Weller et al. [8]	1.154 ± 0.009
Powers et al. [9]	1.17 ± 0.01
Weller et al. [10]	~ 1.2
Weller et al. [11]	1.15 ± 0.01
Indrawirawan et al. [12]	1.12 ± 0.03
DFT calculation by Zhu et al. [20]	0.92

Table 5: Comparison between our value of $\Delta H_O^m(Nb)$ with the results from the literature.

For extremely dilute systems, we have determined the O-V binding energies in Nb, at different distances and the corresponding O migration barrier. We noticed that the O-V interaction in Nb is highly attractive for 1nn but slightly repulsive for 2nn and 3nn positions ($E_{O-1V}^b(1) = +0.5988$ eV, $E_{O-1V}^b(0,1) = -0.0895$ eV and $E_{O-1V}^b(0,0,1) = -0.0193$ eV). These results are in good agreement with those found by Zhu et al. [20], who found the O-V binding energies in Nb-rich alloys equal to 0.58 eV and -0.10 eV at 1nn and 2nn, respectively. Nevertheless, they found an attractive O-V binding energy at 3nn equal to 0.05 eV. Table 6 and Table 7 show a comparison between the DFT calculated binding energies and migration barriers determined in this work and those calculated by Zhu et al. [20].

Configurations	This work (eV)	DFT by ref. [20] (eV)
$E_{O\text{-}1V}^b(1)$	+0.599	+0.58
$E_{O\text{-}1V}^b(0,1)$	-0.090	-0.10
$E_{O\text{-}1V}^b(0,0,1)$	-0.019	-0.05

Table 6: Comparison between the DFT calculated binding energies from this work and the ones from ref. [20].

Configurations	This work (eV)	DFT by ref. [20] (eV)
$\Delta H_O^m(Nb)$	0.991	0.92
$\Delta H_O^m(12)$	1.285	1.23
$\Delta H_O^m(21)$	0.597	0.51
$\Delta H_O^m(23)$	0.918	0.84
$\Delta H_O^m(32)$	0.988	0.90

Table 7: Comparison between the DFT calculated migration barriers from this work and the ones from ref. [20].

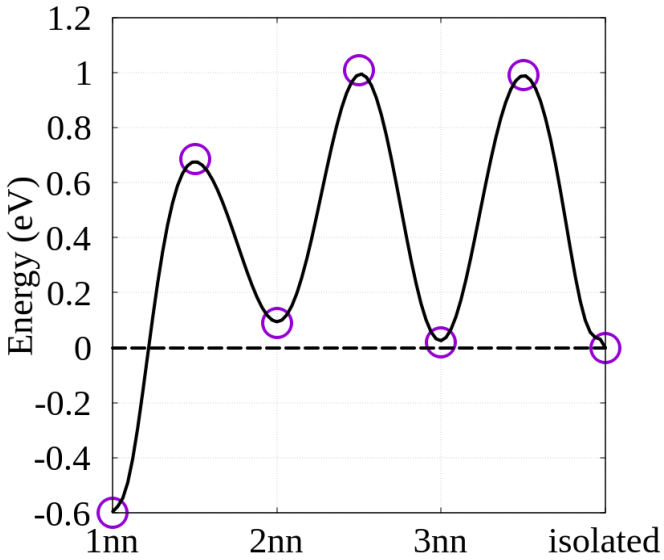

Figure 46: Energetic landscape of an oxygen atom at an ith-nearest neighbor (inn) site from the single V atom in a Nb-rich alloy. The reference state is an isolated oxygen atom, well far from the substitutional solute.

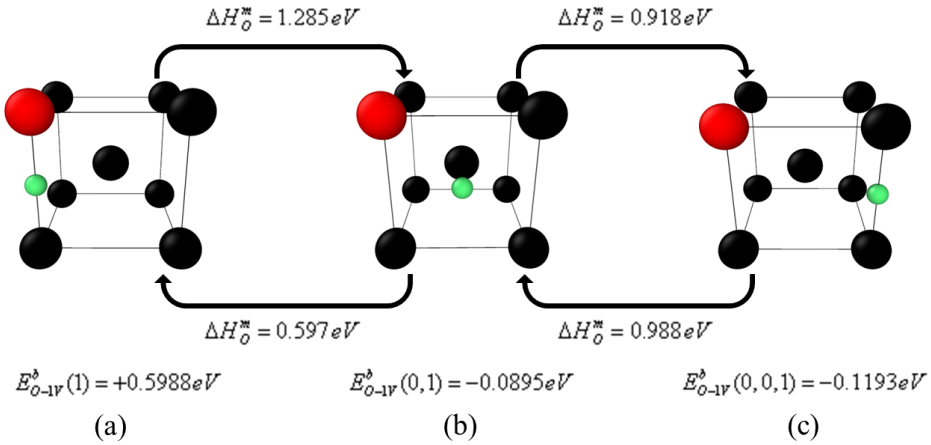

Figure 47: Oxygen (green) migration barriers close to a configuration of V atoms (red) with the corresponding oxygen-vanadium binding energies at the initial position (negative sign corresponds to a repulsive oxygen-vanadium interaction).

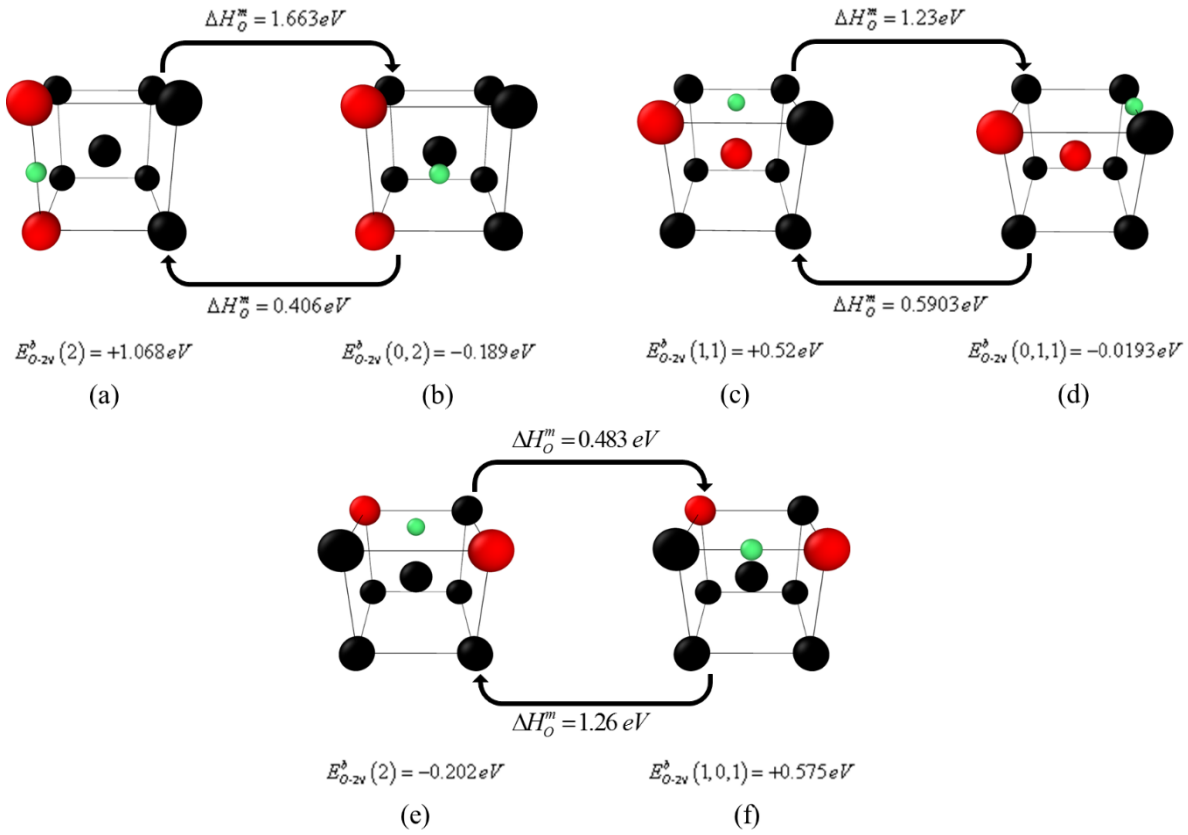

Figure 48: Oxygen (green) migration barriers close to a configuration of V atoms (red) with the corresponding oxygen-vanadium binding energies at the initial position (negative sign corresponds to a repulsive oxygen-vanadium interaction).

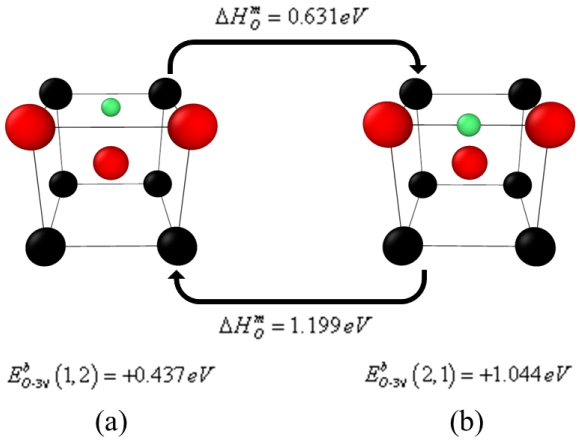

Figure 49: Oxygen (green) migration barriers close to a configuration of V atoms (red) with the corresponding oxygen-vanadium binding energies at the initial position (negative sign corresponds to a repulsive repulsive oxygen-vanadium interaction).

The local oxygen migration barriers in Nb, at 1nn of the V atom ranges from 1.29 eV (1nn to 2nn from the V atom) to 0.59 eV (2nn to 1nn from the V atom). Our values are also in agreement with those found by Zhu et al. [20], even though our values are slightly higher (they found 1.23 eV for the migration barrier corresponding to the jump of the oxygen atom being 1nn to 2nn from the V atom; and 0.51 eV for the reverse jump).

Figure 50 and Figure 51 show the dependence of E^b_{O-nS} and $\Delta H^m_O(ij)$ with respect to the number of substitutional solute atoms around an O atom (up to a 3nn position). Figure 50 shows that for almost any local chemical environment of V, the O-*n*V interaction is attractive, having a maximum when there are 2 V atoms around a O atom ($E^b_{O-nS}(2) = 1.068$ eV) and a minimum when the 2 vanadium atoms are 2nn of the O atom ($E^b_{O-nS}(0,2) = -0.202$ eV).

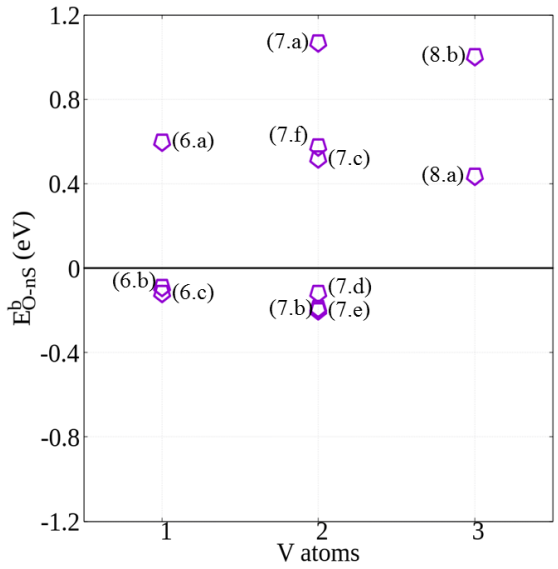

Figure 50: Binding energies as a function of the total number of substitutional solute atoms in the system in Nb-rich alloys. The labels correspond to the configurations from Figure 47, Figure 48 and Figure 49.

The O migration barriers are closely related to the binding energies. In Nb-rich alloys, ΔH^m_O ranges from 0.406 eV to 1.663 eV, with a tendency to remain constant around the value of $\Delta H^m_O(Nb)$ but with a major dispersion when there are 2 V atoms in the vicinity of the oxygen atom. Due to a very strong oxygen-vanadium attraction, we can see that there is a wide spectrum of migration barriers. These interactions lead to strong trapping effects as well. For example, if the O has 2 V as 1nn then $E^b_{O-2S}(2) = +1.068$ eV and $\Delta H^m_O(ij) = 1.663$ eV. The lowest migration barrier is given by the reverse jump, when the 2 V are now 2nn of the oxygen atom: $E^b_{O-nS}(0,2) = -0.189$ and $\Delta H^m_O(ij) = 0.406$ eV.

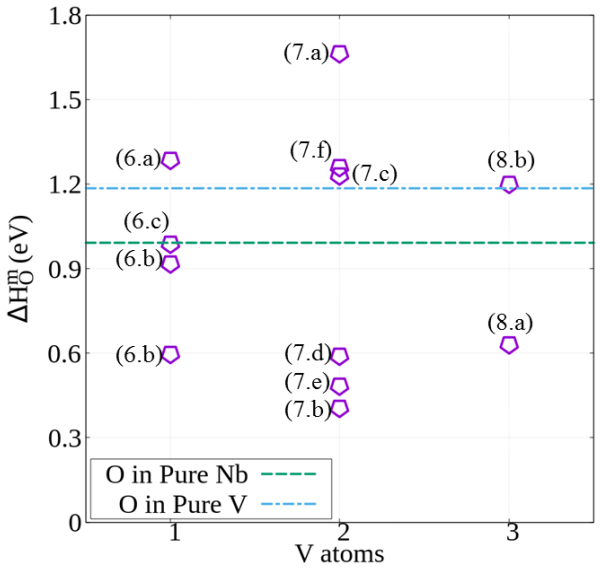

Figure 51: The oxygen migration barriers as a function of the total number of substitutional solute atoms in the system in dilute V alloys. The labels correspond to the configurations from Figure 47, Figure 48 and Figure 49.

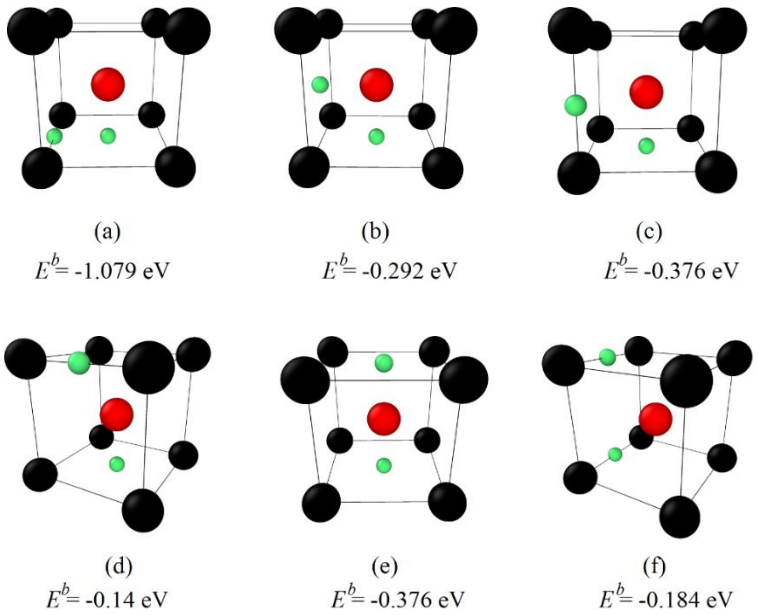

Figure 52: Different configurations of O (green) with V (red) atoms and their respective binding energies (negative sign corresponds to a repulsive interaction).

We also computed the binding energies between an oxygen atom and a 1 nn OV pair and we see that, for any configuration, there is a repulsive interaction between the 'extra' oxygen

atom and the OV pair (Figure 52). Just as a reference, we computed the binding energy of two oxygen atoms in pure Nb at a distance of 4 nn (Figure 52 (e) and (f)) and obtained a value of -0.171 eV. This means that the oxygen-oxygen interaction is even more repulsive if the oxygen atoms are close to a vanadium atom. In order to model this repulsion, we added O-O pair interactions in our model at the octahedral stable position. We must also notice that we did not consider O-O interactions at the saddle point, possibly leading to an overestimation of the effect of the O-O pair interactions on the oxygen migration barriers in the vicinity of other oxygen atoms.

3. Pair interaction model

As we have seen in the previous chapters, the migration barrier between configurations *i* and *j* is defined as:

$$\Delta H_O^m(ij) = H_{i,j}^{SP} - H_i, \tag{3.1}$$

where $H_{i,j}^{SP}$ and H_i are the total enthalpies of system, when the oxygen atom is respectively at the saddle point (SP) and in the initial position. We built a pair interaction model (PIM) following the same procedure as for the computation of the migration barriers using model 1 in chapter 1.

First, we computed by DFT calculations the binding energies between a single oxygen atom and a particular local configuration of vanadium atoms (having at most 3 atoms of vanadium). We used this value in order to compute H_i by counting the number of O-Nb and O-V bonds broken at the octahedral initial position. Then we computed several oxygen migration barriers in these particular local configurations of V around the O atom. From each ΔH_O^m we computed the O-Nb and the O-V bonds formed at the saddle point position. Figure 53 shows the comparison between the DFT values and the pair interaction model (PIM) used to model this system. We computed a total of 11 binding energies and a total of 13 migration barriers using DFT methods. Binding energies and oxygen migration barriers in V-rich alloys were not considered. For the formulation of the pair interaction model, we took into account interactions up to 3 nn in the stable position and up to 2 nn at the saddle point position. Since we only fitted very diluted environments of V, we will only try to reproduce the IF of systems with low concentrations of V (up to 2.5%V) and compare it with [2,3]. Table 8 and Table 9 show the pair interactions between oxygen and each substitutional solute atom at the octahedral position and at the saddle point respectively.

Pair interaction	Value (eV)
$VNbO_1^i$	1.57
VVO_1^i	1.00
$VNbO_2^i$	0.91
VVO_2^i	1.00
$VNbO_3^i$	0.99
VVO_3^i	1.00

Table 8: Nb-O and V-O pair interactions at the octahedral position i and as n nearest neighbors.

Pair interaction	Value (eV)
$VNbO_1^{SP}$	1.00
VVO_1^{SP}	0.77
$VNbO_2^{SP}$	2.91
VVO_2^{SP}	2.86

Table 9: Nb-O and V-O pair interactions at the saddle point SP and as m nearest neighbors.

Unlike the modelling of the binding energies and the carbon migration barriers in Fe-Cr alloys, we can see that for this particular system, a simple pair interaction model can reproduce very well the results found by DFT. There are three reasons why this simple approach works in dilute Nb-V-O alloys. First, we are working in very dilute alloys and there are not many configurations to consider. Second, since our interest is only for this limited range of compositions, we did not try to fit our parameters in V-rich environments, thus having more freedom to choose our parameters. Third, because binding energies of this system have a satisfying additive property, meaning that a binding energy of a complex configuration can be written as a sum of the binding energies of elementary configurations. For example, an O atom with a single 1 nn vanadium atom has a binding energy of $E^b_{O-1V}(1) = +0.5988$ eV, which is roughly half the binding energy of an O with two 1 nn V $E^b_{O-2V}(2) = +1.068$ eV. This is not the case for the C-Cr binding energies in dilute Fe-Cr alloys: $E^b_{C-1Cr}(2) = -0.249$ eV and $E^b_{C-2Cr}(2) = -0.271$ eV.

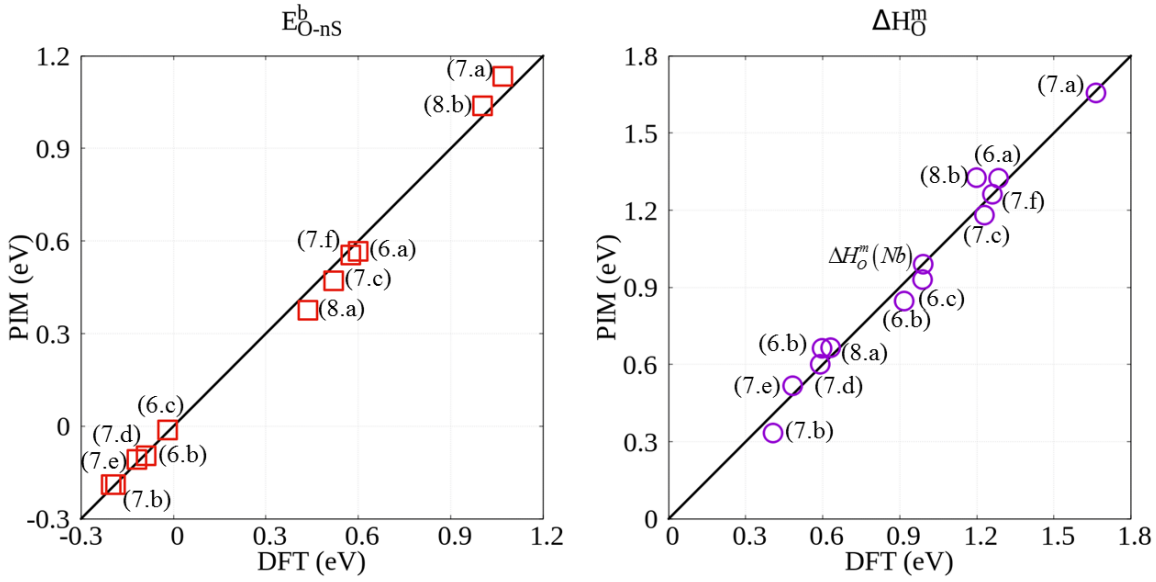

Figure 53: Comparison between the PIM with the DFT results for the binding energies (left) and the migration barriers (right). The labels correspond to the configurations from Figure 47, Figure 48 and Figure 49 and $\Delta H_O^m(Nb)$ as reference.

As we have seen in the previous section, we also computed the binding energy of an extra oxygen atom close to an oxygen-vanadium pair. In order to reproduce these binding energies, we assumed that the niobium-oxygen and the vanadium-oxygen were constant and we added oxygen-oxygen pair interactions. Table 10 shows the values of the oxygen-oxygen pair interactions and the comparison between the DFT values and the predicted values by the model. Our model can predict most of these binding energies but it slightly underestimates the binding energy of the configuration in Figure 52(e) and it highly overestimates the binding energy for the configuration in Figure 52(f).

Pair interaction	DFT (eV)	PIM (eV)
$VOO_1 = 0.9841$	-1.0791	-1.0791
$VOO_2 = 0.8584$	-0.292	-0.292
$VOO_3 = 0.281$	-0.376	-0.376
$VOO_5 = 0.045$	-0.14	-0.14
$VOO_4 = 0.8$	-0.376	-0.2366
$VOO_4 = 0.8$	-0.1838	-0.895

Table 10: Comparison between the binding energies O-OV computed by DFT and those predicted by the model using oxygen-oxygen pair interactions VOO_n, where n corresponds to the nearest neighbors in the cubic lattice. The configurations are shown in Figure 52.

Last, we need to find an appropriate value of υ_0 in order to analyze the Snoek peaks in dilute Nb-V-O alloys. It is well-known that the temperature of the oxygen peak in pure Nb at a low frequency of the applied stress and a low oxygen concentration is between 400 K and 430 K. [2,8,11,13,24]. Since we are mainly interested in showing that the AKMC simulations can reproduce the evolution of the IF peaks with the oxygen concentration, we decided to fit the value of υ_0 using the DFT value of $\Delta H_O^m(Nb)$ in order to have a good agreement with the temperature of the peak P1. We chose to use a value of $\upsilon_0 = 1.1\times10^{12}$ Hz and consequently the temperature of the oxygen Snoek peak in pure Nb to be 410 K at $f = 1$ Hz. This value is smaller than the experimental values of Carlson et al. [2] (5×10^{13} Hz), of Ahmad and Szkopiak [13] (3.6×10^{13} Hz) and of Weller et al. [8] (2×10^{13} Hz).

4. Theoretical model of the Snoek peak in dilute ternary alloys

4.1. The Koiwa model for internal friction

The theoretical model developed by Koiwa [4,5] describes analytically the Internal Friction in ternary dilute alloys due to the diffusion of interstitial atoms. In this model, he assumes that there is only one substitutional solute atom interacting with one interstitial, while there is an applied external stress upon the system. He first describes a 'sphere of influence', where the substitutional solute atom has an effect on the migration barrier of the interstitial jumps, as shown in Figure 54. The assumption made in the model is that the substitutional solutes are fixed on their positions and are far away from each other, so that the diffusion of an interstitial is influenced by a single substitutonal solute atom.

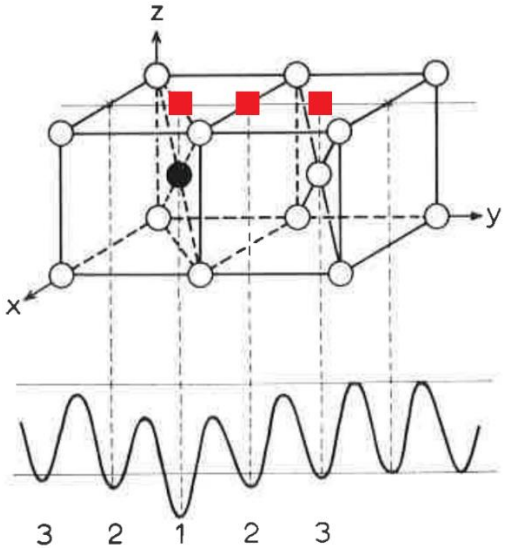

Figure 54: The influence of the substitutional solute atom (black dot) on the different octahedral sites (red squares). The curve shows the energy of interstitial atoms. The numbers indicate the shell numbers. Figure adapted from [4,5].

Rate equations are written for the interstitial concentration at the substitutional solute neighboring. Sites are differentiated by their distance from the substitutional solute atom. Under the applied stress these sites are subdivided into different classes depending on their symmetry with respect to the applied stress. Each class is associated with a different concentration and rate equation.

Koiwa first expresses the steady state average occupation under a constant external stress. He then writes the rate equations for the deviation of the average occupations from their corresponding steady state values. Up to 13 classes of sites and rate equations are included in the resulting system of first order linear differential equations.

The system is Laplace transformed and then solved as an eigenvalue problem. In the case of second shell approximation, there are three distinctive octahedral sites: when the oxygen is at 1 nn and 2 nn from the vanadium atom and when it is very far away. This reduction in symmetry leads to three eigenvalues τ, τ_a and τ_b, which are equal to:

$$\frac{1}{\tau} = 6\Gamma\left(Nb\right), \tag{3.2}$$

$$\tau_a, \tau_b = \frac{6\left(\tau_1+\tau_2\right) \pm 3\sqrt{4\left(\tau_1+\tau_2\right)^2 - 2\left(8-\alpha\right)\tau_1\tau_2}}{8-\alpha}, \tag{3.3}$$

where $\alpha = \tau_2/\tau_2'$. We also define a series of relaxation times that are the inverse of the jump frequencies $\Gamma\left(ij\right)$ (when the oxygen atom jumps from a site i nn to a site j nn from the vanadium atom). For example:

$$\frac{1}{\tau_1} = 6\Gamma\left(12\right) \tag{3.4}$$

corresponds to the jump frequency from an oxygen atom that jumps from a 1 nn to a 2 nn site relative to a vanadium atom. We also define the following elementary jump frequencies:

$$\frac{1}{\tau_2'} = 6\Gamma\left(21\right) \tag{3.5}$$

$$\frac{1}{\tau_3'} = 6\Gamma\left(23\right) \tag{3.6}$$

$$\frac{1}{\tau_2} = \frac{1}{2}\left(\frac{1}{\tau_2'} + \frac{1}{\tau_3'}\right) \tag{3.7}$$

where Eq. (3.7) corresponds to an average jump frequency where the O atom is a 2 nn of a vanadium atom, and Eq. (3.2) corresponds to the jump frequency of oxygen in pure Nb.

From the eigenvalues τ, τ_a and τ_b we deduce the inverse quality factor Q^{-1}:

$$Q^{-1}\left(T\right) = f_1\frac{\omega\tau_a}{1+\left(\omega\tau_a\right)^2} + f_2\frac{\omega\tau_b}{1+\left(\omega\tau_b\right)^2} + f_3\frac{\omega\tau}{1+\left(\omega\tau\right)^2}. \tag{3.8}$$

The parameters f_1, f_2 and f_3 define the height of the Snoek peak. They are equal to the

concentration of free vanadium C_V^F multiplied by a complex function of the binding energies and the jump frequencies:

$$f_1 = 2C_V^F \frac{a_1 b_{11} + 2a_2 b_{21}}{1 + 2C_V^F \left(a_1 + 2a_2 - 3\right)} \tag{3.9}$$

$$f_2 = 2C_V^F \frac{a_1 b_{12} + 2a_2 b_{22}}{1 + 2C_V^F \left(a_1 + 2a_2 - 3\right)} \tag{3.10}$$

$$f_3 = \frac{2C_V^F \left(a_1 S^2 b_{13} + 2a_2 b_{23} - 3\right) + 1}{1 + 2C_V^F \left(a_1 + 2a_2 - 3\right)}, \tag{3.11}$$

where $a_1 = \exp\left(E_{O-V}^b(1)/k_B T\right)$ and $a_2 = \exp\left(E_{O-V}^b(0,1)/k_B T\right)$. $E_{O-V}^b(1)$ and $E_{O-V}^b(0,1)$ are the oxygen-vanadium binding energies as defined in Table 6. C_V^F is computed from the Lomer equations as we will see in the following section.

The b_{ij} are related to the jump frequencies via:

$$\left(\frac{\tau_1}{\tau_a} - \frac{2}{3}\right) b_{11} = \frac{b_{21}}{3} \tag{3.12}$$

$$\left(\frac{\tau_1}{\tau_b} - \frac{2}{3}\right) b_{12} = \frac{b_{22}}{3} \tag{3.13}$$

$$\left(\frac{\tau_1}{\tau} - \frac{2}{3}\right) b_{13} = \frac{b_{23}}{3} \tag{3.14}$$

$$\left(\frac{\tau_2}{\tau_a} - \frac{2}{3}\right) b_{21} = \frac{\alpha b_{11}}{6} \tag{3.15}$$

$$\left(\frac{\tau_2}{\tau_b} - \frac{2}{3}\right) b_{22} = \frac{\alpha b_{12}}{6} \tag{3.16}$$

$$\left(\frac{\tau_2}{\tau} - \frac{2}{3}\right) b_{23} = \frac{\alpha b_{13}}{6} + \frac{\tau_2}{\tau_3' 6} \tag{3.17}$$

If we have the case where $\tau_1 \gg \tau_2$, τ_a and τ_b can be expressed as:

$$\tau_a = \frac{12}{8-\alpha}\tau_1 \left[1 + \frac{\alpha}{8}\left(\frac{\tau_2}{\tau_1}\right) + \frac{8\alpha - \alpha^2}{64}\left(\frac{\tau_2}{\tau_1}\right)^2\right] \simeq \frac{12}{8-\alpha}\tau_1 \tag{3.18}$$

$$\tau_b = \frac{3}{2}\tau_2 \left[1 - \frac{\alpha}{8}\left(\frac{\tau_2}{\tau_1}\right)\right] \simeq \frac{3}{2}\tau_2 \tag{3.19}$$

Figure 55 shows the application of the KMIF for the Nb-0.5%V-0.65%O at an external frequency of 0.35 Hz. We can see that even though there are three eigenvalues, τ_b becomes negligible and we only observe 2 distinctive peaks. The low-temperature peak corresponds to the oxygen Snoek peak in pure Nb and the high-temperature Snoek peak corresponds to

τ_a, which is not exactly equal to τ_1 (Eq. (3.18)). From the height of the peaks, we can see that the amplitude of P2 is larger than P1. Since the height of the peak are proportional to the defect concentration (Eq. (1.59), chapter 1) we can deduce that there is a larger amount of OV pairs than isolated O atoms in the alloy.

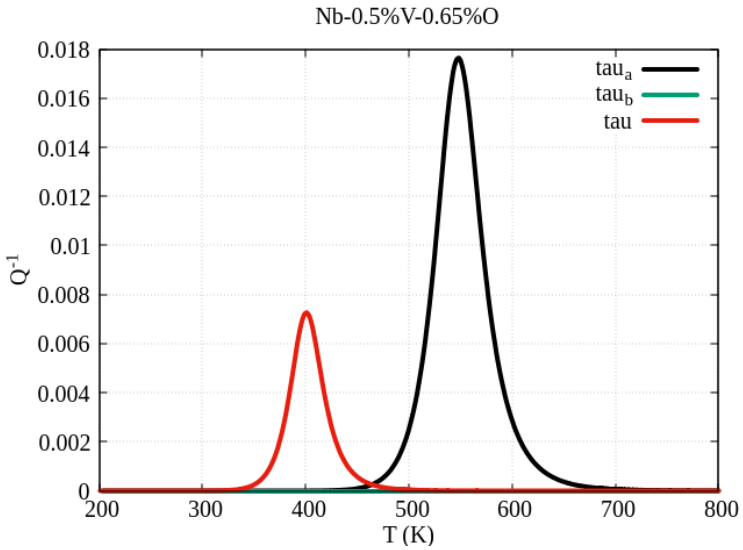

Figure 55: Decomposition of the Snoek peaks for Nb-0.50%V-0.65%O.

We can see very interesting features about the KMIF that are different from the standard approach which consists in expressing the IF spectrum as a sum of independent Debye peaks, such as in [25]. First, the relaxation times that describe the Snoek peaks (Eq. (3.8)) are not simply proportional to jump frequencies of elementary octahedral jumps, but a complex function of them (Eq. (3.3)). Second, the associated jump frequency does not correspond to the inverse of a residential time. Note that according to this model [4,5], due to the reduction of crystal symmetry under stress, the number of configurations which produce a Debye peak can be larger than the number of equilibrium configuration.

4.2. Equilibrium cluster concentration

As shown in the previous section, the height of the Debye peaks are directly related to the concentration of free vanadium C_V^F via f_1, f_2 and f_3. Therefore, we need to study in detail the properties of the clusters (isolated O and V atoms and OV pairs) at equilibrium. We first introduce the Lomer model [26] which provides an exact description of the equilibrium cluster concentration as long as the alloy is infinitely diluted (i. e. a pure metal including a single interstitial and a single substitutional solute).

We start by defining the concentration of vanadium atoms as the number of vanadium atoms n_V divided by the number of bcc sites N: $c_V = n_V / N$. We define as well the oxygen

concentration with respect to the number of bcc sites: $c_O = n_O / N$. Following the Lomer formulation, we write:

$$c_V = [V]\left(1 - [O]\sum_n Z_{VO}^n\right) + [V][O]\sum_n Z_{VO}^n \exp\left(\frac{E_{O-V}^b(n)}{k_B T}\right) \tag{3.20}$$

where Z_{VO}^n is the number of interstitial nearest neighbors of a vanadium atom and $E_{O-V}^b(n)$ is the oxygen-vanadium binding energy at 'n' nn position. $[V]$ and $[O]$ correspond to the so-called vanadium and oxygen monomer concentrations.

As well, we get for the total concentration of oxygen:

$$\frac{c_O}{3} = [O]\left(1 - [V]\sum_n Z_{OV}^n\right) + [V][O]\sum_n Z_{OV}^n \exp\left(\frac{E_{O-V}^b(n)}{k_B T}\right) \tag{3.21}$$

where Z_{OV}^n is the number of substitutional nearest neighbors of an oxygen atom. Eq. (3.21) is divided by 3 in order to account for the fact that there are 3 interstitial sites per bcc site.

From Eqs. (3.20) and (3.21), we identify the concentration of the different clusters. The concentration of free vanadium is:

$$c_V^F = [V]\left(1 - [O]\sum_n Z_{VO}^n\right), \tag{3.22}$$

the concentration of free oxygen:

$$c_O^F = [O]\left(1 - [V]\sum_n Z_{OV}^n\right) \tag{3.23}$$

and the concentration of the OV pairs with respect to the bcc sites:

$$C_{OV} = [V][O]\sum_n Z_{VO}^n \exp\left(\frac{E_{O-V}^b(n)}{k_B T}\right) \tag{3.24}$$

Note that in addition to the pair interactions between O and V, we have introduced O-O repulsive interactions. A Lomer model is not able to consider these repulsive interactions properly. Therefore, we did not include them in the Lomer equations. As an example, we show in Figure 56 the concentrations for the extreme cases where we performed our AKMC simulations: Nb-0.24%V-0.10%O and Nb-0.50%V-0.90%O. In section 6 we will compute Q^{-1} in terms of the KMIF (Eq. (3.8)) by using as inputs the concentrations determined with Eqs. (3.22)-(3.24) and compare them with our AKMC results.

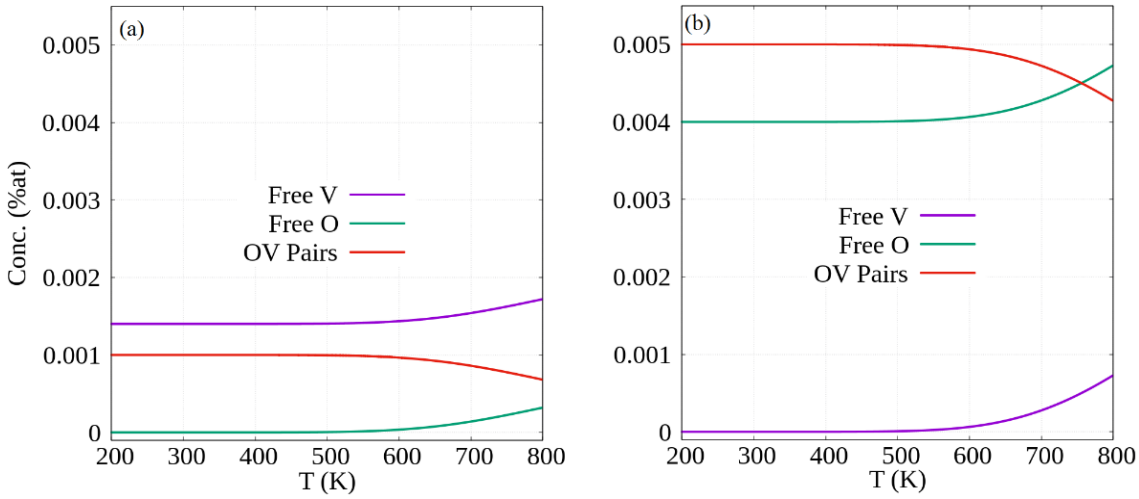

Figure 56: Equilibrium concentrations of C_V^F , C_O^F and C_{OV} for (a) Nb-0.24%V-0.10%O and (b) Nb-0.50%V-0.90%O.

5. AKMC results

5.1. Equilibrium concentrations

Figure 57 up to Figure 61 show the comparison between the equilibrium concentrations given by the AKMC simulations and by Eqs. (3.22)-(3.24). We observe a small discrepancy between the AKMC measurements and the Lomer model. This disagreement is certainly due to the O-O repulsive interactions which were omitted in the Lomer equations. As expected, the discrepancy increases with the oxygen content in the matrix.

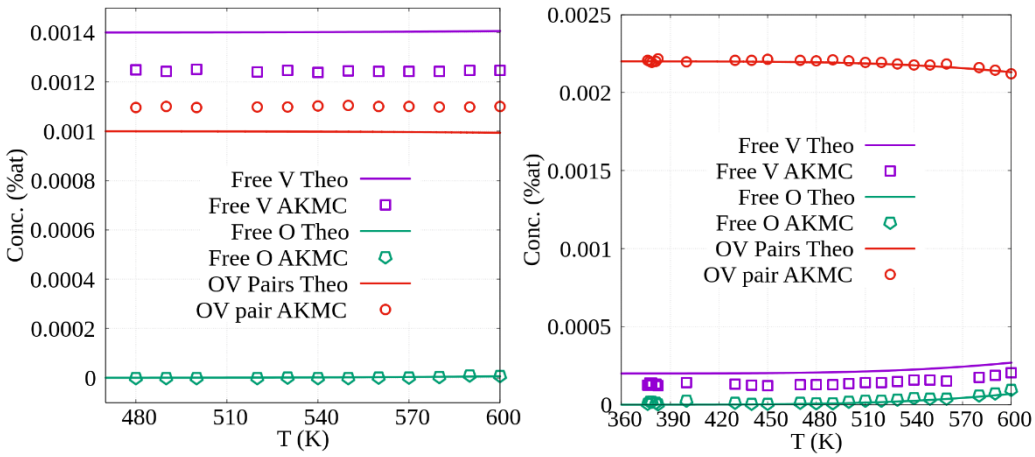

Figure 57: Comparison between the equilibrium concentration given by the AKMC and the theoretical values for Nb-0.24%V-0.10%O (left) and Nb-0.24%V-0.22%O (right) alloys.

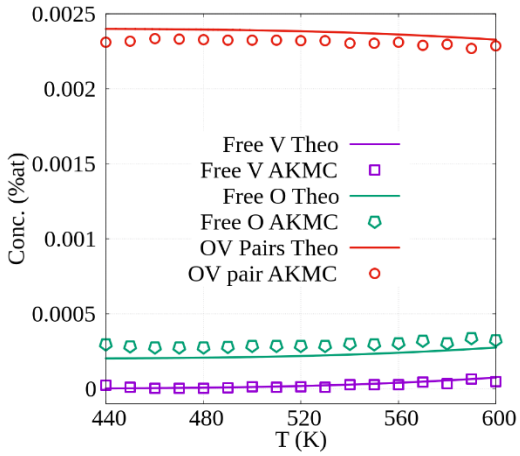

Figure 58: Comparison between the equilibrium concentration given by the AKMC and the theoretical values for Nb-0.24%V-0.26%O alloy.

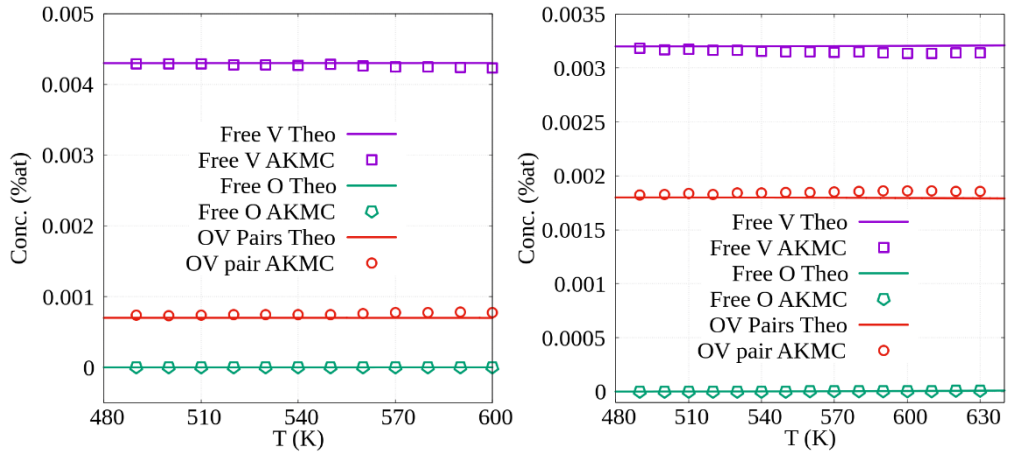

Figure 59: Comparison between the equilibrium concentration given by the AKMC and the theoretical values for Nb-0.50%V-0.07%O (left) and Nb-0.50%V-0.18%O (right) alloys.

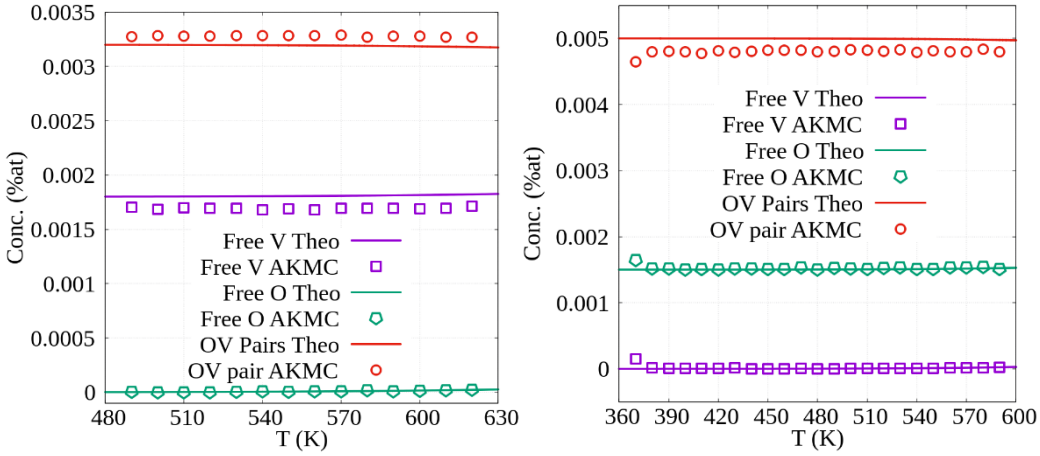

Figure 60: Comparison between the equilibrium concentration given by the AKMC and the theoretical values for Nb-0.50%V-0.32%O (left) and Nb-0.50%V-0.65%O (right) alloys.

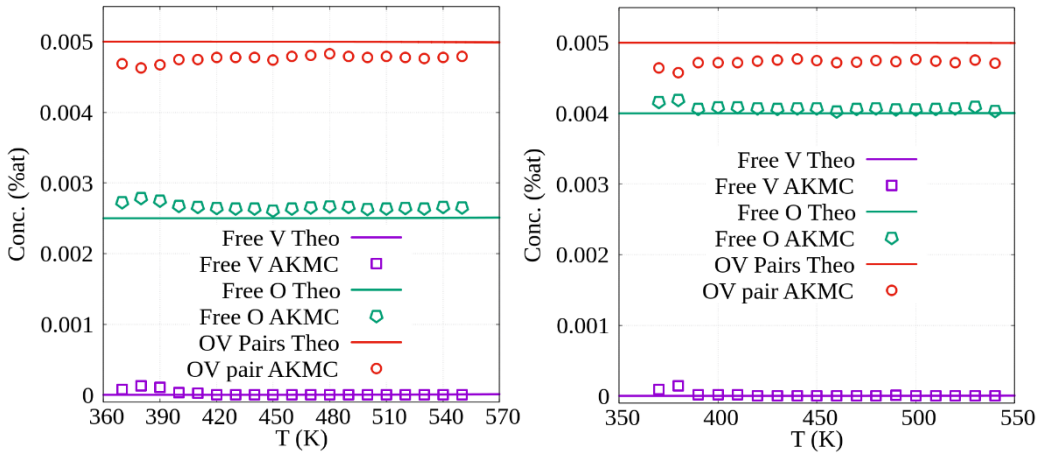

Figure 61: Comparison between the equilibrium concentration given by the AKMC and the theoretical values for Nb-0.50%V-0.75%O (left) and Nb-0.50%V-0.90%O (right) alloys.

5.2. Internal Friction experiments

Figure 62, Figure 63 and Figure 64 show the IF of Nb-0.24%V-O, Nb-0.50%V-O, Nb-1.50%V-0.75%O and Nb-2.50%V-0.50%O alloys respectively. We can see that our AKMC simulations reproduces the Snoek peaks measured by Carlson et al. [2] and by Indrawirawan et al. [3]:

1. When the oxygen concentration is lower than the vanadium concentration, where the free oxygen content is negligible, we find a single Snoek peak at a high temperature (540 K) associated with the OV pair (P2). Carlson et al. [2] find the temperature of P2 at 500 K. We also find that a higher oxygen contents increase the amplitude of P2.
2. When the oxygen concentration is greater than the vanadium content, we see the appearance of P1 at a lower temperature (400 K), which corresponds to the oxygen Snoek peak in pure Nb (P1) and in agreement with the results shown by Carlson et al. [2]. An increase of the oxygen concentration leads to a higher amplitude of P1 while the amplitude of P2 remains constant.

However, our model presents some minor differences with respect to the experimental literature:

1. Our AKMC simulations do not yield P1 for the Nb-0.24%V-0.22%O, in disagreement with the experimental results by Carlson et al. [2].
2. Our AKMC simulations show that, in the Nb-0.5%V system, the T_{max} of P2 is 50 K greater than the experimental value when the concentration of oxygen is smaller than the vanadium content. Carlson et al. [2] show that the position of both peaks is independent of the overall concentration in the alloy.

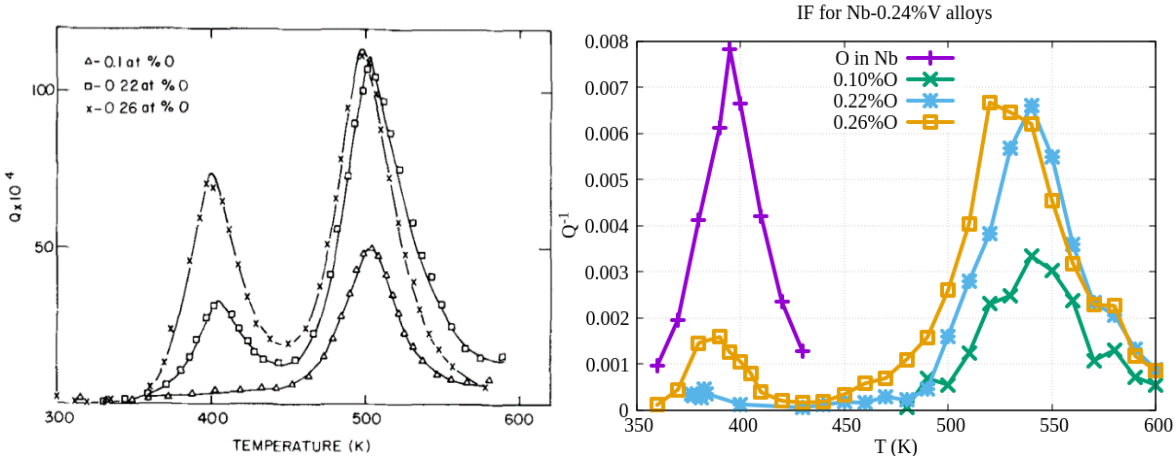

Figure 62: Experimental curves of IF for the Nb-0.24%V alloys (left, extracted from [2]) and AKMC results (right). Oxygen Snoek peak in pure Nb is shown as a reference.

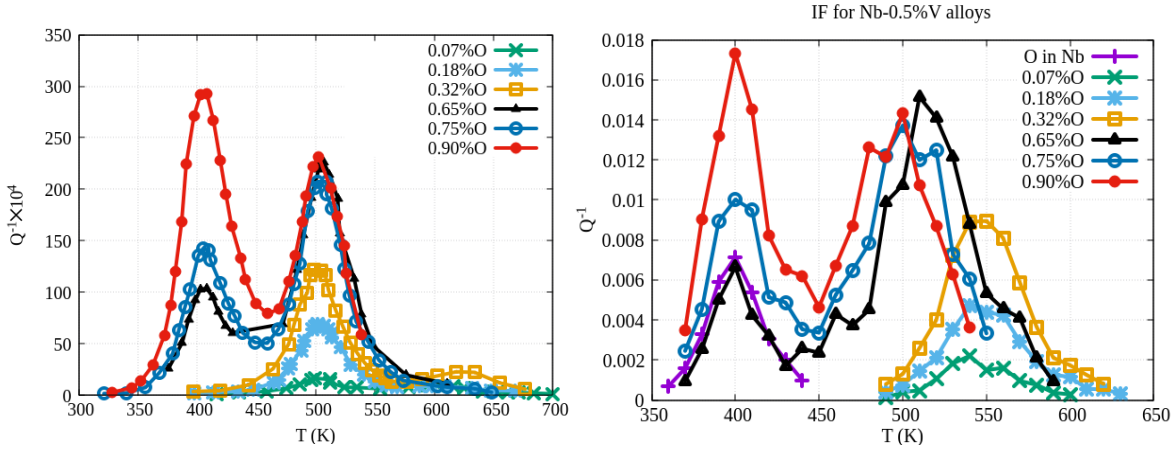

Figure 63: Comparison between experimental results from [2] (left) and AKMC results (right) for Nb-0.50%V alloys. Oxygen Snoek peak in pure Nb is shown as a reference.

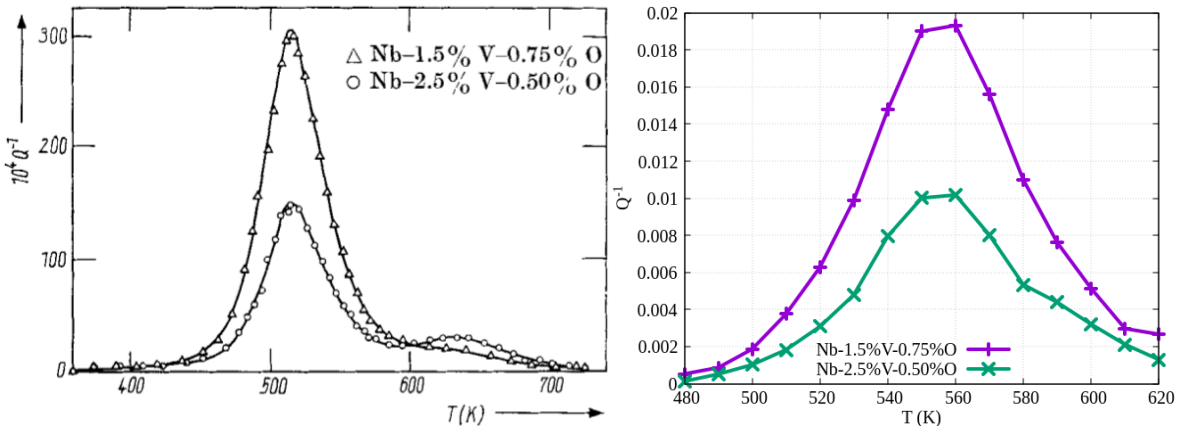

Figure 64: Comparison between experimental results from [3] (left) with AKMC results (right) for Nb-1.50%V-0.75%O and Nb-2.50%V-0.50%O alloys at $f = 0.56$ Hz.

It is worth noticing that the IF simulations of Nb-0.24%V-0.22%O yield a small peak which looks like P1. Nevertheless, the instantaneous oxygen concentration measured on every sublattice is almost constant and very close to the equilibrium concentration (chapter 1, Eq. (1.53)). This means that the oxygen atoms are incapable to follow the stress, and Q^{-1} should be zero. Due to this reason, P1 for the Nb-0.24%V-0.22%O alloy should not be considered as a Snoek peak, but a result of statistical noise. This also reflects a limitation of the AKMC simulations: due to the finite size of the simulation box, the number of free oxygen atoms on which we rely for the computation of Q^{-1} is very small.

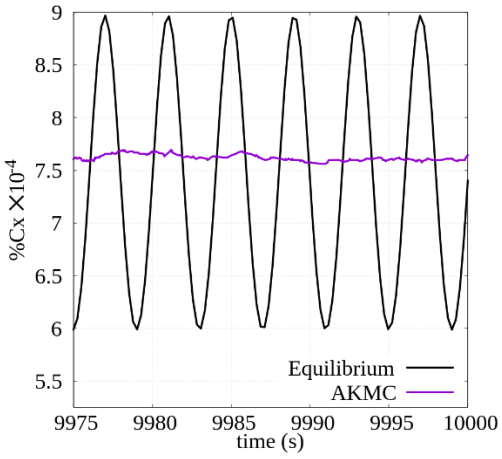

Figure 65: Comparison between the equilibrium concentration and the instantaneous concentration for Nb-0.24%V-0.22%O at 382.5 K and $f = 0.25$ Hz.

In Figure 62 and Figure 63 we have put the oxygen Snoek peak in pure Nb as a reference.

We observe that the position of peak P1 is very close to this reference. Therefore, in agreement with Carlson et al. [2], we attribute the peak P1 to the migration of isolated O in the alloy. Moreover, from the value of the position T_{max} of the peak and Eq. (1.58) in chapter 1, we deduce the corresponding migration barrier: $\Delta\bar{H}_O^m = 0.99$ eV. We find a very good agreement in the temperature of P1 between our AKMC simulations and the experimental result (400 K) due to our fit of υ_0. However, there is a small discrepancy between the values of the oxygen migration barrier in pure Nb by DFT calculations (0.99 eV) and the experimental value (1.15 eV). Regarding the position of the peak P2, the AKMC simulations agree with the experimental observations as long as the amount of oxygen is above the vanadium concentration. However, focusing just on the temperature of P2 can be misleading: the average migration enthalpy of P2 extracted from the first regime is equal to 1.36 eV, being in agreement with the experimental value of 1.4 eV [2]. Although we attribute this peak to the VO pair, the extracted value of $\Delta\bar{H}_O^m$ from P2 slightly differs from the DFT migration barrier associated with the jump of O from a 1 nn to a 2 nn site of a vanadium atom (1.29 eV). The KMIF is able to explain the difference: τ_a does not correspond to a particular jump frequency but to a complex function of them (Eq. (3.18)). However, when the oxygen content is greater than the concentration of vanadium, the extracted average migration enthalpy of P2 is equal to 1.24 eV, which might indicate the formation of a new type of cluster of the form OV-O.

Our AKMC simulations are also in agreement with the results of [3] for the Nb-1.50%V-0.75%O and Nb-2.50%V-0.50%O alloys, even though our value of $T_{max} = 560$ K is higher than their value of 517 K, as shown in Figure 64. But unlike Indrawirawan et al. [3], we do not find any evidence of P3 in these ranges of composition.

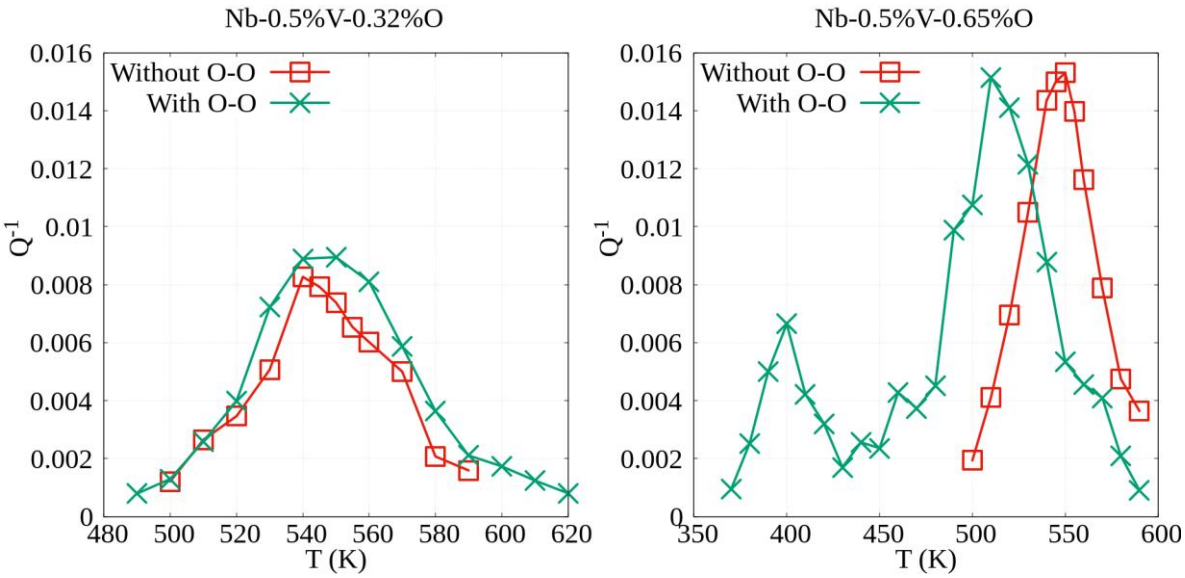

Figure 66: Effect of the O-O interactions in the Snoek peaks for the Nb-0.5%V-0.32%O (left) and Nb-0.5%V-0.65%O (right) systems.

Figure 66 shows the effect of the oxygen-oxygen interactions for the Nb-0.5%V-0.32%O and Nb-0.5%V-0.65%O systems. For the Nb-0.5%V-0.32%O, the effect of the O-O interactions is negligible, where in both cases, the Snoek peak associated with OV pairs conserves its temperature position and its amplitude. For the Nb-0.5%V-0.65%O alloy, when the O-O interactions are switched off, the Debye peak of the pairs remains at 550K, but there is no peak associated with free oxygen. By switching on the O-O interactions, both peaks are present although the position of the OV peak is shifted to a lower temperature. Therefore, the O-O repulsive interactions lead to a cluster distribution in agreement with the experiments by enhancing the formation of O monomers at the expense of the concentration of oxygen-vanadium pairs. Moreover, the shift of the second peak reveals a change of the nature of the cluster, possibly an OV pair surrounded by an additional oxygen atom.

We can conclude from this section that our AKMC simulations reproduce the main trends of the IF in dilute Nb-V-O, even though small discrepancies arise when the concentration of oxygen is larger than the vanadium content. Even though the use of O-O interactions is necessary in order to reproduce the evolution of the Snoek peaks with O concentration, it produces an unexpected shift of P2 to lower temperatures in the Nb-0.5%V-O when $\%O \geq 0.5\%$.

Another way to compare the Lomer model with the AKMC simulations and the experiments performed by Carlson et al. [2] is to perform the ratio of C_O^F / C_{OV} and the ratio of the heights of the peaks P1 and P2 and compare them. The results are shown in Table 11 and Table 12. We can see that both are in the same order of magnitude but C_O^F / C_{OV} is systematically smaller than P1/P2. Also, the ratio given by P1/P2 is smaller than those by Carlson et al. [2] for Nb-0.24%V but in good agreement for Nb-0.50%V.

%O (at)	C_O^F / C_{OV} (AKMC)	P1/P2 (AKMC)	Carlson et al. [2]
0.10	0	0	0
0.22	0	0	0.315
0.26	0.138	0.237	0.52

Table 11: Comparison of P1/P2 with C_O^F / C_{OV} for Nb-0.24%V alloys with Carlson et al. [2].

% O (at)	C_O^F / C_{OV} (AKMC)	P1/P2 (AKMC)	Carlson et al. [2]
0.07	0	0	0
0.18	0	0	0
0.32	0	0	0
0.65	0.311	0.4389	0.45
0.75	0.56	0.7299	0.61
0.90	0.858	1.209	1.27

Table 12 : Comparison of the relative heights between P1 and P2 in Nb-0.5%V alloys.

In the following section we will compare our AKMC results with this model and see if the peaks P1 and P2 truly correspond to the diffusion of isolated O and the dissociation of O from the OV pair.

6. Comparison between AKMC and the KMIF

In this section we assess the KMIF against the AKMC simulations in the dilute Nb-V-O system.

In Figure 67, Q^{-1} is computed for six alloys in which the concentration of vanadium is fixed (0.5%V) while the amount of oxygen is varied from a value below the concentration of vanadium (0.07%O) up to a value above the vanadium content (0.90%O). We observe an excellent agreement between the AKMC and the KMIF results as long as the concentration of oxygen is lower than the concentration of vanadium. When the oxygen content is lower than the vanadium content, the Lomer model, in agreement with the AKMC, predicts a negligible concentration of oxygen monomers, leading to the absence of the oxygen Snoek peak in pure Nb (Figure 67). Therefore, we attribute the single peak to the OV pair. The position of the peak is associated with a migration barrier of 1.354 eV, which is slightly higher than the DFT disassociation barrier of the oxygen from the OV pair (1.289 eV).

If the concentration of oxygen is greater than the concentration of vanadium, the contribution of the free oxygen atoms becomes non-negligible. Thus, a second peak is arising at a lower temperature. Although the KMIF is able to predict the formation of the double peaks and the height of these peaks, it fails in predicting the position of the OV Debye peak for high oxygen concentrations. Indeed, we observe in the AKMC simulations a switch off of the isolated OV peak and the formation of a new Debye peak at a lower temperature. It seems that an increase of the oxygen content tends to decrease the concentration of the free oxygen atoms and leads to the formation of new O_nV clusters. The most probable cluster to be formed is the configuration showed in Figure 52(d) with the smallest repulsive binding energy of -0.14 eV.

Consequently, we observe that the migration of the isolated oxygen and the corresponding peak position is not affected by the oxygen content while the peak position of oxygen within the cluster is affected. From the pair interaction model, we can give an estimation of the associated migration barrier of the corresponding dissociation barrier of this cluster equal to 1.278 eV which is very close to the peak position (510 K): an oxygen atom jumping from the configuration of Figure 52(d) to the new position of Figure 52(e). As expected, the KMIF, which does not include the O-O repulsive interactions is not able to reproduce the AKMC results.

In Figure 68 we observe the same behavior for three alloys which have 0.24%V and different concentrations of oxygen. There is a single Debye peak associated with the OV pairs while the concentration of vanadium is greater than the concentration of oxygen and the formation of a second peak associated with the free oxygen atoms in the Nb-0.24%V-0.26%O system. Surprisingly we see a small discrepancy between the KMIF and the AKMC results not only for the peak associated with the OV pairs but also for P1. This might be due to statistical errors in the AKMC measurements which arises when the concentration of oxygen is small.

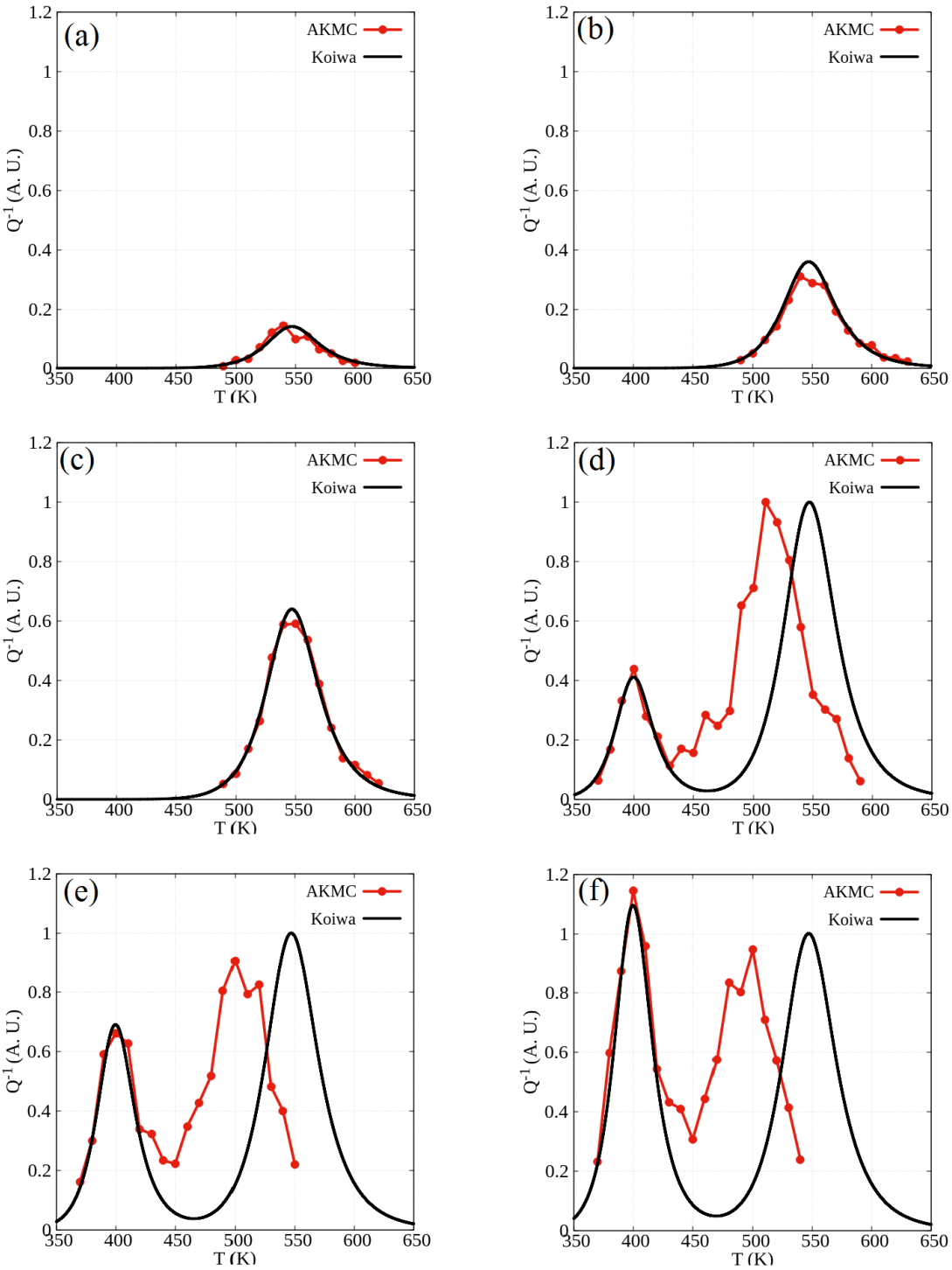

Figure 67: Comparison between the KMIF and the AKMC results for Nb-0.50%V alloys, having oxygen compositions of (a) 0.07%O, (b) 0.18%O, (c) 0.32%O, (d) 0.65%O, (e) 0.75%O and (f) 0.90%O respectively.

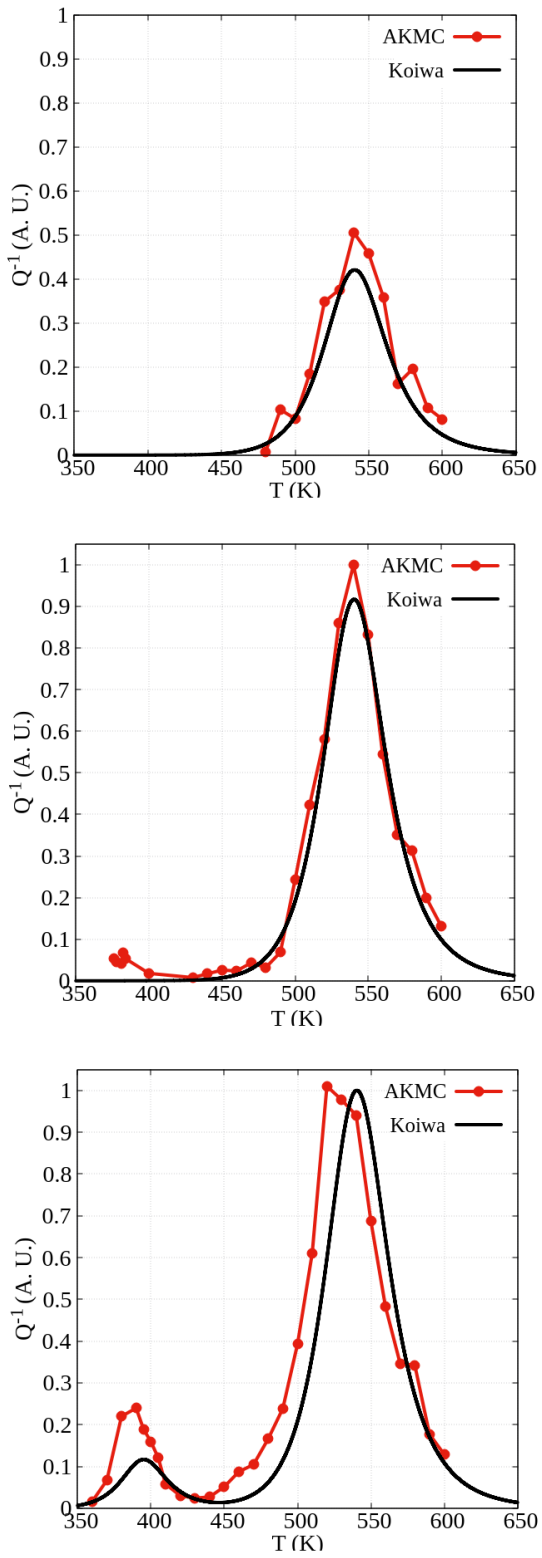

Figure 68: Comparison between the KMIF and the AKMC results for Nb-0.24%V alloys, having oxygen compositions of 0.1%O (top), 0.22%O (center) and 0.26%O (bottom) respectively.

In our AKMC simulations, we calculate the concentration of oxygen atoms on the different sublattices and directly extract Q^{-1}. The advantage of this method is that is not limited to dilute alloys, as we have seen in chapter 2 for the carbon Snoek peak in Fe-Cr alloys. But the main disadvantage is that the precision of the calculations highly depends on the amount of oxygen atoms in the simulation box. This problem is not encountered in the KMIF, due to the fact that the calculation of the concentration of free O and OV pairs are at equilibrium given by Eqs. (3.22)-(3.24). But the main disadvantage of the KMIF is that is only accurate in very dilute alloys.

Another way to compare the KMIF with the AKMC simulations and the experiments performed by Carlson et al. [2] is to perform the ratio of the heights of the peaks P1 and P2 and compare them. Table 13 and Table 14 show this comparison for the Nb-0.24%V-O and the Nb-0.50%V-O systems respectively. We see as well that the ratio is in better agreement for the Nb-0.50%V-O alloys. Moreover, the agreement is degraded when the oxygen content is increased.

%O (at)	AKMC	KMIF	EXP [2]
0.10	0	0	0
0.22	0	0	0.315
0.26	0.237	0.12	0.52

Table 13: Comparison of relative heights P1-P2 for Nb-0.24%V alloys.

% O (at)	AKMC	KMIF	EXP [2]
0.07	0	0	0
0.18	0	0	0
0.32	0	0	0
0.65	0.4389	0.403	0.45
0.75	0.7299	0.7146	0.61
0.90	1.209	1.069	1.27

Table 14 : Comparison of relative heights P1-P2 for Nb-0.50%V alloys.

Although the KMIF represents an approximate solution of the AKMC simulations, it is

interesting to compare it with the experimental results given by Carlson et al. [2] and Indrawirawan et al. [3]. The KMIF reproduces the non-variation of the OV pair Debye peak position with respect to the concentrations of oxygen and vanadium. However, it consistently predicts that P2 is 50 K greater than in the experiments by Carlson et al [2]. On the other hand, the KMIF does not reproduce the shift of P2 to lower temperatures as shown by our AKMC simulations for high oxygen content. We explain it by the fact that in the KMIF, the position of the peak is not affected by the oxygen content because the O-O repulsive interactions are neglected. Moreover, this model which is dedicated to dilute systems artificially excludes the contribution of bigger clusters such as O_nV which would affect the concentration of free oxygen atoms.

7. Conclusions

From DFT calculations of the binding and migration energies of dilute configurations in Nb-V-O, we have developed a jump frequency model of oxygen depending on the local concentration of V and O.

We have performed AKMC simulations of IF experiments. The resulting Q^{-1} yields two separate Debye peaks, the first one associated with the lowest T_{max} position being related to the migration of isolated oxygen atoms and the second peak being related to the dissociation of an oxygen from the OV pair. Both the position and the relative heights of the peaks are in good agreement with the experimental results by Carlson et al. [2] and by Indrawirawan et al. [3] as long as the oxygen concentration is above the vanadium concentration. When the oxygen content is below the vanadium content, there is a disagreement between the AKMC and the experimental results by a difference of 50 K.

The AKMC simulations together with the KMIF yield an explanation of the discrepancy between the AKMC simulations and the experimental results by Carlson et al. [2] and by Indrawirawan et al. [3]. The P1 peak in dilute Nb-V-O alloys with a higher oxygen concentration remains because of the O-O repulsive interactions. However, this repulsive interaction affects the oxygen migration barrier and the position of the second peak attributed to the clusters of O_2V while the corresponding experimental peak remains at the same position whatever the oxygen content in the alloy. Therefore, the thermodynamic interaction model including the O-O repulsive interactions yields the correct equilibrium cluster concentration, especially the concentration of isolated oxygen atoms. However, the corresponding diffusion model underestimates the effect of the O-O repulsive interactions on the migration barriers and thus on the position of the second peak for very dilute oxygen compositions. To improve the model, we should perform DFT calculations for several more configurations between a single vanadium atom and several oxygen atoms, with a series of corresponding migration barriers. Then fit O-O interactions at the stable and the saddle point positions and include them in the diffusion model.

8. References

[1] I.S. Golovin, M.S. Blanter, R. Schaller, Snoek Relaxation in Fe-Cr Alloys and Interstitial-Substitutional Interaction, Physica Status Solidi (A). 160 (1997) 49–60. 1doi:10.1002/1521-396X(199703)160:1<49::AID-PSSA49>3.0.CO;2-P.

[2] O.. N.. Carlson, H. Indrawirawan, C.V. Owen, O. Buck, Internal Friction Study of Substitutional-Interstitial Interaction in Niobium-Vanadium Alloys, METALLURGICAL TRANSACTIONS A. 18 (1987) 1415–1420. doi:https://doi.org/10.1007/BF02646655.

[3] H. Indrawirawan, O. Buck, O.N. Carlson, Substitutional-interstitial solute interactions in niobium-vanadium-oxygen alloys, Physica Status Solidi (A). 104 (1987) 443–451. doi:10.1002/pssa.2211040133.

[4] M. Koiwa, Theory of the Snoek Effect in Ternary B.C.C alloys, Philosophical Magazine. 24 (1971) 81–106. doi:http://dx.doi.org/10.1080/14786437108216426.

[5] M. Koiwa, Theory of the Snoek Effect in Ternary B.C.C. Alloys : II. Simplified Treatment, Philosophical Magazine. 24 (1971) 107–122.

[6] G.B. Fedorov, G.V. Fetisov, N.A. Skakun, O.N. Khar'kov, A.G. Arakelov, A.Y. Kissil, Investigation of Oxygen diffusion in Niobium by means of the isotope O18., Fizika Metallov i Metallovedenie. 38 (1974) 361–365.

[7] M.D. Tseng, H. Indrawirawan, O.N. Carlson, Effect of vanadium on oxygen diffusivity in niobium, Journal of the Less-Common Metals. 136 (1987) 31–39. doi:https://doi.org/10.1016/0022-5088(87)90006-3.

[8] M. Weller, G.Y. Li, J.X. Zhang, T.S. Ke, J. Diehl, Accurate determination of activation enthalpies associated with the stress-induced migration of Oxygen or Nitrogen in Tantalum and Niobium., Acta Metallurgical. 29 (1981) 1047–1054.

[9] R.W. Powers, V. Doyle, Diffusion of Interstitial Solutes in the Group V Transition Metals, Journal of Applied Physics. 30 (1959) 514–524.

[10] M. Weller, J. Diehl, G. Hörz, R. Mann, K. Schulze, Internal friction studies of the oxygen Snoek relaxation in group-Va transition metals, Le Journal de Physique Colloques. 46 (1985) 47–50. doi:https://doi.org/10.1051/jphyscol:19851010.

[11] M. Weller, G. Haneczok, J. Diehl, Internal Friction Studies on Oxygen–Oxygen Interaction in Niobium. I. Experimental Results and Application of Previous Interpretations, Physica Status Solidi (B). 172 (1992) 145–159. doi:10.1002/pssb.2221720115.

[12] H. Indrawirawan, L.J.H. Brasche, C.V. Owen, D.K. Rehbein, O.N. Carlson, D.T. Peterson, O. Buck, Internal friction studies of the effect of hydrogen on the oxygen Snoek peaks in V and Nb, Journal of Physics and Chemistry of Solids. 48 (1987) 535–539. doi:https://doi.org/10.1016/0022-3697(87)90048-5.

[13] M.S. Ahmad, Z. Szkopiak, Snoek relaxation peaks in solid solutions of niobium, Journal of Physics and Chemistry of Solids. 31 (1970) 1799–1804.

[14] G. Haneczok, M. Weller, J. Diehl, Internal Friction Studies on Oxygen–Oxygen

Interaction in Niobium. II. Application of Long-Range Interaction Models, Physica Status Solidi (B). 172 (1992) 557–572.

[15] Z.C. Szkopiak, J.T. Smith, The internal friction of Nb-1 at.% substitutional alloys, Journal of Physics D: Applied Physics. 8 (n.d.) 1273–1284.

[16] O. Buck, H. Indrawirawan, O.N. Carlson, Study of the Hydrogen Internal Friction Peak in Nb-10 At. Pct V in the Presence of Oxygen., Metallurgical Transactions A. 20 (1989) 1215–1219.

[17] N.P. Kushnareva, S.E. Snejko, Internal friction and substitutional-interstitial interaction in niobium-based alloys, Journal of Alloys and Compounds,. 211 (1994) 75–79. doi:https://doi.org/10.1016/0925-8388(94)90451-0.

[18] N.P. Kushnareva, S.E. Snejko, P. Yarosh, Internal friction in Nb-V-O alloys, Acta Metallurgica et Materialia. 43 (1995) 4393–4401. doi:https://doi.org/10.1016/0956-7151(95)00120-K.

[19] M.S. Blanter, Influence of Interatomic Interaction on Internal Friction Spectrum in Nb-V-O Alloys (Computer Simulation), Physica Status Solidi (A). 133 (n.d.) 317–323.

[20] L. Zhu, H. Wang, Q.M. Hu, G.J. Ackland, R. Yang, Trapping of interstitial defects: filling the gap between the experimental measurements and DFT calculations, Journal of Physics: Condensed Matter. 25 (2013) 435402.

[21] A.B. Bortz, M.H. Kalos, J.L. Lebowitz, A new algorithm for Monte Carlo simulation of Ising spin systems, Journal of Computational Physics. 17 (1975) 10–18.

[22] R.A. Oriani, The diffusion and trapping of hydrogen in steels, Acta Metallurgica. 18 (1970) 147–157.

[23] R. Li, P. Zhang, X. Li, C. Zhang, J. Zhao, First-principles study of the behavior of O, N and C impurities in vanadium solids, Journal of Nuclear Materials. 435 (2013) 71–76.

[24] B. Heulin, Internal friction study of multiple relaxation phenomena in Nb-O with high oxygen content, Le Journal de Physique Colloques. 46 (1985) 10–51.

[25] N. Sandberg, K.O.E. Henriksson, J. Wallenius, Carbon impurity dissolution and migration in bcc Fe-Cr: First-principles calculations, Physical Review B. 78 (2008) 094110. doi:https://doi.org/10.1103/PhysRevB.78.094110.

[26] Helmut Mehrer, Diffusion in Solids. Fundamentals, Methods, Materials, Diffusion-Controlled Processes, Springer, 2007.

Chapter 4: Effect of C on the kinetics of Cr precipitation in Fe under irradiation

It is well-known that the precipitation of the α' phase negatively affects the mechanical properties of ferritic steels at temperatures below 600 °C (it is at the origin of the famous "475° C embrittlement" [1]). Experiments [2] and previous modelling [3] have shown that under irradiation, the α' precipitation can be accelerated by several orders of magnitude or on the contrary, that it can be suppressed.

The kinetics of precipitation is controlled by the diffusion properties of self-interstitials with dumbbell configurations (under irradiation) and of vacancies (under thermal ageing as well as under irradiation). DFT calculations and previous experiments have shown that there is an attraction between carbon and vacancies [4–6] and, to a lesser extent, between carbon and dumbbells [7]. The matter that we will discuss here is if carbon atoms affect the kinetics of Cr precipitation, and how strong is this effect. The objective of this preliminary study is to analyze this effect by introducing our model of carbon diffusion in Fe-Cr alloys in AKMC simulations of α' precipitation, previously developed at the Service de Recherches en Métallurgie Physique (SRMP) at CEA Saclay [3,8,9]. We will use model 2 as defined in chapter 2, because it minimizes the correlations effects and is computationally more efficient.

The content of this chapter is divided in three parts. First, we will briefly recall the importance of ferritic steels in the nuclear industry and the problem of α-α' phase separation. Second, we will summarize the previous modelling developed at the SRMP for the α' precipitation under irradiation, and show how the mobilities and concentrations of point defects control the balance between the acceleration of precipitation and the ballistic dissolution. Third, we will present the results given by our AKMC with carbon diffusion and observe the effects of C on the precipitation of Cr.

1. Nuclear applications of ferritic steels – the problem with α' precipitation

Initially, ferritic-martensitic steels (9 %Cr – 12 %Cr) were developed as structural materials for fossil-fuel power plants because they tend to have better corrosion/oxidation resistance than the low-Cr ones [10]. They are promising materials for sodium or lead cooled reactors with a high temperature (<600 °C) and compact primary system, as well as for the pressure vessel of high temperature gas-cooled reactors [11]. They are also considered for core structure materials of fusion reactors [12]. Fe-Cr bcc alloys often present a better behavior under irradiation and thus appear to be candidates for fuel cladding and structural materials in high flux zones. These alloys exhibit a good void swelling resistance and a good creep resistance, lower thermal dilation and are cheaper than alloys used previously in the intermediary circuit of sodium cooled fast reactors, which would help design a much more compact circuit. Also, the hardening and embrittlement are negligible when irradiation occurs at temperatures between 400–550 °C but there are concerns regarding their low long-

term creep rupture strength at higher temperatures and the irradiation embrittlement at temperatures below 400 °C.

Figure 69 shows an equilibrium phase diagram of the Fe-Cr system calculated by the Calphad method, taking into account the results of recent DFT calculations [13]. Below approximately 600°C we can see a miscibility gap between two phases: α (Fe-rich) and α' (Cr-rich), with asymmetric solubility limits. The solubility of Cr in Fe is higher than that of Fe in Cr because of a change between the ordering and clustering tendencies in Fe-Cr solid solutions, around 10 at.% of Cr. This change results from magnetic frustrations when mixing ferromagnetic iron with anti-ferromagnetic chromium [14,15].

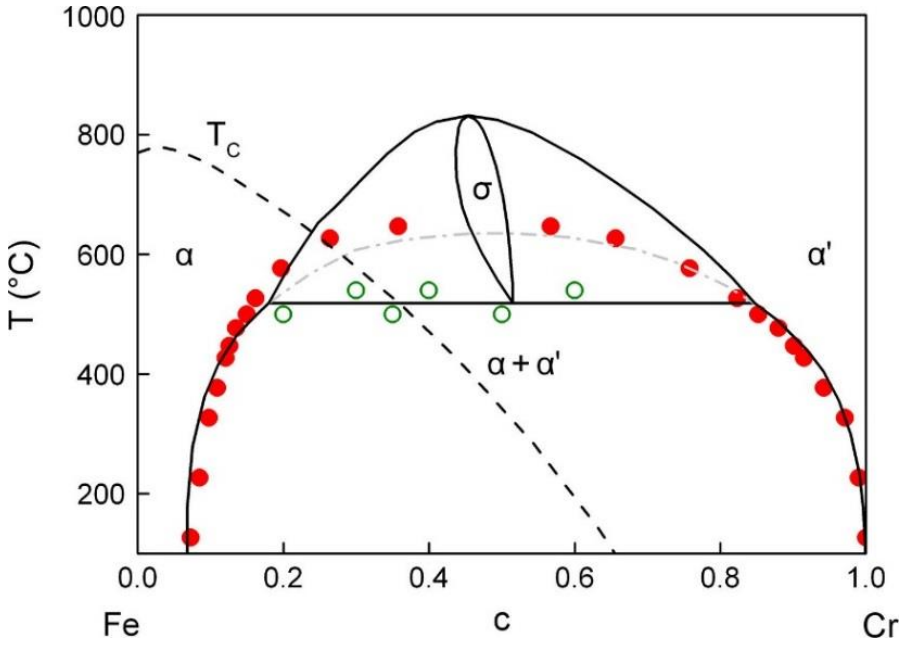

Figure 69: Fe-Cr phase diagram. The black lines show the Calphad phase diagram of Bonny et al. [13], the red dots show the α-α' miscibility gap of the AKMC simulations ([14–16]).

It has been shown that the α' precipitation is very slow at low temperatures (below 500 °C) [3,9,17] but different studies have shown that it was accelerated at moderate dose rates (under electron and neutron irradiation) [18–20]. On the contrary, under ion irradiation at high dose rates, the precipitates formation is prevented and existing precipitates can even be dissolved [2,21,22]. Table 15 shows a summary of experimental results found in the literature.

Irradiation particles	%Cr	T (°C)	Dose rate (dpa/s)	Dose (dpa)	Comments	Ref
Neutrons	2.5 – 12	300	1.3×10^{-7}	0.6	α' phase if %Cr > 9 %Cr	[18]
	3 – 18	290	3.4×10^{-7}	1.82	α' phase if %Cr > 9 %Cr	[19]
Electrons	15	300	3.9×10^{-5}	0.012 – 0.7	α' phase	[20]
Ions	9 – 12	100 – 420	2.2×10^{-4}	0.5	No α' phase	[2]
	15	300	$(3.0-6.0)\times10^{-5}$	0.5 – 1.0	α' phase	[21]
	15 – 19	300	$(1.6-3.5)\times10^{-3}$	70 – 150	Dissolution of α' phase	[22]

Table 15: Experimental studies of the α - α' phase separation in Fe-Cr alloys under different types of irradiation (extracted from ref. [9]).

2. Atomistic modelling of the α' precipitation in binary Fe-Cr alloys: thermal ageing and irradiation

2.1. AKMC Simulations

In this section we will shortly summarize the AKMC simulations previously developed at the Service de Recherches de Métallurgie Physique (SRMP), for the modelling of the Cr precipitation in Fe under thermal ageing or irradiation. These studies have followed a multiscale approach similar to the one presented in our previous chapters. First, they calculated binding and migration energies using DFT calculations. Second, they fitted these quantities using different pair interaction models. Third, they implemented this models in AKMC simulation in order to model diffusion and precipitation phenomena.

Levesque et al. [16] calculated the mixing energies of ordered and special quasi-random structures using DFT calculations. Then, they fitted their database using Fe-Fe, Fe-Cr, Cr-Cr pair interactions which depended on the concentration and on the temperature in order to respectively consider the effects of magnetism, and of the vibrational and magnetic entropies. They later used AKMC simulations in order to model the binary Fe-Cr phase diagram, being in good agreement with the Calphad approach by Bonny et al. [13], as shown in Figure 69.

Martinez et al. [17] computed the vacancy migration barriers in Fe-rich and Cr-rich alloys using DFT calculations. They then developed a pair interaction model [16] in order to include the vacancy diffusion. Last, they used AKMC simulations in order to model the kinetics of Cr precipitation under thermal ageing in Fe-20%Cr at 773K. They found that the evolution

of the radius and the density of the precipitates were in good agreement with the 3D atom probe experimental results by Novy et al. [23].

Senninger et al. [15] further improved the AKMC diffusion model and studied the influence of the ferromagnetic-to-paramagnetic transition on the diffusion coefficients of Fe and Cr. They modelled the decomposition kinetics on highly concentrated Fe-Cr alloys and compared their simulations to small-angle neutron scattering experiments, showing that the magnetic transition could significantly accelerate the transition in alloy with more than 30% of Cr. We must mention that in our present study – which restrict to alloys with less than 20% of Cr – we do not consider this effect.

Senninger et al. [8] introduced the self-interstitial diffusion in the AKMC simulations. The self-interstitials in binary Fe-Cr alloys present a dumbbell configuration in the <110> direction, as shown in Figure 70. They also studied the radiation-induced segregation of Cr at grain boundaries with alloys having a Cr concentration between 1%Cr and 15%Cr, and between 650 K and 950 K. In pure iron, the migration energies of vacancies and dumbbells are respectively $\Delta H_{vac}^{m} = 0.69$ and $\Delta H_{i}^{m} = 0.34\,\text{eV}$. In alloys with concentrations less than 15%Cr, the addition of Cr induced a moderate acceleration of the self-interstitial and vacancy diffusion. They found that sinks (in their case a grain boundary) will be enriched with Cr for temperatures lower than a threshold (~ 600 K). At higher temperatures they found that near the grain boundary there was a depletion of Cr but they found Cr precipitates in the matrix.

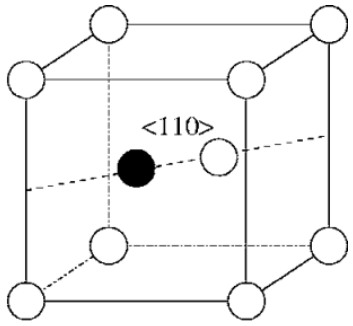

Figure 70: A mixed Fe-Cr dumbbell in Fe (110 orientation). The Cr atom is represented by the black circle. Image extracted from ref. [24].

The two last studies made in SRMP [3,9] used the same vacancy and dumbbell diffusion model as developed by Senninger et al. [8]. They simulated the acceleration of Cr segregation and precipitation under different irradiation conditions on the binary Fe-Cr system. The same diffusion model will be adapted for the present study of Fe-Cr-C alloys, so we recall its main features:

1) For the vacancy and dumbbell formation, simple models of replacement collision sequences (electron irradiations) or displacement cascades (neutron and ion irradiations) are used. The frequency of formation is given by the damage rate (in displacements per atom and per second, or dpa/s). For each Frenkel pair that is created, 10 to 100 atomic exchanges are performed within a sphere of 5 nm.
2) The diffusion of vacancies and dumbbells are modelled using the approaches by Martinez et al. [17] and Senninger et al. [8] respectively. Their pair interaction model follows the same structure as our model 1 (chapter 1), where they consider pair interactions at the saddle point position and at the initial position of the jumping point defect.
3) The vacancy and dumbbell eliminations are given by two different mechanisms. First, when the vacancy and the dumbbell are close within a recombination distance, the vacancy disappears and one atom of the dumbbell takes its place. Second, a point defect can be eliminated at sinks, such as dislocations [25], grain boundaries [3,8] and point defect clusters [9]. The evolution of sink densities is made by using cluster dynamics using the Crescendo code [26].

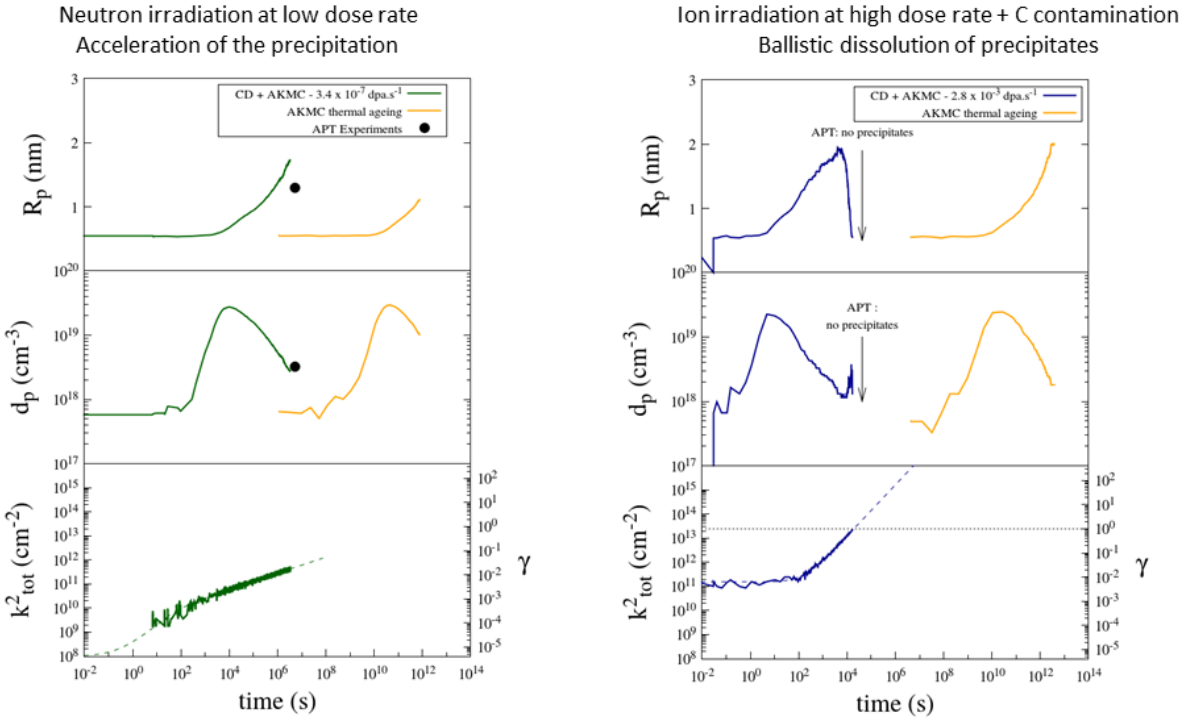

Figure 71: Two different evolutions of Cr precipitation (left) under neutron irradiation and (right) under ion irradiation. Image extracted from [9].

Figure 71 shows two typical examples of the modelling of Cr precipitation under irradiation. For the case of the neutron irradiation at a low dose rate, we can see that there is a strong

acceleration of the precipitation under irradiation. We can observe that the qualitative evolution of the nucleation, growth and coarsening stages are the same as under thermal annealing but accelerated by several orders of magnitude. On the other hand, in the case of ion irradiation, we can observe the nucleation and growth stages taking place, again with a very strong acceleration by comparison with thermal ageing, but at 10^4 seconds (~ 2.8 hours), the precipitates are dissolved in the matrix.

2.2. Diffusion of substitutional solute atoms under irradiation

To understand these behaviors, it is important to consider the diffusion coefficients of substitutional solutes (Fe and Cr) under irradiation. They are proportional to the concentration of point defects (i.e. vacancies and self-interstitials). The thermally activated self-diffusion coefficient of a substitutional solute atom s is given by [27]:

$$D_s = f_v c_v D_v + f_i c_i D_i \tag{4.1}$$

where $f_{vac,i}$ corresponds to the correlation factors, $c_{vac,i}$ are the atomic fractions and $D_{vac,i}$ are the diffusion coefficients of vacancies vac and dumbbells i respectively. The time-evolution of c_{vac} and c_i are given by:

$$\frac{dc_{vac}}{dt} = G - Rc_{vac}c_i - k^2 D_{vac}\left(c_{vac} - c_{vac}^{eq}\right) \tag{4.2}$$

$$\frac{dc_i}{dt} = G - Rc_{vac}c_i - k^2 D_i\left(c_i - c_i^{eq}\right), \tag{4.3}$$

where G is the rate of formation of Frenkel pairs (in dpa/s), R is the rate of dumbbell-vacancy recombination, k^2 is the sink strength (proportional to the sink density), and D_{vac} and D_i are the diffusion coefficients of vacancies and dumbbells respectively. In the steady state, under thermal ageing without irradiation (i. e. $G = 0$):

$$c_{vac} = c_{vac}^{eq} \tag{4.4}$$

and c_i^{eq} is negligible due to the high dumbbell formation energies. Under irradiation, $G \neq 0$ and if the concentration of dumbbells and vacancies are much higher than their concentrations at thermal equilibrium (i. e. $c_{vac} \gg c_{vac}^{eq}$ and $c_i = c_i^{eq}$), it can be shown that:

$$c_{vac}D_{vac} = c_i D_i . \tag{4.5}$$

We can rewrite Eq. (4.1) using Eq. (4.5) as:

$$D_s = 2c_{vac}D_{vac} . \tag{4.6}$$

The steady-state solutions of Eqs. (4.2) and (4.3) in the steady state are:

$$c_i = -\frac{k^2 D_{vac}}{2R} + \sqrt{\left(\frac{k^2 D_{vac}}{2R}\right)^2 + \frac{GD_{vac}}{RD_i}} \tag{4.7}$$

$$c_v = -\frac{k^2 D_i}{2R} + \sqrt{\left(\frac{k^2 D_i}{2R}\right)^2 + \frac{GD_i}{RD_{vac}}}\,. \tag{4.8}$$

When the point defect elimination at sinks is dominant, the concentrations of vacancies and dumbbells are:

$$c_{vac} = \frac{G}{k^2 D_{vac}} \tag{4.9}$$

$$c_i = \frac{G}{k^2 D_i}\,. \tag{4.10}$$

In the case where recombination is dominant, the point defect concentrations can be expressed as:

$$c_{vac} = \sqrt{\frac{GD_i}{RD_{vac}}} \tag{4.11}$$

$$c_i = \sqrt{\frac{GD_v}{RD_i}} \tag{4.12}$$

On the other hand, the ballistic diffusion coefficient D_{bal}, corresponding to the forced mixing in replacement sequences and displacement cascades is defined as:

$$D_{bal} = a^2 n_{rep} G\,, \tag{4.13}$$

where n_{rep} is the number of replacements and a is the lattice parameter. The competition between the acceleration of diffusion and the ballistic mixing can be characterized by the irradiation intensity γ:

$$\gamma = \frac{D_{bal}}{D_s}\,. \tag{4.14}$$

The ballistic mixing is important when $\gamma > 1$. In the simple case where the point defect elimination is dominant at sinks (Eq. (4.9)) and under irradiation (Eq. (4.6)), the irradiation intensity can be expressed as:

$$\gamma = \frac{a^2 k^2 n_{rep}}{2}\,. \tag{4.15}$$

Eq. (4.15) shows that the irradiation intensity only depends on the sink strength. In other words, the dissolution of the Cr precipitates occurs when the density of sinks becomes important, as it can be observed on Figure 71, in the case of ion irradiation.

3. Effect of C on the α' precipitation under irradiation

3.1. Introduction

In previous simulations, a possible effect of carbon was only indirectly taken into account [9]: the idea was that carbon atoms can increase the sink density and sink strength and,

according to Eq. (4.15), favor the ballistic mixing and the dissolution of precipitates. In this study, we are going to analyze a more direct effect that can influence the precipitation of the α' phase at a given sink density: the interactions of C atoms with vacancies and dumbbells.

Different DFT calculations have shown that carbon atoms have a strong attractive binding energy with vacancies, close to 0.4 eV (Jourdan et al. [5] and by Barouh et al. [4], Liu et al. [6]). A more moderate attraction with dumbbells is suggested by experiments (a value of 0.11eV was obtained by Takaki et al. [7] using resistivity recovery). These attractive interactions would increase the average migration enthalpies of vacancies $\left(\Delta H_{vac}^{m}\right)$ and dumbbells $\left(\Delta H_{i}^{m}\right)$ and consequently decreasing D_{vac} and D_i. By slowing down the vacancies and self-interstitials, an addition of carbon could affect the diffusion of substitutional solutes (Fe and Cr), and limit the acceleration of the α' precipitation observed under irradiation. But it is not always the case since a decrease in D_{vac} and D_i maybe compensated by an increase in c_{vac} and c_i, as shown by equations (4.5) to (4.12).

3.2. AKMC simulations

To study the effect of point defect-carbon interactions on Cr precipitation under irradiation, we added the direct interstitial diffusion of C atoms in the AKMC simulations of binary Fe-Cr alloys [3,9]. The carbon migration barriers were reproduced by using model 2 as described in chapter 2. This choice is due to two reasons. First, it takes less computational time to get results. Second, it (slightly) better reproduces the carbon migration barriers in Fe-rich alloys compared to model 1. All the simulations are performed with a typical and constant sink strength of 10^{11} cm^{-2} [8]. Sinks are introduced as a random distribution of point-like sites. We decided to use a carbon-dumbbell binding energy of 0.10 eV and two different carbon-vacancy binding energies: 0.6 eV and 0.8 eV, up to 1 nn (as a first approximation, these binding energies are considered as independent of the local Cr concentration). As we will see in the following pages, having a large amount of carbon atoms makes the simulations very time consuming. We decided to put a small carbon concentration (0.0069%C and 0.0143%C) and focus our analysis by changing the binding energy between the direct interstitials and the other point defects and see what would be the evolution of the Cr precipitation. We added the C atoms in a Fe-18%Cr alloy at temperature of 563 K and irradiated at a dose rate of $10^{-3}\,\mathrm{dpa/s}$.

Figure 72 and Figure 73 show the evolution of the Cr precipitates during thermal ageing, under irradiation without C atoms and under irradiation with C atoms. In order to analyze the segregation and precipitation of Cr we will study the radius of precipitates R_p, their density d_p, the vacancy concentration c_{vac} and the dumbbell concentration c_i.

In the case of thermal ageing, there is no formation of dumbbells in the simulation box and the concentration of vacancies if at a thermal equilibrium ($\sim 10^{-17}$). From these curves we can see the nucleation, growth and coarsening stages of α' precipitation, which occur at very

long times during this scenario. For example, the nucleation stage starts at $\sim 10^{7}$ seconds (115 days) and the d_p reaches a maximum of $\sim 7\times10^{19}$ cm^{-3} at $\sim 10^{10}$ seconds (317 years). Then the coarsening stage starts and the precipitates reach a radius of 3 nm at the end of the simulation (approximately $\sim 6.3\times10^{4}$ years).

Under irradiation and without C atoms, we observe an acceleration of the precipitation by several orders of magnitude. We see an increase of c_{vac} (10^{-8}) and the presence of dumbbells with a concentration of (10^{-10}). The concentration of vacancies is much higher than the self-interstitial concentration due to the more rapid diffusion and elimination at sinks of the self-interstitials. In this case, the nucleation stage starts very rapidly and the density of precipitates reaches a maximum at 1 second. Moreover, the radius of the precipitates is 2 nm at 100 seconds (1.6 hours). This acceleration is due to the supersaturation of point defects (both dumbbells and vacancies).

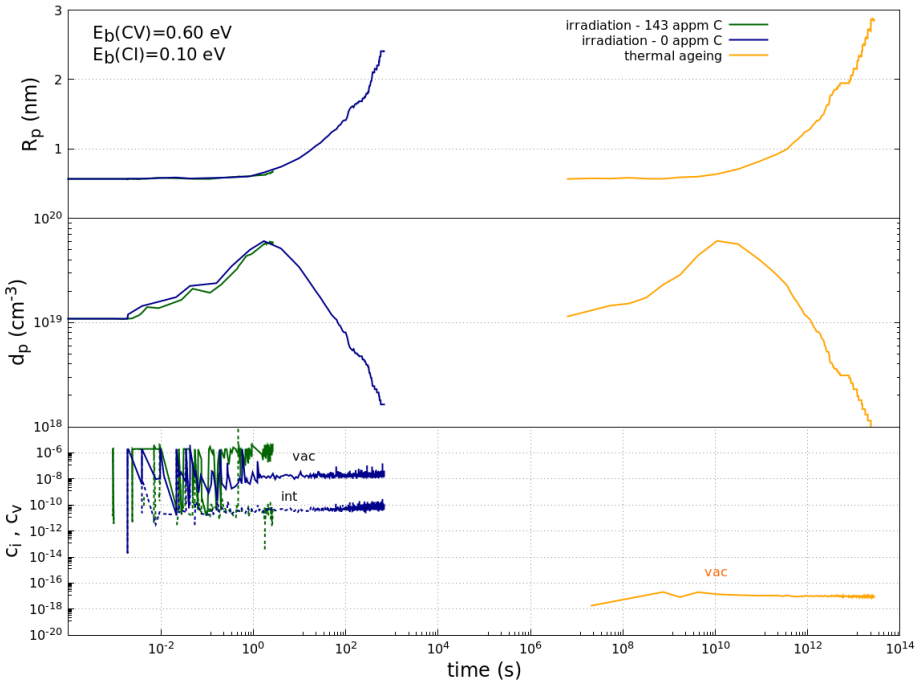

Figure 72: Evolution of R_p, d_p, c_{vac} and c_i over time and during thermal ageing, under irradiation and under irradiation with C atoms. The carbon concentration is 0.0143%C. The carbon-vacancy and carbon-dumbbell binding energies are 0.60 eV and 0.10 eV respectively.

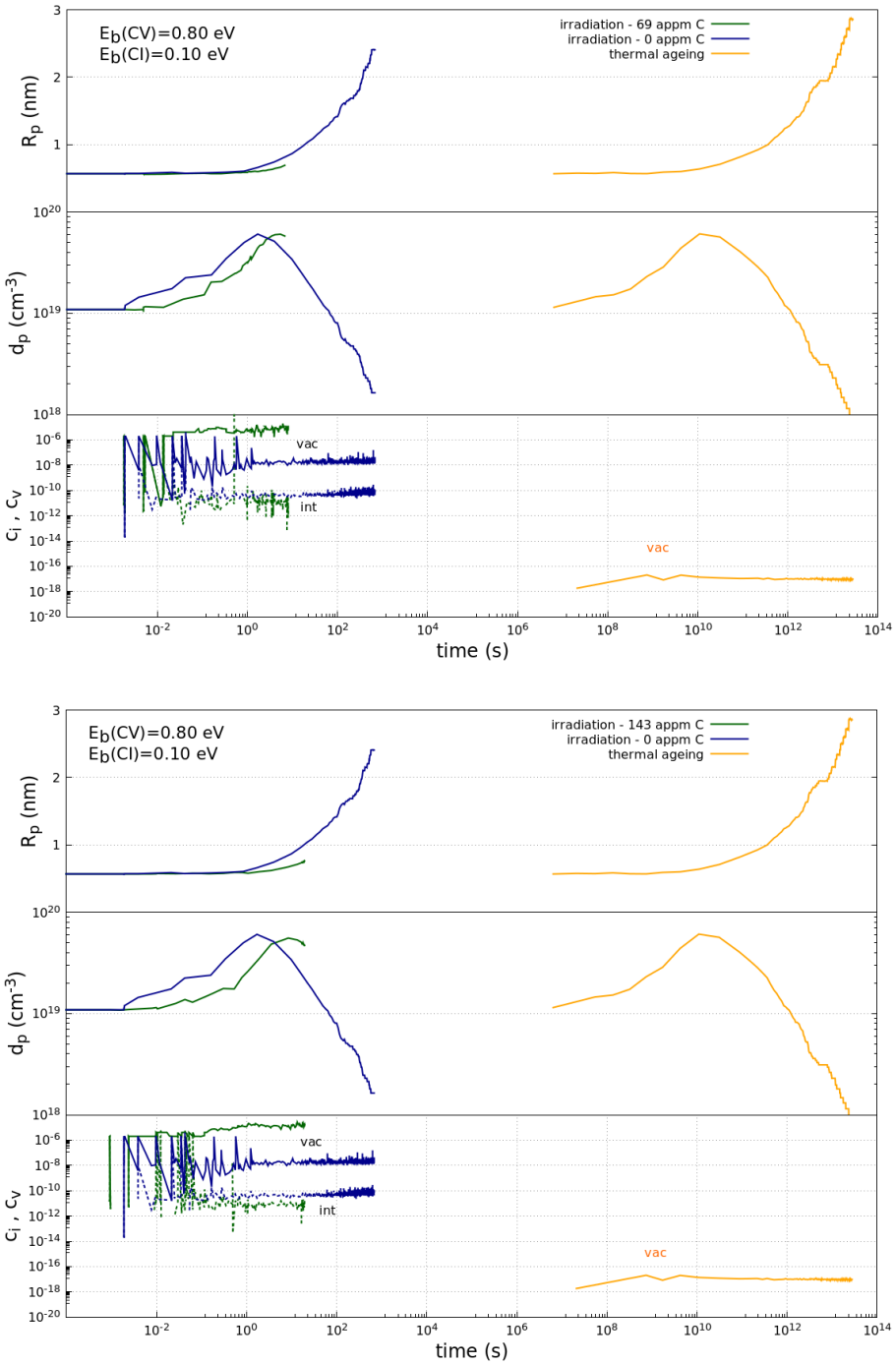

Figure 73: Evolution of R_p, d_p, c_{vac} and c_i over time and during thermal ageing, under irradiation and under irradiation with C atoms. The carbon concentrations are (top) 0.0069%C and (bottom) 0.0143%C. The carbon-vacancy and carbon-dumbbell binding energies are 0.80 eV and 0.10 eV respectively.

Figure 72 shows a scenario in which the C atoms do not affect the precipitation of Cr. In this

particular system we have a carbon concentration of 0.0143%C and constant carbon-vacancy and carbon-dumbbell binding energies of 0.60 eV and 0.10 eV respectively. We can see that the vacancy concentration c_{vac} increases from 10^{-8} to 10^{-6} with the addition of C (due to a strong slowing down of vacancies), but that the overall effect on the density and radius of Cr precipitates is negligible. This observation suggests a full compensation in Eq. (4.6) between the slowing down of point defect and their increase in concentration. In other words, we have a higher amount of vacancies that diffuse more slowly than without carbon, and it has no net effect on the diffusion of the substitutional solutes.

Figure 73 shows an example where the addition of carbon atoms has a significant effect on the Cr precipitation. In these AKMC simulations, carbon-vacancy and carbon-dumbbell binding energies are equal to 0.80 eV and 0.10 eV respectively and the C content is 0.0069%C. The higher C-Vac binding energy and carbon concentration result in a stronger slowing down of the vacancies than in Figure 72, and to a higher vacancy concentration (almost 10^{-5}). The dumbbell concentration is decreased (from 10^{-10} up to 10^{-11}) because recombination increases with the vacancy concentration. By comparison with thermal ageing, the Cr precipitation is still increased by orders of magnitude, but it is significantly slower than without carbon (approximately by a factor 3). The increase of the point defect concentrations is not completely compensated by their retardation, resulting in a decrease of the diffusion of substitutional solute atoms Fe and Cr. It is worth noticing that due to the high carbon concentration, i.e. to the high number of possible C jumps, the simulations of Figure 73 are much more time consuming that those with no carbon, or lower C concentrations. The kinetics of Cr precipitation is limited to the nucleation and growth regimes and the coarsening remains out of reach.

3.3. Analysis

The above results can be understood by considering the effect of C atoms on the diffusion of vacancies, self-interstitials and Cr atoms under irradiation. As we have seen in section 2.2, when the sinks are the dominant mechanisms of point defect elimination, the vacancy concentration is:

$$c_{vac} = \frac{G}{k^2 D_{vac}} \tag{4.16}$$

Combining Eq. (4.16) with Eq. (4.6), we express the Cr diffusion coefficient D_{Cr} as:

$$D_{Cr} = \frac{2G}{k^2} \tag{4.17}$$

We can observe from Eq. (4.17) that D_{Cr} only depends on the rate of formation of Frenkel pairs and on the sink strength and it is independent of the vacancy migration barrier ΔH_{vac}^{m}. In other words, C atoms indeed slow down the vacancy diffusion, but it is compensated by a higher oversaturation of vacancies. Under these circumstances the C atoms do not have an

effect on D_{Cr} and on the Cr precipitation (Figure 72).

On the other hand, when the carbon concentration is high enough, or the carbon-vacancy binding energy is very attractive, the concentration of vacancies becomes sufficient to produce a significant contribution of the recombination. If the recombination is dominant the steady-state vacancy concentration is:

$$c_{vac} = \sqrt{\frac{GD_i}{RD_{vac}}}\,. \tag{4.18}$$

In that case, D_{Cr} depends on the vacancy migration barrier ΔH^m_{vac}, according:

$$D_{Cr} = 2\sqrt{G}\exp\left(\frac{-\Delta H^m_{vac}}{2k_BT}\right). \tag{4.19}$$

Eq. (4.19) shows that an increase of the vacancy migration barrier produces a decrease D_{Cr} and reduces the acceleration on the Cr precipitation. The simulations of Figure 73 correspond indeed to an intermediate situation (those corresponding to Eqs. (4.7) and (4.8)), where both recombination and elimination at sinks are significant.

4. Conclusions and perspectives

In this chapter we have presented a short study of the possible effects of C atoms on the Cr precipitation under irradiation. Under such conditions, the vacancy and dumbbell concentrations are much higher than in thermal equilibrium, and in the steady-state D_{Cr} only depends on the vacancy concentration c_{vac} and diffusion coefficient D_{vac}.

A systematic study remains to be done, but some tentative conclusions can be drawn from our simulations. Two different situations have been observed. When the elimination of vacancies and self-interstitials is dominated by sinks, their slowing down by binding with C atoms is fully compensated by an increase in concentration. The carbon concentration has no effect of the Cr diffusion and precipitation. When the contribution of recombination is significant, the compensation is partial, and C carbon can slow down the Cr precipitation (or, more precisely, reduce its acceleration by irradiation). The conditions that favors the second situation are those which tend to increase the recombination, i.e. a low mobility and high concentration of vacancies and self-interstitials: low temperatures, high dose rates, high concentrations of carbon. One can also anticipate that in such conditions, the ballistic dissolution of Cr-rich precipitates will be favored. For instance, if we have used a C-Vac binding energy between 0.4 eV up to 0.6 eV, as predicted by several authors [4–6] and a carbon concentration lower than 0.0143%C, we should have not seen an effect on the accelerated Cr precipitation under irradiation. On the other hand, if we have used a C-Vac binding energy as low as 0.4 eV, it is very likely that in order to have a retardation of the accelerated Cr precipitation, we would have needed to increase the C concentration by at

least one order of magnitude.

In this chapter we have used strong assumptions such as constant carbon-vacancy and carbon-dumbbell binding energies in Fe-Cr alloys, and a constant sink strength. In order to provide a better description of the influence of carbon atoms on the Cr precipitation, we must give a more realistic description of the binding energies and migration barriers of vacancies and self-interstitials in the vicinity of carbon atoms. The study of ballistic dissolution will require simulations with higher sink strengths, if possible, by taking explicitly into account the effect of carbon atoms on the sink strength density.

Finally, we have mentioned that AKMC simulations become more time consuming with the addition of carbon atoms, because a considerable number of jumps and jump frequencies have to be considered. A possible way to overcome this problem is using parallelization techniques [28,29] which have been recently applied to our model of C diffusion in Fe-Cr by Enrique Martinez (Los Alamos National Laboratory).

5. References

[1] R.M. Fisher, E.J. Dulis, K.G. Carroll, Identification of the precipitate accompanying 885 F embrittlement in chromium steels., Transactions of the Metallurgical Society of AIME. 197 (1953) 690–695.

[2] C. Pareige, V. Kuksenko, P. Pareige, Behaviour of P, Si, Ni impurities and Cr in self ion irradiated Fe–Cr alloys – Comparison to neutron irradiation, Journal of Nuclear Materials. 456 (2015) 471–476.

[3] F. Soisson, T. Jourdan, Radiation-accelerated precipitation in Fe–Cr alloys, Acta Materialia. 103 (2016) 870–881. doi:https://doi.org/10.1016/j.actamat.2015.11.001.

[4] C. Barouh, T. Schuler, C.C. Fu, M. Nastar, Interaction between vacancies and interstitial solutes (C, N, and O) in α-Fe: From electronic structure to thermodynamics, Physical Review B. 90 (2014) 054112. doi:10.1103/PhysRevB.90.054112.

[5] T. Jourdan, C.C. Fu, L. Joly, J.L. Bocquet, M.J. Caturla, F. Willaime, Direct simulation of resistivity recovery experiments in carbon-doped α-iron, Physica Scripta. 2011 (2011) 014049.

[6] P. Liu, W. Xing, X. Cheng, D. Li, Y. Li, X.Q. Chen, Effects of dilute substitutional solutes on interstitial carbon in α-Fe: Interactions and associated carbon diffusion from first-principles calculations, Physical Review B. 90 (2014) 024103.

[7] S. Takaki, J. Fuss, H. Kuglers, U. Dedek, H. Schultz, The resistivity recovery of high purity and carbon doped iron following low temperature electron irradiation, Radiation Effects. 79 (1983) 87–122. doi:https://doi.org/10.1080/00337578308207398.

[8] O. Senninger, F. Soisson, E. Martinez, M. Nastar, C.C. Fu, Y. Bréchet, Modeling radiation induced segregation in iron–chromium alloys, Acta Materialia. 103 (2016) 1–11. doi:https://doi.org/10.1016/j.actamat.2015.09.058.

[9] F. Soisson, E. Meslin, O. Tissot, Atomistic modeling of α' precipitation in Fe-Cr alloys under charged particles and neutron irradiations: Effects of ballistic mixing and sink densities, Journal of Nuclear Materials. 508 (2018) 583–594.

[10] P. Yvon, F. Carré, Structural materials challenges for advanced reactor systems, Journal of Nuclear Materials. 385 (2009) 217–222.

[11] K.L. Murty, I. Charit, Structural materials for Gen-IV nuclear reactors: Challenges and opportunities, Journal of Nuclear Materials. 383 (2008) 189–195.

[12] S.J. Zinkle, J.T. Busby, Structural materials for fission & fusion energy, Materials Today. 12 (2009) 12–19.

[13] G. Bonny, D. Terentyev, L. Malerba, New contribution to the thermodynamics of Fe-Cr alloys as base for ferritic steels., Journal of Phase Equilibria and Diffusion. 31 (2010) 439–444.

[14] O. Senninger, Ségrégation et précipitation dans les alliages Fer-Chrome hors et sous irradiation, Doctorat, Université de Grenoble, 2014.

[15] O. Senninger, E. Martinez, F. Soisson, M. Nastar, Y. Bréchet, Atomistic simulations of the decomposition kinetics in Fe–Cr alloys: Influence of magnetism, Acta

Materialia. 73 (2014) 97–106. doi:https://doi.org/10.1016/j.actamat.2014.03.019.

[16] M. Levesque, E. Martinez, C.C. Fu, M. Nastar, F. Soisson, Simple concentration-dependent pair interaction model for large-scale simulations of Fe-Cr alloys, Physical Review B. 84 (2011) 184205. doi:https://doi.org/10.1103/PhysRevB.84.184205.

[17] E. Martinez, O. Senninger, C.C. Fu, F. Soisson, Decomposition kinetics of Fe-Cr solid solutions during thermal aging, Physical Review B. 86 (2012) 224109. doi:10.1103/PhysRevB.86.224109.

[18] V. Kuksenko, C. Pareige, P. Pareige, Cr precipitation in neutron irradiated industrial purity Fe–Cr model alloys, Journal of Nuclear Materials. 432 (2013) 160–165.

[19] M. Bachav, G.R. Odette, E.A. Marquis, Alpha' precipitation in neutron-irradiated Fe–Cr alloys, Scripta Materialia. 74 (2014) 48–51.

[20] O. Tissot, C. Pareige, E. Meslin, B. Decamps, J. Henry, Kinetics of α′ precipitation in an electron-irradiated Fe15Cr alloy, Scripta Materialia. 122 (2016) 31–35.

[21] O. Tissot, C. Pareige, E. Meslin, B. Decamps, J. Henry, Influence of injected interstitials on α′ precipitation in Fe–Cr alloys under self-ion irradiation, Materials Research Letters. 5 (2017) 117–123.

[22] O. Tissot, Effets de l'irradiation sur la démixtion du Cr dans les alliages FeCr, Doctorat, Université de Rouen, 2016.

[23] S. Novy, P. Pareige, C. Pareige, Atomic scale analysis and phase separation understanding in a thermally aged Fe–20 at.%Cr alloy, Journal of Nuclear Materials. 384 (2009) 96–102.

[24] P. Olsson, C. Domain, J. Wallenius, Ab initio study of Cr interactions with point defects in bcc Fe, Physical Review B. 75 (2007) 014110.

[25] L. Malerba, G. Bonny, D. Terentyev, E.E. Zhurkin, M. Hou, K. Vörtler, K. Nordlund, Microchemical effects in irradiated Fe–Cr alloys as revealed by atomistic simulation, Journal of Nuclear Materials. 442 (2013) 489–498.

[26] T. Jourdan, G. Bencteux, G. Adjanor, Efficient simulation of kinetics of radiation induced defects: A cluster dynamics approach, Journal of Nuclear Materials. 444 (2014) 298–313.

[27] R. Sizmann, The effect of radiation upon diffusion in metals, Journal of Nuclear Materials. 69 (1978) 386–412.

[28] E. Martinez, J. Marian, M.H. Kalos, J.M. Perlado, Synchronous parallel kinetic Monte Carlo for continuum diffusion-reaction systems, Journal of Computational Physics. 227 (2008) 3804–3823.

[29] E. Martinez, P.R. Monasterio, J. Marian, Billion-atom synchronous parallel kinetic Monte Carlo simulations of critical 3D Ising systems, Journal of Computational Physics. 230 (2011) 1359–1369.

Conclusions and Perspectives

The main objective of this study was to model the diffusion of interstitial atoms in bcc alloys. We used a multiscale approach combining DFT calculations, pair interaction models and AKMC simulations in order to model tracer diffusion and internal friction experiments. We also showed the first direct atomistic modeling of the Snoek peak in concentrated alloys.

The present pair interaction models are very simple and cannot always exactly reproduce all the binding energies and migration barriers calculated by DFT calculations, especially in concentrated alloys. However, it is possible to reproduce key properties: in Fe-Cr-C alloys, a C-Cr repulsion in Fe-rich configurations, a C-Fe attraction in Cr-rich configurations, and a global increase of the C migration barriers with the Cr concentration. In Nb-V-O dilute alloys, the strong O-V attraction and the O-O repulsion. Thanks to this, we can better understand the results given by the experimental literature.

In dilute Fe-Cr alloys, the AKMC simulations are in good agreement with the majority of the experimental studies, which show that the addition of a few atomic percent of Cr barely affects the average migration enthalpy. This is due mainly to the repulsion between C and Cr atoms. A few experimental IF studies have shown a very strong increase of the carbon average migration enthalpy within these ranges of composition. We conclude that this increase is most likely due to an interaction between C atoms and other defects, such as dislocations and vacancies and wrongly interpreted as a Snoek effect. In Cr-rich alloys, we predict an unexpected result: our simulations of TD yield a higher average migration enthalpy than our simulations of IF. We conclude that it is due to the trapping of C in Fe-rich environments, which has a stronger effect on the long-range diffusion (TD) than in the short-range diffusion (IF). This difference results from the attraction between C and Fe atoms, revealed by DFT calculations, a feature which should remain in more sophisticated models. An experimental validation is still required and, we believe, would worth a try. The same tendency should be observed in other systems with similar properties and could provide an experimental way to study trapping effects.

In dilute Nb-V-O alloys, a strong O-V attraction produces the formation of several Snoek peaks that are related to different O-V complexes. The height of each Snoek peak is related to the concentration of each cluster in the alloy. A close interpretation of the IF response thanks to the Koiwa model coupled with the AKMC simulations shows non-dilute effects such as the formation of VO-O complexes at very low oxygen concentrations, despite the strong oxygen-oxygen repulsion revealed by DFT calculations. Moreover, the Koiwa model shows that the IF response in infinitely dilute alloys can be written as a sum of Debye peaks and that each peak is associated with a particular cluster. But it is not possible to directly relate the temperatures of the Snoek peaks with elementary jump frequencies. The Koiwa model could be improved by considering the effect of bigger complexes on the IF response in order to study the Snoek peak in more concentrated alloys.

We have finally performed a preliminary study on the effect of C on the kinetics of the Fe-Cr phase separation under irradiation. The mobility of vacancies and self-interstitials is reduced because of a strong binding energy between them and carbon atoms. At a constant sink density, the decrease in the mobility of Fe and Cr atoms is less pronounced because the slowing down of vacancies and self-interstitials is compensated by an increase in their concentrations. In the final analysis, the effect of carbon on the precipitation kinetics mainly depends on the dominant mechanisms for point defect elimination. If there is an important recombination, the acceleration of the precipitation due to the irradiation can be significantly reduced by carbon impurities. If annihilation at sinks is dominant, the effect is negligible. Our preliminary results must be improved by using better parameters for the carbon-vacancies and carbon-dumbbells binding energies in alloys and a more realistic description of the effect of C on the sink density.

In conclusion, our results are in good agreement with the majority of the experimental data and provides a validation of our multiscale modelling. It would be interesting to improve our model by considering a segregation enthalpy which is dependent on the local chemical environment by computing the elastic dipole of interstitials close to different substitutional solute clusters via DFT calculations. This improved multiscale modelling could be applied to other physical phenomena, such as creep, elastic after-effect and stress relaxation experiments in metals and alloys. However, some technical problems remain to be solved: the addition of interstitials makes our AKMC simulations very time consuming due to a large amount of possible interstitials jumps and due to strong trapping and correlations. We intend to solve this issue by parallelizing our AKMC code. More complex effective interaction models (using for example cluster expansion methods) could then be used to give more realistic energetic landscapes.

Résumé du manuscript

Les aciers ferritiques, basés sur le système binaire Fe-Cr cubique centré (cc), ont une large gamme d'applications en raison de leur résistance à la corrosion et de leurs propriétés mécaniques. Dans l'industrie nucléaire, ils sont considérés comme de possibles matériaux de structure des futurs réacteurs de fusion et de fission (par exemple pour les gaines de combustible et les structures dans les zones soumises à des flux élevés de neutrons), en raison de leur bonne résistance à certains effets d'irradiation, en particulier au gonflement. Mais l'irradiation pourrait avoir d'autres effets, tels que l'accélération de la précipitation d'une phase riche en Cr (α'), entrainant une dégradation des propriétés mécaniques. Des études expérimentales et théoriques antérieures ont montré que de tels processus hors d'équilibre dépendent fortement des propriétés des défauts ponctuels, en particulier des lacunes et des auto-interstitiels.

D'autre part, il est courant de trouver des impuretés interstitielles dans les alliages ferritiques, telles que le carbone, l'oxygène et l'azote. Du fait de leur taille inférieure à celle des solutés substitutionnels, ces éléments occupent les sites octaédriques du réseau cc et diffusent par un mécanisme interstitiel direct. Il a été démontré que les impuretés interstitielles interagissent fortement avec les lacunes et les auto-interstitiels, ce qui pourrait affecter la cinétique de précipitation sous irradiation. Cette étude se concentre sur ces questions. La première étape consiste à comprendre les propriétés de diffusion des impuretés interstitielles à différentes échelles, tant dans les alliages dilués que concentrés.

Un aspect central de la diffusion à l'état solide consiste à établir le lien entre les mécanismes de diffusion atomique, les fréquences de saut des défauts ponctuels et les coefficients de transport expérimentaux. La plupart des études expérimentales dans la littérature portent sur les coefficients de diffusion de traceurs (TD) et d'interdiffusion. Celles-ci sont effectuées à des températures élevées et fournissent une description de la diffusion à longue distance (quelques microns). Une autre technique expérimentale peut être utilisée pour analyser le mécanisme de diffusion interstitiel direct: le frottement interne (IF), qui fournit des informations sur la diffusion à courte portée (quelques sites atomiques) et peut être réalisée à des températures plus basses. Les modèles théoriques qui analysent la diffusion par le mécanisme interstitiel direct sont beaucoup moins développés que ceux consacrés à la diffusion des solutés substitutionnels par le mécanisme d'échange lacunaire. La relation entre les fréquences de sauts élémentaires et le pic de friction interne a été étudiée de manière approfondie dans les alliages dilués, mais elle n'est pas encore bien connue pour les alliages concentrés.

Nous résumons ici notre mémoire de recherche rédigé en anglais et structuré autour de quatre chapitres, répondant à trois objectifs principaux.

Dans le chapitre 1, nous analysons la relation entre les coefficients de diffusion de traceur, le

facteur de qualité de la friction interne, et les fréquences de saut élémentaires, via une enthalpie de migration moyenne dans les alliages. Nous présentons également notre approche multi-échelles, développée pour modéliser la diffusion interstitielle directe - en particulier le frottement interne - dans les alliages concentrés, et nous examinons les modèles précédents trouvés dans la littérature. Cette modélisation consiste en trois étapes distinctes. Tout d'abord, nous obtenons des informations précises sur les interactions entre les atomes interstitiels et les solutés substitutionnels (énergies de liaison et barrières de migration) à l'aide de calculs basés sur la théorie de la fonctionnelle de la densité (DFT). Deuxièmement, nous développons des modèles d'interaction de paires, ajustés sur ces données, qui permettent de calculer rapidement les barrières de migration dans tout environnement chimique local. Troisièmement, nous implémentons ces modèles dans nos codes AKMC (Atomistic Kinetic Monte Carlo) afin de modéliser des expériences TD et IF.

Au chapitre 2, nous modélisons la diffusion du carbone dans des solutions solides aléatoires de Fe-Cr. Il existe des données expérimentales TD et IF dans ce système ternaire pour les alliages dilués et concentrés, qui présentent des contradictions surprenantes. Comme le montre la Figure 74, la plupart des données expérimentales [1–8] montrent que l'enthalpie de migration moyenne du carbone reste relativement constante avec des ajouts de Cr limités à quelques pourcents. D'autres [3,9–11] indiquent au contraire qu'elle augmente très fortement. Nos simulations AKMC sont en accord le premier type d'expériences, et nous aide à comprendre les différentes observations. Dans les alliages riches en Fe, les interactions C-Cr sont répulsives, ce qui implique un faible effet du chrome sur la migration du carbone. La friction interne étant une technique très sensible, l'augmentation rapide de l'enthalpie de migration constatée par quelques auteurs pourrait être due à une interaction entre les atomes de carbone et d'autres défauts, tels que des lacunes et des dislocations. Dans les alliages riches en Cr, un comportement original est prédit: les enthalpies de migration moyennes mesurées par les expériences TD et IF sont différentes - comme le montre la Figure 75 - en raison d'une forte attraction C-Fe, qui produit de forts effets de piégeage et de corrélation. Cette différence pourrait être vérifiée expérimentalement.

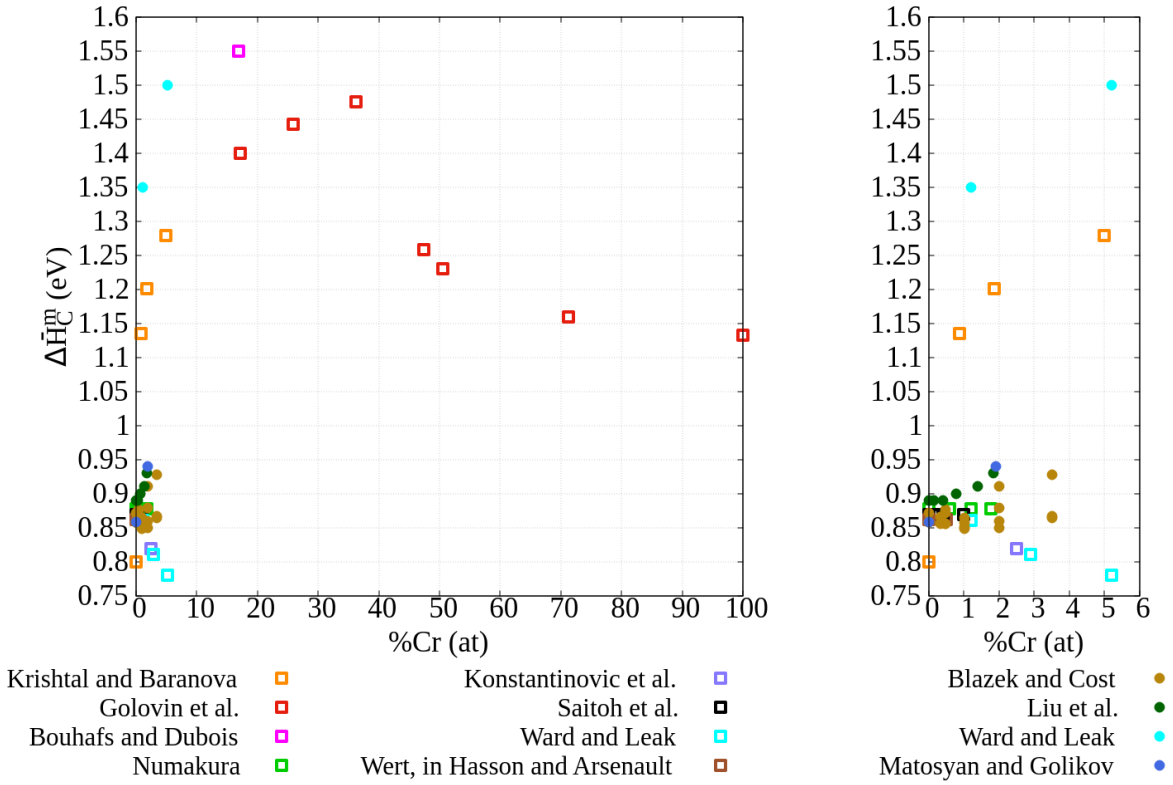

Figure 74: Evolution de l'enthalpie de migration moyenne du carbone avec la concentration en Cr selon les résultats expérimentaux IF et TD. Les valeurs ont été extraites de [1–11].

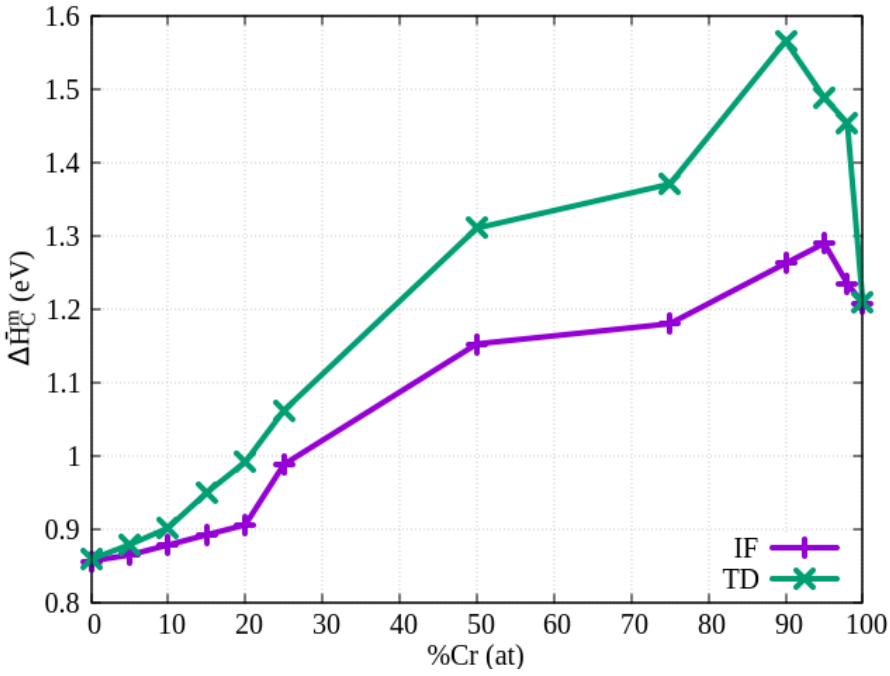

Figure 75: Evolution de l'enthalpie de migration moyenne avec la concentration en Cr, selon les simulations AKMC de diffusion du traceur et de frottement interne.

Au chapitre 3, nous testons la même méthode sur un cas bien différent: les alliages Nb-V-O dilués. Il s'agit d'un système bien connu du point de vue expérimental, dans lequel la forte attraction oxygène-vanadium joue un rôle clé, comme le montre les spectres obtenus par Carlson et al. [12]. La Figure 76 présente des spectres IF d'alliages Nb-0,5%V obtenus avec différentes concentrations en oxygène. On peut voir deux régimes distincts. Dans le premier, lorsque la concentration en oxygène est inférieure à la teneur en vanadium, on observe un seul pic («P2») à une température voisine de 500 K. L'amplitude de ce pic augmente avec la concentration en oxygène, tant que celle-ci est inférieure à la teneur en vanadium. Dans le deuxième régime, lorsque la concentration en oxygène est supérieure à la teneur en vanadium, on assiste à l'apparition d'un pic à basse température («P1») à 400 K. D'après Carlson et al. [12], le pic P1 correspond à la diffusion de l'oxygène dans le Nb pur, alors que le pic P2 est lié à la dissociation du groupe oxygène-vanadium. Nous avons réalisé une étude systématique en utilisant notre approche multi-échelles, qui nous a permis de reproduire l'évolution des deux régimes. Nous avons également appliqué le modèle de Koiwa [13,14] qui permet d'analyser les effets des concentrations de complexes V-O et de montrer que les pics IF ne correspondent à des fréquences de saut élémentaires, mais à des fonctions complexe de celles-ci.

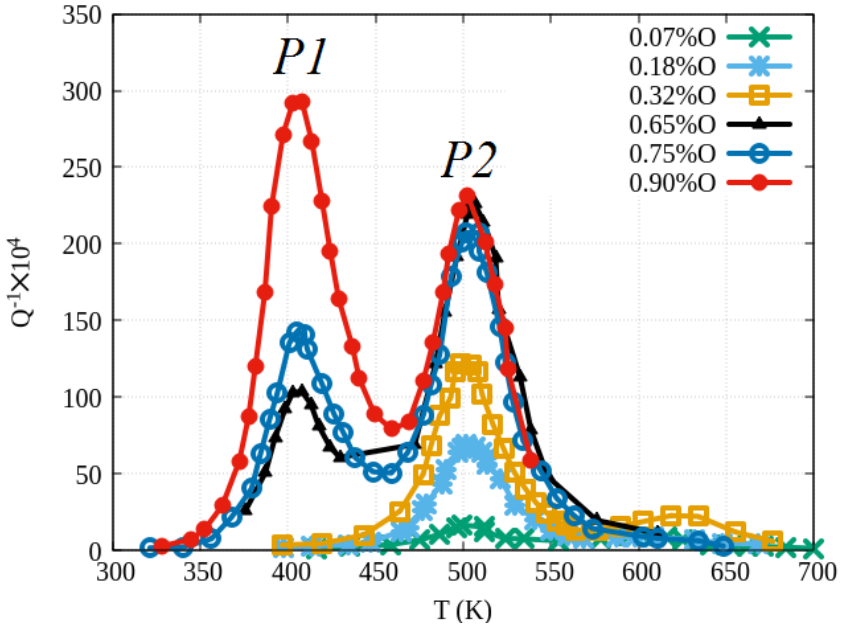

Figure 76: Courbes IF expérimentales pour les alliages Nb-0,50% V à différentes concentrations en oxygène. Courbe expérimentale extraite de [12].

Au chapitre 4, nous présentons une étude préliminaire sur l'effet du carbone sur la cinétique de la précipitation α' sous irradiation. Les atomes de carbone ont une interaction attractive avec les lacunes (entre 0,4 et 0,6 eV selon les calculs DFT [15,16]), ce qui ralentit la diffusion

de celles-ci. Lors d'un vieillissement thermique, cela ne ralentit pas la diffusion des atomes substitutionnels (Fe et Cr) et donc la cinétique de précipitation, car de nouvelles lacunes sont créées afin de maintenir la concentration de lacunes à l'équilibre thermique. Sous irradiation, la création d'un excès de lacunes et d'auto-interstitiels accélère la précipitation de la phase α'. Nous montrons que l'effet d'une addition de carbone sur la cinétique de précipitation du Cr dans alliage Fe-18% Cr à une température de 563 K et irradiée à un débit de dose de $10^{-3}\,\mathrm{dpa/s}$ dépend du mécanisme d'élimination des défauts ponctuels dominant. Lorsque l'élimination des lacunes est dominée par les puits, leur ralentissement par le carbone est entièrement compensé par une augmentation de leur concentration. Par conséquent, la concentration en carbone n'a pas d'effet sur la diffusion du Cr. En revanche, lorsque la contribution des recombinaisons est significative, la compensation est partielle et les atomes de carbone peuvent réduire l'accélération de la précipitation du Cr par l'irradiation. Les recombinaisons sont favorisées, par une faible mobilité et une forte concentration de lacunes et d'auto-interstitiels : à basses températures, à des débits de dose élevés et à de fortes concentrations de carbone.

Références

[1] K.E. Blazek, J.R. Cost, Carbon Diffusivity in Iron-Chromium Alloys, Transactions of the Japan Institute of Metals. 17 (1976) 630–636. doi:http://doi.org/10.2320/matertrans1960.17.630.

[2] M.A. Matosyan, V.M. Golikov, Effect of prior cold plastic deformation on diffusion of Carbon in alloys with iron base, Fizika Metallov i Metallovedenie. 25 (1968) 377–379.

[3] C.R. Ward, G.M. Leak, Mobilita di piccole aggiunte di elementi interstiziali in leghe ferrose, Metallurgical Italiana. 62 (1970) 302–306.

[4] P. Liu, W. Xing, X. Cheng, D. Li, Y. Li, X.Q. Chen, Effects of dilute substitutional solutes on interstitial carbon in α-Fe: Interactions and associated carbon diffusion from first-principles calculations, Physical Review B. 90 (2014) 024103.

[5] H. Numakura, Solute–Solute Interaction in α IRON: The Status QUO, Archives of Metallurgy and Materials. 60 (2015) 2061–2068. doi:https://doi.org/10.1515/amm-2015-0349.

[6] M.J. Konstantinovic, W. Van Renterghem, M. Matijasevic, B. Minov, M. Lambrecht, T. Toyama, M. Chiapetto, L. Malerba, Mechanical and microstructural properties of neutron irradiated Fe–Cr–C alloys, Physica Status Solidi (A). 213 (2016) 2988–2994. doi:10.1002/pssa.201600316.

[7] H. Saitoh, N. Yoshinaga, K. Ushioda, Influence of substitutional atoms on the Snoek peak of carbon in b.c.c. iron, Acta Materialia. 52 (2004) 1255–1261. doi:10.1016/j.actamat.2003.11.009.

[8] D.F. Hasson, R.J. Arsenault, Substitutional-interstitial interactions in bcc alloys, in: Treatise on Materials Science and Technology: Materials Science Series, 1972nd ed., n.d.

[9] M.A. Krishtal, V.I. Baranova, Temperature Dependence of the vacancy concentration in iron-chromium and iron-molybdenum, Fizika Metallov i Metallovedenie. 16 (n.d.) 626–628.

[10] M. Bouhafs, B. Dubois, Influence of the Carbon Content on the Internal Friction of Iron-17% Chromium Alloys, in: Internal Friction and Ultrasonic Attenuation in Solids, Pergamon Press, England, 1979: pp. 343–348. doi:https://doi.org/10.1016/B978-0-08-024771-7.50060-0.

[11] I.S. Golovin, M.S. Blanter, R. Schaller, Snoek Relaxation in Fe-Cr Alloys and Interstitial-Substitutional Interaction, Physica Status Solidi (A). 160 (1997) 49–60. doi:10.1002/1521-396X(199703)160:1<49::AID-PSSA49>3.0.CO;2-P.

[12] O.. N.. Carlson, H. Indrawirawan, C.V. Owen, O. Buck, Internal Friction Study of Substitutional-Interstitial Interaction in Niobium-Vanadium Alloys, METALLURGICAL TRANSACTIONS A. 18 (1987) 1415–1420. doi:https://doi.org/10.1007/BF02646655.

[13] M. Koiwa, Theory of the Snoek Effect in Ternary B.C.C alloys, Philosophical

Magazine. 24 (1971) 81–106. doi:http://dx.doi.org/10.1080/14786437108216426.

[14] M. Koiwa, Theory of the Snoek Effect in Ternary B.C.C. Alloys : II. Simplified Treatment, Philosophical Magazine. 24 (1971) 107–122.

[15] C. Barouh, T. Schuler, C.C. Fu, M. Nastar, Interaction between vacancies and interstitial solutes (C, N, and O) in α-Fe: From electronic structure to thermodynamics, Physical Review B. 90 (2014) 054112. doi:10.1103/PhysRevB.90.054112.

[16] T. Jourdan, C.C. Fu, L. Joly, J.L. Bocquet, M.J. Caturla, F. Willaime, Direct simulation of resistivity recovery experiments in carbon-doped α-iron, Physica Scripta. 2011 (2011) 014049.

Modélisation de la diffusion des impuretés interstitielles et de leur impact sur le vieillissement des aciers ferritiques

Mots clés: diffusion dans les solides, simulations Monte Carlo, Frottement Interne, Diffusion de traceur, physique du solide

Résumé: Nous modélisons la diffusion des atomes interstitiels (C et O) dans des solutions solides (Fe-Cr et Nb-V) et comparons nos résultats aux données expérimentales disponibles dans la littérature. Un ensemble d'énergies de liaisons entre interstitiels et solutés substitutionnels, et de barrières de migration des interstitiels, ont d'abord été calculés en utilisant la théorie de la fonctionnelle de la densité. Des modèles d'interactions de paires ont ensuite été ajustés sur ces données pour calculer les barrières de migration dans n'importe quel environnement chimique local. Ces modèles de paires sont enfin intégrés dans des simulations Monte Carlo cinétiques, afin de modéliser des expériences de diffusion de traceur et de frottement interne. Dans les alliages Fe-Cr-C, les simulations prévoient la formation d'un pic de Snoek unique, dans tout le domaine de composition entre le fer pur et le chrome pur. La barrière de migration moyenne du carbone, donnée par la température de ce pic, augmente progressivement avec la teneur en chrome, l'augmentation étant très faible en dessous de 6% de Cr. Dans les alliages riches en Cr, la barrière de migration moyenne obtenue lors d'une simulation de diffusion de traceur est plus grande que celle obtenue lors d'une simulation de frottement interne. Nous en concluons que la barrière mesurée lors d'une expérience de diffusion de traceur est fortement affectée par le piégeage du carbone dans des environnements riches en fer, qui limite la diffusion à grande distance ; alors que la barrière mesurée par friction interne, qui ne nécessite qu'une diffusion à courte distance, est principalement contrôlée par les barrières de migration des configurations les plus probables. Dans les alliages Nb-V-O dilués, les simulations font apparaitre un pic de Snoek à haute température lorsque la concentration en oxygène est plus faible que celle en vanadium. Quand la concentration en oxygène devient plus importante, un deuxième pic apparait à plus basse température, tandis que le premier pic se déplace vers des températures plus petites. Nous en concluons que le pic à haute température correspond à des paires V-O, et que celui à basse température correspond à la diffusion de l'oxygène dans le niobium pur. Les simulations sont utilisées pour tester le modèle de Koiwa, dans la limite de l'alliage ternaire infiniment dilué. Les deux approches sont en bon accord et nous montrons que la position du pic à haute température n'est pas reliée à une fréquence de saut unique, mais à une fonction complexe de plusieurs fréquences de sauts. Nous présentons enfin les résultats d'une étude préliminaire sur l'effet du carbone sur les cinétiques de séparation de phases dans les alliages fer-chrome irradiés. Nous montrons que la forte attraction entre atomes de carbone et défauts d'irradiation (auto-interstitiels et surtout lacunes) peut dans certaines conditions limiter l'accélération de la précipitation du chrome habituellement provoquée par l'irradiation.

Modeling the diffusion of interstitial impurities and their impact on the ageing of ferritic steels.

Keywords: diffusion in materials, Monte Carlo simulations, Internal Friction, Tracer Diffusion, solid-state physics

The diffusion of interstitial atoms (C and O) in bcc solid solutions (Fe-Cr and Nb-V) is modelled and compared to experimental data. A set of binding energies and migration barriers for the direct interstitial diffusion mechanism in different local chemical environments are first calculated using Density Functional Theory. Two different pair interaction models are developed in order to reproduce these data and predict the migration barriers in all possible environments. The diffusion models are then implemented in a kinetic Monte Carlo method to simulate tracer diffusion experiments, using a standard procedure, and internal friction experiments, using a novel method. In the Fe-Cr-C systems our internal friction simulations show a unique Snoek peak in the whole concentration range, between pure iron and pure chromium. The average migration enthalpy for C diffusion in Fe-Cr alloys is found to increase progressively with the Cr concentration, with a small rate below 6 %Cr. In Cr-rich alloys, the effective migration barrier for C diffusion is found to be larger in tracer diffusion than in the internal friction simulations. We conclude that the effective migration barrier extracted from tracer diffusion is closely related to trapping effects of C atoms in Fe-rich local environments, whereas the migration barrier associated with internal friction is mainly controlled by the spectrum of migration barriers of the most frequent configurations, as it is clearly shown in the Cr-rich domain. In the dilute Nb-V-O alloys, we find a high temperature Snoek peak when the concentration of oxygen is lower than the vanadium content. But when the oxygen concentration is higher, we see the appearance of a second peak but at a lower temperature and a shift of the first peak to lower temperatures. We conclude that the high temperature peaks correspond to the oxygen-vanadium pairs, and the low temperature peak corresponds to the oxygen Snoek peak in pure Nb. We also use our model in order to validate the Koiwa model in infinitely dilute ternary alloys. Both approaches are in good agreement and we observe that the high temperature peak cannot be directly related to a single jump frequency but to a complex function of them. We also show preliminary results on the effect of C in the precipitation of the Fe-Cr phase separation under irradiation. We observee that a strong attraction between carbon atoms and point defects (vacancies and self-interstitials) might be able to slow down the acceleration of the α' precipitation.